Two Dimensional Superconductors for Infrared Photodetection

Gavin John Orchin

Submitted in fulfilment of the requirements for the degree of Doctor of Philosophy

James Watt School of Engineering
University of Glasgow
Scotland
April 2021

Abstract

There is increasing interest in discovering novel superconducting materials for use in photodetection. Superconductivity has for a long time been known to exist in layered materials but with recent advances in two dimensional (2D) materials processing, it is now possible to cleave these materials down to single and few layer thicknesses. For the first time we are now in a position to fabricate superconducting strips that are only a single molecular layer thick. Such an ultimately thin material offers exciting possibilities in both photodetection and materials science research. Presented here, is an original work investigating the photoresponse of few-layered niobium diselenide ($NbSe_2$), a superconducting transition metal dichalcogenide.

Current biased $NbSe_2$ samples were tested optically at 1550 nm at cryogenic temperatures down to 350 mK. They show bolometric behaviour where the output signal amplitude increases with absorbed laser energy. At high currents, samples were observed to latch to intermediate resistances and become less sensitive to further laser excitations. A model has been developed which describes the observations as the result of a thermally stable hotspot due to the balance of Joule heating and in-plane heat conduction.

These measurements mark the first successful demonstration of a photo-response in an exfoliated superconducting sample and will hopefully pave the way for future integration of 2D materials in complex optical systems.

Contents

List of Figures

Acknowledgements

I would like to thank my supervisor, Professor Robert Hadfield, for offering me this PhD position and for his continued support throughout my work. Robert has been approachable, encouraging and generous with his time. I have been lucky to have him as my supervisor. I would also like to thank my second supervisor, Dr Alessandro Casaburi, who always showed a keen interest in my research and made himself available for valuable discussions.

I am grateful to Dr Robert Heath for sharing his experimental knowledge, python programs and coffee. He welcomed me to the research group and made me feel like part of it. I'd also like to thank Dr Luke Baker who was an instrumental guide during my first experiments. It was a pleasure to work alongside Dr Kleanthis Erotokrito, Dr Robert Kirkwood and Dr Chandra Natarajan who made this journey an enjoyable one. To the rest of the Quantum Sensors Group, thank you all for the camaraderie and making me feel like part of a team. I have greatly valued our time together.

I thank my collaborators for making this project possible, especially Dr Domenico de Fazio and Dr Matthew Hamer for their dedicated work during fabrication difficulties. I would also like to acknowledge the Engineering and Physical Sciences Research Council (EPSRC) for funding my studentship.

Special thanks go to my family for their encouragement and interest in my research. I hope to see you all more frequently in the future. Finally, I would like to thank my best friend and partner Nicola for her unending support, both practical and emotional. She has pushed me to succeed and given me something to look forward to at the end of each week. I am eternally grateful to have her in my life.

Author's declaration

Name: Gavin John Orchin
Registration Number:

I certify that the thesis presented here for examination for a PhD degree of the University of Glasgow is solely my own work other than where I have clearly indicated that it is the work of others (in which case the extent of any work carried out jointly by me and any other person is clearly identified in it) and that the thesis has not been edited by a third party beyond what is permitted by the University's PGR Code of Practice.

I declare that the thesis does not include work forming part of a thesis presented successfully for another degree.

I declare that this thesis has been produced in accordance with the University of Glasgow's Code of Good Practice in Research.

I acknowledge that if any issues are raised regarding good research practice based on review of the thesis, the examination may be postponed pending the outcome of any investigation of the issues.

Signature: .....

Date: .....

Definitions and abbreviations

Acronyms

1D	One Dimensional
2D	Two Dimensional
AC	Alternating Current
ADI	Alternating Direction Implicit
AFM	Atomic Force Microscope
BCS	Bardeen, Cooper and Schrieffer
CNP	Charge Neutrality Point
CPW	CoPlanar Waveguide
DBR	Distributed Bragg Reflector
DC	Direct Current
DCR	Dark Count Rate
EM	Electro-Magnetic
FWHM	Full Width at Half Maximum
IPA	IsoPropyl Alcohol
IR	InfraRed
KID	Kinetic Inductance Detector
LIDAR	LIght Detection And Ranging
NEP	Noise Equivalent Power
QP	QuasiParticle
PMMA	PolyMethyl MetAcrylate
PPG	Pulse Pattern Generator
PTE	Photo-Thermoelectric Effect
PVA	PolyVinyl Alcohol
RF	Radio Frequency
RIE	Reactive Ion Etching
RMS	Root Mean Square
SEM	Scanning Electron Microscope
SLD	SuperLuminescent Diode
SNSPD	Superconducting Nanowire Single Photon Detector
SQUID	Superconducting QUantum Interference Device

SMF	Single Mode Fibre
STJ	Superconducting Tunnel Junction
TES	Transition Edge Sensor
TMD	Transition Metal Dichalcogenides

Mathematical symbols

Unless otherwise stated, the following definitions apply throughout this document:

A	Magnetic vector potential
B	The magnetic flux density
c	Volumetric heat capacity
D	Electric displacement field strength
d	Depth of the superconductor
E	Electric field strength
$E_{50\%}$	Pulse energy resulting in 50% count rate
e	Elementary charge
H	Magnetic field strength
h	Planck's constant
$\hbar$	Reduced Planck's constant
I	Current
I_c	Superconducting critical current
I_{latch}	Current required for a self sustaining hotspot
I_r	Retrapping current
J	Current density
k_B	The Boltzmann constant
L	Total superconductor length in the direction of current flow
L_k	Kinetic inductance
l	Resistive region length
$l_{1,2}$	Steady state solutions for the self sustaining resistive length
M	Magnetization field strength
m_e	Electron rest mass
$N(0)$	Density of states at the Fermi energy
n	Charge carrier density
n'	Complex refractive index
P	Polarization field strength
P_J	Power density of Joule heating
P_L	Laser power density
P_{SS}	Power necessary to balance heat flow in the steady state
p	Momentum
q	Electric charge
R	Resistance

R_N	Normal state resistance immediately above superconducting transition
R_S	Series resistance measured in the superconducting state
S	Poynting vector
T	Temperature
T_b	Ambient temperature
T_c	Superconducting critical temperature
t	Time
V	Potential difference
v	Velocity
w	Width of superconductor perpendicular to current flow
x	Position
α	Thermal boundary conductivity per unit area
Δ	The superconducting energy gap
ϵ_0	The permittivity of free space
η	Thermal healing length
η_{DDE}	Device detection efficiency
η_{SDE}	System detection efficiency
κ	Thermal conductivity
λ	The superconducting penetration length
μ_0	The permeability of free space
ξ	The superconducting coherence length
ρ	Resistivity
ρ_b	Bound charge density
ρ_f	Free charge density
σ	Standard deviation
Φ	Magnetic flux
Ψ	Wavefunction
ω_D	Debye frequency
∇	The differential operator, del

Chemical symbols

Au	Gold
$Bi_2Sr_2CaCu_2O_{8+\delta}$	Bi-2212
C_2F_6	Hexafluoroethane
C_4F_8	Octafluorocyclobutane
CF_4	Carbon tetrafluoride
CHF_2	Fluoroform
FeSe	Iron selenide
hBN	Hexagonal boron nitride
^{3}He	Helium-3

^4He	Helium-4
InGaAs	Indium gallium arsenide
$NbSe_2$	Niobium diselenide
MoS_2	Molybdenum disulfide
Pd	Paladium
SF_6	Sulphur hexafluoride
Si	Silicon
SiO_2	Silicon dioxide
Ti	Titanium

Chapter 1

Introduction

1.1 Motivation

The detection of light and other electro-magnetic (EM) waves is a critical technology that has a great many applications across a wide technological remit. From astronomy to communications to computing and metrology the detection of light is of the utmost importance. Optical communications operate in the telecommunications band at wavelengths of 1330nm-1550nm. This wavelength band is used for two chief reasons, the photons are non-ionizing and therefore inherently safe at low powers, but most importantly semiconductor oxides have very low absorption is this region. Therefore high transmission, low loss fibre optic cables can be made. The challenge of operating at these wavelengths arises from the same issue: the photon energy is below the band-gap of silicon. This means that traditional silicon p-n junctions have little to no sensitivity to the light signals. Therefore there is a demand for high sensitivity fast detectors for infrared communications and astronomy.

Superconducting detectors, having a energy gap on the order of milli electron-volts (meV) ($\approx 10^{-22}$ J) are capable of absorbing and detecting electromagnetic radiation deep into the infrared spectrum. Detectors such as the kinetic inductance detector (KID) have become the gold standard for infrared astronomy and single photon detectors such as the superconducting nanowire single-photon detector (SNSPD) are being actively researched for single photon counting technologies such as quantum key distribution and LIDAR (light detection and ranging).

In 2006 the first truly two dimensional (2D) material was discovered. Graphene, a new allotrope of carbon, was first isolated by peeling a layer of Scotch Tape from a large graphite crystal before placing this tape onto an oxidized silicon wafer. Small crystals (1-10 μm) of graphene and few layered graphite can then be seen with a simple optical microscope. Since then many layered materials have been exfoliated and found to be stable in single layer form. Graphene itself has been shown to have excellent electrical conductivity and mobility while transistors have been fabricated from semiconducting 2D materials such as MoS_2. Most intriguingly, a few 2D superconductors have been discovered, the most stable of which, $NbSe_2$,

is a promising candidate for the realization of a 2D photodetector.

1.2 Thesis structure

I completed my PhD studies in Prof. Hadfield's Quantum Sensors group at the University of Glasgow. My work has principally involved the optical testing and data analysis of $NbSe_2$ samples that were fabricated by our collaborators at the Universities of Manchester and Cambridge.

Chapter 1 Details the motivation and structure of the thesis.

Chapter 2 serves as comprehensive overview of the theories and technologies relevant to this thesis. A brief overview of superconducting theory is given followed by a literature review of superconducting detectors covering the operating principle of each detector type. A review of photodetection using two dimensional (2D) materials follows and promising 2D superconducting materials are discussed for photodetection applications.

Chapter 3 describes the systems and processes that were experimentally used in this project. I begin with an overview of nanoscale fabrication techniques including: E-beam lithography, metal depositions, etching and 2D materials processing. Next the experimental set-up is discussed where I describe the operation of a pulse tube and sorption refrigerator to achieve temperatures down to 350 mK. I also describe the electrical and optical testing techniques employed for the characterisation of superconducting photodetectors. Finally I describe the method used to estimate the optical coupling efficiency to a $NbSe_2$ device.

Chapter 4 summarises the experimental results obtained, analysing device performance and investigating the detection mechanism. The central results of this chapter were published in Applied Physics Letters [1].

Chapter 5 describes the development of a thermal model of a $NbSe_2$ photodetector. Simulations of the device operation are performed and electrical output signals are compared with experimental results.

Chapter 6 summarises the outcomes of this project and ends with a discussion of possible future research topics in the field of 2D superconducting materials for photodetection applications.

Chapter 2

Background

This chapter provides an overview of the scientific discoveries and theories that are relevant for understanding the operation of a 2D superconducting photodetector. There is a discussion of the nature of superconductivity before moving on to the operating principles of several superconducting detectors. Photodetection methods for 2D materials are discussed and the methods of viewing and distinguishing the thickness of a multi-layered material are described.

2.1 Maxwell's equations

Listed below are James Clerk Maxwell's four equations describing electromagnetism in a vacuum in their derivative form.

$$\boldsymbol{\nabla} \cdot \boldsymbol{E} = \frac{\rho}{\epsilon_0} \tag{2.1}$$

$$\boldsymbol{\nabla} \cdot \boldsymbol{B} = 0 \tag{2.2}$$

$$\boldsymbol{\nabla} \times \boldsymbol{E} = -\frac{\partial \boldsymbol{B}}{\partial t} \tag{2.3}$$

$$\boldsymbol{\nabla} \times \boldsymbol{B} = \mu_0 \boldsymbol{J} + \frac{1}{c^2}\frac{\partial \boldsymbol{E}}{\partial t} \tag{2.4}$$

Where $\boldsymbol{E}$ is the electric field strength, ρ is the charge density, ϵ_0 is the permittivity of free space, $\boldsymbol{B}$ is the magnetic flux density, μ_0 is the permeability of free space, $\boldsymbol{J}$ is the current density and c is the speed of light in a vacuum.

When using Maxwell's equations in a medium, we are often not interested in the variation of the electric and magnetic fields on an atomic length scale but instead on the average fields over a macroscopic scale. Therefore the polarization ($\boldsymbol{P}$) and magnetization ($\boldsymbol{M}$) fields are introduced which are defined as the electric and magnetic dipole density within a medium.

The electric and magnetic fields are related to each other by the constitutive relations:

$$\epsilon_0 \boldsymbol{E} = \boldsymbol{D} - \boldsymbol{P} \tag{2.5}$$

$$\boldsymbol{B} = \mu_0 \boldsymbol{H} + \mu_0 \boldsymbol{M} \tag{2.6}$$

Where ($\boldsymbol{D}$) is the electric displacement field and ($\boldsymbol{H}$) is the magnetic field strength.

The macroscopic description of the electric and magnetic fields separates charges and currents into bound states and free states. Bound charges are charges which are fixed in place creating electric dipole moments. They are not free to move and are associated with a polarized medium. Similarly, bound currents are the currents which flow due to magnetization of the medium or a time-varying polarization.

$$\rho = \rho_f + \rho_b \tag{2.7}$$

$$\rho_b = -\boldsymbol{\nabla} \cdot \boldsymbol{P} \tag{2.8}$$

$$\boldsymbol{J} = \boldsymbol{J_f} + \boldsymbol{J_b} \tag{2.9}$$

$$\boldsymbol{J_b} = \boldsymbol{\nabla} \times \boldsymbol{M} + \frac{\partial \boldsymbol{P}}{\partial t} \tag{2.10}$$

Using the above definitions, Maxwell's four equations in a medium can be written as:

$$\boldsymbol{\nabla} \cdot \boldsymbol{D} = \rho_f \tag{2.11}$$

$$\boldsymbol{\nabla} \cdot \boldsymbol{B} = 0 \tag{2.12}$$

$$\boldsymbol{\nabla} \times \boldsymbol{E} = -\frac{\partial \boldsymbol{B}}{\partial t} \tag{2.13}$$

$$\boldsymbol{\nabla} \times \boldsymbol{H} = \boldsymbol{J_f} + \frac{\partial \boldsymbol{D}}{\partial t} \tag{2.14}$$

2.2 2D materials

A two dimensional (2D) material is the thinnest possible example of a material, a single molecular plane of the crystal. For a long period of time such 2D crystal structures were thought to be unstable due to thermal fluctuations. However, the discovery of graphene showed that such materials could exist [2]. Since then, there have been numerous examples found including insulators [3], semiconductors [4, 5] and superconductors [6]. Many of these materials have also have a large potential for applications in the field of optical communications, photon detection [7] and single photon generation [8].

Graphene itself possesses several unique and useful characteristics in this field. For example, it has an ultrawide absorption bandwidth from the terahertz to the ultraviolet [9] and a tunable

bandgap which can be formed by chemical doping or by the application of an electric field [10]. But graphene is not the only 2D material of interest for light detection [11]. Transition metal dichalcogenides (TMDs) are layered crystal materials which have strong intra-layer bonds but weak van der Waals bonds between layers [12]. Similarly to graphene, this property enables singular layers to be separated easily by mechanical exfoliation.

Figure 2.1: *An image of the exhibit for the discovery of graphene, Nobel Prize Museum, Stockholm. Photograph courtesy of R. Hadfield.*

2D materials are often similar in characteristics to their bulk counterparts; however, emergent or enhanced properties have been discovered [13–15]. Fabrication of heterostructures, materials that are comprised of several stacked 2D components, is a new research field. Heterostructures could potentially be designed to have novel characteristics or a combination of properties from several materials [16–18].

2.3 Superconductivity

2.3.1 The fundamental properties of superconductors

In 1908 Heike Kamerlingh Onnes succeeded in liquefying helium-4 (^{4}He) and began studying the properties of metals at low temperature. In 1911 he observed the resistance of mercury suddenly decrease to zero at 4.2 K. In doing so he inadvertently discovered superconductivity and its first characteristic property, zero DC resistance. Over the next several years, many elemental metals were observed to be superconducting at low temperatures. The temperature at which the superconducting transition occurs is a material dependent property known as the critical temperature (T_c).

Any resistance free metal would be expected to also possess perfect diamagnetism as any applied magnetic field would induce a circulating current in the metal which would act to exactly cancel the applied field. This would result in no magnetic flux penetrating the metal. However, it has been shown that the expulsion of magnetic fields from superconductors differs from this behaviour in a significant manner. The difference occurs when an initially normal material is cooled below its transition temperature in the presence of a magnetic field.

One would expect that the penetration of the magnetic field into the superconductor would be unaffected by the phase change because since there is no time varying field, there should be no induced current. However, a superconductor will expel an applied magnetic field as it is cooled through its transition temperature. This behaviour is known as the Meissner effect.

The expulsion of magnetic field from the superconducting volume requires energy and therefore the Meissner effect implies that the superconducting state will become energetically unfavourable in a large magnetic field. This implies that a strong magnetic field can destroy the superconducting state [19]. The magnetic field strength required to suppress superconductivity in a classical superconductor is called the thermodynamic critical field and is defined by the following equation:

$$F_{N,0} - F_{S,0} = \frac{B_c^2}{2\mu_0} = \frac{\mu_0 H_c^2}{2} \tag{2.15}$$

Where $F_{N,0}$ and $F_{S,0}$ are the free energy densities in the superconducting and normal states in zero magnetic field.

2.3.2 The London equations

To explain the Meissner effect, the brothers Fritz and Heinz London developed a macroscopic theory of superconductivity. They introduced two equations describing magnetic field penetration and current flow inside a superconductor. They also introduced a length scale over which the magnetic field decays which is now called the penetration depth.

$$\boldsymbol{E} = \mu_0 \lambda_L^2 \frac{d}{dt} \boldsymbol{J} \tag{2.16}$$

$$\boldsymbol{B} = -\mu_0 \lambda_L^2 \boldsymbol{\nabla} \times \boldsymbol{J} \tag{2.17}$$

$$\lambda_L = \sqrt{\frac{m_e}{\mu_0 n e^2}} \tag{2.18}$$

Equation 2.16 states that an electric field will cause continual acceleration of charge carriers rather than maintaining a constant average velocity as described by Ohm's Law. The London penetration depth, λ_L, is the value that would be expected from a theoretical perfect conductor whose charge carriers experience an accelerating force of $e|\boldsymbol{E}|$ [19].

Meissner effect and screening currents

By substituting the time independent value of current density from equation 2.4 into equation 2.17, it can be shown that a magnetic field in a superconductor is described by the Helmholtz

equation:

$$\boldsymbol{B} = -\mu_0 \lambda^2 \, \boldsymbol{\nabla} \times \left(\frac{1}{\mu_0} \boldsymbol{\nabla} \times \boldsymbol{B} \right) \tag{2.19}$$

$$\boldsymbol{B} = -\lambda^2 \Big(\boldsymbol{\nabla} \big(\boldsymbol{\nabla} \cdot \boldsymbol{B} \big) - \nabla^2 \boldsymbol{B} \Big) \tag{2.20}$$

$$\nabla^2 \boldsymbol{B} = \frac{\boldsymbol{B}}{\lambda^2} \tag{2.21}$$

The London equations can be used to show the behaviour of zero DC resistance, magnetic field expulsion and quantization of magnetic flux through a superconducting loop.

To illustrate the mechanism by which a superconductor expels magnetic flux, I now apply the second London equation to a bulk superconductor in a magnetic field. The superconductor has a width (w) of 1 µm a penetration depth of 39 nm and a magnetic field is applied parallel to the Z axis as shown in figure 2.2 a). The superconductor is assumed to be much longer in the Z axis than the penetration depth so that the $\boldsymbol{H}$ field can be regarded as continuous at the superconductor boundary. Solving equation 2.21 for $|x| < w/2$ gives the magnetic field decay within the superconductor. The induced screening currents can be found by then applying equation 2.10:

$$B_z(x) = B_0 \frac{\cosh(x/\lambda)}{\cosh(w/2\lambda)} \tag{2.22}$$

$$\mu_0 \, H_z = B_0 \tag{2.23}$$

$$\mu_0 \, M_z(x) = B_0 \left(\frac{\cosh(x/\lambda)}{\cosh(w/2\lambda)} - 1 \right) \tag{2.24}$$

$$J_y(x) = \frac{-B_0 \, \sinh(x/\lambda)}{\mu_0 \, \lambda \, \cosh(w/2\lambda)} \tag{2.25}$$

The interior of a superconductor is shielded from the magnetic field by circulating screening currents which flow around the surface of the material. The screening current is associated with the magnetization of the medium which exactly cancels with the applied magnetic field in all but the surface layer of the superconductor [20].

Figure 2.2 plots equations 2.22 - 2.25 showing how an applied magnetic field, B_0, is screened from the interior of a superconductor.

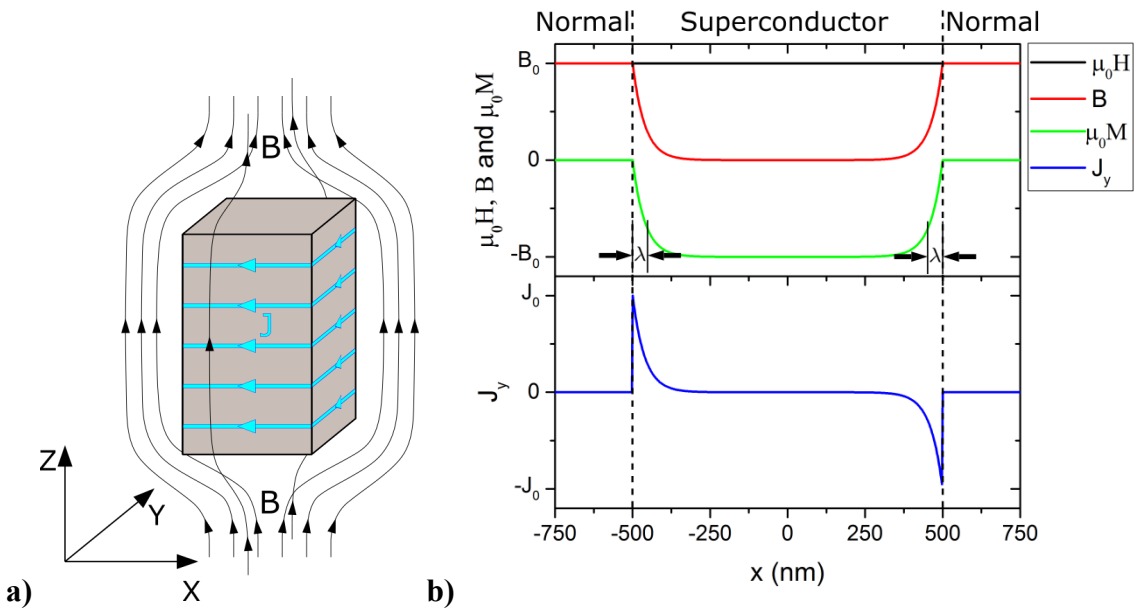

Figure 2.2: ***a)*** *A diagram showing the magnetic field lines around a superconductor. The induced current density, J, screens the superconductor from the magnetic field.* ***b)*** *A graph showing the penetration of the magnetic fields in the superconductor and the density of current along a cross section of the superconductor. The formulae of the plots are shown in equations 2.22 - 2.25. Also shown is the penetration depth* $\lambda = 39\,nm$.

Flux quantization

The Meissner effect states that magnetic flux cannot penetrate the interior of a bulk superconductor. However flux can still penetrate through a hole in a superconductor such as when the superconductor is shaped as a hollow cylinder or ring. In 1950 Fritz London calculated the flux through such a hole as:

$$\Phi' = \iint_S \boldsymbol{B} \cdot d\boldsymbol{S} + \mu_0 \lambda^2 \oint_C \boldsymbol{J} \cdot d\boldsymbol{l} \tag{2.26}$$

$$\Phi' = \iint_S \left(\boldsymbol{B} + \mu_0 \lambda^2 \boldsymbol{\nabla} \times \boldsymbol{J}\right) \cdot d\boldsymbol{S} \tag{2.27}$$

Where $\boldsymbol{S}$ is a surface bounded by the line $\boldsymbol{C}$.

In equation 2.26, the first term is the flux passing through the surface $\boldsymbol{S}$ and the second term is the flux outside the surface $\boldsymbol{S}$ which penetrates into the superconductor in the vicinity of a hole.

If the surface $\boldsymbol{S}$ does not contain a hole in the superconductor, then by the second London equation (equation 2.17) it is clear that $\Phi' = 0$. Since $\Phi' = 0$ for all surfaces except those containing holes, the value of Φ' must be independent of the chosen surface around a hole. If the magnetic field is written as the curl of the magnetic vector potential, $\boldsymbol{A}$, and the Bohr-Sommerfeld condition is then applied, it can be shown that the value of Φ' must be quantized.

$$\Phi' = \iint_S \boldsymbol{\nabla} \times \boldsymbol{A} \cdot d\boldsymbol{S} + \mu_0 \lambda^2 \oint_C \boldsymbol{J} \cdot d\boldsymbol{l} \tag{2.28}$$

$$\Phi' = \oint_C \left(\boldsymbol{A} + \mu_0 \lambda^2 \boldsymbol{J}\right) \cdot d\boldsymbol{l} \tag{2.29}$$

$$\Phi' = \frac{1}{2e} \oint_C \left(2e\boldsymbol{A} + 2m_e \boldsymbol{v}\right) \cdot d\boldsymbol{l} \tag{2.30}$$

$$\Phi' = \frac{1}{2e} \oint_C \boldsymbol{p} \cdot d\boldsymbol{l} \tag{2.31}$$

$$\Phi' = \frac{nh}{2e} = n\Phi_0 \tag{2.32}$$

Where n is an integer, h is Planck's constant and Φ_0 is the magnetic flux quantum. Equation 2.32 states that the flux through and in the vicinity of a hole through a superconductor must be a multiple of the flux quantum Φ_0.

2.3.3 Ginzburg-Landau theory

The next theoretical breakthrough in superconductivity was made in 1950 with the publication of Ginzburg-Landau theory [21]. This theory sought to improve upon the London theory in two respects: Firstly, the London equations make no reference to a field dependent density of superconducting carriers even though it was known that a strong magnetic field could destroy the superconducting state. Secondly, the London equations assume no spatial dependence of the density of superconducting carriers inside a superconducting volume. This leads to the problem that in a strong magnetic field, the surface energy of the superconductor would be negative, driving the superconductor to split into several volumes. However, the surface energy had experimentally been measured to be positive.

In the absence of an applied magnetic field, the superconducting transition is of second order at T_c. Landau's theory of phase transitions states that all second order transitions can be described by an order parameter (ψ). The order parameter describes the degree of order in the system, having the value of zero in the disordered phase (normal) and non-zero in the ordered phase (superconducting). Ginzburg and Landau suggested that the order parameter describing the superconducting transition was an effective wavefunction describing the density of the superconducting carriers.

$$n_s = 2|\psi(\boldsymbol{r})|^2 \tag{2.33}$$

ψ is assumed to be a complex scalar field and can therefore be written with an amplitude ($|\psi|$) and a phase (ϕ):

$$\psi(\boldsymbol{r}) = |\psi(\boldsymbol{r})|e^{i\phi} \tag{2.34}$$

Writing the current as being carried by particles of mass, m^* and charge, q, the free energy density of the superconducting state can be written as:

$$F_S = F_{N,0} + \alpha|\psi(\boldsymbol{r})|^2 + \frac{\beta}{2}|\psi(\boldsymbol{r})|^4 + \frac{1}{2m^*}\Big|\big(-i\hbar\boldsymbol{\nabla} - q\boldsymbol{A}\big)\psi(\boldsymbol{r})\Big|^2 + \frac{B^2(\boldsymbol{r})}{2\mu_0} - \mu_0\boldsymbol{H}(\boldsymbol{r})\cdot\boldsymbol{M}(\boldsymbol{r}) \tag{2.35}$$

The first term of equation 2.35 is the free energy density in the normal state with no magnetic field present. The second and third terms are the first two terms in a power series expansion of the order parameter. This form comes from Landau's theory of second order phase transitions and should be valid near the transition temperature where the order parameter is close to zero. The forth term is the gauge invariant kinetic energy written using quantum mechanical operators. The fifth term is the energy density of the magnetic field and the last term is the energy due to magnetization of the superconductor.

Remarkably, equation 2.35 can describe the free energy of the superconducting state in any superconductor and it has only two material dependent quantities, α and β. It is assumed that near T_c, they have the following temperature dependencies:

$$\alpha(T) \approx \alpha_0\big(\frac{T}{T_c} - 1\big) \tag{2.36}$$

$$\beta(T) \approx \beta_0 \tag{2.37}$$

If you calculate the minimum of equation 2.35 with respect to changes in the order parameter and the vector potential you arrive at the two Ginzburg-Landau equations:

$$0 = \alpha\psi + \beta|\psi|^2\psi + \frac{1}{2m^*}\big(-i\hbar\boldsymbol{\nabla} - q\boldsymbol{A}\big)^2\psi \tag{2.38}$$

$$\frac{1}{\mu_0}\boldsymbol{\nabla}\times\boldsymbol{B} = \boldsymbol{J} = \frac{-i\hbar q}{2m^*}\big(\psi^*\boldsymbol{\nabla}\psi - \psi\boldsymbol{\nabla}\psi^*\big) - \frac{q^2}{m^*}\boldsymbol{A}|\psi|^2 \tag{2.39}$$

Equation 2.38 is very similar to the Schrödinger equation for a charged particle of energy $-\alpha$, the only difference being the addition of the non-linear second term. 2.39 is the usual quantum mechanical equation for current density and can be rewritten in terms of the velocity of the charge carriers:

$$\boldsymbol{J} = \frac{q}{m^*}\big(\hbar\boldsymbol{\nabla}\phi - q\boldsymbol{A}\big)|\psi|^2 = q\boldsymbol{v}_s|\psi|^2 \tag{2.40}$$

where ϕ is the phase of the order parameter and $\boldsymbol{v}_s$ is the velocity of charge carriers.

Material parameters α and β

Two material dependent parameters were used in forming the Ginzburg-Landau equations but their relationship to measurable quantities is yet to be defined. In Ginzburg-Landau theory the order parameter varies in space, asymptotically approaching a constant value (ψ_∞) deep within a superconductor where there is no magnetic field or surface effects. Evaluating equation 2.38 under these conditions:

$$0 = \alpha\psi_\infty + \beta|\psi_\infty|^2\psi_\infty \tag{2.41}$$

$$|\psi_\infty|^2 = \frac{-\alpha}{\beta} \tag{2.42}$$

Substituting this value for the order parameter into equation 2.35 for the zero field case and using the definition of the thermodynamic critical field from equation 2.15 gives:

$$F_{N,0} - F_{S,0} = \frac{\alpha^2}{2\beta} = \frac{\mu_0 H_c^2}{2} \tag{2.43}$$

$$\alpha = -\frac{\mu_0\, H_c^2}{|\psi_\infty|^2} \tag{2.44}$$

$$\beta = \frac{\mu_0\, H_c^2}{|\psi_\infty|^4} \tag{2.45}$$

Equations 2.44 and 2.45 show that the values of α and β depend solely on the density of the superconducting charge carriers in a bulk sample and on the magnitude of the thermodynamic critical field.

Length scales

One of the goals of Ginzburg-Landau theory was to show how surface boundaries affected the superconducting state. Solving equation 2.38 at the boundary of a superconductor, the value of the order parameter as a function of position can be calculated. For an infinite superconductor meeting a normal material at the plane x=0, with zero magnetic field, the solution is:

$$\psi = \psi_\infty \tanh\left(\frac{x}{\sqrt{2}\,\xi}\right) \quad \text{for } x \geq 0 \tag{2.46}$$

$$\text{where: } \xi^2 = \frac{\hbar^2}{2m^*|\alpha|} \tag{2.47}$$

The coherence length, ξ, is then the length scale over which the order parameter can change substantially. In general, the order parameter will monotonically increase from zero at a sur-

face to a constant value deep within a superconductor. If the size of the superconductor is similar to the coherence length, the order parameter will be reduced throughout the superconducting volume.

In Ginzburg-Landau theory, the magnetic behaviour of a superconductor is almost the same as the London theory. The only difference is that the penetration depth (λ) depends on the order parameter and therefore on the magnetic field strength, temperature and geometry of the superconductor. λ approaches the London value λ_L deep within a superconductor.

$$\lambda_L^2 = \frac{m^*}{\mu_0 q^2 |\psi_\infty|^2} \tag{2.48}$$

$$\lambda^2 = \frac{m^*}{\mu_0 q^2 |\psi|^2} \tag{2.49}$$

Ginzburg-Landau critical current

The maximum current density will occur when there is no magnetic field contribution to the free energy density and $|\psi|$ has no spatial dependence. This will be the case for a thin superconducting wire with a thickness smaller than the coherence length and penetration depth. The free energy density of the superconducting state can then be written as:

$$F_S = F_N + \alpha|\psi|^2 + \frac{\beta|\psi|^4}{2} + \frac{m^* \boldsymbol{v}_s^2 |\psi|^2}{2} \tag{2.50}$$

The optimum value of the charge carrier density can then be calculated as a function of velocity by minimizing the free energy.

$$0 = \alpha + \beta|\psi|^2 + \frac{m^* \boldsymbol{v}_s^2}{2} \tag{2.51}$$

$$|\psi|^2 = |\psi_\infty|^2 \Big(1 + \frac{m^* \boldsymbol{v}_s^2}{2\alpha}\Big) \tag{2.52}$$

The current density as a function of velocity can now be calculated. It has a cubic dependence on velocity reaching a peak value when the carrier density drops to $^2/_3\,|\psi_\infty|^2$. The maximum current density which can be transported is the Ginzburg-Landau critical current density (J_c). The corresponding velocity of charge carriers is v_c.

$$\boldsymbol{J} = q\boldsymbol{v}_s|\psi|^2 \tag{2.53}$$

$$\boldsymbol{J} = q\boldsymbol{v}_s\left(1 - \frac{\boldsymbol{v}_s^2}{3v_c^2}\right)|\psi_\infty|^2 \tag{2.54}$$

$$J_c = qv_c\frac{2}{3}|\psi_\infty|^2 \tag{2.55}$$

$$\text{where: } v_c = \sqrt{\frac{-2\alpha}{3m^*}} \tag{2.56}$$

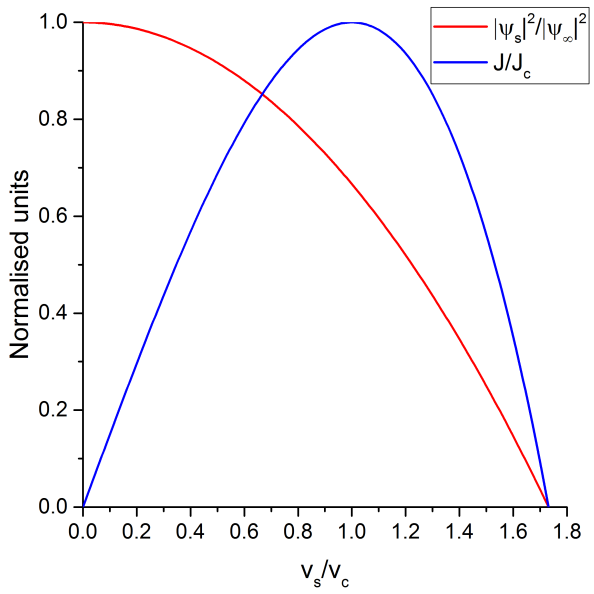

Figure 2.3: *A graph showing normalised values of carrier density and current density as a function of the supercurrent velocity.*

Kinetic inductance

A superconductor has no resistance to DC current; however, since the current is carried by particles with mass, it requires energy to change the current flow. Therefore a superconductor behaves as an inductor to alternating currents.

The potential difference across a superconductor with inductance L_k will be:

$$V = L_k\frac{dI}{dt} \tag{2.57}$$

The acceleration of charge carriers will be:

$$\frac{dv_s}{dt} = \frac{Vq}{lm^*} \tag{2.58}$$

Using equations 2.57 and 2.58, the kinetic inductance can be written as:

$$L_k = \frac{lm^*}{q}\left(\frac{dI}{dv_s}\right)^{-1} = L_k(0)\left(\frac{d}{dv_s}\left(\frac{v_s|\psi|^2}{|\psi_\infty|^2}\right)\right)^{-1} \tag{2.59}$$

$$\text{where: } L_k(0) = \frac{lm^*}{Aq^2|\psi_\infty|^2} = \frac{\mu_0 l\lambda_L^2}{A} \tag{2.60}$$

The order parameter cannot instantaneously change and so at high frequencies, it would be expected to respond to the average current rather than the instantaneous current. The order parameter can then be regarded as constant with respect to v_s and so at high frequencies:

$$\frac{L_k(I)}{L_k(0)} = \left(\frac{|\psi|^2}{|\psi_\infty|^2}\right)^{-1} \tag{2.61}$$

$$\frac{L_k(I)}{L_k(0)} = \frac{3}{1 + 2\cos\left(\frac{2}{3}\sin^{-1}\left(\frac{I}{I_c}\right)\right)} \tag{2.62}$$

and at low frequencies:

$$\frac{L_k(I)}{L_k(0)} = \left(3\frac{|\psi|^2}{|\psi_\infty|^2} - 2\right)^{-1} \tag{2.63}$$

$$\frac{L_k(I)}{L_k(0)} = \frac{1}{2\cos\left(\frac{2}{3}\sin^{-1}\left(\frac{I}{I_c}\right)\right) - 1} \tag{2.64}$$

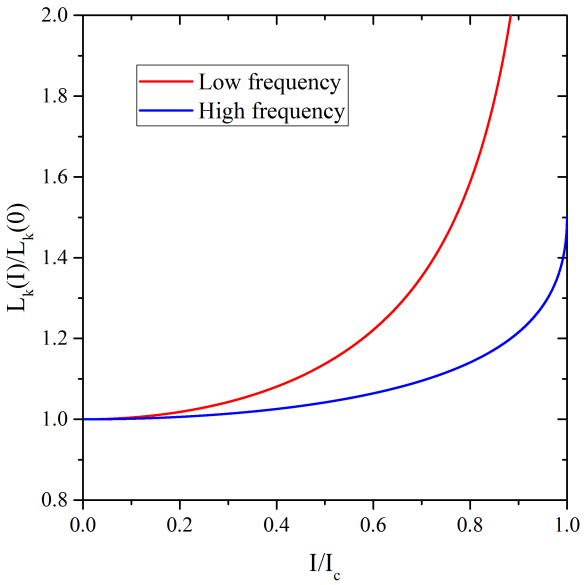

Figure 2.4: *The current dependence of the kinetic inductance of a thin superconducting wire at high and low frequencies.*

Fig. 2.4 shows that at high bias currents the kinetic inductance tends to infinity in the low frequency regime and to 1.5 $L_k(0)$ in the high frequency regime [22, 23] .

If a superconducting wire has a non-uniform cross-sectional area, the current density will vary across the wire's length. Therefore an experimentally observed switching current will be the current at which the thinnest section of wire turns resistive. Since just a fraction of the critical current can be applied to the wire, the kinetic inductance will show only a small increase before the wire switches to the normal state. In this way, the current dependence of the kinetic inductance can be used as a measure of the wire's uniformity [24].

Surface energy

One of the advantages of Ginzburg-Landau theory is the ability to describe the decrease and breakdown of superconductivity due to an applied magnetic field. In their seminal paper [21], one of the geometries they studied was a superconductor of infinite size that has a boundary with a normal state material along the plane $x = 0$. A magnetic field is applied parallel to the z-axis.

The free energy density of the superconductor is given by equation 2.35. Multiplying the first Ginzburg-Landau equation by the complex conjugate of the order parameter and substituting this value into 2.35 gives:

$$F_S = F_{N,0} - \frac{\beta|\psi(\boldsymbol{r})|^4}{2} + \frac{B^2(\boldsymbol{r})}{2\mu_0} - \mu_0 \boldsymbol{H}(\boldsymbol{r}) \cdot \boldsymbol{M}(\boldsymbol{r}) \tag{2.65}$$

$$F_S = F_{N,0} - \frac{\mu_0 H_c^2|\psi(\boldsymbol{r})|^4}{2|\psi_\infty|^4} + \frac{B^2(\boldsymbol{r})}{2\mu_0} - \mu_0 \boldsymbol{H}(\boldsymbol{r}) \cdot \boldsymbol{M}(\boldsymbol{r}) \tag{2.66}$$

Deep within the superconductor: $\psi = \psi_\infty$, $\boldsymbol{M} = -\boldsymbol{H}$ and $\boldsymbol{B} = 0$ and so the free energy density is:

$$F_S = F_{N,0} - \frac{\mu_0 H_c^2}{2} + \mu_0 H^2(\boldsymbol{r}) \tag{2.67}$$

Outside the superconductor, the free energy density is:

$$F_N = F_{N,0} + \frac{\mu_0 H^2(\boldsymbol{r})}{2} \tag{2.68}$$

Comparing equations 2.67 and 2.68 it is clear that when $H(\boldsymbol{r}) = H_c$, the free energy outside the superconductor will be exactly equal to the free energy deep within the superconductor. However, the free energy near the surface of the superconductor will be different. Near the surface of the superconductor, the free energy density will be increased because of a smaller order parameter but also decreased because of less magnetisation than in the bulk.

The surface energy is defined as the difference between the free energy in the bulk and at the surface when the critical field is applied:

$$\sigma = \int_{-\infty}^{\infty} \Big(- \frac{\beta|\psi(x)|^4}{2} + \frac{B^2(x)}{2\mu_0} - \mu_0 H_c M(x) - \frac{\mu_0 H_c^2}{2} \Big) dx \tag{2.69}$$

$$\sigma = \int_{-\infty}^{\infty} \Big(- \frac{\beta|\psi(x)|^4}{2} + \frac{\mu_0 M^2(x)}{2} \Big) dx \tag{2.70}$$

$$\sigma \approx \frac{\mu_0 H_c^2}{2} \int_0^{\infty} \left(- \tanh^4 \left(\frac{x}{\xi\sqrt{2}} \right) + \left(1 - \exp\left(\frac{-x}{\lambda} \right) \right)^2 \right) dx \tag{2.71}$$

The integrand of equation 2.70 is non-zero only near the surface of the superconductor. Deep within the superconductor the magnetization and order parameters reach their bulk values and their energy contributions cancel exactly. Therefore the magnitude and sign of the surface energy depends on the length scales over which the order parameter and magnetization reach their bulk values. These two length scales are respectively the coherence length, ξ, and the penetration depth, λ.

The Ginzburg-Landau parameter is the ratio of the coherence length and the penetration depth, $\kappa = \frac{\lambda}{\xi}$. Ginzburg and Landau showed that the surface energy is positive when $\kappa < \frac{\sqrt{2}}{2}$ and negative when $\kappa > \frac{\sqrt{2}}{2}$. Since experimental evidence at the time suggested that $\kappa << 1$ for all superconductors, a full analysis of a theoretical negative surface energy superconductor was not carried out and positive surface energy was considered a requirement for the stability of the superconducting state.

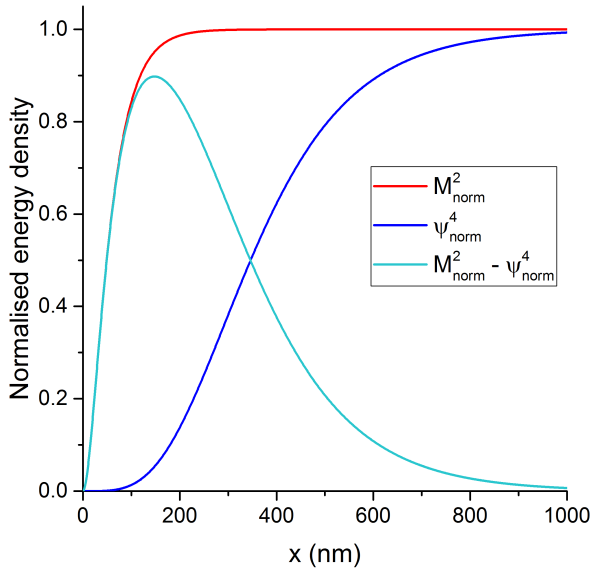

Figure 2.5: *A graph showing the normalised values of $M^2(x)$, $\psi^4(x)$ and the resulting positive surface energy for ξ =200 nm, λ =40 nm.*

2.3.4 Type I and type II superconductivity

In 1950 [21], Ginzburg and Landau only studied the possibility of positive surface energy, when $\kappa < \frac{\sqrt{2}}{2}$, since that was the only behaviour that had been observed up until that point. Such superconductors are now known as type I superconductors. In a type I superconductor, an applied magnetic field suppresses superconductivity completely when it exceeds the thermodynamic critical field as discussed in section 2.3.1.

In 1957, A. A. Abrikosov theoretically studied what would occur if $\kappa > \frac{\sqrt{2}}{2}$ and the surface energy was negative [25]. The magnetic behaviour of this type of superconductor was found to be drastically different from the behaviour of previously understood superconductors. Therefore, if $\kappa < \frac{\sqrt{2}}{2}$ the superconductor is called type I, and if $\kappa > \frac{\sqrt{2}}{2}$ it is called type II. In a strong magnetic field, a type II superconductor has the lowest free energy density at its surface, it is therefore driven to increase its surface area by creating lines of normal state material throughout its volume. When this occurs, the superconductor is said to be in the mixed state and in this way, superconductivity can persist in magnetic fields greater than the thermodynamic critical field (H_c).

The mixed state consists of a superconductor penetrated by a lattice of magnetic flux lines. At the centre of each flux line the order parameter is zero ($\psi = 0$) and so the core of each flux line is in the normal state. Circulating shielding currents flow around each of the flux lines, as described by the second London equation (2.17). Therefore, the flux lines penetrating a type II superconductor are referred to as vortices.

Since each vortex is a hole in the superconducting volume, it carries a quantised flux equal to the magnetic flux quantum Φ_0, as shown in section 2.3.2. When a magnetic field greater than a lower critical field (B_{c1}) is applied, vortices begin to penetrate the superconductor.

Their density increases with the magnetic field strength eventually forming a dense hexagonal lattice when the applied field is equal to the upper critical field (B_{c2}). If a field greater than B_{c2} is applied, the mixed state is destroyed and the material undergoes a second order transition to the normal state.

$$B_{c1} < B_c < B_{c2} \tag{2.72}$$

$$B_{c1} = \frac{B_c \ln(\kappa)}{\kappa\sqrt{2}} \tag{2.73}$$

$$B_{c2} = B_c \kappa \sqrt{2} \tag{2.74}$$

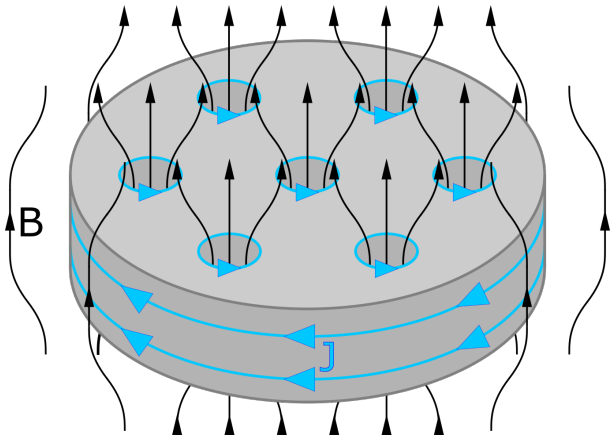

Figure 2.6: *A diagram depicting the mixed state of a cylindrical type II superconductor. Magnetic flux (black lines) penetrates the superconductor through vortices. Screening currents (blue lines) flow around the material's surface and around each of the vortices.*

2.3.5 BCS theory

Ginzburg-Landau theory was able to describe the breakdown of superconductivity due to high magnetic fields and its spatial dependence near surfaces. However, the theory doesn't describe the physical processes which causes superconductivity to exist and for this reason it was initially disregarded by the scientific community.

In 1956 L. N. Cooper investigated what would occur if a small attractive potential existed between two electrons in a metal at zero temperature [26]. He considered electrons of opposite spin and with a momentum greater than the Fermi momentum forming a pair, such a pair later became known as a Cooper pair. It was shown that the Cooper pair would always have an energy lower than the Fermi energy, no matter how small the attractive potential. It was theorised that electrons near the Fermi energy would form Cooper pairs and thereby create an energy gap, Δ. The energy gap would be the energy required per electron to separate a Cooper pair and is typically on the order of 1 meV. A Cooper pair is a boson rather than a fermion and therefore many Cooper pairs can share the same energy levels as each other. Similar to a charged superfluid, a system of Cooper pairs can flow without dissipation but will resist any rotational force such as the Lorentz force from an applied magnetic field.

The following year J. Bardeen, L. N. Cooper and J. R. Schrieffer published the first microscopic theory of superconductivity [27, 28]. They suggested that the attractive potential between electrons was due to electron-phonon interactions which was supported by the observed isotope effect, where a superconducting element will have a transition temperature that depends on its atomic mass. Since the electron attraction is mediated by phonons, the approximation was made that only electrons within $\hbar\omega_D$ of the Fermi energy are affected by the attractive potential.

Each Cooper pair in a superconductor has the same momentum. When no persistent current flows, this momentum is zero and so the electrons forming a Cooper pair have opposite momenta and spin to each other. When a current flows, the centre of mass momentum is non-zero and each of the electrons in a Cooper pair have opposite relative momentum.

The energy gap created is related to the attractive potential, V, by the following equation:

$$\Delta = \hbar\omega_D \text{ csch}\left(\frac{1}{N(0)\,V}\right) \tag{2.75}$$

A famous result from BCS theory is that the energy gap at zero temperature is proportional to the transition temperature:

$$\Delta_0 = \alpha_{BCS}\, k_B T_c \tag{2.76}$$

$$\alpha_{BCS} = \pi\, e^{-\gamma_E} \approx 1.764 \tag{2.77}$$

where γ_E is Euler's constant.

The BCS energy gap is temperature dependent and can be calculated numerically by solving the following integral for a given value of $N(0)\,V$.

$$\frac{1}{N(0)\,V} = \int_0^{\hbar\omega_D} (\xi^2 + \Delta^2)^{-1/2} \tanh\left(\frac{(\xi^2+\Delta^2)^{1/2}}{2\,k_B\,T}\right) d\xi \tag{2.78}$$

Where $N(0)$ is the density of states at the Fermi energy, V is the attractive potential between electrons, ξ is the energy of the electron state relative to the Fermi energy.

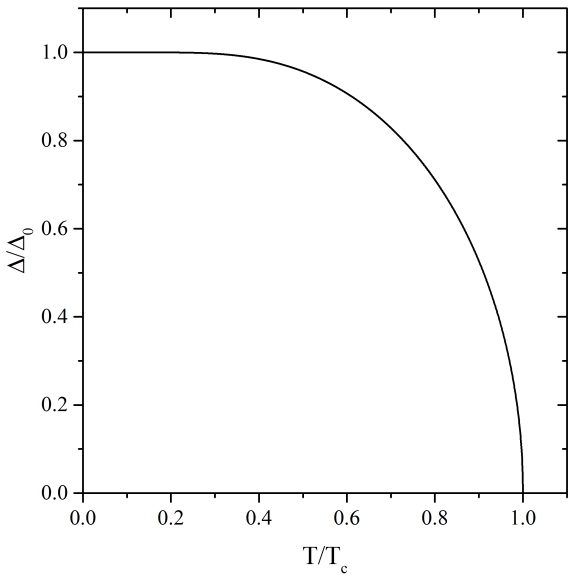

Figure 2.7: *A graph showing the temperature dependence of the BCS energy gap. This was obtained by numerically solving equation 2.78 in the weak coupling limit where* $N(0)V \approx 0.3$.

Excitations of the superconducting state are known as quasiparticles (QP) and are fermions with energies, $E_{\boldsymbol{k}}$, greater than the energy gap, Δ. The equilibrium density of quasiparticles increases with temperature. The excitation probability at finite temperature is given by the Fermi function:

$$f(E_{\boldsymbol{k}}) = \left(\exp\left(\frac{E_{\boldsymbol{k}}}{k_B T}\right) + 1 \right)^{-1} \tag{2.79}$$

$$\text{where: } E_{\boldsymbol{k}} = \left(\xi_{\boldsymbol{k}}^2 + \Delta^2\right)^{1/2} \tag{2.80}$$

BCS theory was a breakthrough in the theoretical understanding of superconductivity however it is only easy to apply to geometries where the energy gap is constant in space. In 1959 L. P. Gor'kov showed that the Ginzburg-Landau equations could be directly derived from BCS theory [29]. Valid in the region near T_c, in this derivation the Ginzburg-Landau order parameter is found to be proportional to the BCS energy gap. The order parameter can then be interpreted as a macroscopic wavefunction of Cooper pairs. It also showed that the mass and charge of the Ginzburg-Landau charge carriers are the same as the mass and charge of a Cooper pair:

$$m^* = 2m_e \tag{2.81}$$

$$q = -2e \tag{2.82}$$

Gor'kov provided a microscopic justification for the Ginzburg-Landau equations, this was a hugely significant contribution because Ginzburg-Landau theory can be much more easily applied to complex geometries and superconductors in the mixed state where the energy gap

has strong spatial dependence.

2.3.6 Heat capacity

The superconducting transition is of second order and there is therefore no latent heat, however the heat capacity of a superconductor exhibits a discontinuity at the transition temperature. The total heat capacity of a material is the sum of electronic and lattice contributions.

$$C(T) = C_e(T) + C_{lattice}(T) \tag{2.83}$$

The electronic heat capacity in the normal state ($C_{e,N}$) is linear with temperature; however, in the superconducting state ($C_{e,S}$) it is non-linear and increases rapidly near T_c. When electron-phonon coupling is small, BCS theory predicts that difference between superconducting and normal state heat capacities increase will be:

$$\frac{C_{e,S}(T_c) - C_{e,N}(T_c)}{C_{e,N}(T_c)} = 1.43 \tag{2.84}$$

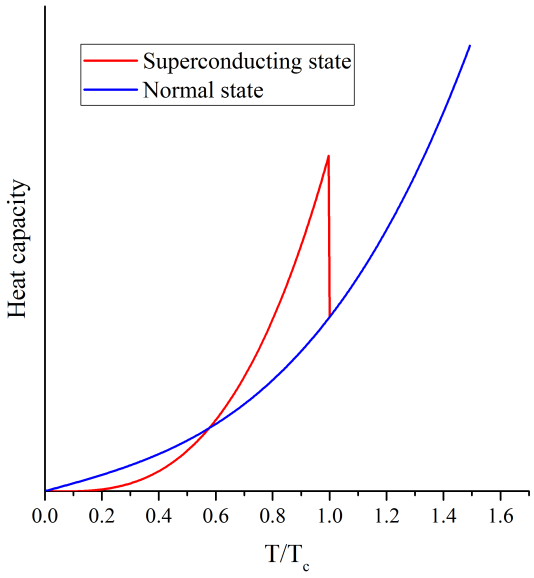

Figure 2.8: *An illustration of the temperature dependence of heat capacity in the normal and superconducting states. At T_c there is a discontinuity in the heat capacity as the material transitions between the superconducting and normal states.*

2.3.7 Two fluid model

Superconductivity can be modelled as the coexistence of two fluids, where the total electron density (n) is divided into normal (n_n) and superconducting (n_s) components.

$$n = n_n + n_s \tag{2.85}$$

Rewriting equation 2.18, the penetration length (λ) can be linked to the superconducting carrier density:

$$\lambda(T)^2 = \frac{m_e}{\mu_0\, e^2\, n_s(T)} \tag{2.86}$$

$$\frac{n_s}{n} = \left(\frac{\lambda_0}{\lambda(T)}\right)^2 \tag{2.87}$$

Assuming the following temperature dependence for the penetration depth:

$$\lambda = \lambda_0 \left(1 - \left(\frac{T}{T_c}\right)^4\right)^{-1/2} \tag{2.88}$$

The equilibrium temperature dependence of n_s and n_n can be approximated as the following equations and are plotted in figure 2.9:

$$n_s = n\left(1 - \left(\frac{T}{T_c}\right)^4\right) \tag{2.89}$$

$$n_n = n\left(\frac{T}{T_c}\right)^4 \tag{2.90}$$

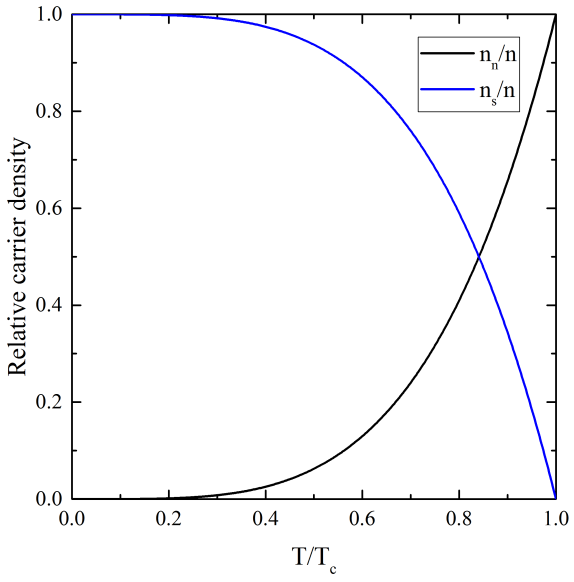

Figure 2.9: *Approximations of the temperature dependence of the superconducting and normal electron densities in equilibrium.*

As shown in figure 2.9, the superconducting electron density increases as temperature decreases, reaching the full electron density when temperature is zero.

Each of the two fluids can be modelled as providing a parallel conduction path, leading to a

complex conductivity for the superconductor:

$$J = \sigma(\omega)\, E \tag{2.91}$$

$$\sigma(\omega) = \sigma_1(\omega) - i\,\sigma_2(\omega) \tag{2.92}$$

Where J is the total current density, E is the electric field, $\sigma(\omega)$ is the total conductivity at frequency ω, σ_1 is the real component of the conductivity and σ_2 is the imaginary component of the conductivity.

The electrical resistivity (ρ) of the system is given by:

$$\rho = J^2\ \mathrm{Re}\left(\frac{1}{\sigma}\right) \tag{2.93}$$

$$\rho = J^2\,\frac{\sigma_1}{\sigma_1^2 + \sigma_2^2} \tag{2.94}$$

From equation 2.94 it can be seen that resistance occurs in the system due to the real component of the conductivity, σ_1.

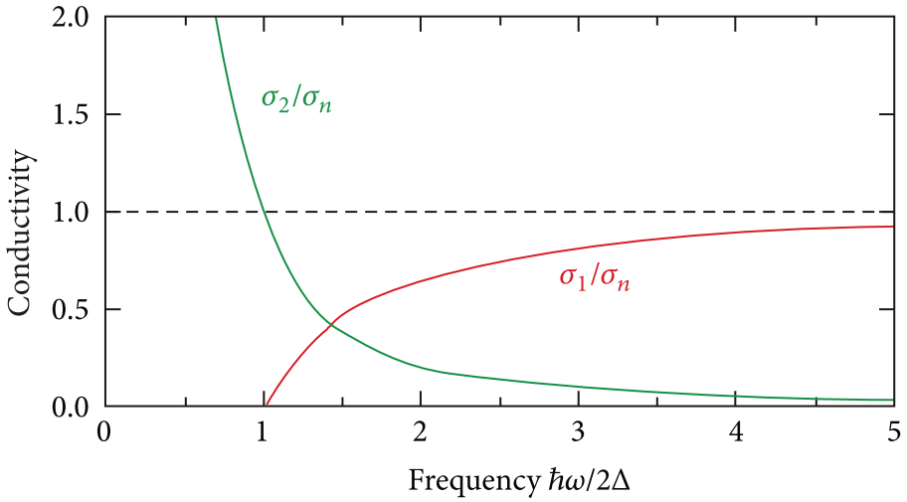

Figure 2.10: *The frequency dependence of the complex conductivity at zero temperature relative to the normal state conductivity (σ_n). Image from [30].*

DC currents can flow in the system without dissipation because the superconducting carriers effectively short circuit the system. However, as shown in figure 2.10, at high frequencies (high microwave range) the real conductivity dominates leading to the majority of the current being carried with resistance [19].

2.4 Superconducting photodetectors

Presented here is an overview of some relevant superconducting photodetectors and a description of the principles of their operation. This is done to provide insight into the various ways in which a superconductor can be used as an optical detector and how a two-dimensional superconductor might be beneficial to the design or fabrication the detector.

2.4.1 Superconducting nanowire single photon detectors (SNSPD)

An SNSPD is a single photon detector which can operate in the visible to mid-infrared spectrum [31]. It is a superconducting wire, typically 100nm wide and 5nm thick, which is usually patterned to meander across a large area for better optical coupling efficiency. It is current biased close to its critical current so that, upon absorption of a photon, the SNSPD becomes resistive and produces a measurable voltage pulse. A typical biasing circuit utilizes a small parallel resistor which will divert the majority of the current from the wire when it is in the resistive state. This allows the wire to recover superconductivity and return to its initial state, ready to detect another photon.

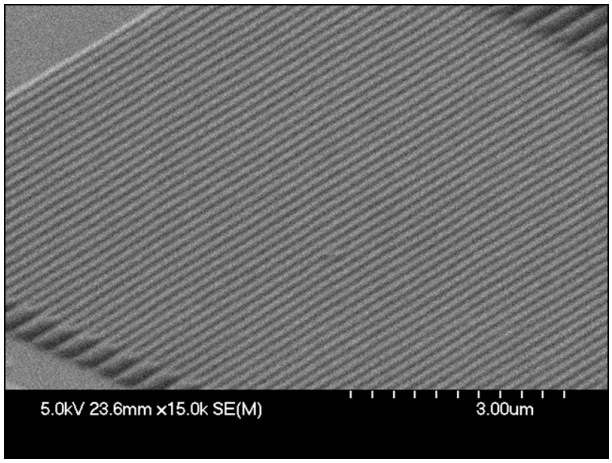

Figure 2.11: *A scanning electron microscope (SEM) image of an SNSPD meander. Image courtesy of Robert A. Kirkwood.*

SNSPDs can typically operate at count rates over 10 MHz and have demonstrated timing resolution (jitter) of less than 20 ps [32–34]. By using an optical cavity, SNSPDs have shown system detection efficiencies (SDE) of over 85% with dark count rates of less than 100 counts /s [35–37] at the wavelength 1550 nm.

Ideally, an SNSPD has a uniform cross section throughout its length, however fabricating a uniform wire of such extreme dimensions over millimetre length scales is a considerable challenge and variation in the wire's cross section can cause current constrictions and poor device permanence [24, 38].

Detection mechanism

An infra-red photon has an energy several orders of magnitude greater than the binding energy of a Cooper pair. When a photon is absorbed by a Cooper pair in a superconductor it is immediately broken, forming two quasiparticles (QPs). These QPs will diffuse from the absorption site and interact with nearby Cooper pairs, creating further QPs. The multiplication process causes the creation of a small volume around the absorption site where a significant fraction of Cooper pairs have been broken, locally increasing the electron temperature in a volume called the hotspot. If the superconductor thickness is much smaller than the material's coherence length, it can be assumed QP density is uniform in this axis. The system can

then be treated as two dimensional and the area of the initial hotspot can be calculated with the following equation [39].

$$R_{init}^2 \approx D\tau_{e-e} \tag{2.95}$$

Where R_{init} is the radius of the initial hotspot, D is the electron diffusion constant and τ_{e-e} is the electron-electron inelastic relaxation time which has a value of a few picoseconds [40].

If the electron diffusion constant is too large, or if electron-phonon coupling is strong, the resultant hotspot will have an electron temperature that is only slightly elevated. This will reduce the probability of a normal band forming across the wire's width for a given photon energy. Therefore, the material chosen to fabricate an SNSPD should have a weak electron-phonon interaction and a low electron diffusion constant [41].

The initial hotspot is not typically large enough to span the entire width of an SNSPD. Another process must occur to cause a resistive region to form across the entire width of the wire. There are several competing theories of what this process is. The original theory proposed to explain the formation of a resistive band was the normal core model [42]. In this model, it is assumed that the hotspot is entirely in the normal state. Current redistribution around the normal core causes an increase in the current density in the surrounding area. The current density then increases above the material's critical current density causing a band of the wire to become resistive. A significant problem with this model is that it predicts a sharp cut-off in detection efficiency with wavelength which has been shown to be incorrect [43].

The normal core model was improved upon by the diffusion model [44] where instead of the core being fully normal, it is regarded as having a reduced current carrying capacity. The current carrying capacity of the wire is assumed to be proportional to the number of Cooper pairs in a slab of thickness, ξ. After absorption of a photon, the current carrying capacity of the wire is reduced below the applied bias current and a detection event occurs.

A competing theory is that of vortex assisted photon detection [45–47]. Under this theory, absorption of a photon causes the depression of superconductivity across a band of the superconductor which lowers the barrier to entry of a vortex into the wire. A vortex then enters the wire and is driven across its width by the Lorentz force caused by the transport current. Vortex movement is a dissipative process and therefore leads to the effective temperature of the electron system increasing and the formation of a normal state band across the superconducting wire.

Although the process involved in the initial formation of a normal state band is still disputed, the subsequent behaviour of an SNSPD is agreed [48]. Joule heating of the resistive region exceeds the local cooling rate and so the resistive region grows hotter and expands along the wire's length. It is required that the resistive heating of the normal region exceeds the conduction of heat away from the area. The condition that Joule heating exceeds heat conduction

can be written as:

$$I^2 > \alpha w^2 d(T_c - T_b) \tag{2.96}$$

where α is the heat transfer coefficient per area, w is the width of the wire, d is the thickness of the wire and T_b is the temperature of the environment.

If the condition of equation 2.96 is met, the normal-state band will expand along the length of the wire reaching either the full length of the wire or until the current is reduced by the biasing circuit.

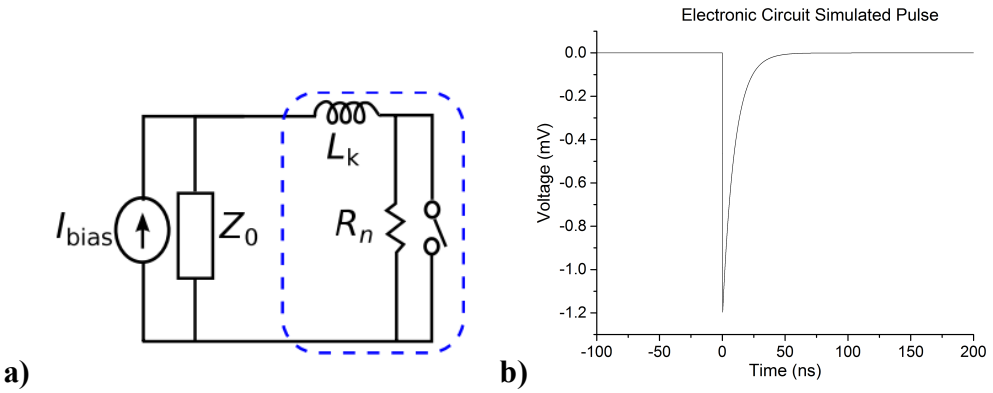

Figure 2.12: a) *This circuit approximates the electronic behaviour of an SNSPD. L_k is the kinetic inductance of the superconducting wire, R_n is the resistance of the hotspot, Z_0 is the impedance of a shunt resistor.* ***b)*** *An electrical pulse simulated from the electronic circuit using Tanner S-Edit and T-Spice software. The values used for the simulation were: L_k = 500 nH, Z_0 = 50 Ω and R_n = 500 Ω*

The circuit shown in figure 2.12a approximates the electronic behaviour of an SNSPD. In the superconducting state the switch is closed and therefore all current flows through the superconducting wire. Upon absorption of a photon, the superconducting wire becomes resistive and the switch opens. Since the hotspot resistance is much greater than the shunt resistance, the current is diverted to flow through the shunt resistor. This generates a voltage drop across the resistor which is amplified and measured. The superconducting wire regains superconductivity but the inductor resists the return of current to the SNSPD. The result is an exponentially decaying current flow through the shunt resistor as shown in figure 2.12b.

Typically, increasing the width of an SNSPD decreases cut-off wavelength of the detector [43]. However, it has recently been demonstrated that if care is taken to avoid current constrictions, the wire width can be increased to several microns and still be single photon sensitive at 1550 nm. This is achieved by avoiding sharp corners in the wire design and instead using a curved constriction as the sensitive section of the wire [49]. The author's calculate that this technique allowed them to bias their detectors at currents up to 0.7 I_{dep} where I_{dep} is the theoretical critical current of a uniform superconducting wire.

Material choice for SNSPDs

The first SNSPDs used NbN as the superconducting material [42]. Subsequently SNSPDs were fabricated from NbTiN [50], a similar material but with a lower sheet resistance and kinetic inductance therefore enabling faster reset times. These materials were chosen due to their high transition temperatures (approximately 11 K) and high critical current densities [51]. Recently however, amorphous materials such as WSi [35], MoSi [52] and MoGe [53] have been used for the fabrication of SNSPDs. The amorphous nature of the materials is thought to make them less sensitive to inhomogeneities and defects that can be introduced in the fabrication process [35].

SNSPDs have also been fabricated from NbC [41] however it was concluded that the large electron diffusivity and long energy down-conversion time increases the photon energy that is required to cause a detection event.

2.4.2 Kinetic inductance detectors (KID)

A KID is an energy resolving detector capable of being manufactured in large arrays with several thousand pixels [54–57]. It can be designed to operate from the X-ray to submillimeter spectrum [58, 59] and has shown shot noise limited sensitivity [60]. For these reasons, KIDs have seen widespread use as detectors for submillimeter astronomy.

Operating principle

There are two types of charge carriers inside a superconductor: Cooper pairs and quasiparticles. The two systems of carriers can be thought of as parallel electrical components. Cooper pairs can carry current without dissipation but have a kinetic inductance. Quasiparticles, like normal state electrons, carry current with electrical resistance, for this reason they do not usually play a role in DC conduction as they are effectively shorted by the Cooper pairs. However, for AC currents, quasiparticles can play a significant role in conduction.

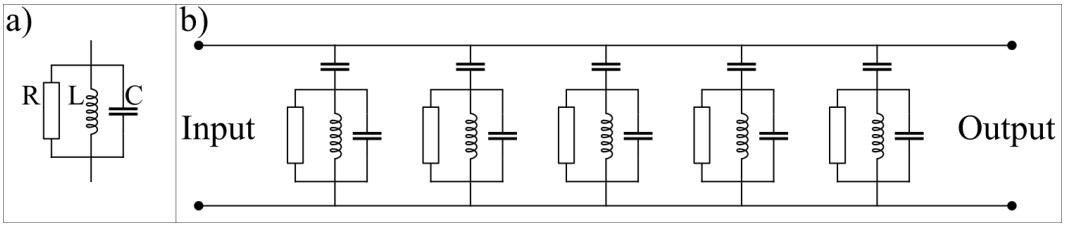

Figure 2.13: a) *A circuit showing the electrical behaviour of a superconducting wire. The resistor represents the quasiparticle resistance, the inductor represents the kinetic inductance of the Cooper pairs and the capacitor is due to the geometry of the wire,* ***b)*** *A series of KIDs capacitively coupled to a single transmission line. Each KID is designed to have a different resonant frequency so that they can all be measured independently*

As shown in figure 2.13b), a KID is a parallel RLC circuit capacitively coupled to a transmission line. It therefore functions as a band-stop filter with a resonant frequency $\omega_0 =$

$(LC)^{-0.5}$. The bandwidth of the resonance will be $\Delta\omega = (RC)^{-1}$ and the quality factor will be $Q = R\sqrt{\frac{C}{L}}$ [61].

The KID is operated in the GHz regime where its inductance is inversely proportional to the Cooper pair density, see equation 2.61. As a result the inductance in the RLC circuit will increase when Cooper pairs are broken. The resistance of the quasiparticle system will be inversely proportional to the density of quasiparticles and so absorption of energy will lead to the resistance in the RLC circuit decreasing. This introduces more attenuation to the resonant circuit resulting in a lower quality factor. Therefore, when a KID absorbs radiation, its resonant frequency will decrease, and the quality of the resonance will decrease. Measuring either of these parameters allows a determination of the absorbed power in the device [62].

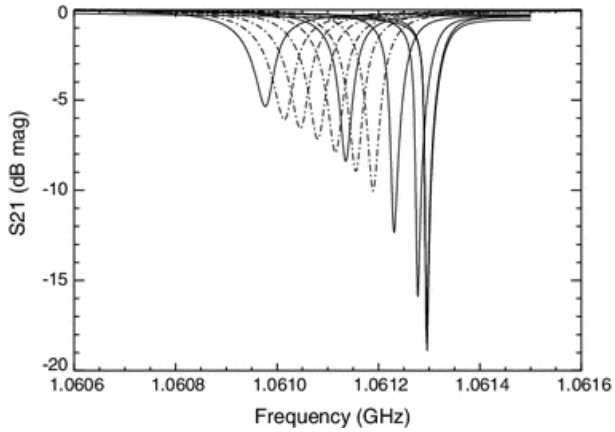

Figure 2.14: *A graph showing the transmitted power through a KID as a function of frequency for a series of optical powers. With increasing optical power, the resonant frequency shifts to lower frequencies and the resonance becomes increasingly broad. Reproduced from [63]*

Since the output of a KID is measured in the frequency domain, it is a simple step to multiplex an array of KIDs. As shown in figure 2.13b) this can be achieved by capacitively coupling detectors with different resonant frequencies to a mutual transmission line.

2.4.3 Transition edge sensor (TES)

A TES is a voltage biased superconducting bolometer which is maintained by electro-thermal feedback in the superconducting to normal transition. The rapid change of resistance at the superconducting transition is used to achieve high detector sensitivity and energy resolving detection of near IR [64] to X-ray radiation [65]. Absorption of radiation leads to a small increase of the superconductor's resistance and the resulting drop in current is measured by an inductively coupled SQUID array [66].

2.4.4 Superconducting tunnel junction (STJ)

An STJ is a superconductor-insulator-superconductor junction which is biased at a voltage $V < \frac{2\Delta}{e}$ such that only a small, thermally activated, leakage current flows. An absorbed photon breaks Cooper pairs creating energetic quasiparticles which are capable of tunnelling

across the insulating barrier [67]. The detector output is then the integral of the resulting current pulse. Since the device is operated well below the transition temperature, the optically generated quasiparticles far exceed the thermal number and single photon detection is possible [68].

2.5 2D photodetectors

2.5.1 Graphene photodetection

Graphene, a 2D material as described in section 2.2, has led to something of a revolution in scientific research with thousands of papers published on the subject since its discovery [69]. This huge research effort was fuelled by the many astonishing properties possessed by graphene. It has extremely high mechanical strength, electrical mobility, conductivity, scattering length on the order of 1 µm and a high optical absorption considering its thickness [70]. These properties have motivated the development of several novel photodetector designs [71–73]. In addition, the small electronic heat capacity of graphene combined with its weak electron-phonon coupling means that it is a very suitable material for use in thermal photon detectors [74–76].

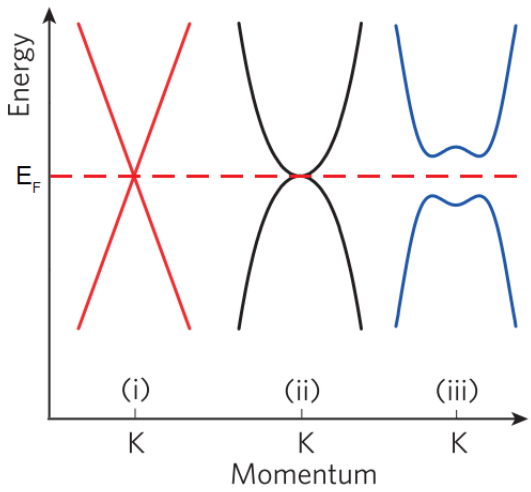

Figure 2.15: *This picture illustrates the shape of graphene's band structures for (i) monolayer (ii) bilayer and (iii) gated bilayer graphene samples. Picture edited from [77].*

Probably the most unusual property of graphene is its unique band structure. The valence and conduction bands in monolayer graphene meet at the intrinsic Fermi level and around these points energy has a linear relationship to momentum. This linear relationship corresponds to a massless particle and therefore the electrons and holes in graphene behave as massless fermions described by the famous Dirac equation [78]. The total absence of a bandgap in graphene leads to an ultra-wide absorption bandwidth with no cut-off energy over which there is almost uniform absorption [79]. The two layer variant, bilayer graphene, has a slightly different band structure. In it there is again no bandgap however the band structure is modified slightly as can be seen in figure 2.15.

Photodetectors based upon a p-n junction require a bandgap to avoid a high dark count rate. Silicon, the industry standard, has an intrinsic bandgap of 1 eV. This means that photons of energy less than 1 eV are typically not absorbed by the detector. This results in low absorption of background blackbody radiation and therefore reduced noise but it also means that the detectors cannot be used to detect signals with a wavelength greater than 1 μm. Therefore for the detection of mid-IR communications a material with a smaller bandgap is required. A graphene based detector would be a suitable choice for this application.

p-n Junction by electrostatic gating

When a metal is placed in an electric field, charge builds up on its surface screening the bulk of the material from the effects of the field. This occurs over distances of less than 1 nm [80]. Since the electrons in the bulk of the metal far outnumber the surface electrons, an applied electric field has little effect on the metal's Fermi level. In contrast, a 2D conductive material is incapable of charge screening and therefore the Fermi level will be modified by an applied electric field. You can therefore, directly alter the charge carrier density in a 2D material such as graphene by the electric field effect.

Although graphene does not intrinsically have a band gap, it was discovered that one can be induced by applying an electric field to the sample. In Ref. 10 the authors cover an electrically connected graphene sample with an insulating material and then deposit a top gate. By applying voltages to both the dielectric substrate and the top gate they developed a means to independently control the sample's band gap and Fermi level. Each of the two gates applies an electric displacement field to the graphene. It was found that the difference between the two fields controls the doping of the sample while the average of the two fields controls the band gap size in bilayer graphene. A band gap of 250 meV was achieved by applying a net displacement field of 3 $V\,nm^{-1}$.

To create a p-n junction across a graphene sample we would require that the Fermi level at one side of the junction was higher than at the other. A simple way to achieve this is to gate the sample using a sloped top gate and substrate as done in [81]. Since the distance between the graphene and the top gate varies with position, the Fermi energy and therefore doping of the sample will change across its length. Using the substrate back gate, a band gap was opened in the graphene and a rectifying p-n junction was formed.

Any p-n junction is sensitive to light and graphene based p-n junctions formed by gating have been shown to produce a photocurrent which is dependent on the applied fields [82]. Such devices benefit from the direct control of graphene's band gap and can therefore be tuned to have broadband absorption (no band gap) or could be designed to have a cut-off wavelength at any value greater than 5 μm.

Normally a p-n junction produces a photocurrent because its built in electric field causes photogenerated carriers to accelerate out of the junction. This effect is known as the photovoltaic effect but it is not the only means by which a graphene p-n junction generates current. When

a photon is absorbed in graphene by an electron the excited electron hole pair will quickly decay and redistribute the absorbed energy among local carriers. This leads to a local carrier temperature above the temperature of the graphene lattice [83]. In an equally doped graphene sample this local temperature difference would not lead to any current because of a constant charge carrier density. However, where the photon absorption occurs in a graphene p-n junction, the photo-thermoelectric effect (PTE) can generate a current.

$$V_{PTE} = (S_1 - S_2)\Delta T_e \tag{2.97}$$

Where V_{PTE} is the voltage produced by the PTE, $S_{1,2}$ is the Seebeck coefficient across a junction and ΔT_e is the difference in electron temperature between the area of optical excitation and its surroundings.

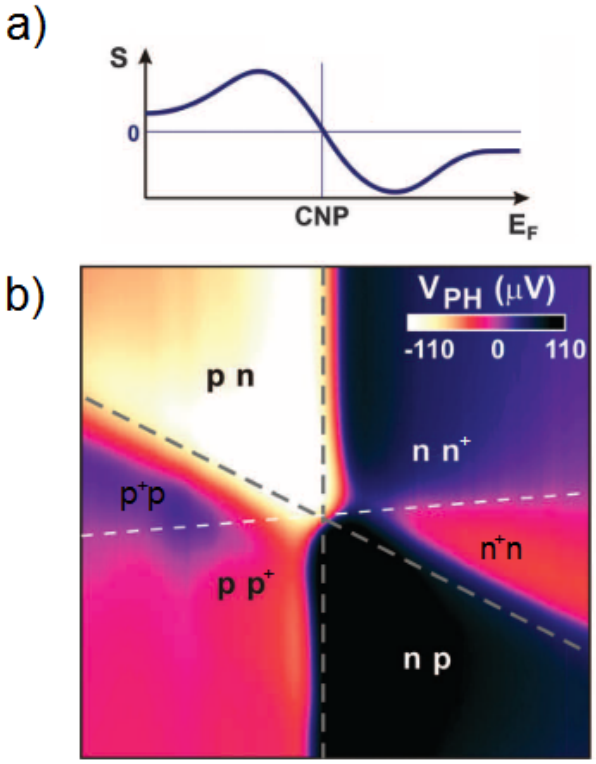

Figure 2.16: a) *A sketch of the dependence of carrier doping on the Seebeck coefficient in graphene.* ***b)*** *A graph of the photovoltage generated by a graphene p-n junction with varying doping where the PTE effect is dominant. Image after [83].*

The Seebeck coefficient can be evaluated using the Mott formula [7] and varies with Fermi level. A sketch of the Seebeck co-efficient with doping in graphene is shown in figure 2.16a. It can be seen that at a p-n junction the PTE will generate a current in the same direction as the photovoltaic effect but in p^+- p and n^+-n junctions the two effects will be of opposite sign [83, 84] allowing determination of the strength of the PTE effect. It has been shown that the PTE often has a larger contribution to the photocurrent than the photovoltaic effect. This is especially true in suspended graphene structures where electron cooling via the substrate is reduced and so a larger proportion of heat dissipation takes place through carrier transport [85].

p-n Junction by Metallic Contact Doping

When two materials of different Fermi levels come into contact with each other carrier diffusion will occur leading to the formation of a p-n junction. With graphene this can be used to locally dope intrinsic graphene which is in contact with a metal. You would assume that if the metal's work function is greater than graphene's that electrons would transfer from the metal to the graphene making the graphene n doped and if the reverse were true graphene would become p doped. Ref. 86 found that this is a reasonable approximation for a large separation between graphene and the metal (>0.5 nm). However, chemical interactions between graphene and the metal were found to move the point of zero doping to a metal with a work function 0.9 eV greater than graphene. Using the values calculated in Ref. 86, the materials used for metal contacts can be chosen to create the required doping in graphene.

When a graphene sample has two contacts of the same metal attached to it, a photocurrent can be produced within roughly half a micron of each metal graphene edge [87]. However, the direction of each photocurrent will be opposite at one edge to the other and therefore when the whole device is illuminated there will be little or no net photocurrent [88].

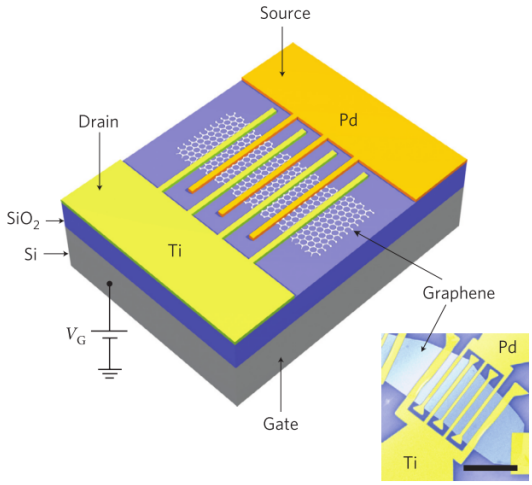

Figure 2.17: *A graphene photodetector with asymmetrical metal contacts. Picture from [89].*

In [89] the authors chose to use two different metals to contact their graphene device. In doing so they created an asymmetrical doping of the graphene across each metal-graphene-metal (MGM) junction. They were then able to independently change the Fermi level across the graphene sample by gating. This resulted in a monotonic field profile across the p-n junction between each metal contact. This meant that the photocurrents generated at all points were of the same sign leading to a greatly enhanced photoresponse.

Graphene Bolometers

When a material absorbs radiation its temperature will increase. This temperature change can often be detected by a change in the material's conductivity either because of a variation in carrier mobility or charge carrier density. In graphene, the energy absorbed from radiation

is quickly distributed around the charge carriers but cooling via electron-phonon coupling acts on a much slower time scale [7]. Graphene also has a low electron heat capacity. These two properties mean that radiation absorbed in graphene leads to a large electron temperature change [90]. The resistance of gated bilayer graphene has a strong dependence on electron temperature because of its flat valence and conduction band edges. This allows accurate reading of temperature and therefore absorbed power, delivering a responsivity of 2×10^5 V W^{-1} a value competitive with commercially available bolometers. It has even been theorised that a graphene thermal detector could operate as a single photon sensitive calorimeter for terahertz frequencies [91].

2.5.2 Two dimensional superconducting detector

The field of two dimensional materials is still relatively new but several 2D materials have been discovered showing superconducting characteristics. In 2010, single layer sheets of both lead and indium were grown on silicon substrates by molecular beam epitaxy [92]. Scanning tunnelling microscopy was then performed on the samples which showed signatures of a superconducting state. The superconducting transition temperatures (T_c) were calculated to be 3.18 K for In and 1.83 K for Pb. These temperatures are much lower than their bulk values, agreeing with the general trend that T_c decreases with material thickness. Unfortunately the samples were unstable when removed from the ultra high vacuum in which they were grown making them unsuitable for device manufacture.

Contrary to this trend however is a recent observation of enhanced superconductivity in single layer FeSe [14] where T_c was observed to be 40.2 K. This value is much higher than in the bulk material where T_c is around 8 K. However one unit cell FeSe is an extremely fragile material and so making use of it for device fabrication would be challenging.

A promising material is $NbSe_2$. It, like graphene, has a layered structure with strong, covalent intra-layer bonds and weak van der Waals interlayer bonds. This allows layers of $NbSe_2$ to be individually separated by mechanical exfoliation techniques. However, in bulk form $NbSe_2$ is a superconductor with a superconducting transition temperature of 7.2 K [93]. The question then arises if the superconducting state can exist in single layer $NbSe_2$.

In 2009, Stanley et al. [93] published a paper showing the systematic decrease of T_c in $NbSe_2$ with material thickness and were unable to observe any superconducting transition in the thinnest of their samples, which they identified as being 2-3 layers thick. This would seem to suggest that the single layer variant of $NbSe_2$ could not support superconductivity. However, recent work has shown that when properly isolated from the environment, even single layers of $NbSe_2$ are superconducting. In Ref. 95, $NbSe_2$ was exfoliated to produce single layer flakes and then encapsulated by hexagonal boron nitride (hBN) to protect it from chemical decomposition. All this was done in the inert atmosphere of a glove box with a custom built micromanipulation station operated remotely via programmed commands and joystick control. Although this is a complex fabrication process, samples prepared in this way could

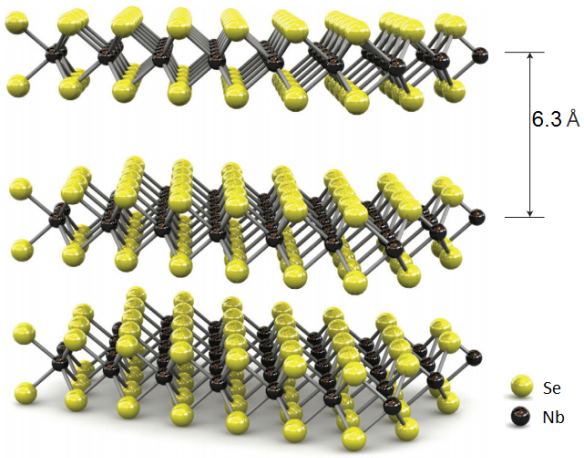

Figure 2.18: *$NbSe_2$ consists of covalently bonded layers with weak van der Waals bonding between layers. The above image shows three molecular layers. Image edited from [94].*

be used to fabricate a 2D superconducting detector.

Although not experimentally demonstrated, in principle a 2D material could be used as the basis for any of the detector types described in section 2.4. Due to the simplicity of the fabrication and the local availability of testing equipment, it was decided that a $NbSe_2$ photodetector could be fabricated based on a modified version of an SNSPD (see section 2.4.1 for further information). This detector design would be fabricated by collaborators specialising in 2D materials processing and tested by the author.

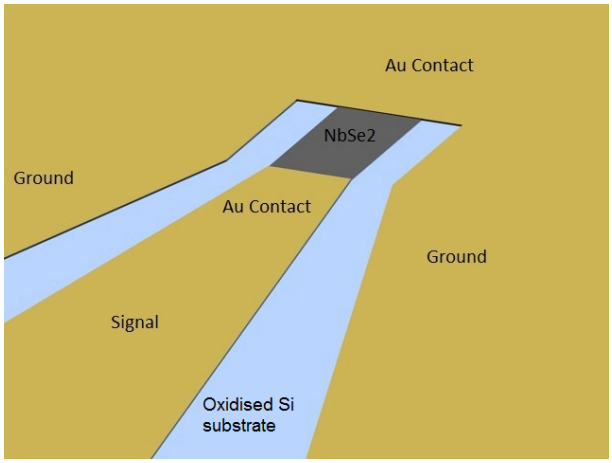

Figure 2.19: *A proposed design for a superconducting single photon detector. The superconducting flake has been shaped to have a constant width and a tapered coplanar waveguide has been fabricated around the sample for signal transmission and wire bonding to external electronics.*

2.5.3 Enhancing absorption

The obvious drawback to using a 2D material in a photon detector is the low absorption rate. Graphene will absorb around 2.3% of vertically incident light per layer and although this is high considering the material is only 1 atomic layer thick, for many applications this value is too small.

Waveguide Integration

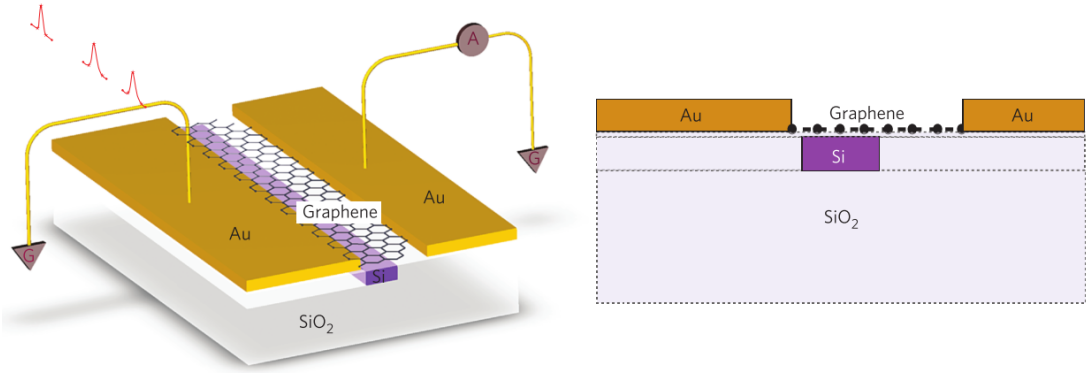

Figure 2.20: *This image taken from [96] shows a schematic of a graphene photodetector incorporated with a waveguide fabricated on an SOI substrate.*

An optical waveguide uses the principal of total internal reflection to confine EM waves inside the structure. Although most of the EM field is confined to within the waveguide a small amount of the field propagates along the surface of the waveguide. The field outside of the waveguide is referred to as the evanescent field or a surface wave. The evanescent field does not propagate away from the waveguide but instead decays exponentially with distance from it.

Gan et al. [96] developed a graphene based photodetector with waveguide coupling, designed for the purpose of fast optical communications. It was able to demonstrate response rates greater than 20 GHz and a responsivity of 15.7 mA W^{-1}. The waveguide fabricated was 220 nm thick and 520 nm wide thereby ensuring single mode transmission at telecommunication wavelengths. The waveguide mode interacts with the graphene layer via its evanescent field along the length of the 53 µm long bilayer sheet. As seen in figure 2.20 the silicon waveguide has been positioned off centre relative to the gold contacts. This has been done to ensure that absorption occurs close to the nearer metal-graphene edge where a photocurrent will be produced and to avoid absorption at the far edge where a photocurrent of opposite sign would be generated. This device was operated without bias and so had a negligible dark count rate and no intentionally formed band gap. Such a device would be expected to have broadband absorption of any radiation that could be coupled into the waveguide.

Optical Cavity Integration

Another method of enhancing the absorption into a 2D material is to place the material inside an optical cavity, as seen in figure 2.21. Such a cavity will greatly enhance the optical field at a designed wavelength. Furchi et al. [97] fabricated a graphene photodetector enclosed by two distributed Bragg reflectors (DBR). The DBRs are formed with alternating layers of material with thicknesses equal to one quarter of the resonance wavelength. Incoming radiation will partially reflect at each of the material boundaries in the DBRs causing constructive interference at the resonant frequency and destructive interference at off-resonant frequencies. Therefore the graphene photodetector will have greatly enhanced absorption at the cavity's

resonant wavelength but greatly reduced absorption at all other wavelengths. At the resonant wavelength of 850 nm the device was shown to have greater than 60% absorption into the graphene.

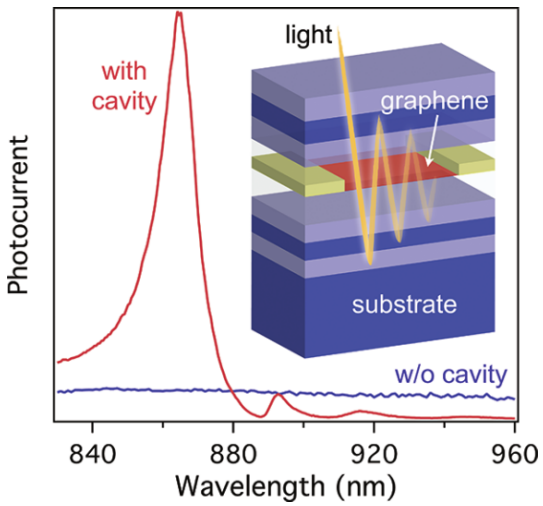

Figure 2.21: *This image taken from [97] shows a graphene photodetector fabricated inside an optical cavity and the enhanced photocurrent the cavity produced.*

The graphene photodetector in [97] was not doped by any means and so to generate an electric field, a source-drain bias was required. This meant that a constant current flowed through the device during operation with an enhanced current seen when radiation was absorbed. A pulsed laser was used to illuminate the photodetector and a lock-in amplifier used to separate the bias current from the photocurrent. By this means the device was shown to have a responsivity of 21 mA W^{-1}.

A similar device was fabricated by Engel et al. [98]. It also featured an undoped graphene absorber and so required the use of a lock in amplifier to isolate the photocurrent signal. The key difference between the two devices was that the device fabricated by Engel et al. used metallic mirrors rather than DBRs to create the optical cavity. This is a simpler design to fabricate and offers the benefit of being able to apply a gate voltage to the sample however the quality factor of the cavity was much lower (20 compared to 95 for [97]) and therefore showed less enhancement of the electric field and photocurrent.

Chapter 3

Experimental methods

This chapter will describe in detail the techniques used to manufacture, operate and characterise a series of photodetectors based on superconducting $NbSe_2$ microstrips. The design and testing of samples was primarily performed by the author at the University of Glasgow and the fabrication of devices was primarily performed by our collaborators: Matthew Hamer and Roman Gorbachev - University of Manchester; Domenico de Fazio and Andrea Ferrari - University of Cambridge.

3.1 Fabrication

This section describes the fabrication methods used to produce the $NbSe_2$ photodetectors that were tested.

The standard processes for nano-scale fabrication will be described, including: how lithographic designs are produced and how resist is applied, exposed and developed. How a patterned resist is used for metal deposition and etching of thin films.

The fabrication procedures specific to 2D materials processing will follow. These are the methods of exfoliation, identification, and transfer of 2D samples to chosen substrates. Using these techniques, our collaborators at the universities of Manchester and Cambridge created encapsulated $NbSe_2$ heterostructures for infrared photodetection.

3.1.1 Nano-scale patterning

Resist patterning

Lithography is the process by which a design is transferred onto a substrate. Industrial processes typically utilise photo-lithography since large areas of substrate can be exposed simultaneously, allowing rapid fabrication. However photo-lithography requires a photomask to be produced for each design so is not very suitable for prototyping designs. Additionally, it is challenging to produce small feature sizes (<1 μm) however advanced techniques allow photo-lithography to produce features <100 nm in size [99]. Electron-beam (e-beam)

lithography is more suitable for small feature sizes, rapid prototyping of designs and was used exclusively in this project. E-beam lithography works by directing a focussed beam of accelerated electrons to write the design onto a substrate that has been coated in an electron sensitive polymer called a resist. The e-beam exposure chemically alters the resist allowing its selective removal from either the exposed (positive tone resist) or unexposed (negative tone resist) areas during resist development.

Resist is produced as a solution in a solvent. A couple of drops of the solution are applied to a substrate which is then span at a high speed, 1000 - 6000 rpm. This ensures that the solution forms an even coating across the substrate at a consistent thickness. The substrate is then heated using either a hot plate or oven to evaporate the solvents, leaving a thin layer (50 nm - 1 μm) of solid resist.

The substrate is loaded into the sample chamber of an e-beam tool and the designed pattern is written onto the resist. The substrate is unloaded and developed by submerging it in a developer which will be specific to the resist used. The temperature and time of development must be tightly controlled for a repeatable process. Once complete, the development is halted by removing the substrate from the developer, rinsing it, typically isopropanol (IPA) is used, and then drying it using nitrogen gas.

Metal deposition

Lift-off is the process used to deposit shaped layers of metals onto a substrate. This process was used extensively throughout this project to deposit metal contacts, optical grid markers and coplanar waveguides (CPWs). The most common lift-off process is to use two stacked layers of polymethyl metacrylate (PMMA) resist, the upper layer having a higher molecular weight so that it has a higher clearing dose. Upon development, this leads to an undercut resist profile as shown in figure 3.1. Using an electron evaporator, metal is deposited on the surface of the sample. The undercut resist profile causes the metal on top of the resist to be unconnected from the metal on the surface of the substrate. The sample is submerged in resist stripper and agitated in an ultrasonic bath. This causes the metal on top of the resist to be removed while the metal on the substrate remains.

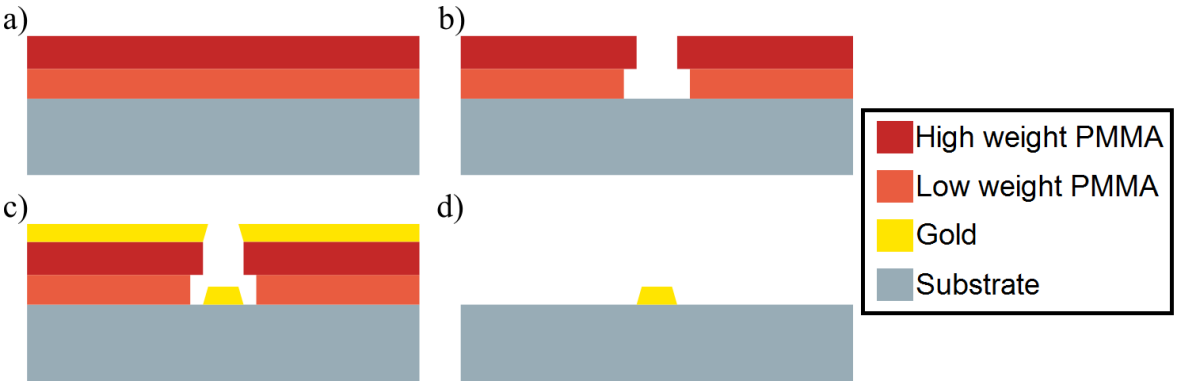

Figure 3.1: a) *A substrate is spin-coated in two layers of PMMA resist. The lower layer has a smaller molecular weight than the upper layer so that more of it will be cleared after development.* ***b)*** *The substrate is exposed and developed.* ***c)*** *A metal is evaporated onto the substrate.* ***d)*** *The substrate is submerged in warm acetone for several hours and gentle ultrasound agitation is used to strip the remaining resist and complete the lift-off process.*

Reactive ion etching (RIE)

A patterned resist can be used as a protective layer during an etching process. This allows selective removal of a material from a substrate and was used to shape few layered $NbSe_2$ flakes to have a constant width.

In RIE, a chemically reactive plasma is used to bombard the surface of a substrate with ions. This is both a chemical and physical process and results in the removal of material from the surface of the substrate. RIE is anisotropic, meaning that material is removed at a faster rate vertically than horizontally. The reactive gas is usually fluorine based (eg C_2F_6, CHF_3, C_4F_8, CF_4, SF_6) as the fluorine can be readily ionised by the application of RF power and forms extremely reactive radicals.

The resist chosen for an etching process should in general etch at a slower rate than the material to be removed. CSAR62 and ZEP520A are suitable resists for etch processes due to their high resistance to etching.

3.1.2 2D materials processing

Exfoliation

In 2004 [80] it was discovered that when a piece of adhesive tape, such as Scotch Tape, is peeled away from a graphite crystal, thin layers of graphite will be exfoliated from the crystal and remain stuck to the tape. After repeated peeling of the adhesive tape single atomic layers of graphite (graphene) can be produced. The graphene flakes can then be placed onto a chosen substrate by simply pressing the tape against it and then slowly removing the tape. The vast majority of flakes found on the substrate will be many layers thick but there will be a small proportion of flakes which are only a few layers thick and some which are singular layers. Since this initial discovery, several methods have been discovered to produce graphene samples [100–102]. But the original Scotch Tape method [2] has remained as the

most suitable method for the production of large, high quality graphene flakes for small scale research [70].

Using the Scotch Tape method, several layered materials such as, transition metal dichalcogenides (TMDs) and hexagonal boron-nitride (hBN) can be mechanically exfoliated from bulk crystals to produce single or few layered samples.

Identifying few-layered samples

Graphene only absorbs 2.3% of incident light and is therefore invisible when placed on most substrates. However, when graphene is placed on a silicon substrate with an oxide layer of an appropriate thickness, it can be viewed easily under an optical microscope. Originally substrates with a 300 nm oxide thickness were used as this is an industry standard but subsequently, substrates have been specifically grown with thicknesses optimized for 2D material characterization. Graphene can be seen on oxidised Si substrates because of thin film interference between the Si and SiO_2 surfaces. The reflectance of the stack is dependent upon the illumination wavelength and the thickness of the SiO_2. Placing a layer of graphene on top of this stack extends the optical path of light which passes through it causing a different interference colour to be seen for graphene compared to the substrate [103]. This enables promising few-layered samples to be found by manually searching the substrate for flakes of the correct colour.

Substrates with an oxide thickness of 285 nm are routinely used to exfoliate 2D materials on to as they cause a very high optical contrast. This is because SiO_2 has a refractive index of approximately 1.474 [104] in the middle of the visible spectrum and so it forms a $^3/_4\,\lambda$ layer with green light (λ =560 nm) when 285 nm thick. This makes a small change to the optical path length easy to perceive allowing single layer samples to be distinguished from the substrate and accurate estimation of the sample thickness. Substrates with a SiO_2 thickness of 95 nm can also be used since these form a $^1/_4\,\lambda$ layer for visible light. By utilizing optical filters, exfoliated crystals can be seen on a wide variety of substrates and thin films. [103].

Raman spectroscopy

Raman spectroscopy is a method of analysing and identifying molecular structures. The sample under test is illuminated with a monochromatic laser and the scattered light is analysed with a spectrometer. A small fraction of the scattered light will have interacted with the material's phonon system resulting in a small change to the wavenumber of the light, a Raman shift. The Raman shift is proportional to the energy of the phonon state and therefore the Raman spectra reveals information on the phonon states available in the material.

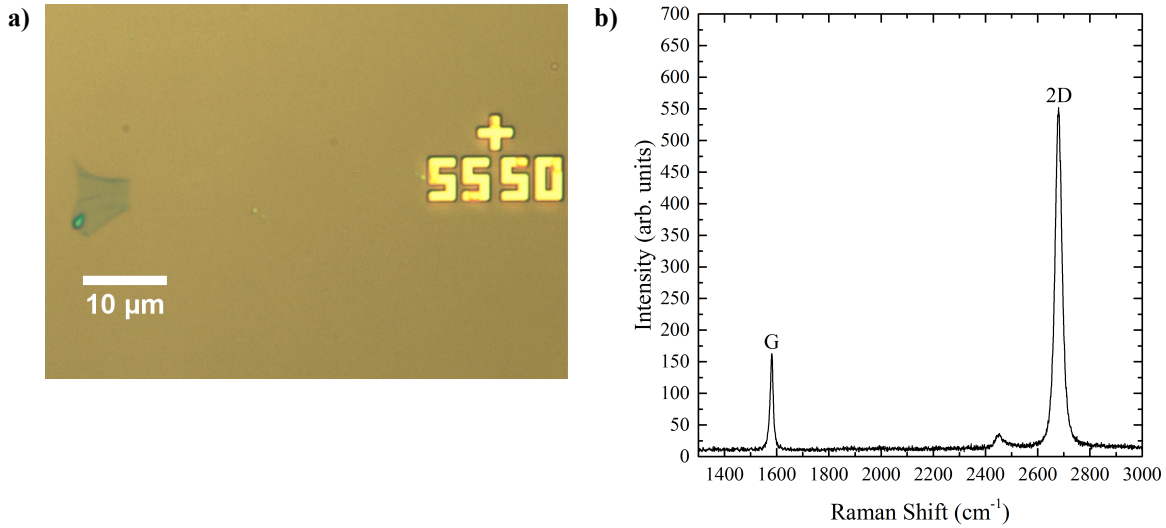

Figure 3.2: a) *An optical image of a graphene sample, exfoliated and examined at the James Watt Nanofabrication centre.* ***b)*** *The Raman spectra of the same sample measured using the Raman spectroscopy tool at the Imaging Spectroscopy and Analysis Centre, University of Glasgow.*

Raman spectroscopy is an invaluable tool in 2D material identification since the intensity, shape and position of each peak will depend on the structure of the sample. Raman spectroscopy can therefore be used to identify how many molecular layers thick a sample is with a high degree of certainty. An example of the technique is shown in figure 3.2 where an exfoliated sample of graphene is analysed.

The Raman spectra of graphene has been extensively studied [105–107]. The shape of the 2D peak (2700 cm^{-1}) varies strongly with the sample thickness and a narrow, symmetric peak such as the one shown in figure 3.2b) indicates a single layer sample.

Dry transfer

Dry transfer is the process of deterministically placing a layered material in a desired location without exposing it to liquids [108]. In this project, dry transfer processes were used to encapsulate $NbSe_2$ samples with hBN or graphene. Few layered samples of $NbSe_2$ require encapsulation immediately after exfoliation to protect them from degrading [95]. Dry transfer was also used to place encapsulated $NbSe_2$ on top of prefabricated electrical contacts.

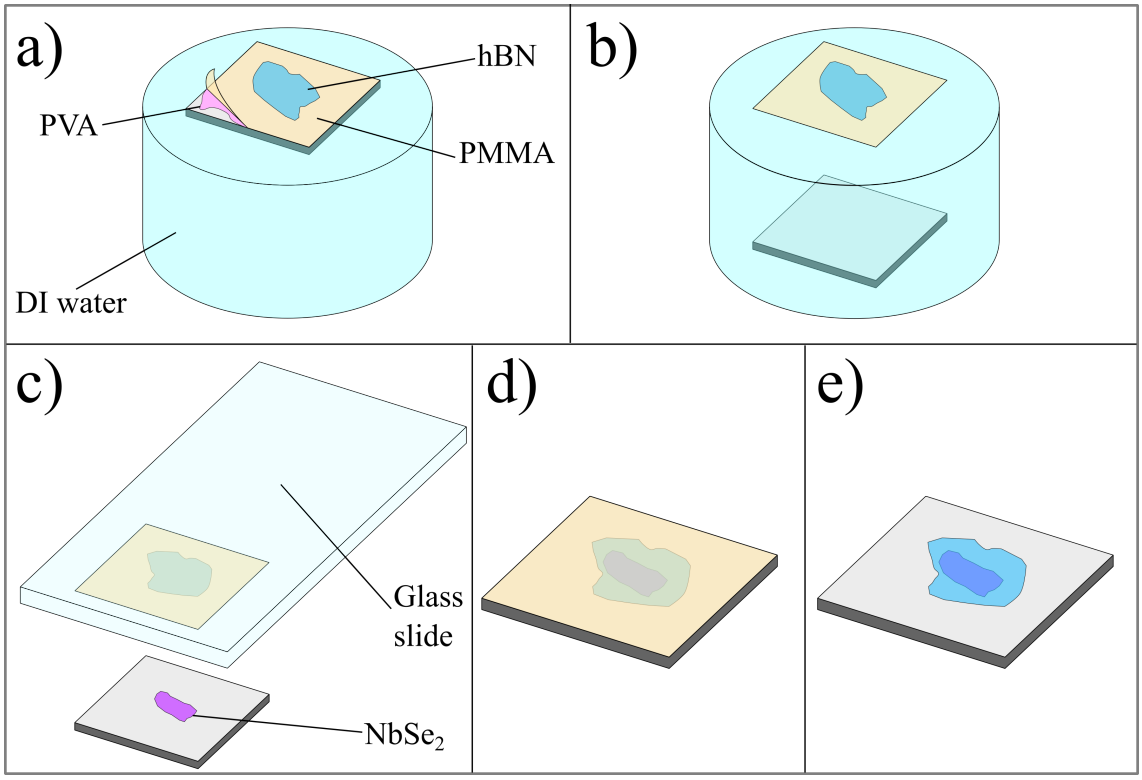

Figure 3.3: *Using the PVA transfer technique to encapsulate a $NbSe_2$ sample with a hBN layer.* ***a)*** *A substrate is spin coated in a water-soluble layer such as polyvinyl alcohol (PVA) followed by a layer of PMMA. The hBN is exfoliated onto this substrate and lowered into a breaker of deionized water where is floats due to the hydrophobic nature of PMMA.* ***b)*** *The PVA layer dissolves and the substrate sinks to the bottom of the beaker leaving the PMMA and hBN floating on the surface of the water.* ***c)*** *The PMMA film is lifted from the water using a glass slide, turned upside down and loaded into the micro-manipulation stage of a microscope. Using the microscope, the hBN and PMMA film are moved into position over the $NbSe_2$.* ***d)*** *The PMMA film is applied onto the target substrate and released, placing the hBN with an accuracy of a few microns.* ***e)*** *The PMMA film is then dissolved in acetone leaving an encapsulated sample.*

Figure 3.3 shows how dry transfer was used to encapsulate a $NbSe_2$ sample in hBN. Although both water and acetone are involved, this process is considered dry because the contacting surface of the layered material is never exposed to any liquids. A different transfer method which doesn't involve any liquids (see ref. 109) was also used in the fabrication of some $NbSe_2$ devices.

3.2 Testing set-up

Electrical and optical testing was performed in a cryogenic cooler. This system uses a two-stage ^{4}He pulse tube to reach a temperature of 4.5 K. This temperature can be maintained for as long as is required. An additional stage pumps on liquefied ^{4}He followed by ^{3}He to reach 350 mK for several hours before returning to 4.5 K.

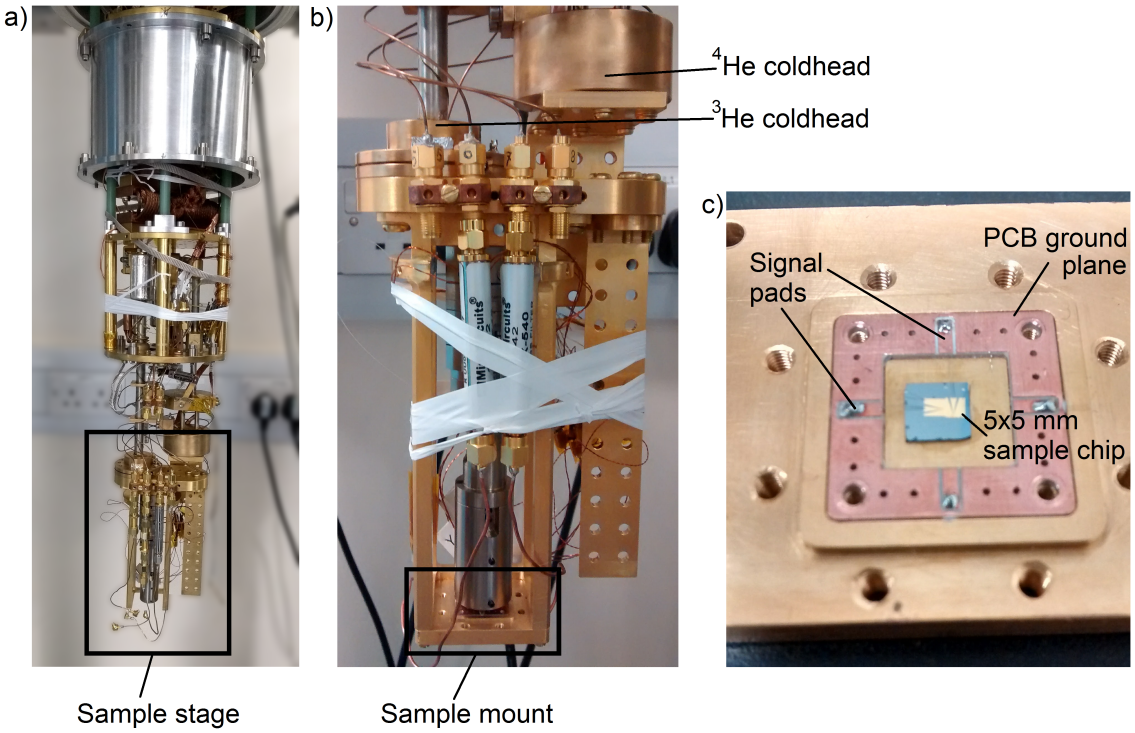

Figure 3.4: a) *An image of the cryogenic testing setup that was used to perform the majority of low temperature measurements described here. It uses a Cryomech PT405-RM pulse tube and a Chase Research Cryogenics GL7 sorption stage to reach a base temperature of 350 mK. The labelled box highlights the sample stage where the minature confocal microscope and sample mount are attached.* ***b)*** *A detailed view of the sample stage. The sample mount (highlighted with a labelled box) is attached at the bottom of the sample stage, immediately below the confocal microscope.* ***c)*** *A deatiled view of a sample mount. A sample mount can accomodate samples up to 10 x 10 mm in size. It has four PCB signal pads, each of which are soldered to the pin of an SMP connector which is accessed from the rear of the sample mount. Aluminium wire bonds are used to connect the sample to the signl pads and the electrical ground.*

3.2.1 Vacuum requirements

To reach cryogenic temperatures, it is required that the system is first pumped to a high vacuum 1×10^{-5} mBar to insulate the system from its environment. At these pressures, the system is in the free molecular flow regime, meaning that the mean free path of gas molecules exceeds the chamber size.

When at atmospheric pressure, system components will absorb gases from the air. Therefore when the system is evacuated, gasses will be released from the system components in a process called out-gassing. To allow the system to fully out-gas it is pumped for over an hour using a turbo pump (Adixen ATP80) before the pulse tube compressor is turned on. As the system temperature decreases, it will begin to act as a cryopump. The residual gas molecules in the system will condense, further lowering the internal pressure and helping to maintain a low pressure for extended time periods.

3.2.2 Pulse tube operation

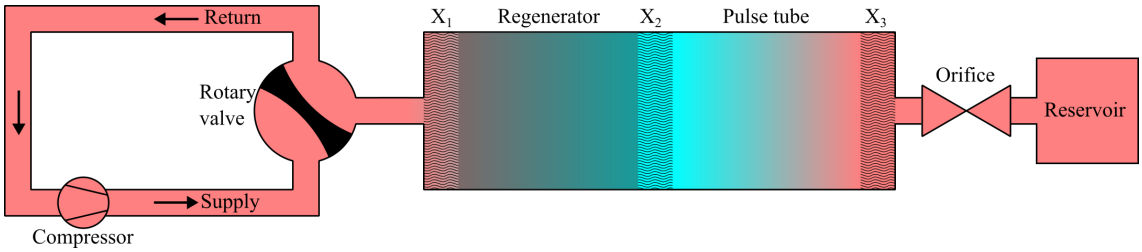

Figure 3.5: *A schematic of a pulse tube cryocooler showing three heat exchangers ($X_{1\text{-}3}$). The red sections of the diagram show components which are held at room temperature with the blue sections representing the cold section of the cryocooler where experimental devices are mounted.*

The operation of a pulse tube is as follows: The rotary valve periodically connects the pulse tube to the supply and return lines of a helium compressor. As the pressure in the pulse tube oscillates helium flows in and out of the pulse tube at both ends. Helium in each of the three heat exchangers (labelled $X_{1\text{-}3}$) and in the regenerator is well thermally coupled to its environment. This means that upon compression the gas changes pressure isothermally. The helium gas inside the pulse tube however is thermally isolated and so undergoes adiabatic compression and expansion cycles. The regenerator is composed of a material with a high heat capacity so that it can thermalise passing helium without much change in its own temperature.

Consider a mass of helium oscillating through X_2 as the pressure of the system is cycled.

Process	**Gas temperature**	**Gas pressure**
The helium is inside the regenerator at the temperature of the regenerator and low pressure	T_{reg}	P_{low}
The pressure increases and the gas moves into the pulse tube, isothermally expanding at X_2	T_{reg}	P_{high}
The pressure decreases causing adiabatic expansion of the gas in the pulse tube	$<T_{reg}$	P_{low}
The helium returns to the regenerator, cooling the heat exchanger, X_2, as the helium is warmed	T_{reg}	P_{low}

Table 3.1: *This table describes the cyclic pressure and temperature changes of a mass of helium around the heat exchanger X_2*

The cycle described in table 3.1 results in the cooling of the area surrounding the heat exchanger X_2. This is the cold area of the cryocooler where devices are mounted. A pulse tube cryocooler is manufactured in a U shape so that the cold section is at one end and the two room temperature sections are next to one another.

3.2.3 Sorption refrigerator operation

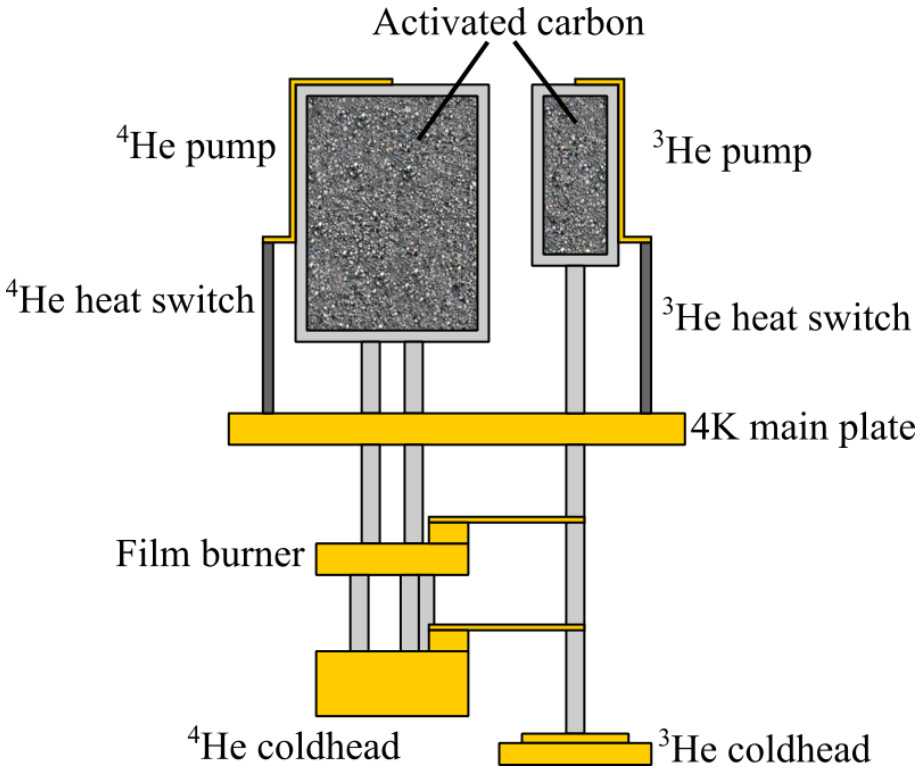

Figure 3.6: *A diagram of the 350 mK sorption refrigerator. The pulse tube in the system is used to liquefy ^{4}He which pools on the ^{4}He cold head. The activated carbon is then cooled, pumping on the liquid ^{4}He. This liquefies ^{3}He which is then pumped on to reach the base temperature.*

A diagram of the sorption refrigerator is shown in figure 3.6. Activated carbon is used inside the ^{3}He and ^{4}He pumps to adsorb helium gas and reduce the helium vapour pressure in the system. The activated carbon will adsorb helium when colder than 5 K and expel it when heated [110]. The temperature of the pumps is controlled by two resistive heaters and the thermal contact between the pumps and the main plate of the system is controlled using gas-gap heat switches.

The heat switches are essentially miniature versions of the pumps. They each contain activated carbon, a small mass of ^{4}He and a resistive heater. When cold, the heat switches will adsorb all helium vapour creating a vacuum and poor thermal conductivity across the heat switch. When heated to around 15 K, helium gas is released and allows thermal transfer from the pumps to the main plate.

Using the resistive heaters, both pumps are warmed to 40 K so that as much helium is released from the activated carbon as possible. The heat switches are kept cold to thermally isolate the pumps from the rest of the system. After about an hour, the ^{4}He will have liquefied and gathered at the ^{4}He coldhead. The system can be kept in this state permanently and will be ready to cycle to 350 mK. The system is typically left in this state when not in use so that the ^{3}He cold head is thermally connected to the main plate and the system is ready to cycle immediately.

To cycle the fridge to 350 mK the ^{4}He pump heater is turned off and the ^{4}He heat switch is turned on so that the activated carbon will cool and pump on the liquefied ^{4}He. This lowers the temperature of the ^{4}He cold head to around 0.8 K. Since the ^{4}He cold head is connected to the ^{3}He gas line, ^{3}He will begin to condense and gather at the ^{3}He cold head. When all of the ^{4}He liquid has evaporated and the temperature of the ^{4}He head begins to rise, the ^{3}He pump heater is turned off and the ^{3}He pump switch is turned on. The activated carbon will cool and pump on the liquefied ^{3}He. This lowers the temperature of the ^{3}He cold head to its base temperature of around 350 mK. The system will remain at its base temperature until all of the ^{3}He has evaporated. This time is dependent on the heat load applied to the ^{3}He cold head which is caused by thermal conduction and heat dissipation from electrical components. With the current wiring, the system can maintain 350 mK for approximately four hours.

3.2.4 Confocal microscope

A confocal microscope is mounted at the 350mK stage of the fridge, its input fibre is single mode and designed to carry 1550nm wavelength light (SMF-28). The confocal microscope uses a collimating lens (354280-C, NA = 0.15) and objective lens (354330-C, NA = 0.68) to focus the light from the fibre ferrule onto the substrate. Using the Rayleigh criterion, the theoretical minimum separation (r) of two resolvable objects will be the following:

$$r = \frac{0.61\lambda}{NA} = 1.39\,\mu\text{m} \tag{3.1}$$

where the wavelength $\lambda = 1550$ nm and numerical aperture $NA = 0.68$.

The Rayleigh criterion specifies a resolution slightly larger than the full width at half maximum (FWHM) of the Airy disc diffraction pattern:

$$FWHM = \frac{0.514\lambda}{NA} = 1.17\,\mu\text{m} \tag{3.2}$$

The theoretical values given by equations 3.1 and 3.2 are the minimum values possible with a perfect measurement system. The resolution achievable by any real system will be larger than those stated above.

The microscope is mounted on a set of piezoelectric positioners that allow 3-axis movement for positioning and focussing the laser spot. There are coarse “stepper” modules used for moving distances of up to 4mm in each of the three axes and a fine “scanner” module for precise X-Y movement.

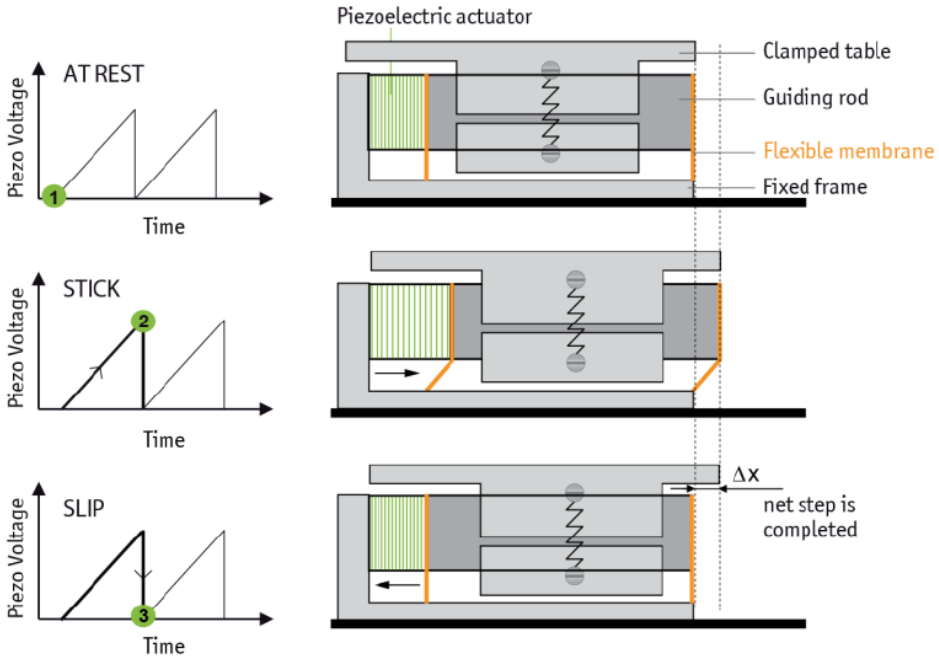

Figure 3.7: *The "stick and slip" principle used in Attocube stepper positioners. Image from Attocube FlexPositioner manual.*

The scanner module moves by applying a constant voltage of up to 140V across a piezoelectric material allowing a movement range of 35 µm. To achieve their large range, the stepper modules use a "stick and slip" principle. As shown in figure 3.7, the table of each stepper module is mounted on a guiding rod. A sawtooth electric waveform is supplied to the piezoelectric material causing it to oscillate in a similar pattern. Friction between the table and the rod holds the table in place during the ramp of the sawtooth but it "skips", remains stationary, during the rapid fall of the sawtooth. Hence, each period of the sawtooth wave causes a net movement of the stepper module.

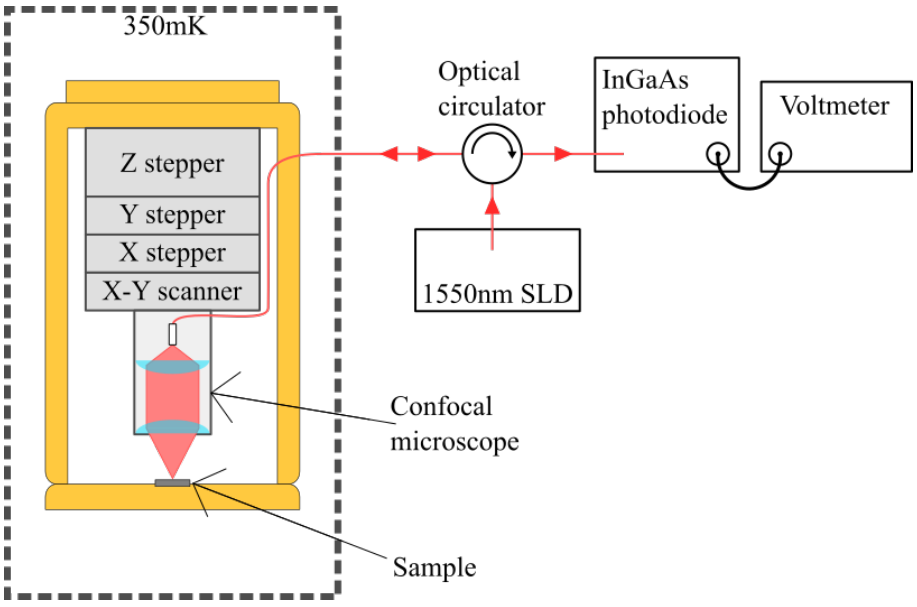

Figure 3.8: *The apparatus used to measure the reflected power from a sample.*

The equipment shown in figure 3.8 is used to measure a reflected signal from a sample. An optical circulator is used to avoid any reflected signal being directed back to the superluminescent diode (SLD) source (Thorlabs SLD1128S).

The reflected power coupled back into the fibre will be maximised when the microscope is in focus. Therefore, focus can be found by moving the microscope towards a sample while measuring the reflected power. Care needs to be taken when finding focus since if the maximum is missed and the user continues moving the microscope closer, the microscope can come into contact with the sample, damaging it. When in focus the objective lens of the microscope will be only 3.1 mm from the sample. A wide bandwidth (110 nm) SLD is used to find focus and image samples so that if the microscope to chip distance changes slightly during a scan, interference fringes will not be visible.

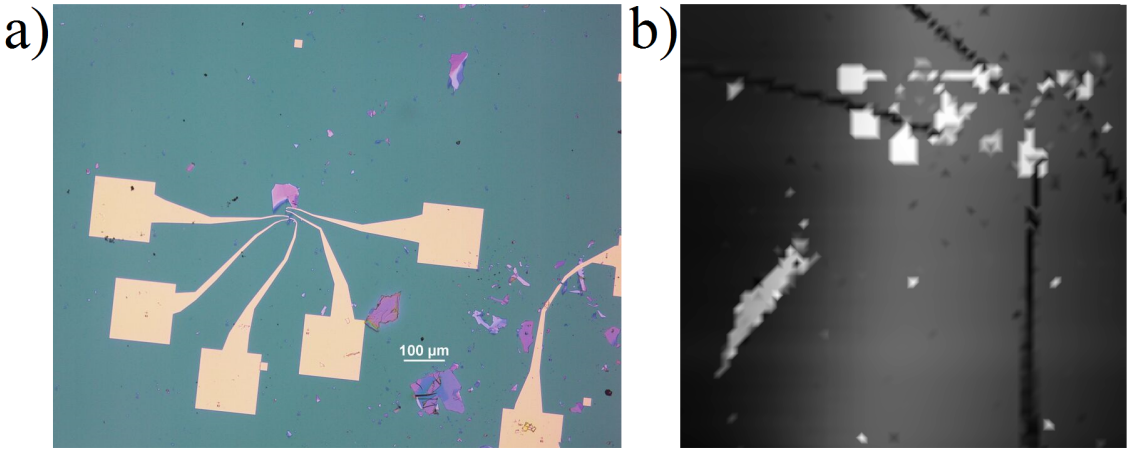

Figure 3.9: ***a)*** *An optical image of two $NbSe_2$ samples showing the large bond pads that surround each sample* ***b)*** *An image of the same samples obtained with 1550 nm light by raster scanning the confocal microscope at 5 K. The wire bonds attached to some of the bond pads can also be seen in this image.*

Once focus is found, the microscope can be raster scanned using the stepper positioners. By recording the reflected power at each position, an image of the sample can be built up. An example image obtained in this way is shown in figure 3.9b. In figure 3.9b the bright areas are the metal features on the sample, the bond pads and electrodes. The vertical streak across the centre of the image is a consequence of the substrate being at a slight angle relative to the microscope's movement. Points along the line produce a higher reflected signal since they are the points at which the microscope is most in focus.

After the large area image has been taken, a smaller more detailed image is normally performed over the area of interest using the microscope's fine positioners. Once the exact position of interest has been located, the microscope can be moved back to that location with an error of less than a micron.

3.2.5 Photoresponse mapping

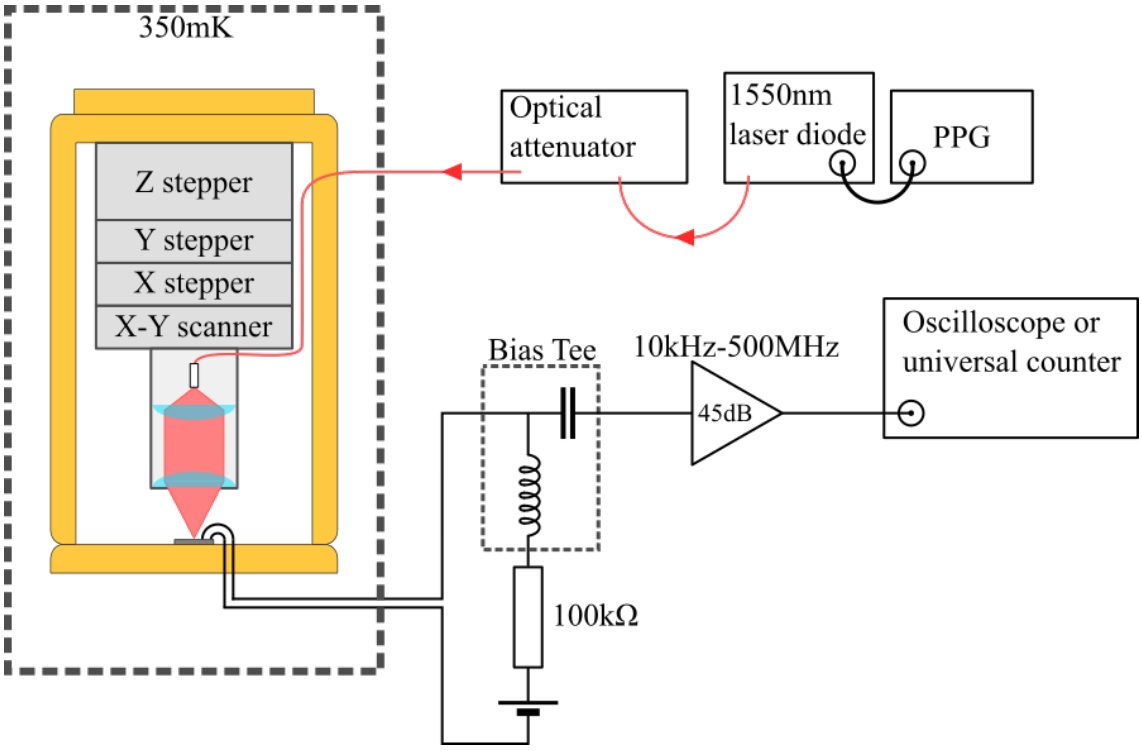

Figure 3.10: *The set-up used to measure the optical response of a $NbSe_2$ device.*

Figure 3.10 shows the apparatus used when optically characterising a $NbSe_2$ superconducting detector. The room temperature amplifier is a RF bay LNA-545 which produces 45dB of amplification across the bandwidth 10 kHz to 500 MHz. The bias tee is a Tektronix PSPL5541A which has a −3 dB bandwidth from 80 kHz to 26 GHz.

A pulse pattern generator (PPG) (Agilent 33220A, 20 MHz bandwidth) is used as the power supply for a 1550nm laser diode, producing a train of laser pulses at 1 MHz repetition rate, 20 ns pulse width with an average power of 1.04 µW. The laser is attenuated by a calibrated optical attenuator (Agilent 8156A). A bias tee is used to separate the biasing circuitry from the amplifier, thereby isolating the response of the detector. A high bandwidth oscilloscope (Agilent DSO80804A) can be used to view pulse shapes produced by the detector or the pulses can be detected by a universal counter (Agilent 53132A) using a threshold criteria. When making an optical measurement, the voltmeters shown in figure 3.13 are usually disconnected from the system as they produce large electrical noise transients.

Using the process described in section 3.2.4, the microscope is positioned over and focussed on the detector. The universal counter is used to count the number of voltage signals produced by the detector per second. The count rate varies with position reaching a maximum when the focussed laser is positioned over the optically sensitive $NbSe_2$ flake. The optical coupling to the detector is maximised by locally scanning the microscope in the X and Y axes. Since the sensitive area of the measured detectors is a similar size to the optical spot, the area with the highest count rate often appears as a single spot of FWHM ∼5 µm.

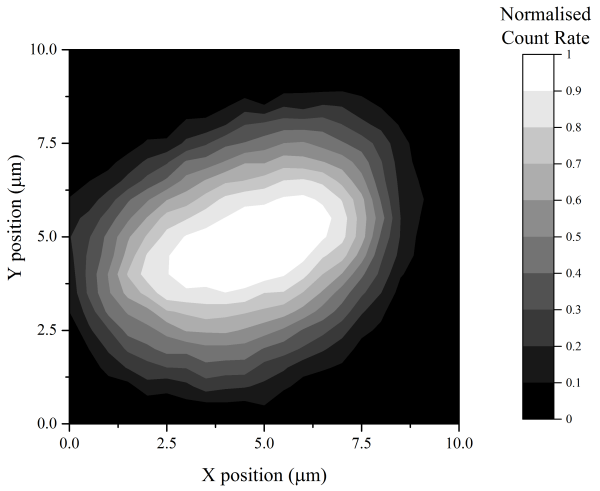

Figure 3.11: *A typical photoresponse map showing the photosensitive area of a $NbSe_2$ detector.*

For further optical characterisation, the coupling efficiency to a detector is maximised by positioning the focussed laser over the area of maximum count rate in a photoresponse map.

3.2.6 Optical testing

Once the coupling to the detector has been maximised, the count rate of the detector can be measured as a function of bias current and attenuation. Using the oscilloscope, response characteristics such as the rise time, decay time and pulse height can be measured as a function of bias current and optical power. Analysing these parameters and the general shape of the output voltage signal under varying conditions provides insight to the detection mechanism at play.

3.2.7 Measuring spot size

The resolution of any image measured by the confocal microscope will be determined by the the spot size of the laser. Mathematically, any image obtained will be a convolution of the sample's features with the profile of the spot. In essence, all optical features will be blurred by an amount determined by how tightly focussed the spot is. Therefore by measuring the reflection profile of a known structure, a measurement of the spot size can be made.

A simple structure to use for this measurement is the edge of a large gold feature. This reduces the problem to being one-dimensional and the convolution can be calculated analytically. The reflection profile across the edge is approximated as a simple step function:

$$f(x) = \begin{cases} a, & \text{if } x < x_0 \\ b, & \text{otherwise} \end{cases} \tag{3.3}$$

and the beam profile is assumed to be Gaussian:

$$g(x) = \frac{1}{\sigma\sqrt{2\pi}} \exp\left(\frac{-x^2}{2\sigma^2}\right) \tag{3.4}$$

The measured reflection profile will therefore be:

$$\begin{aligned} R(x) &= f * g && (3.5)\\ &= \int_{-\infty}^{\infty} f(x-t)g(t)\,dt && (3.6)\\ &= a\int_{x-x_0}^{\infty} g(t)\,dt + b\int_{-\infty}^{x-x_0} g(t)\,dt && (3.7)\\ &= a\int_{0}^{\infty} g(t)\,dt + a\int_{x-x_0}^{0} g(t)\,dt + b\int_{0}^{x-x_0} g(t)\,dt + b\int_{-\infty}^{0} g(t)\,dt && (3.8)\\ &= \frac{1}{2}(a+b) + (b-a)\int_{0}^{x-x_0} g(t)\,dt && (3.9) \end{aligned}$$

To evaluate the integral within equation 3.9 the error function is used. It is defined as:

$$\text{erf}(z) = \frac{1}{\sqrt{\pi}} \int_{-z}^{z} \exp\left(-t^2\right) dt \tag{3.10}$$

By changing the integration variable, it can be shown that:

$$\int_{-a}^{a} g(x)\,dx = \text{erf}\left(\frac{a}{\sigma\sqrt{2}}\right) \tag{3.11}$$

Therefore equation 3.9 is evaluated as:

$$R(x) = \frac{1}{2}(a+b) + \frac{1}{2}(b-a)\,\text{erf}\left(\frac{x-x_0}{\sigma\sqrt{2}}\right) \tag{3.12}$$

The reflection profile across a gold edge was measured and equation 3.12 was used to fit the data, thereby obtaining a value of σ and therefore the FWHM of the optical spot.

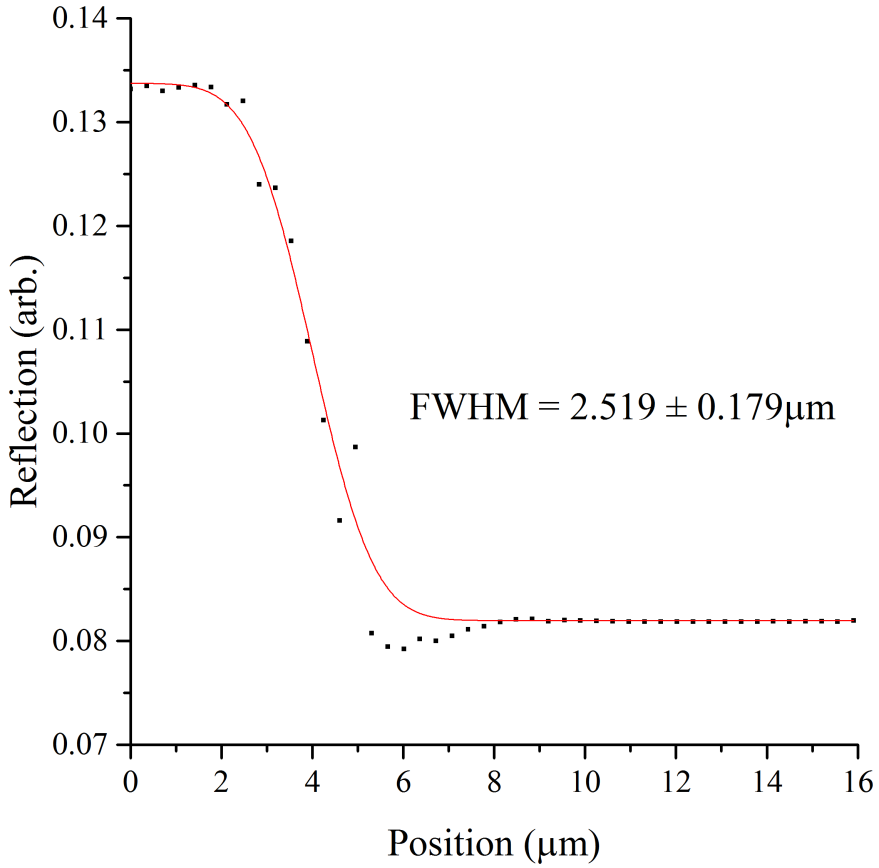

Figure 3.12: *The measured reflection profile as the microscope was moved across the edge of a large gold structure. Equation 3.12 was used to fit the data and extract the FWHM of the focussed spot.*

The FWHM calculated in figure 3.12 is slightly larger than the theoretical minimum for the system (1.17 µm from equation 3.2). Some factors which may have increased the laser spot size include: mechanical vibrations from the running pulse tube, imperfections in the microscope alignment, being slightly out of focus, lens defects or dirt and measurement noise.

3.2.8 Electrical characterisation

When electrically testing samples, the following circuit diagram was routinely used:

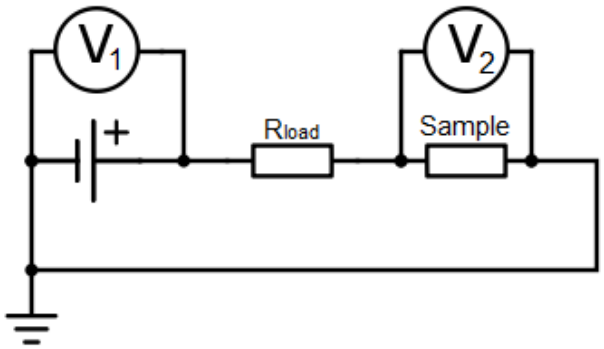

Figure 3.13: *A diagram of the circuit used to measure I-V profiles and the temperature dependence of the sample's critical current. The load resistor has a significantly higher resistance than the sample under test so that the power source will act like a current source.*

An experimentally accessible characteristic of a superconductor is its critical current, I_c. The experimental critical current is the bias current above which the superconductor develops a resistance. An experimentally measured critical current is often just a fraction of the theoretical depairing current predicted by BCS and Ginzburg-Landau theory (equation 2.55). This is because of a non-uniform current density within a superconductor caused by its geometry or by magnetic effects.

The critical current is measured using the set-up shown in figure 3.13. The voltage supply is provided by an isolated, battery powered source to minimise noise. The voltmeters and voltage source are both connected to a Stanford Research Systems SIM 900 mainframe which allows the system to be operated and measured over a GPIB connection to a computer. Python scripts are used to issue instructions to the SIM900 mainframe, allowing automation of time consuming measurements such as measuring the resistance of a superconductor from room temperature to below T_c.

$$I = \frac{V_1 - V_2}{R_{load}} \tag{3.13}$$

In the circuit depicted in figure 3.13, the current flowing through the sample can be calculated using equation 3.13. This current can then be plotted against V_2 to obtain the sample's I-V curve.

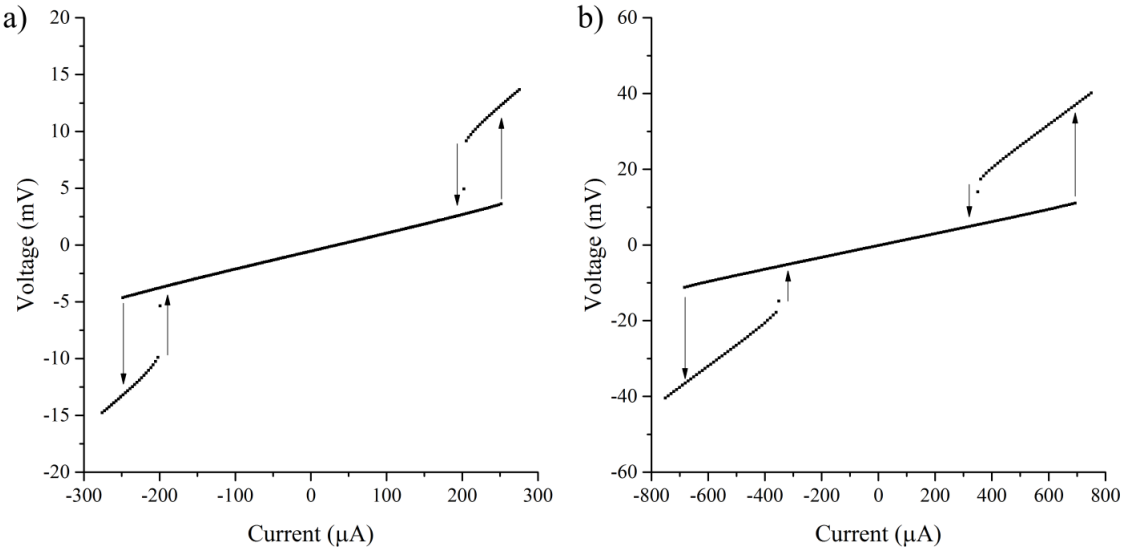

Figure 3.14: a) *An example of a current-voltage (I-V) measurement of a $NbSe_2$ superconducting device at 5 K.* ***b)*** *The same superconducting device measured at 360 mK. Of note is the greatly enhanced critical current at this lower temperature.*

In the superconducting state, a superconductor has zero resistance to DC current, however since electrical measurements are usually performed using a 2-terminal set-up, resistances of all the electrical components in series with the superconductor will also be measured. The wiring inside the cryostat has a resistance of 3-5 Ω additionally, wire bonds and gold electrodes contribute to a series resistance. As shown in figure 3.14, I-V profiles of the measured superconducting detectors were usually highly hysteric around the critical current. This behaviour is caused by the superconductor being electrically heated when it is in the

normal state, thereby reducing its critical current to a lower value. When the device returns to the superconducting state, the local temperature quickly returns to equilibrium with its environment.

The proximity effect

When a superconductor is in physical contact with a metallic material, charge carrier diffusion leads to some of the Cooper pairs crossing into the metallic material. The Cooper pairs will undergo scattering in the metal but a significant density of Cooper pairs will exist near the material boundary and be capable of carrying current without dissipation. This phenomenon, known as the proximity effect, can cause the metal to become superconducting, albeit with a smaller transition temperature and energy gap than the superconductor.

Several of the devices tested in this project had the superconducting $NbSe_2$ covered with a single layer of graphene, a conductive material. It is likely that the proximity effect would cause the graphene to become superconducting at low temperature and therefore operating the detector near T_c could potentially eliminate any effects on the detector performance due to the proximitised graphene. However, no clear second resistive transition with temperature was observed for any device, so if the graphene was in fact superconducting, it is unknown at what temperature this may have occurred.

3.3 Estimating optical absorption

The samples consist of a multi-layered stack of exfoliated materials on an oxidised Si substrate. They are illuminated perpendicularly with a focussed laser with a spot which is approximately Gaussian in shape with a full width at half maximum (FWHM) of 2.5 µm.

$$FWHM = 2\sigma\sqrt{2\ln(2)} \tag{3.14}$$

where σ is the standard deviation of the Gaussian spot.

The coupling efficiency of the laser to the superconducting sample can be approximated as a product of the coupling efficiency in the direction of propagation (η_z) and perpendicular to it (η_{x-y}). Where η_z is the coupling efficiency to the superconducting layer when the structure is viewed as one dimensional and η_{x-y} is the overlap between the spot profile and the superconducting device in the 2D x-y plane.

$$\eta_{optical} \approx \eta_z \times \eta_{x-y} \tag{3.15}$$

3.3.1 X-Y coupling efficiency

Approximating the device as a rectangle, the x-y coupling efficiency is calculated as the overlap between the Gaussian laser spot and the rectangular superconductor. For a device of

width W and length L, the x-y coupling efficiency can be approximated as:

$$\eta_{x-y} = \int_{\frac{-L}{2}}^{\frac{L}{2}} \int_{\frac{-W}{2}}^{\frac{W}{2}} \frac{1}{2\,\pi\,\sigma^2} \exp\left(\frac{-x^2-y^2}{2\,\sigma^2}\right) dx\,dy \tag{3.16}$$

$$= \text{erf}\left(\frac{W}{2\sqrt{2}\sigma}\right) \text{erf}\left(\frac{L}{2\sqrt{2}\sigma}\right) \tag{3.17}$$

Figure 3.15 shows a sketch of a Gaussian spot incident on a rectangular device and the resulting coupling efficiency in the x-y plane calculated using equation 3.17.

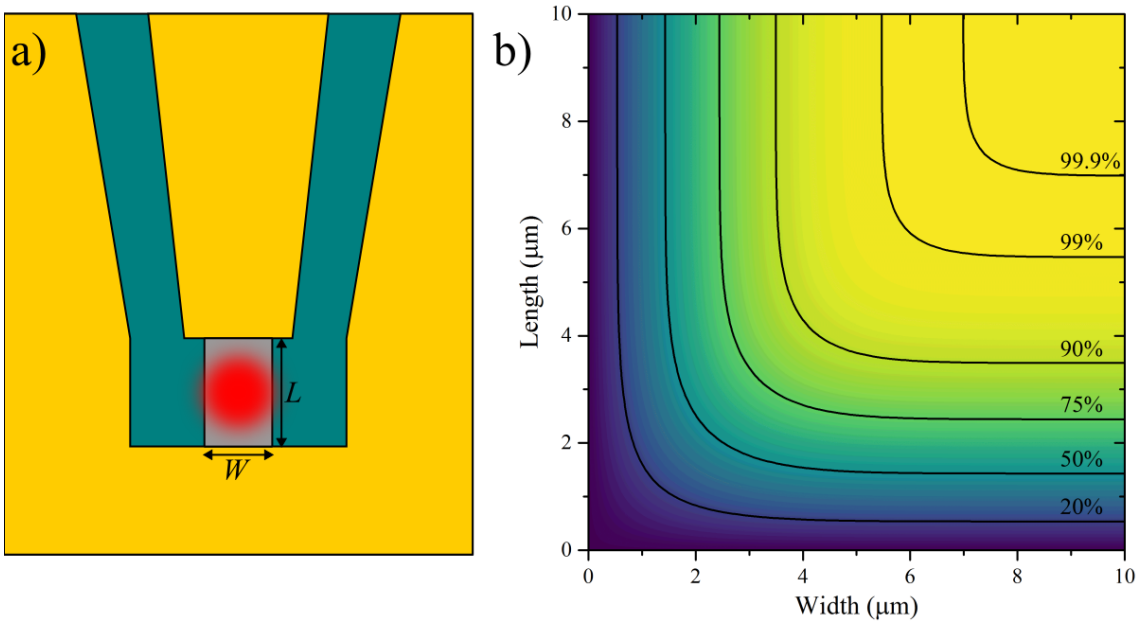

Figure 3.15: ***a)*** *A sketch of a rectangular superconducting device illuminated by a Gaussian laser spot.* ***b)*** *The x-y coupling efficiency of a Gaussian spot to a centred rectangular box of varying dimensions. The FWHM used for the Gaussian distribution was 2.5 μm.*

3.3.2 Coupling efficiency to a layer within an optical stack

Viewing the devices as a 1D stack of thin films, the fraction of optical power absorbed in any of the layers can be calculated analytically using Fresnel's equations. This is most easily achieved using complex numbers to represent the phase and amplitude of the propagating electric field. Absorption and phase change of the wave during propagation are taken into account with a complex refractive index for each layer, $n' = n + i\kappa$. Similarly, the amplitude reflection and transmission coefficients at each interface are also, in general, complex.

Following a similar method to Byrnes [111]: a system of N layers is considered where light is injected at layer 0 and propagates towards layer $N-1$. The subscript j is used to denote the layer number so that each of the layers has a thickness d_j and a complex refractive index n'_j. For $j > 0$, v_j and w_j are defined as the forward and backward propagating amplitudes of the electric field within layer j, at the interface between the layers $j-1$ and j. v_0 and w_0 are defined as the amplitudes of the electric field within layer 0 incident on the interface between layers 0 and 1. This is done so that the thicknesses of layers 0 and $N-1$ do not need to be

specified and these layers can be taken as being semi-infinite.

The phase and amplitude of the electric field will change as it propagates across a layer. This is handled though multiplication by the complex factor $\exp(i\,\delta_j)$ where:

$$\delta_j = \begin{cases} 0, & \text{if } j = 0 \\ \dfrac{2\,\pi\,d_j\,n'_j}{\lambda}, & \text{otherwise} \end{cases} \tag{3.18}$$

For perpendicular illumination, the amplitude reflection and transmission coefficients for each interface are written as:

$$r_{j,\,j+1} = \frac{n'_j - n'_{j+1}}{n'_j + n'_{j+1}} = -r_{j+1,\,j} \tag{3.19}$$

$$t_{j,\,j+1} = \frac{2\,n'_j}{n'_j + n'_{j+1}} = t_{j+1,\,j} \tag{3.20}$$

The forward and backward propagating wave amplitudes can now be written as a sum of transmitted and reflected waves from adjacent layers:

$$v_{j+1} = v_j\,\exp(i\,\delta_j)\,t_{j,\,j+1} + w_{j+1}\,r_{j+1,\,j} \tag{3.21}$$

$$w_j = v_j\,\exp(2\,i\,\delta_j)\,r_{j,\,j+1} + w_{j+1}\,\exp(i\,\delta_j)\,t_{j+1,\,j} \tag{3.22}$$

Equations 3.21 and 3.22 can be rearranged and combined into a matrix equation. The 2×2 transfer matrix $\boldsymbol{M}_j$ relates the forward and backward amplitudes in layer j to those in layer $j+1$.

$$\begin{bmatrix} v_j \\ w_j \end{bmatrix} = \boldsymbol{M}_j \begin{bmatrix} v_{j+1} \\ w_{j+1} \end{bmatrix} \tag{3.23}$$

Where:

$$\boldsymbol{M}_j = \frac{1}{t_{j,\,j+1}} \begin{bmatrix} \exp(-i\,\delta_j) & r_{j,\,j+1}\,\exp(-i\,\delta_j) \\ r_{j,\,j+1}\,\exp(i\,\delta_j) & \exp(i\,\delta_j) \end{bmatrix} \tag{3.24}$$

If the complex refractive index and thickness of each layer is known, $\boldsymbol{M}_j$ can be calculated for each layer. Therefore if the incident light on the stack is known, the electric field amplitudes v_j and w_j can be calculated for all layers.

The transfer matrix of the entire multilayer stack, $\widetilde{\boldsymbol{M}}$, can be used to relate the amplitudes of the electric field in layer 0 to those in layer $N-1$.

$$\begin{bmatrix} v_0 \\ w_0 \end{bmatrix} = \widetilde{\boldsymbol{M}} \begin{bmatrix} v_{N-1} \\ w_{N-1} \end{bmatrix} \tag{3.25}$$

Where:

$$\widetilde{\boldsymbol{M}} = \boldsymbol{M}_0 \times \boldsymbol{M}_1 \times \boldsymbol{M}_2 \times \ldots \times \boldsymbol{M}_{N-4} \times \boldsymbol{M}_{N-3} \times \boldsymbol{M}_{N-2} \tag{3.26}$$

To find the reflection (r) and transmission (t) coefficients of the optical stack, the values of

v_0 and w_{N-1} are set to 1 and 0 respectively. Consequently equation 3.25 can be written as:

$$\begin{bmatrix} 1 \\ r \end{bmatrix} = \widetilde{\boldsymbol{M}} \begin{bmatrix} t \\ 0 \end{bmatrix} \tag{3.27}$$

r and t can be calculated as:

$$r = \frac{\widetilde{\boldsymbol{M}}_{21}}{\widetilde{\boldsymbol{M}}_{11}} \tag{3.28}$$

$$t = \frac{1}{\widetilde{\boldsymbol{M}}_{11}} \tag{3.29}$$

The subscripts used in equations 3.28 and 3.29 are used to denote elements of the matrix $\widetilde{\boldsymbol{M}}$.

The power absorbed in a layer of an optical stack can be calculated as the difference between the power entering and exiting the layer. The power transfer per unit area of an EM field is given by the Poynting vector, the time averaged value of which is given by:

$$\langle \boldsymbol{S} \rangle = \text{Re}\left(\frac{1}{2}\boldsymbol{E}^* \times \boldsymbol{H}\right) \tag{3.30}$$

For a plane wave, $\boldsymbol{H}$ is perpendicular to and proportional to $\boldsymbol{E}$.

$$\boldsymbol{H} = \frac{1}{\mu_0 \omega}\boldsymbol{k} \times \boldsymbol{E} \tag{3.31}$$

where for a forward propagating wave:

$$\boldsymbol{k} = \frac{2\pi n'}{\lambda}\hat{\boldsymbol{z}} \tag{3.32}$$

and for a backward propagating wave:

$$\boldsymbol{k} = -\frac{2\pi n'}{\lambda}\hat{\boldsymbol{z}} \tag{3.33}$$

For perpendicular illumination, the definition of x-y orientation is arbitrary. Defining the y-axis to be the axis of electric field oscillation, the amplitudes of the electric and magnetic field at the material interfaces are:

$$\boldsymbol{E}_j = (v_j + w_j)\,\hat{\boldsymbol{y}} \tag{3.34}$$

$$\boldsymbol{H}_j = \frac{n'_j}{\mu_0\, c}(-v_j + w_j)\,\hat{\boldsymbol{x}} \tag{3.35}$$

Using equations 3.30, 3.34 and 3.35 the optical power entering each layer in the stack is:

$$\langle \boldsymbol{S}_j \rangle \cdot \hat{\boldsymbol{z}} = \text{Re}\left(\frac{n'_j}{2\,\mu_0\, c}(v_j^* + w_j^*)(v_j - w_j)\right) \tag{3.36}$$

Therefore, the out of plane coupling efficiency (η_z) to a layer will be the power absorbed in that layer, normalised to the input power.

$$\eta_{z,j} = \frac{\left(\langle \boldsymbol{S}_j \rangle - \langle \boldsymbol{S}_{j+1} \rangle\right) \cdot \hat{\boldsymbol{z}}}{\langle \boldsymbol{S}_0 \rangle \cdot \hat{\boldsymbol{z}}} \tag{3.37}$$

Calculating the power absorbed in a layer within an optical stack is a complex process to do by hand, so a Matlab script has been written which follows the method above to calculate all of the transfer matrices, Poynting vectors and the absorbed power in each layer.

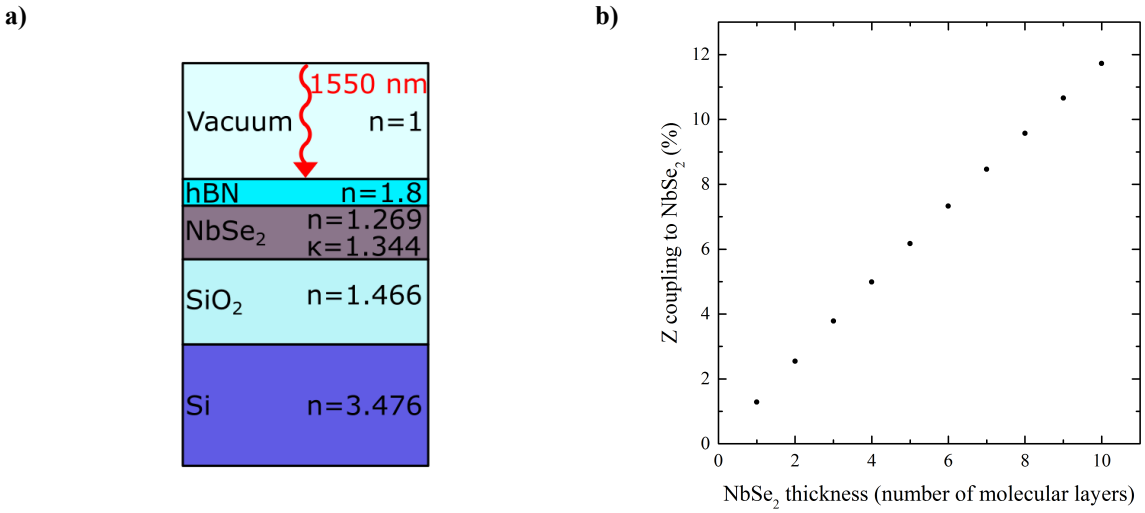

Figure 3.16: ***a)*** *A sketch showing the multilayered optical stack of a encapsulated $NbSe_2$ detector. The refractive index data shown was obtained from the following: hBN data from Ref. 112, $NbSe_2$ data from Ref. 113, SiO_2 data from Ref. 104, Si data from Ref. 114.* ***b)*** *The proportion of 1550 nm light absorbed into a $NbSe_2$ crystal of varying thickness, encapsulated by hBN, on an oxidised Si substrate with an oxide thickness of 285 nm.*

3.4 Detector performance metrics

3.4.1 Responsivity

Responsivity measures the signal produced by a detector relative to the input power. It is therefore a measure of how sensitive a detector is with larger values indicating better detector performance. For a current biased device where the signal is measured as a voltage, responsivity has units $\mathrm{V\,W^{-1}}$.

To calculate the responsivity of a $NbSe_2$ detector, the amplitude of voltage signal was divided by the maximum instantaneous input laser power and by the amplifier gain.

Responsivity measures the magnitude of a detector's response relative to the optical input power. It is therefore dependent on several detector characteristics and would be expected to increase with optical coupling efficiency, bias current and the normal state resistance of the detector. The responsivity values measured for the $NbSe_2$ devices tested in this project

varied from 42-230 V W^{-1} with the lowest responsivity values recorded for devices that had been shaped by etching.

3.4.2 Noise equivalent power (NEP)

NEP is a metric commonly used to access the performance of photodetectors. It is the input power which when measured over a 1 Hz output bandwidth produces a signal to noise ratio of one. A lower NEP indicates that less power is required to distinguish the detector response from noise. It has units of $WHz^{-0.5}$ and may be calculated by dividing the noise spectral density of a detector by its responsivity.

To calculate the NEP of $NbSe_2$ detectors the noise spectral density was measured in the absence of illumination and divided by the detector responsivity. The calculated NEP does not take into account the optical coupling efficiency of the detector and is therefore referred to as an optical NEP. NEP calculated in this manner may only be applied to detectors whose output signal varies continuously with input power and therefore is not used when the response measured from a $NbSe_2$ detector was found to be binary.

The signal to noise ratio of a detector is dependent on the amplitude of signals that it generates which, in this case, will be dependent on the bias current and size of the resistive transition. It is therefore not surprising that the lowest NEP measured in this project (3.2×10^{-14} $WHz^{-0.5}$) was produced by the detector which had the highest product of critical current and normal state resistance (sample 19).

3.4.3 System detection efficiency

The system detection efficiency (η_{SDE}) is a parameter used to quantify the performance of single photon detector systems [31]. It is the probability of detecting a photon incident on the detector system. It is therefore dependent on the optical coupling as well as the efficiency of the device (η_{DDE}). η_{SDE} typically increases with bias current until I_c is exceeded. However, high quality SNSPDs show a plateau in η_{SDE} immediately below I_c which is thought to indicate saturation of the device detection efficiency (η_{DDE}) [115].

3.4.4 Dark count rate

Click detectors such as SNSPDs will produce detection events in the absence of light. The count rate of the detector without optical stimulation is the dark count rate (DCR). The DCR of an SNSPD is current dependent, typically showing an exponential growth in DCR as the critical current is approached [116]. None of the devices tested in this thesis showed any dark count rate which is typical of superconducting detectors which are not single photon sensitive [117].

3.4.5 Timing jitter

The time between the absorption of a photon in a detector and the generation of a signal will vary between detection events. Time correlated single photon counting (TCSPC) can be used to obtain a histogram of the device response times to a repetitive laser source [118]. The timing jitter of the device is then defined as the FWHM of the histogram.

3.4.6 Dead time

After a detection event, a detector may be unresponsive to further illumination for a period of time while it resets. This period of time is known as the dead time and it can vary from microseconds for transition edge sensors to a few nanoseconds for SNSPDs.

Chapter 4

Experimental results

Since the discovery of graphene in 2004 [80] significant efforts have been made to use 2D materials in a variety of detector applications [7, 119–121]. Since 2D materials have a very large surface area compared to their volume, they can be extremely sensitive to their electrical, chemical and thermal environment.

It has been known since the 1960s [122] that bulk $NbSe_2$ is a superconductor ($T_c = 7.2\,\mathrm{K}$) and being a transition metal dichalcogenide (TMD), bulk $NbSe_2$ crystals are comprised of molecular layers that are weekly bonded together via the van der Waals force. Individual molecular layers of $NbSe_2$ can therefore be exfoliated to create ultimately thin samples. Initial experiments with few layered $NbSe_2$ showed that its superconducting critical temperature (T_c) was strongly suppressed in few layered samples and superconductivity did not exist in samples thinner than three molecular layers. However it has recently been shown that if few-layered samples are prepared without exposure to atmospheric gasses, a superconducting state remains even in single layer $NbSe_2$ [95]. Such a material allows the fabrication of an ultimately thin superconducting detector.

The detector designs implemented in this work are variants of the Superconducting Nanowire Single Photon Detector (SNSPD), the operating mechanism of which is described in section 2.4.1. In summary, a superconducting wire is current biased close to its critical current so that when a photon is absorbed in the wire, a section of the material is driven to the normal state. The resulting increase in electrical resistance causes Joule heating around the normal region causing heating and further expansion of the normal area. A detection event results in a voltage pulse which may be observed using an oscilloscope or measured with a pulse counter.

Throughout this work, the design of the $NbSe_2$ based detector was an evolving process. In this chapter, I will explain the iterations of detector design and present a summary of the optical and electrical characterisation that was performed on the detectors.

4.1 Graphene encapsulated $NbSe_2$ flakes

Several fabrication methods were used to produce $NbSe_2$ photodetectors. In the first instance a simple fabrication recipe was used to try to establish if micron sized superconducting $NbSe_2$ samples could be fabricated and if they would show photodetection. The first samples obtained for testing were few-layered flakes of $NbSe_2$ encapsulated with a single layer of graphene to prevent degradation of the superconducting properties. Graphene was chosen as the encapsulation material because it is impermeable to water and atmospheric gasses [123]. It is also extremely transparent, transmitting 97.7% of incident light [124, 125] and it is conductive allowing electrical contacts to be fabricated on top of the graphene-$NbSe_2$ stack.

The $NbSe_2$ flakes were exfoliated onto an oxidised silicon substrate which had a pre-patterned grid of optical markers (100 µm spacing). The substrate was manually scanned with an optical microscope and once promising samples were located, a pre-prepared layer of graphene was placed over the $NbSe_2$ flake using the dry transfer method described in section 3.3. The procedure from exfoliation to encapsulation was completed quickly, typically under one hour, to minimise oxidation of the $NbSe_2$ as much as possible. Using optical images of the encapsulated samples, bespoke electrodes were designed and fabricated on top of the encapsulated sample. The contacts are Ti/Au 5/50 nm and were fabricated using bilayer PMMA liftoff.

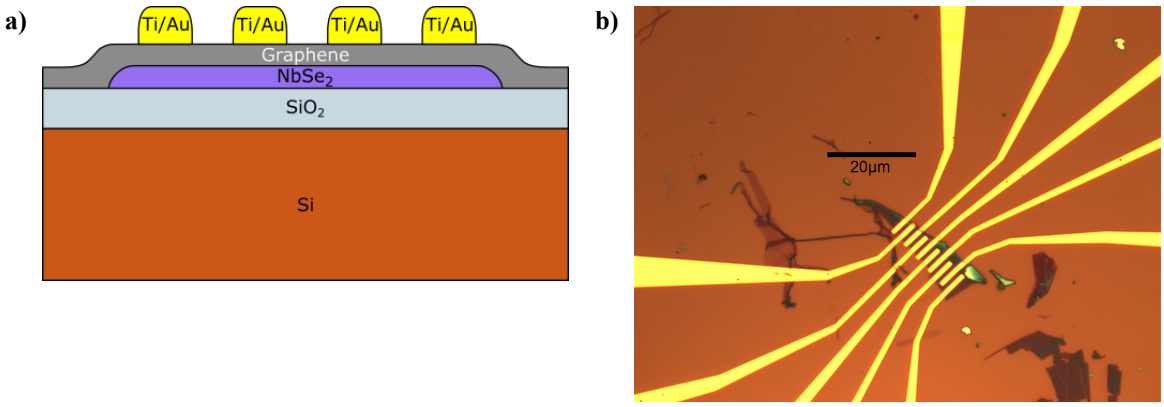

Figure 4.1: ***a)*** *A schematic of the first $NbSe_2$ detectors that were tested.* ***b)*** *An optical image of a graphene encapsulated $NbSe_2$ flake with several titanium gold electrodes (Sample 6)*

Eight samples of this design were tested electrically and optically, the width of the $NbSe_2$ flakes between the contacts was approximately 5 µm and the separation between the metal contacts was 1 µm. The thickness of the $NbSe_2$ was estimated from optical contrast and ranged from 2 layers (1.25 nm) to 5 molecular layers (3.14 nm) thick. The yield of the electrical contacts was expected to be poor and so multiple sets of electrodes were patterned onto each sample (Fig. 4.1b).

4.1.1 Electrical characterisation

Of the eight devices of this type tested, a clear superconducting transition was only observed in two devices (device numbers 5 and 6). The other six had large (>2 kΩ) resistances below 5 K. The lack of superconductivity in these samples is attributed to oxidation of the $NbSe_2$ prior to encapsulation. The two samples which were superconducting were amongst the thickest samples tested (5 layers) agreeing with the general trend that has been observed in literature that few-layered $NbSe_2$ readily degrades in air and must therefore be exfoliated in an inert atmosphere to preserve superconductivity.

Sample ID	Number of layers	R_N	R_S	T_c	I_c (360 mK)
1	5	521 Ω	466 Ω	5.7 K	-
2	3	2.17 kΩ	2.14 kΩ	3.5 K	-
3	2	4.1 kΩ	-	-	-
4	2	25.5 kΩ	-	-	-
5	5	75 Ω	49 Ω	5.8 K	265 μA
6	5	56 Ω	41 Ω	4.8 K	224 μA
7	4	8.4 kΩ	-	-	-
8	3	27.3 kΩ	-	-	-

Table 4.1: *The electrical properties of the graphene encapsulated $NbSe_2$ flakes tested. The thicknesses of the samples were estimated from their optical contrast. R_N is the 2-point resistance of the sample in the normal state above the superconducting transtition temperature, R_S is the 2-point resistance of the sample in the superconducting state. The critical temperature (T_c) is defined as the temperature midway through the superconducting transition and the critical current (I_c) is the bias current at which the resistance of the sample was observed to increase from its zero bias resistance.*

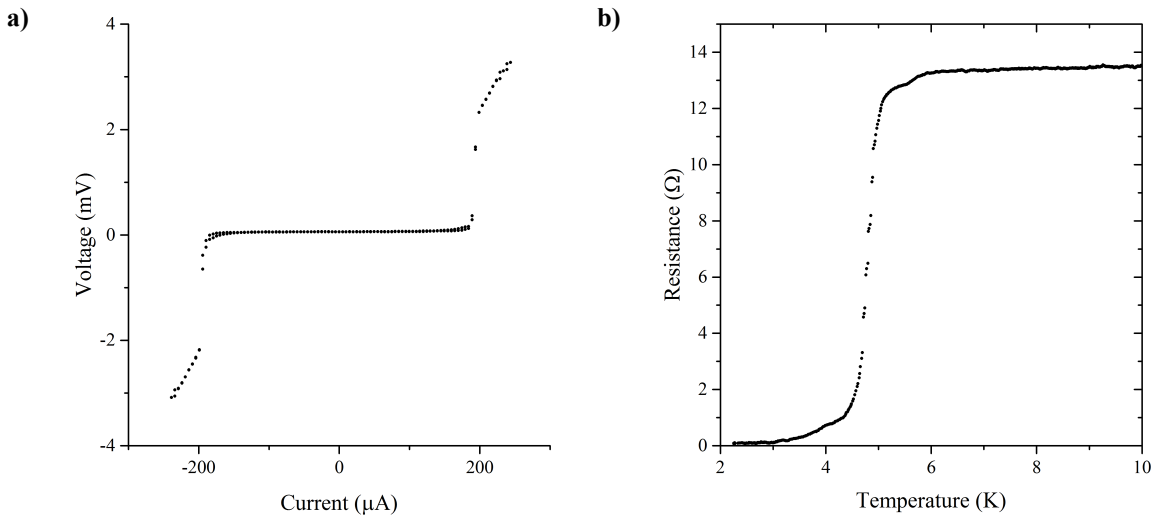

Figure 4.2: a) *The 4-point I-V profile of sample 6 measured at 2.2 K.* ***b)*** *The 4-point resistance of sample 6 as a function of temperature, showing a transition temperature of 4.8 K*

Of the eight graphene encapsulated samples that were tested, only samples 5 and 6 showed a clear superconducting switching current in their I-V curves. However, as shown in table 4.1, samples 5 and 6 did not drop to zero resistance in a 2-point measurement but instead maintained a finite resistance of around 45 Ω in the superconducting state. The wiring in

series with the samples will contribute a resistance but is believed to be less than 5 Ω. To determine the origin of the remaining resistance a 4-point measurement was performed on both samples. In both cases, the 4-point resistance of the samples was observed to drop to zero, as shown in figure 4.2, suggesting that the resistance observed under 2-point testing must be due to resistive elements in series with the superconductor.

Since the electrical contacts were fabricated on top of the encapsulation layer (see figure 4.1a), the current must flow through it to reach the $NbSe_2$. Therefore, in a 2-point measurement, the resistance of the encapsulation layer will be measured. A similar series resistance was observed by Jiang [126], where a thin film of the high T_c superconductor $Bi_2Sr_2CaCu_2O_{8+x}$ was encapsulated by a layer of graphene. It is also possible that the gold electrodes are not well adhered to the superconducting samples causing a contact resistance.

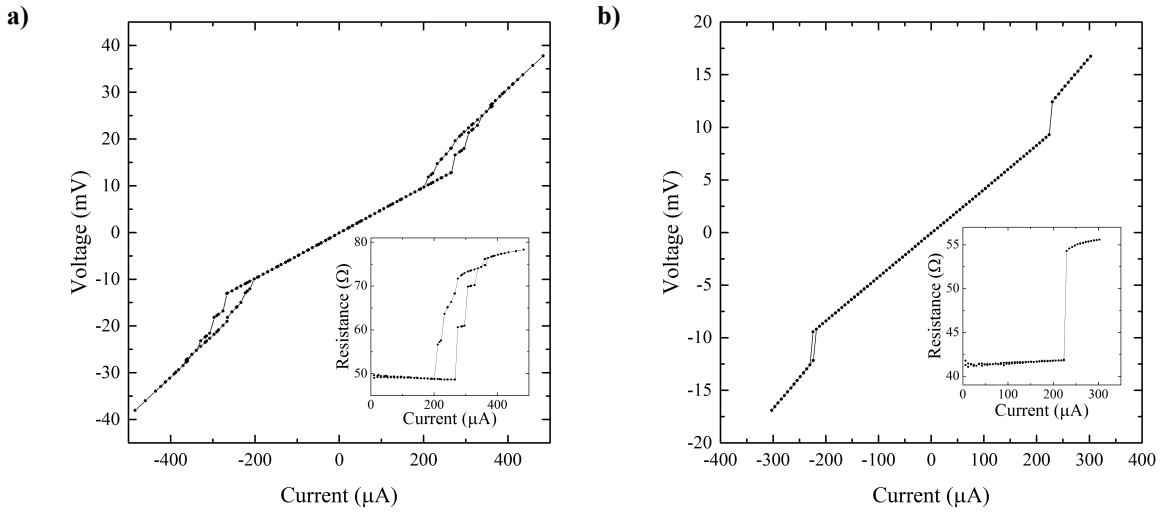

Figure 4.3: a) *The 2-point I-V profile of sample 5 at 360 mK. The device is hysteretic and has multiple transitions.* ***b)*** *The 2-point I-V profile of sample 6 at 360 mK.*

Unlike sample 6, sample 5 shows multiple resistive steps with increasing bias current. This implies that there are areas of the device capable of carrying a higher current than others. This may be a result of partial oxidation of the $NbSe_2$ prior to encapsulation, physical damage to the sample during manipulation or a non-uniform cross sectional area of the superconductor across its length. The superconducting transitions are also hysteretic meaning that once in a resistive state, Joule heating of the sample prevents it from returning to the superconducting state until the current is reduced below a retrapping current.

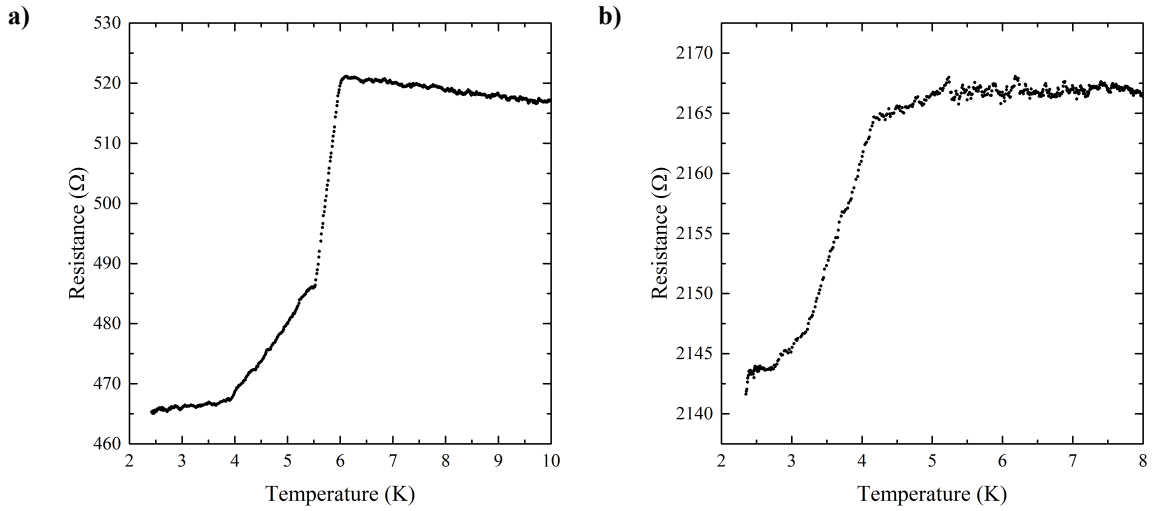

Figure 4.4: *The two-point resistance of samples 1 and 2 as temperture slowly increases from 2 K. The applied current for these measurements was 15 μA.* ***a)*** *Sample 1.* ***b)*** *Sample 2.*

As shown in figure 4.4, samples 1 and 2 showed some evidence of a superconducting transition with temperature. However the samples remained at a high resistance below the transition temperature, showing no clear critical currents and no response to illumination. Such a high resistance in series with the superconducting $NbSe_2$ must imply that the electrical connection to the sample is of poor quality and a large contact resistance is present either between the graphene encapsulation layer and the Ti/Au contact or between the graphene and the $NbSe_2$.

4.1.2 Optical characterisation

Sample 6

Following the procedure described in section 3.2.4, a focussed 1550 nm laser spot was raster scanned over sample 6. The reflected laser power was used to image the large gold structures on the chip which were readily identified as the electrical bond pads and wiring. The point where the electrical wires converge gives the approximate co-ordinates of the $NbSe_2$ flake. To investigate if the device responds to illumination and to locate its photosensitive position, the procedure described in section 3.2.5 was used. In summary, the AC signal line from the sample is connected to a universal pulse counter (Agilent 53132A). The sample is current biased near its critical current and a pulsed 1550 nm laser is raster scanned across the device area (as identified by the reflection map). The count rate obtained from a universal counter is recorded as a function of position and may be plotted as shown in Fig. 4.5b. The universal counter was set to detect voltage pulses greater than 10 mV.

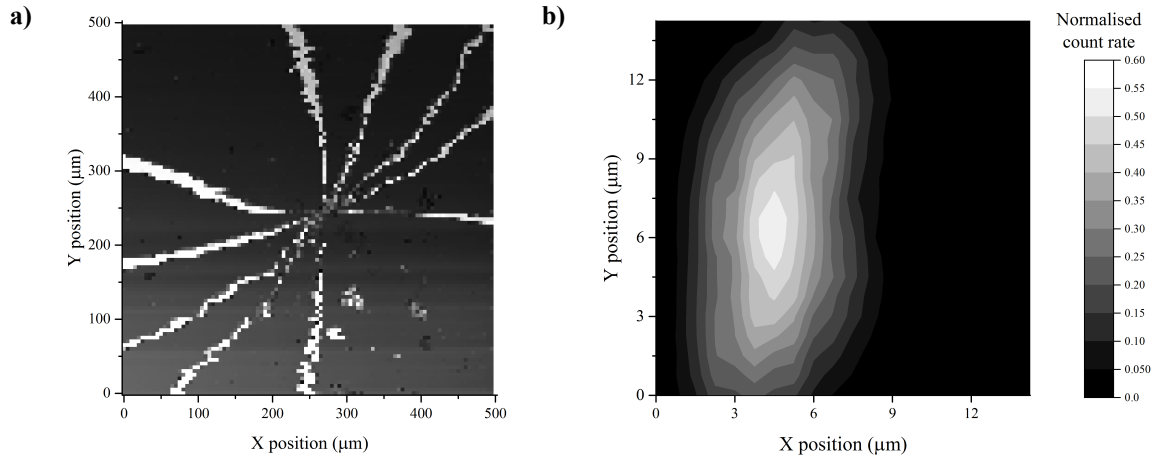

Figure 4.5: a) *An in-situ image of sample 6 recorded at 5 K using 1550 nm illumination. The gold wires converging on the $NbSe_2$ strip are clearly visible.* ***b)*** *The positional dependence of the photoresponse of sample 6 to 1550 nm pulsed illumination. This measurement was made at 5 K with a bias current of 0.95 I_c, an optical pulse width of 20 ns, a pulse energy of 1.04 $\times$ 10^{-13} J and a repetition rate of 1 MHz.*

As shown in Fig. 4.5b, sample 6 was found to be sensitive to pulsed illumination and appeared to have a single active area of approximate dimensions 3 µm $\times$ 12 µm which matches well with the dimensions of the $NbSe_2$ flake. Interestingly, the background count rate (dark count rate) was found to be zero, no voltage signals are detected without illumination on the device.

Positioning the focussed laser spot in the centre of the photosensitive region, the bias current and optical attenuation were swept. As shown in figure 4.6a, at 5.1 K device 6 is most sensitive to low energy pulsed illumination at a bias current of 100 µA. At 5.1 K device 6 is partway through its superconducting transition. As the bias current is increased, there is a gradual increase of the sample's resistance in the current range 95 µA-105 µA.

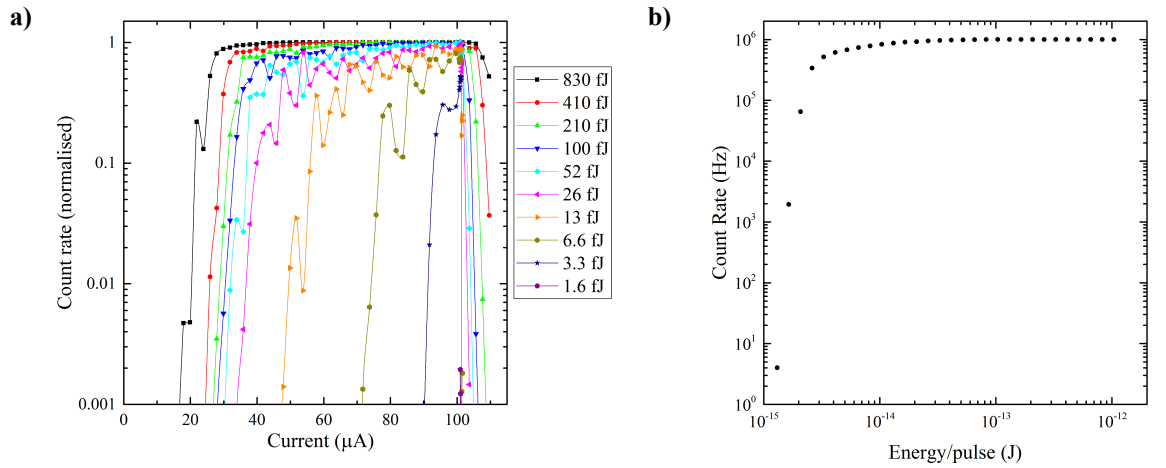

Figure 4.6: a) *The count rate of device 6 normalised to the laser repetition rate with varying current at laser pulse energies ranging from 1.6 fJ to 830 fJ in steps of 3 dB. Measured at 5.1 K under 1550 nm pulsed illumination.* ***b)*** *The count rate of device 6 with varying pulse energy at 5.1 K with a bias current of 100 µA, in the middle of the superconducting transtition.*

At 5.1 K, the count rate obtained from sample 6 shows a sharp response cut-off to pulsed

illumination. At a given bias current, there is a value of pulse energy below which the sample shows no detectable response and above which the measured count rate increases rapidly. When biased in the middle of the superconducting transition the sample reaches its highest sensitivity to low illumination levels and at this point the count rate decreases from 3×10^5 to less than 1 counts per second with just a 4 dB increase of optical attenuation as shown in figure 4.6b.

The count rate shown in figure 4.6 is the rate of voltage signals produced, which have an amplitude greater than 10 mV after amplification. Therefore a drop in count rate could indicate that fewer signals are being produced by the detector or that the signal amplitude has decreased below 10 mV. To investigate the origin of the drop in count rate, a high bandwidth oscilloscope (Keysight Infiniium DSO80804A 8 GHz) was used to measure the shape and amplitude of the signals with varying optical pulse energy.

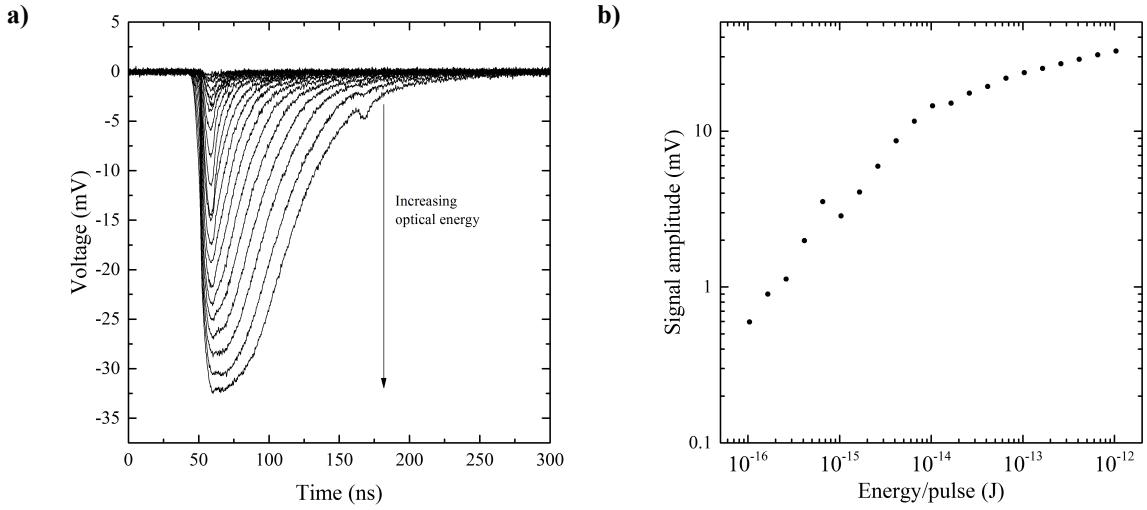

Figure 4.7: ***a)*** *Each trace is an average of 256 signals recorded from sample 6 with optical pulse energy varying from 1×10^{-16} J to 1×10^{-12} J in steps of 2 dB.* ***b)*** *The signal amplitudes from sample 6 with varying optical energy. Measured at 5.1 K with an applied bias current of 102.4 μA.*

Figure 4.7 shows that the signal magnitude varies greatly with the applied attenuation. The average voltage signal amplitudes vary from 30 mV at 1 pJ per pulse to less than 1 mV at 100 aJ per pulse where the average signal drops below the noise floor of the measurement. The small secondary peak visible around 170 ns (100 ns after the primary peak) is most likely an electrical distortion caused by imperfect impedance matching to the transmission line.

The oscilloscope measurements indicate that the drop in count rate that is observed with increasing optical attenuation is due to the amplitude of the signals decreasing below the threshold voltage of the universal counter (10 mV) and not that the signals are being produced at a lower rate. Indeed, by comparing figures 4.6b and 4.7b it can be seen that the measured count rate begins to decrease rapidly as the average signal amplitude drops below 10 mV at an optical pulse energy of approximately 4 fJ.

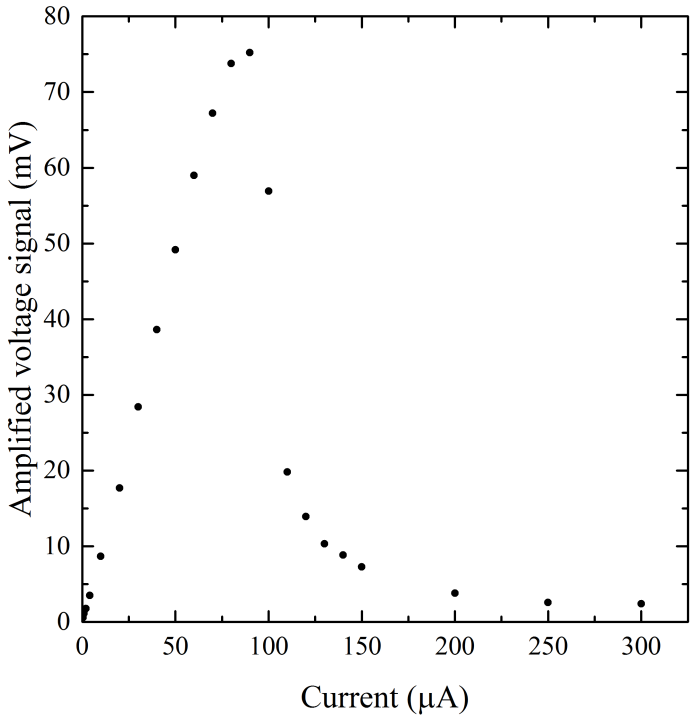

Figure 4.8: *Average voltage signal amplitudes obtained at 5.1 K from bright optical pulses at 1 pJ per pulse with varying bias current.*

Figure 4.8 shows the average amplitude of voltage signals from sample 6 at 5.1 K under strong pulsed illumination. The response is initially linear with current, assuming that the gain of the readout circuit is linear, this implies that the resistance generated in the $NbSe_2$ by the optical pulse is independent of the current through the sample. The signal amplitude reaches a peak around the critical current before falling. I believe that this behaviour is caused by most of the sample switching to the normal state. Since the majority of the sample is in the normal state, optical illumination has a reduced ability to raise the sample resistance further and so the signal amplitude falls. As more current is applied, a larger proportion of the $NbSe_2$ is driven normal by the current and the optical response continues to fall.

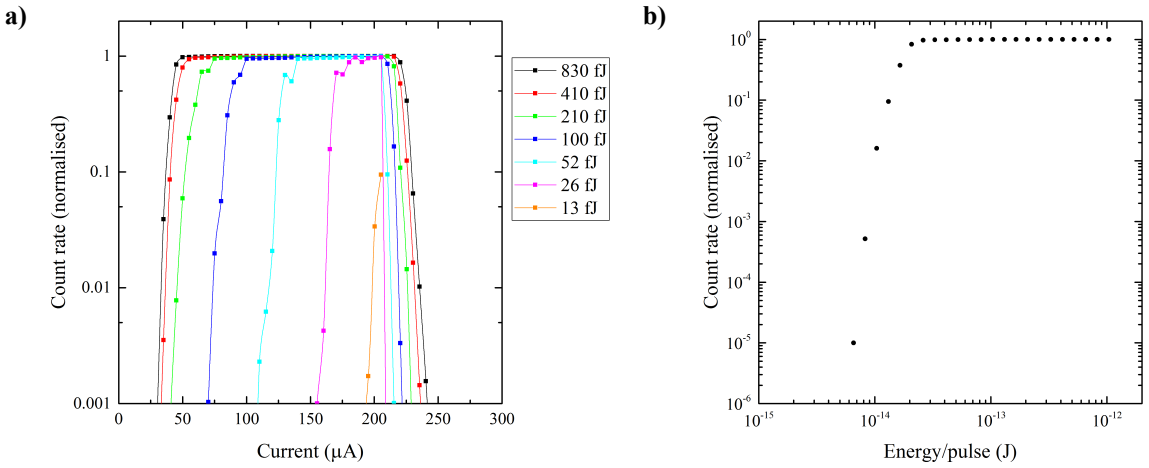

Figure 4.9: ***a)*** *The count rate of sample 6 at 5.1 K with a parallel 50 Ω shunt resistor, varying current and varying optical pulse energy.* ***b)*** *The amplitude of voltage signals at 205 μA, the bias current where the device showed the highest sensitivity to low energy optical pulses.*

Figure 4.9 shows the count rate of sample 6 at 5.1 K as a function of applied bias current with a 50 Ω resistor connected in parallel with the device. Such resistors are commonly used with SNSPDs to prevent latching behaviour and allow device operation at currents closer to I_c, thereby increasing device efficiency. In this case however, the two-point resistance of sample 6 is 41 Ω in the superconducting state and 56 Ω in the normal state. Therefore the parallel resistor acts as a current divider, diverting approximately half of the current away from the sample. Therefore the supply current required to reach I_c is approximately two times larger than without the shunt resistor and peak sensitivity to low illumination levels is reached at 205 μA instead of 100 μA.

Other than an increased current scale, the behaviour with a shunt resistor is similar to that without one. The other difference being that the count rate begins to decrease at an energy of 2×10^{-14} J per pulse instead of 4×10^{-15} J per pulse. This behaviour can be explained by examining the expected increase of the circuit resistance when the sample is driven normal: If a bright optical pulse were to drive the superconductor fully into the normal state, you would expect a voltage signal to be produced proportional to the change in the circuit resistance. The resistance change for device 6 without a shunt would be $56\,\Omega - 41\,\Omega = 15\,\Omega$ whereas with a 50 Ω shunt in parallel the resistance increase would be $26.4\,\Omega - 22.5\,\Omega = 3.9\,\Omega$. The smaller resistance increase should result in smaller voltage signals produced. Additionally, the shunted device will have poorer impedance matching to the amplifier chain resulting in a smaller fraction of the signal being transmitted. Therefore the voltage signals transmitted to a universal pulse counter would be significantly smaller when using a shunt resistor than without, resulting in more optical energy being required to generate a measurable voltage signal.

Sample 6 was then optically tested far below its transition temperature, at the base temperature of the fridge (360 mK). As before, the bias current supplied to the sample and the optical attenuation applied to the pulsed laser were swept as the count rate was recorded.

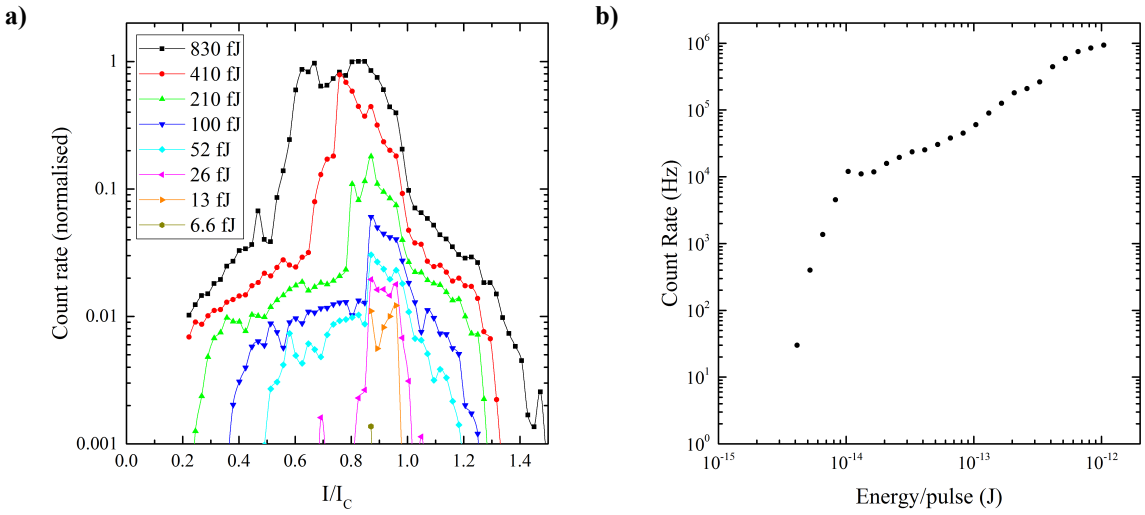

Figure 4.10: a) *The count rate of device 6 normalised to the laser repetition rate with varying current at laser pulse energies ranging from 6.6 fJ to 830 fJ in steps of 3 dB. Measured at 360 mK under 1550 nm pulsed illumination.* ***b)*** *The count rate of device 6 with varying pulse energy at 360 mK with a bias current of 195 μA (*$0.87\ I_c$*).*

Figure 4.10 shows the count rate of sample 6 recorded under pulsed 1550 nm illumination at 360 mK. Compared to the result at 5.1 K, overall the sensitivity to low level illumination is slightly reduced. There are significantly more counts above I_c, with detection continuing up to nearly $1.4\ I_c$. Sensitivity to light above the experimental critical current is an indication that some residual superconductivity may be present in the sample.

At 5.1 K the count rate rises suddenly from very small values up to the repetition rate of the laser. Whereas at 360 mK the normalised count rate jumps to 1% and then increases with current. At 5.1 K the sample is in the middle of its superconducting transition and so large energy optical pulses are capable of driving the sample into the normal state even at low bias currents. Therefore the device response to illumination is less current dependent than far below T_c where the bias current plays a more critical role in establishing a resistive region.

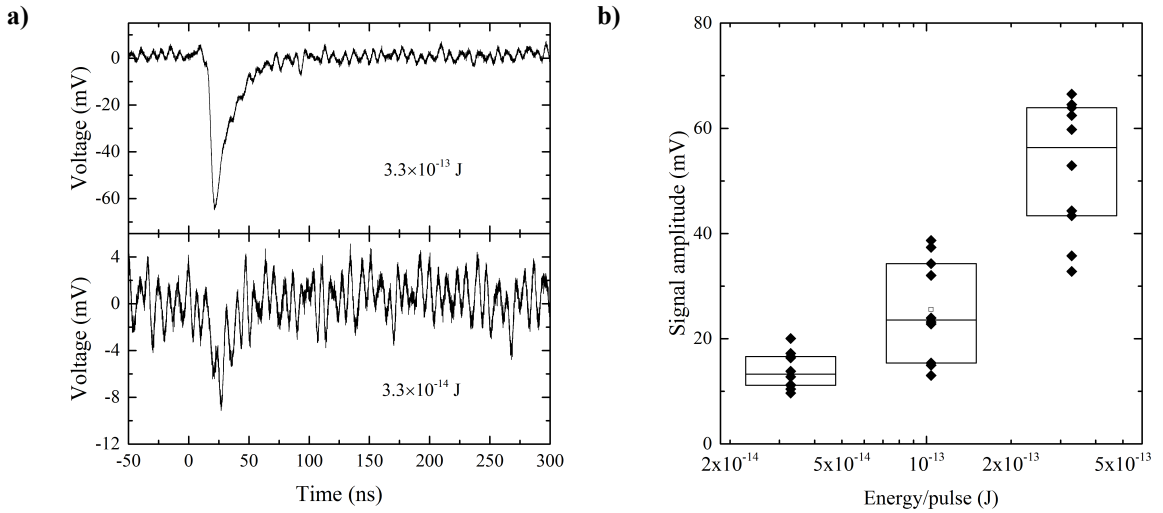

Figure 4.11: a) *Single shot oscilloscope traces obtained from optical pulse energies of 3.3 × 10^{-13} J and 3.3 × 10^{-14} J at 360 mK. At higher levels of attenuation the signal becomes difficult to distinguish from noise.* ***b)*** *Box plots showing the wide distribution of signal amplitudes produced by sample 6 at 360 mK with an applied bias current of 191 μA (*$0.85\, I_c$*).*

Figure 4.11 shows the amplitude and distribution of voltage signals at 360 mK. 4.11a shows two oscilloscope traces at different energy levels. Of note is that at the lower energy the signal becomes of similar size to the system noise and as the optical attenuation is increased further, it becomes impossible to tell if a signal is present or not. 4.11b shows box plots demonstrating the wide range of signal amplitudes that were obtained under pulsed illumination. Although it was clear that the signals had a wide distribution of amplitudes, they occurred at regular 1 μs intervals with no absences.

Sample 5 optical characterisation

The geometry of sample 5 is very different to that of sample 6. Sample 5 is a large 30× 20 μm flake of $NbSe_2$ with step like variation in thickness. One edge of the flake has a thickness of approximately 5 layers (judging from optical contrast) and has been encapsulated with graphene. Electrical contacts were fabricated on the few-layered edge as shown in figure 4.12. Five contacts were fabricated on sample 5 because the contacts had previously been found to have a high variation in junction resistance. Following room temperature testing, contacts 3 and 4 were identified as having a low resistance (318 Ω). Contact 4 was connected to the electrical ground and contact 3 was used to bias the device.

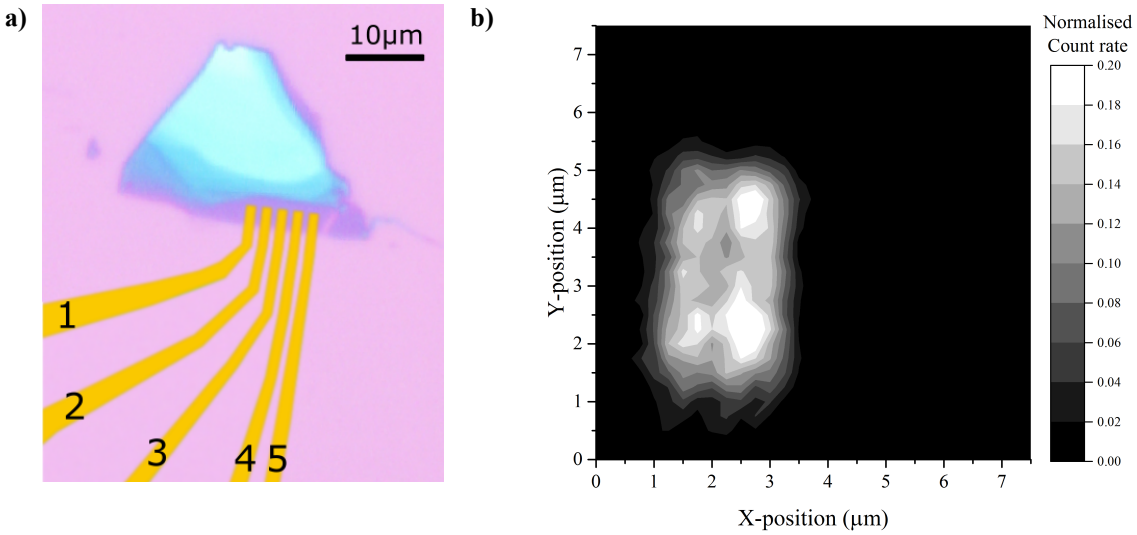

Figure 4.12: a) *An optical image of sample 5 showing the contact layout. The contacts are 1 µm wide with on a pitch of 2 µm.* ***b)*** *The count rate of sample 5 with varying microscope position normalised to the laser repetition rate. Measured at 350 mK at a bias current of 277 µA with an optical energy of 26 fJ per pulse.*

Illuminating the device, sample 5 was found to be photosensitive in a region of approximately 2×4 µm which implies that the photosensitive area is the small section of $NbSe_2$ directly between the electrical contacts (1×3 µm) where the current density is expected to be highest.

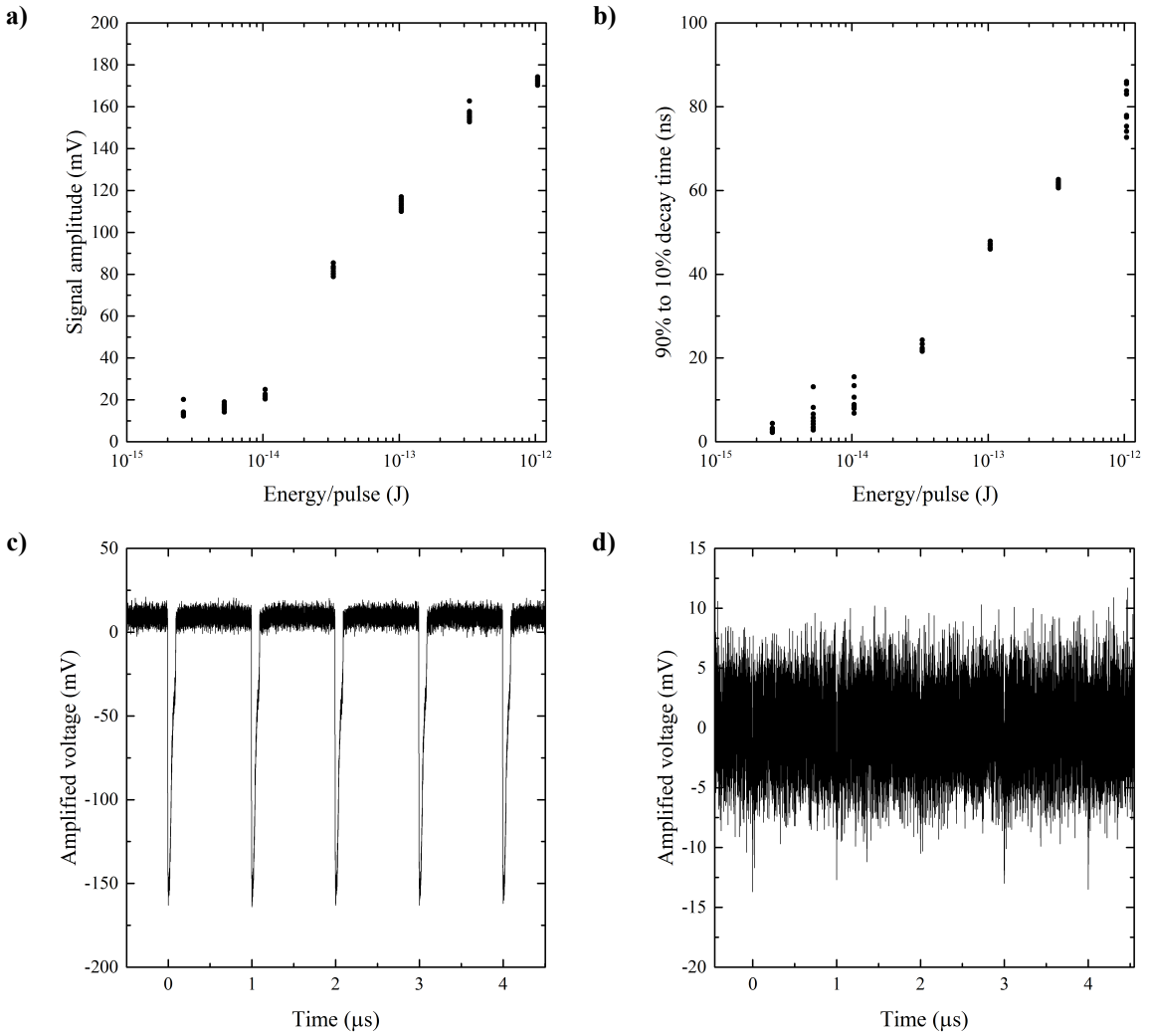

Figure 4.13: *Amplified voltage signal characteristics at 5 K with a bias current of 155 μA (0.91 I_c).* ***a)*** *The amplitude of voltage signals with varying optical pulse energy.* ***b)*** *The decay time of voltage signals from 90% to 10% of the peak voltage.* ***c)*** *A series of five voltage signals recorded with an optical pulse energy of 1.0 pJ and a 1 MHz repetition rate.* ***d)*** *A series of five voltage signals recorded with an optical pulse energy of 2.6 fJ and a 1 MHz repetition rate. The signals are difficult to distinguish from the electrical noise at this optical energy but can be seen at 1 μs intervals at the labelled times.*

The amplitude of voltage signals obtained from sample 5 was found to be dependent on the incident optical pulse energy as shown in figure 4.13a. Simultaneously as optical pulse energy is increased the decay time of the voltage signals also increases from 3 ns at 2.6 fJ per pulse to 80 ns at 1 pJ per pulse (figure 4.13b). The extreme change in the signal characteristics with optical pulse energy is shown in Figure 4.13c and d. At high optical power the voltage signals are very large and easily distinguished from electrical noise while at 2.6 fJ per pulse, the lowest optical energy at which they were found to be visible, the signals are only just above the electrical noise and can be seen at 1 μs intervals (the laser repetition period).

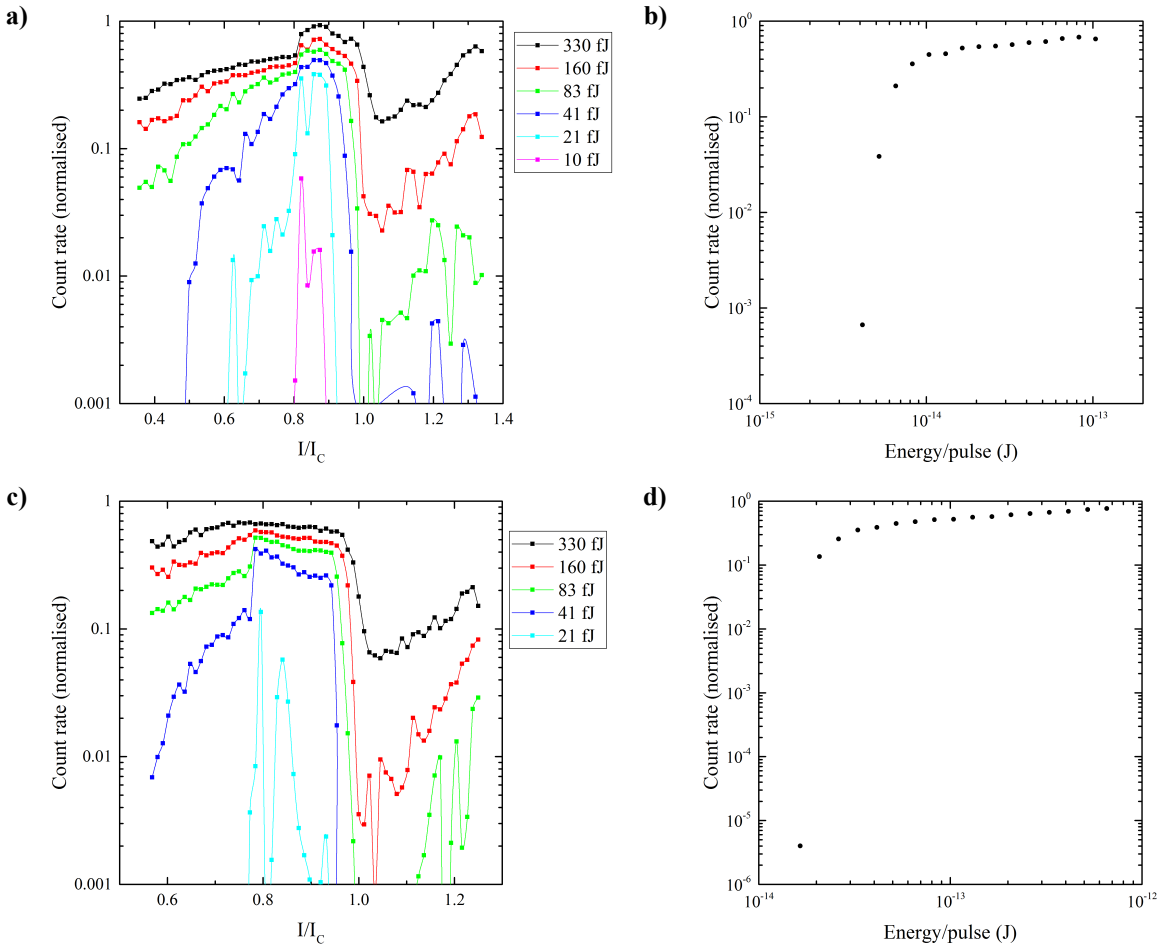

Figure 4.14: a) *Count rate at 5 K with varying optical pulse energy and bias current with a trigger level of 15 mV. The current scale is normalised to the critical current at 5 K, 170 µA.* ***b)*** *Count rate at the optimised bias current (139 µA, 0.82 I_c) at 5 K* ***c)*** *Count rate at 360 mK with varying optical pulse energy and bias current. I_c has been taken as the first superconducting transition (265 µA).* ***d)*** *Count rate at 360 mK with an applied bias current of 211 µA (0.8 I_c).*

As shown in figure 4.13, the electrical noise from sample 5 regularly exceeded 10 mV and so, when measuring the count rate from the sample, the trigger value of the universal counter was set to 15 mV. Figure 4.14 shows that the count rate from sample 5 reaches a maximum for low illumination levels around 0.8 I_c. The lowest energy of pulse that triggered a count was at 4.1 fJ per pulse at 5 K and at 16 fJ per pulse at 360 mK. The count rate obtained from sample 5 falls steeply as the current is increased above I_c but then increases gradually as the current is increased further. I believe this is due to the sample geometry and I-V curve. Since the sample is a large flake (30 µm) with multiple superconducting transitions visible on its I-V curve (see 4.3), I believe that as the bias current is increased above the first transition, I_c, superconductivity is suppressed locally. However, the bulk of the large flake may remain superconducting even after I_c is exceeded and act to reduce the resistance between the two contacts. As the current is increased further an increasing region around the contacts may be driven normal, leading to multiple transitions in the I-V curve. The final superconducting transition visible in the I-V curve occurs at 1.4 I_c at 360 mK, I would expect the count rate to drop steeply after this bias current was exceeded.

4.2 Non-encapsulated $NbSe_2$ flakes

4.2.1 Introduction

The graphene encapsulated samples characterised in the previous section showed a high contact resistance which may have reduced the critical current of the samples and increased electrical noise. It was thought that by removing the graphene encapsulation layer, the series resistance observed would decrease which may lead to improved detector performance. The graphene may also have been acting as a parallel current path to the $NbSe_2$, reducing the normal state resistance of the device and thereby reducing the amplitude of voltage signals when a section of the $NbSe_2$ is driven into the normal resistive state by optical stimulation. A final consideration was that the photoresponse may have somehow been generated by the graphene layer itself. Either a photoconductive or photo-thermal effect in the graphene layer could potentially be the source of the previously observed response.

For these reasons it was decided that several non-encapsulated samples should be characterised, allowing the intrinsic photoresponse of the $NbSe_2$ to be measured. Since $NbSe_2$ readily degrades when exposed to atmosphere, it was known that very thin samples would be unlikely to survive through to optical testing. For this reason, some thicker and wider samples than previous were fabricated by Domenico de Fazio.

4.2.2 Device layout

As with the previous batch of samples, the $NbSe_2$ was exfoliated onto an oxidised silicon substrate and optically scanned to locate promising few-layer crystals. Custom titanium-gold electrical contacts were then designed and fabricated via liftoff. The electrical contacts were designed to span the width of the $NbSe_2$ crystal so that the current path between the gold contacts was rectangular. This was done so that the current density in the superconductor was as uniform as possible. The samples were then stored under vacuum and transferred to Glasgow for electrical and optical testing.

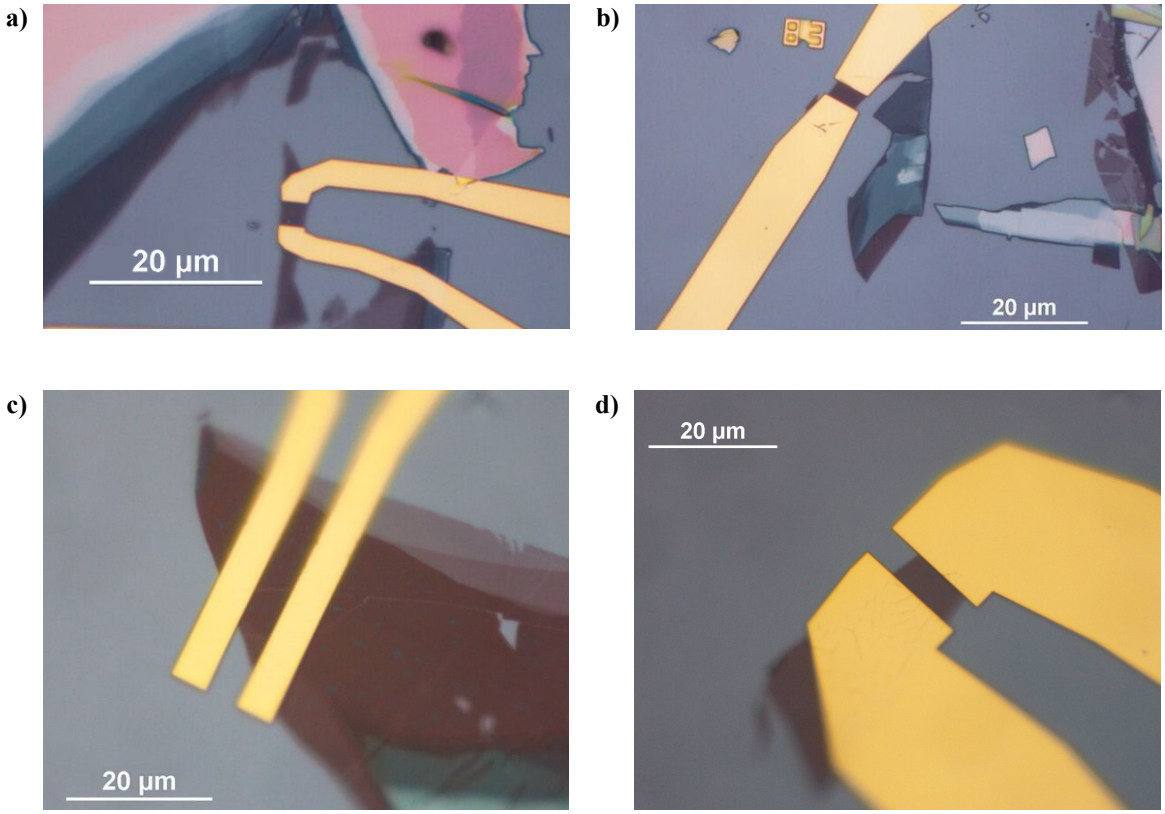

Figure 4.15: *Optical images of $NbSe_2$ devices fabricated without an encapsulation layer. Electrical contact is made by 50 nm gold electrodes with a 5 nm titanium adhesion layer fabricated on top of the exfoliated crystals.* ***a)*** *Sample 9* ***b)*** *Sample 10* ***c)*** *Sample 15* ***d)*** *Sample 16.*

Nine samples of this type were fabricated and although exposure to atmosphere was reduced as much as possible, only three samples of this design showed superconducting properties (samples 9, 10 and 15). It is believed that the other six samples degraded because of oxidation prior to cryogenic testing.

Sample ID	Number of layers	R_N	R_S	T_C	I_C (360 mK)
9	5	157 Ω	44 Ω	<5 K	61 µA
10	5	47 Ω	7 Ω	5.2 K	165 µA
15	5	71 Ω	23 Ω	2.5 K	36 µA

Table 4.2: *The electrical properties of the three non-encapsulated $NbSe_2$ flakes which showed superconducting properties. The thicknesses of the samples were estimated from their optical contrast. R_N is the 2-point resistance of the sample in the normal state above the superconducting transtition temperature, R_S is the 2-point resistance of the sample in the superconducting state. The critical temperature (T_c) is defined as the temperature midway through the superconducting transition and the critical current (I_c) is the bias current at which the resistance of the sample was observed to increase from its zero bias resistance.*

Sample 15 is a relatively thick and wide sample, being approximately 5 layers thick across the majority of the flake and 20 µm wide. However, as shown in figure 4.16b, the superconducting transition temperature is degraded substantially from the bulk value of 7.2 K. The critical current of the sample 15 is also relatively low, implying that exposure to atmosphere may have degraded superconductivity in the crystal. Similarly, sample 9 showed no signs of

superconductivity at 5 K. However, despite only having a width of 3 µm the critical current of the sample was 61 µA.

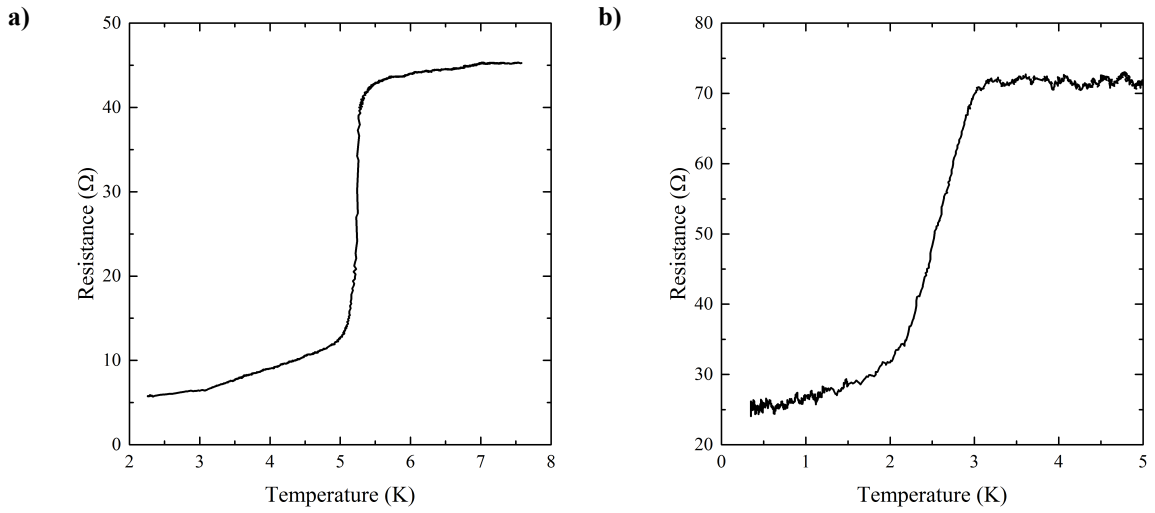

Figure 4.16: *Resistance against temperature curves acoss the superconducting transition.* ***a)*** *Sample 10.* ***b)*** *Sample 15. The reduced T_c of sample 15 is an indication that exposure to atmosphere may have degraded its superconducting properties.*

Reducing contact resistance was one of the motivating factors for fabrication of these non-encapsulated samples and indeed the resistance of samples 10 and 15 in the superconducting state are much lower than the resistances of the graphene encapsulated samples. Only sample 9 shows a contact resistance similar to the previously measured values (49 Ω). The large contact resistance for sample 9 may be due to the small region of overlap between the $NbSe_2$ and gold, estimated to be 7 μm^2 per contact.

4.2.3 Characterisation

Sample 9

Sample 9 was cooled to 5 K and located optically by raster scanning the confocal microscope across the chip. The images shown in figure 4.17 clearly show the contacts of the device and figure 4.17b) is centred over the area expected to be photosensitive.

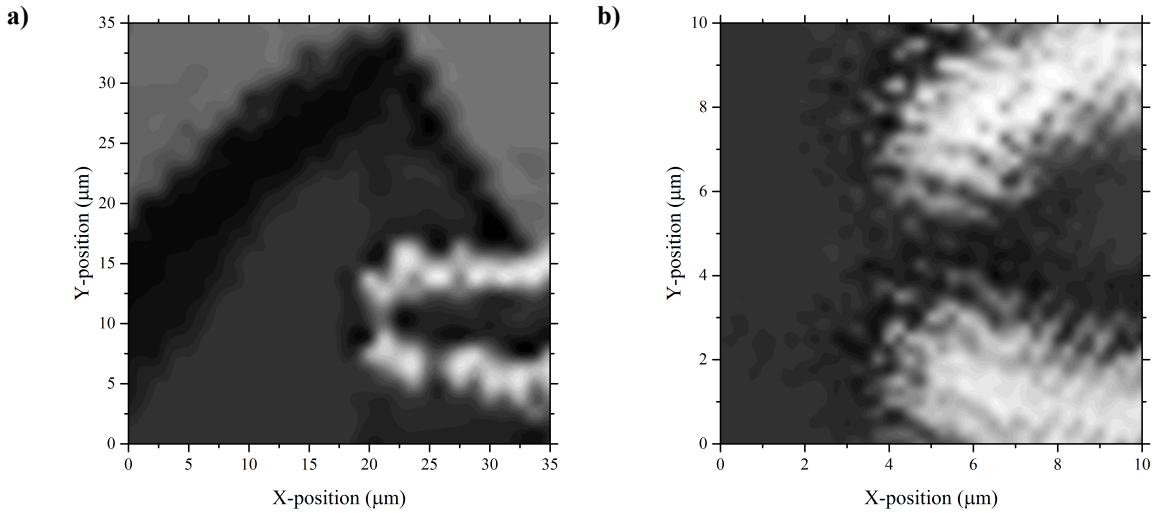

Figure 4.17: *Images of sample 9 recorded at 5 K with 1550 nm illumination by scanning the confocal microscope over the samle area.* ***a)*** *A large area 35 µm scan where the electrical contacts and nearby bulk crystals are clearly shown.* ***b)*** *A higher detail scan centred over device area.*

At 5 K, sample 9 had a resistance of 157 Ω with no superconducting transition and there was no measurable photoresponse. The confocal microscope was placed over the device area and the system was cooled to 360 mK.

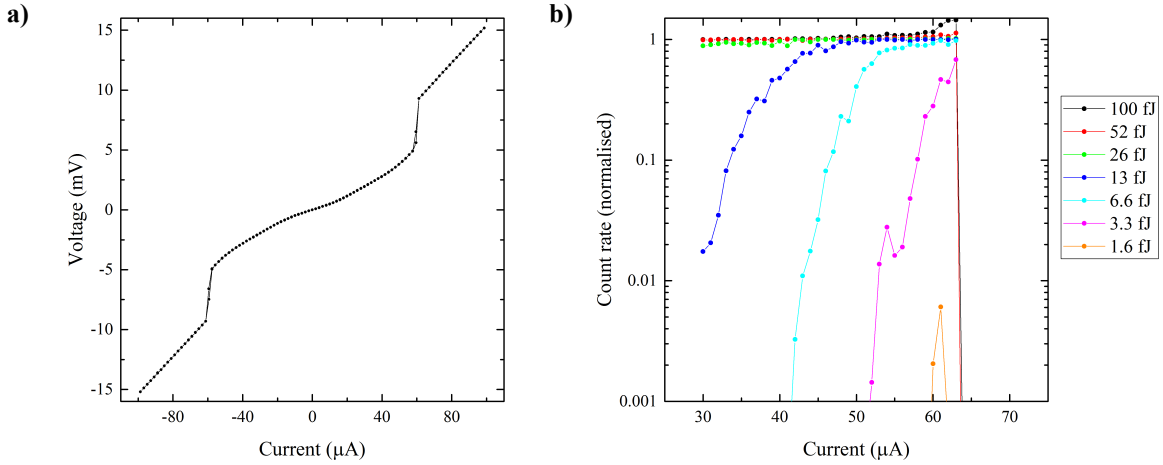

Figure 4.18: ***a)*** *The I-V profile of sample 9 at 360 mK* ***b)*** *The count rate from sample 9 at 360 mK with varying optical pulse energy and current normalised to the laser repetition rate (1 MHz).*

At 360 mK sample 9 showed a clear superconducting critical current at 60 µA but with a high series resistance of 44 Ω in the superconducting state, figure 4.18a). The I-V profile was non-hysteretic showing that Joule heating in the normal state does not significantly increase the temperature of the sample.

The count rate from sample 9 is shown in figure 4.18b), it clearly shows that the optical sensitivity of the sample increases with bias current, reaching a maximum at the critical current. As the current is increased above its critical value, the count rate dramatically falls off. This is a clear indication that the observed optical response is due to disruption of the superconducting state. When biased close to I_c, fewer Cooper pairs need to be broken to reduce the current

carrying capacity below the bias current and so it follows that optical sensitivity should be highest at this point.

Sample 10

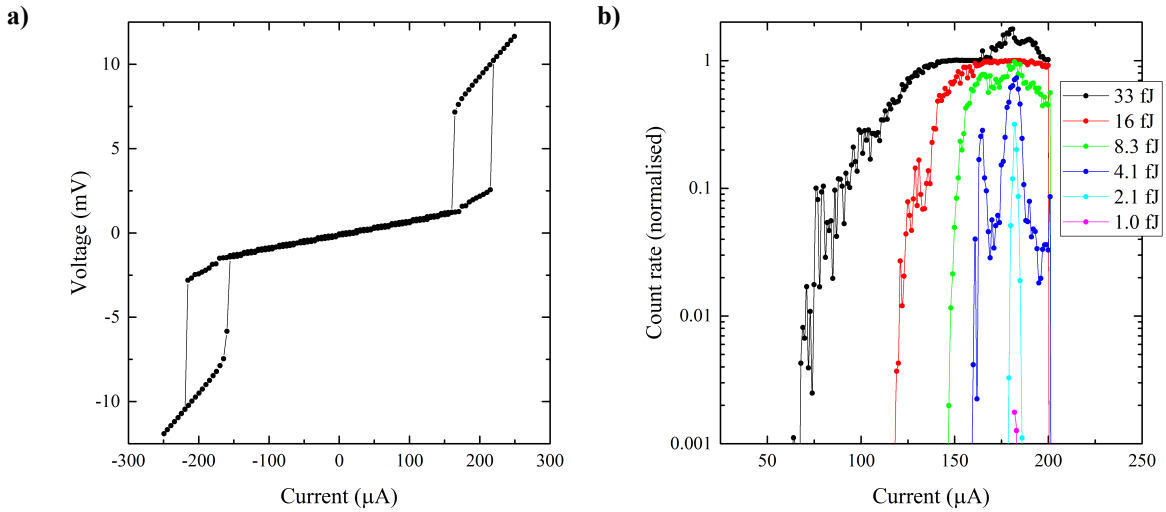

Figure 4.19: a) *The I-V profile of sample 10 at 360 mK.* ***b)*** *The count rate measured from sample 10 under pulsed illumination at 360 mK with varying optical pulse energy.*

Figure 4.19a) shows the I-V profile of sample 10 at 360 mK. It has a 2-point series resistance of 7 Ω. Between 170 μA and 185 μA there are a couple of small voltage increases and the gradient in the I-V changes to a differential resistance of 25 Ω. At 215 μA the resistance of the sample jumps to its normal state value of 47 Ω.

Figure 4.19b) shows the count rate of sample 10 with varying bias and optical pulse energy under 1550 nm pulsed illumination. The count rate reaches a maximum for low illumination levels at 183 μA the current at which the differential resistance of the sample increases. The count rate drops to zero for all optical pulse energies above 201 μA, the current at which I believe the device switched to the normal state. It can also be seen that around 180 μA the count rate measured exceeds the repetition rate of the laser, reaching 1.6 MHz for the highest energy pulses. Figure 4.20a) shows that the voltage signals at high energy have a significant secondary peak around 15 ns after the first peak. The second peak is caused by electrical reflections in the signal line and result in the same voltage signal being counted twice by the universal counter which was set with a trigger voltage of 10 mV. This measurement error only occurs for very large voltage signals (>100 mV) and so is not thought to have an impact on most of the optical measurements.

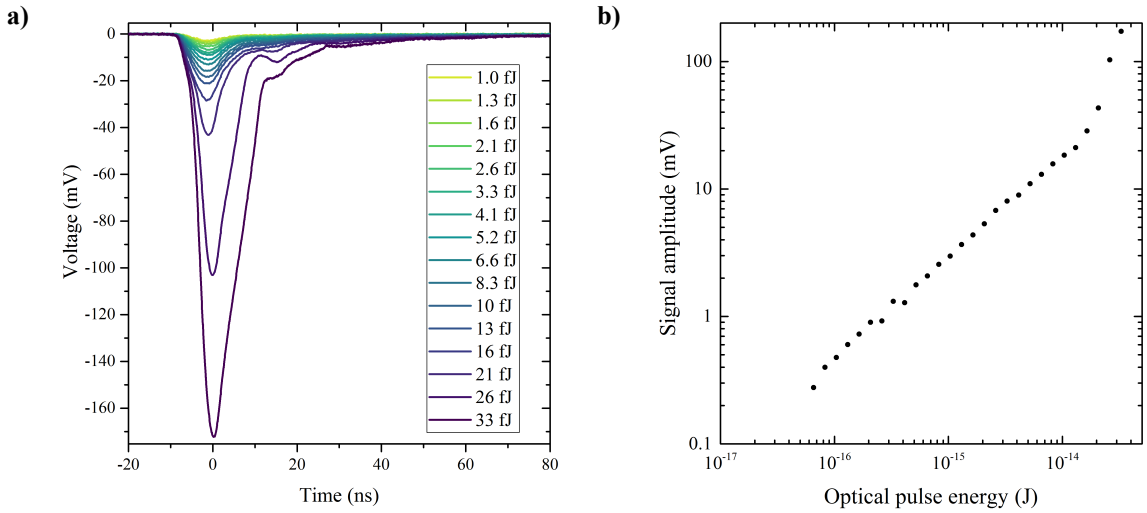

Figure 4.20: a) *Average voltage signal traces from sample 10 recorded at 360 mK with varying optical pulse energy. The bias current used was 183 μA.* ***b)*** *The amplitude of voltage signals with varying optical pulse energy.*

The amplitudes of voltage signal from sample 10 increase steadily with optical pulse energy, 4.20b). This behaviour is qualitatively very similar to the behaviour shown by the graphene encapsulated samples (samples 5 and 6), with the voltage signals varying by more than two orders of magnitude as the optical pulse energy is varied over a similar range.

Sample 15

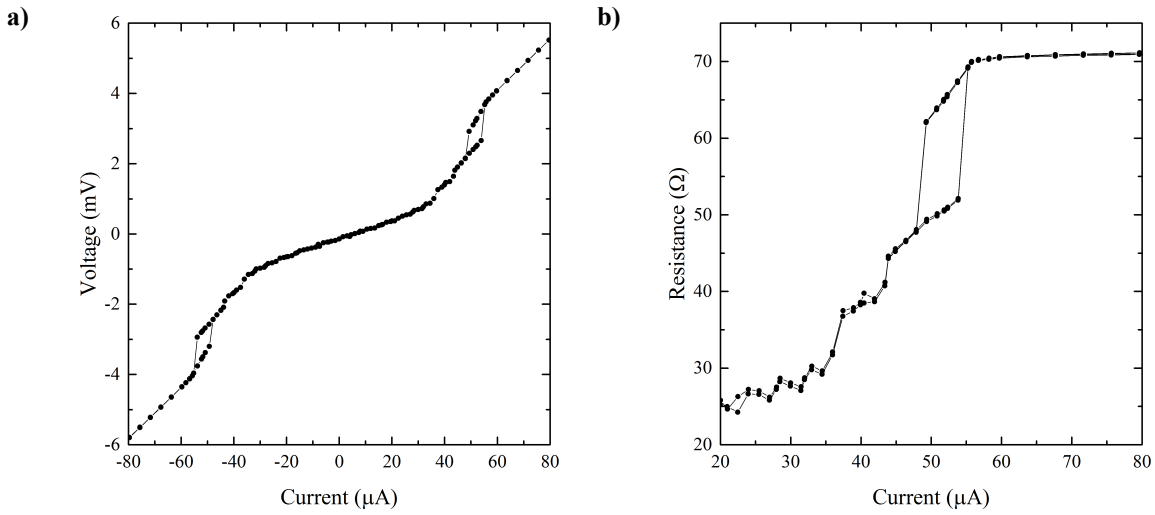

Figure 4.21: a) *The two-point I-V profile of sample 15 recorded at 360 mK.* ***b)*** *The resistance of sample 15 as the applied bias current is swept. Three resistance steps are visible at 36 μA, 43 μA and 54 μA. The final resistance step is hysteretic with a retrapping current of 48 μA.*

Sample 15 was found to have a transition temperature of 2.5 K with a normal state resistance of 71 Ω. The I-V profile of sample 15 is shown in figure 4.21 where it can be seen that there are multiple resistance steps and a hysteretic region between 48 μA and 54 μA. The fact that there are multiple resistance steps and that they occur at relatively low bias currents

for such a wide superconducting strip implies the $NbSe_2$ in this device may have degraded superconducting properties because of exposure to atmosphere.

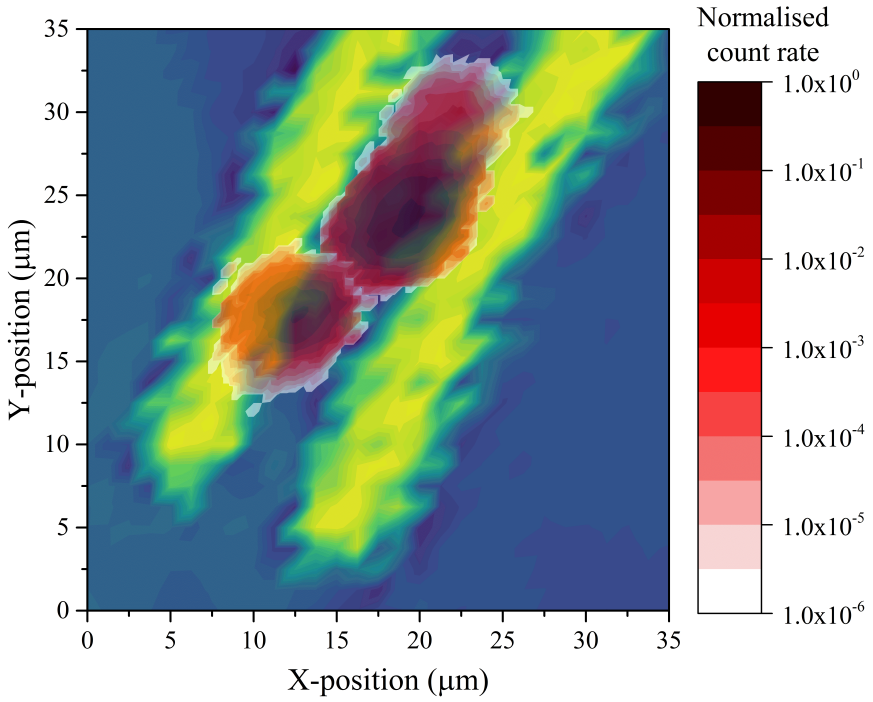

Figure 4.22: *A reflection profile of sample 15 is shown in blue to yellow, with the electrical contacts clearly visible. Overlaid in white-red is the count rate measured at a pulse energy of 660 aJ and a bias current of 35 µA (at the first switching current).*

At 360 mK sample 15 was imaged with a 1550 nm SLD over a 35 µm square area. Immediately after the scan was complete, another scan was initiated over the same area, now measuring the count rate of voltage signals to pulsed illumination. The two measurements have been overlaid and are shown in figure 4.22.

In figure 4.22, it can be seen that the sample is photosensitive when illuminated between the two electrical contacts. The count rate peaks at two different locations, which is atypical. However, upon close inspection of figure 4.15 a small crack can be seen in the $NbSe_2$ crystal which may have the effect of dividing the sample into two parallel superconducting paths which may explain why there are two regions of optical sensitivity.

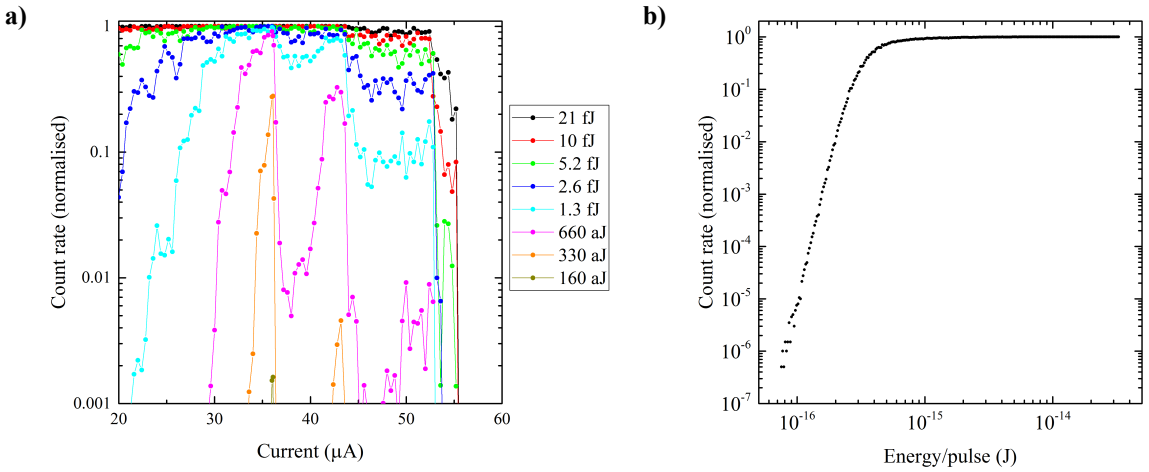

Figure 4.23: a) *The count rate measured from sample 15 at 0.36 K normalised to the laser repetition rate (1 MHz).* ***b)*** *The count rate of sample 15 biased at 36.1 μA, the current at which the sample showed the highest sensitivity to low energy optical pulses.*

Figure 4.23a) shows the count rate of sample 15 under illumination by a 1550 nm pulsed laser at 360 mK. As the bias current is increased from zero, the count rate at all optical energies increases until 36 μA when the count rate drops suddenly. The count rates rise again before falling above 43 μA, the count rates drop again at 53 μA and fall to zero above 55 μA. The bias currents at which the count rates fall clearly correspond with the resistive steps seen on the I-V profile of the sample (figure 4.21).

Sample 15 had the highest response to low illumination at 36.1 μA, the bias current corresponding to the first resistive step in the I-V profile. The count rate measured at 36.1 μA is shown in figure 4.23b) with varying optical pulse energy. Sample 15 showed a high sensitivity to pulsed illumination, the count rate dropped below 50% at 380 aJ and optical pulses were counted at energies as low as 75 aJ, an energy corresponding to an average of around 585 photons at 1550 nm wavelength. Considering that the optical coupling efficiency to the $NbSe_2$ can be estimated as 6% (see section 3.3), sample 15 only requires a few tens of infrared photons to be absorbed to generate a measurably large voltage signal.

4.3 hBN encapsulated $NbSe_2$ flakes

4.3.1 Device layout

In general the non-encapsulated samples which maintained superconductivity had lower contact resistances and higher sensitivity to low illumination levels than graphene encapsulated samples. However, the non-encapsulated samples were prone to oxidation and only three out of nine samples showed clear superconducting properties. Therefore it was decided that future samples should be encapsulated but that the gold contacts should make direct contact with $NbSe_2$. To achieve this design gold contacts were patterned first and then the $NbSe_2$ flakes were placed over the contacts using dry transfer. An encapsulation layer of hexagonal

boron nitride (hBN) was then placed over the $NbSe_2$ to prevent it degrading. hBN was chosen as the encapsulation layer for this design since it is an insulator and highly transparent.

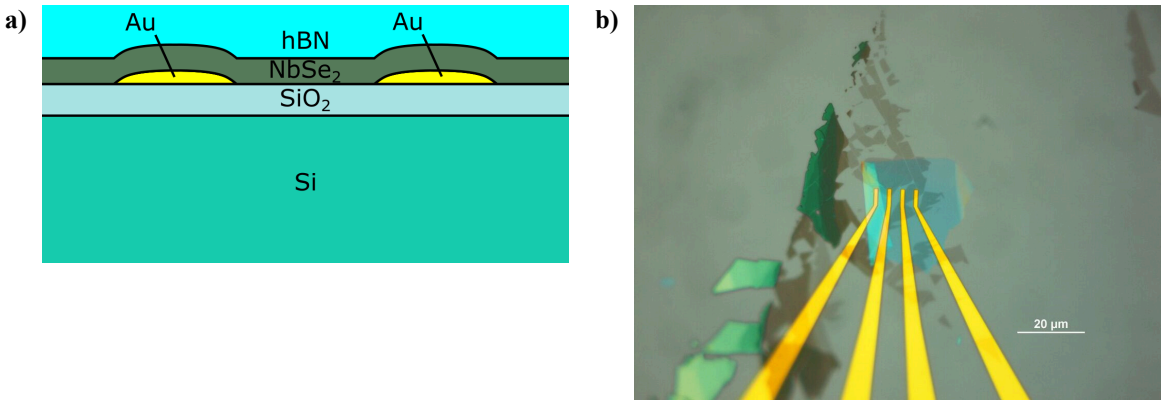

Figure 4.24: a) *A diagram showing the layers of hBN ecapsulated samples.* ***b)****An optical image of sample 18. As the $NbSe_2$ crystal was transferred onto the prepatterned contacts, it shattered into several pieces.*

Unfortunately it was found that when $NbSe_2$ flakes were placed on top of the pre-patterned gold contacts, the uneven surface often caused the $NbSe_2$ to shatter. Figure 4.24b) is an image of sample 18, which broke into several pieces as it was placed.

4.3.2 Characterisation

Two samples of this design were provided for characterisation, samples 18 and 19. Sample 18 is extremely thin, estimated to be 2 molecular layers thick but during fabrication the $NbSe_2$ broke into several flakes and therefore there may be multiple current paths between the electrical contacts. Sample 19 is four molecular layers thick and survived the fabrication process intact.

Sample 18

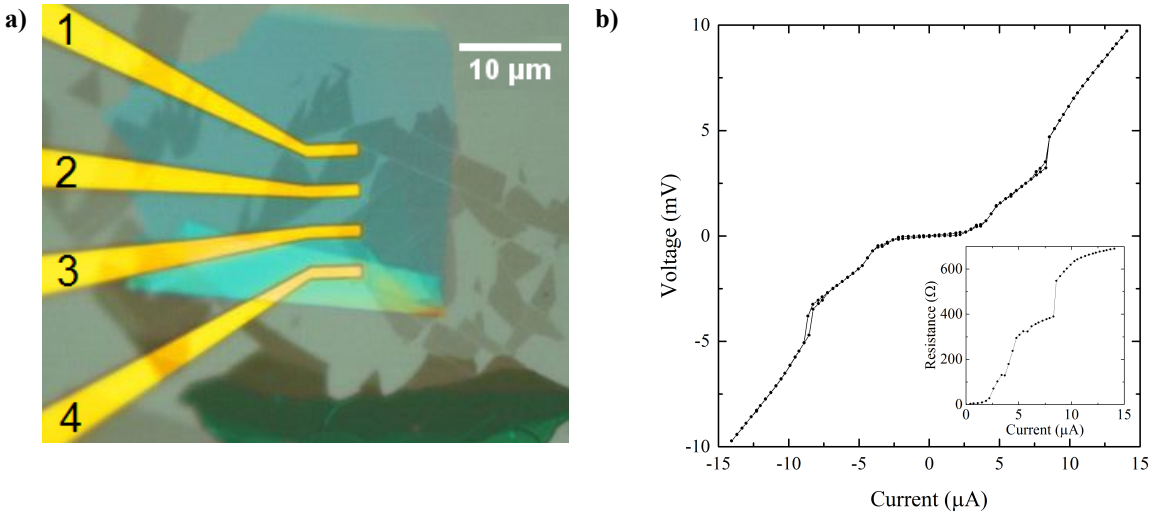

Figure 4.25: a) *An optical image of sample 18. Multiple flakes of $NbSe_2$ can be seen bridging the electrical contacts.* ***b)*** *The I-V profile of sample 18 at 360 mK.*

Of the four contacts on sample 18, only one pair (contacts 1 and 2 as labelled in figure 4.25a)) showed a superconducting transition. The I-V profile at 360 mK is shown in figure 4.25b). The resistance of the sample around zero bias current is 20 Ω, but this rises to 300 Ω between 2 µA and 5 µA and jumps to 550 Ω at 8.5 µA. As the current is increased further, the resistance increases to 750 Ω gradually. The I-V profile is non-hysteretic which is not surprising considering the low current range.

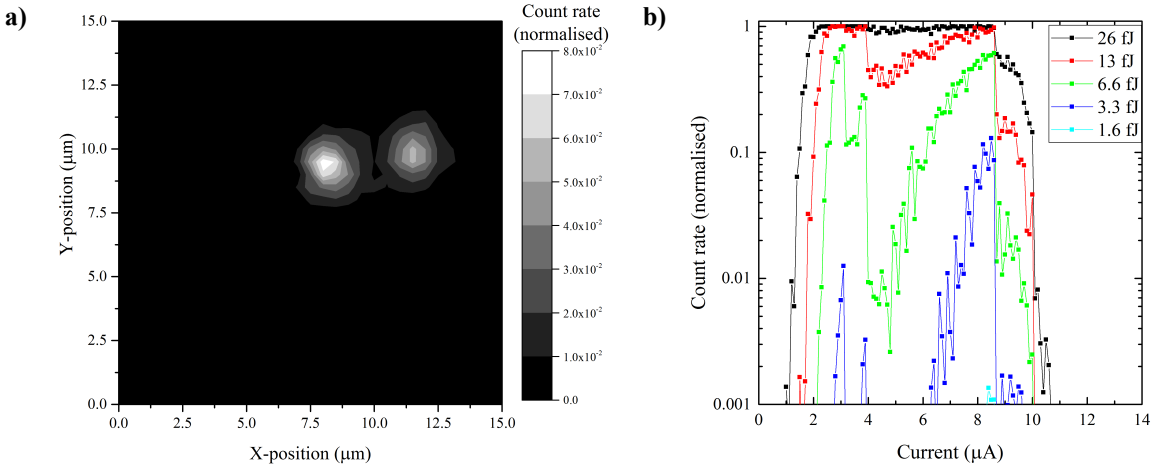

Figure 4.26: ***a)*** *The count rate of sample 18 across a 15 µm square area at 360 mK, bias current 2.6 µA and optical pulse enegy of 3.3 fJ.* ***b)*** *The count rate of sample 18 to pulsed illumination at 360 mK with varying bias current and optical energy.*

It can be seen in figure 4.26a) that there are two optically sensitive areas of sample 18, spaced approximately 4 µm away from each other. These areas most likely correspond to the two flakes of $NbSe_2$ that can be seen bridging the upper two electrical contacts in figure 4.25a). 4.26b) shows the count rate of sample 18 to 1 MHz 20 ns optical pulses with varying bias current. Comparing the result to the I-V profile, the count rate peaks at 3.1 µA, 3.9 µA and 8.6 µA which agree well with the switching currents observed in figure 4.25b). The highest count rate for low optical pulse energies was achieved when the sample was biased at 8.6 µA, where the sample resistance was observed to rise from 400 Ω to 550 Ω. It has been a clear trend that the count rate measured from samples reaches local maxima at switching currents. However, this is the first time that the highest sensitivity has occurred when biased at a current where part of the sample is clearly already resistive.

Sample 19

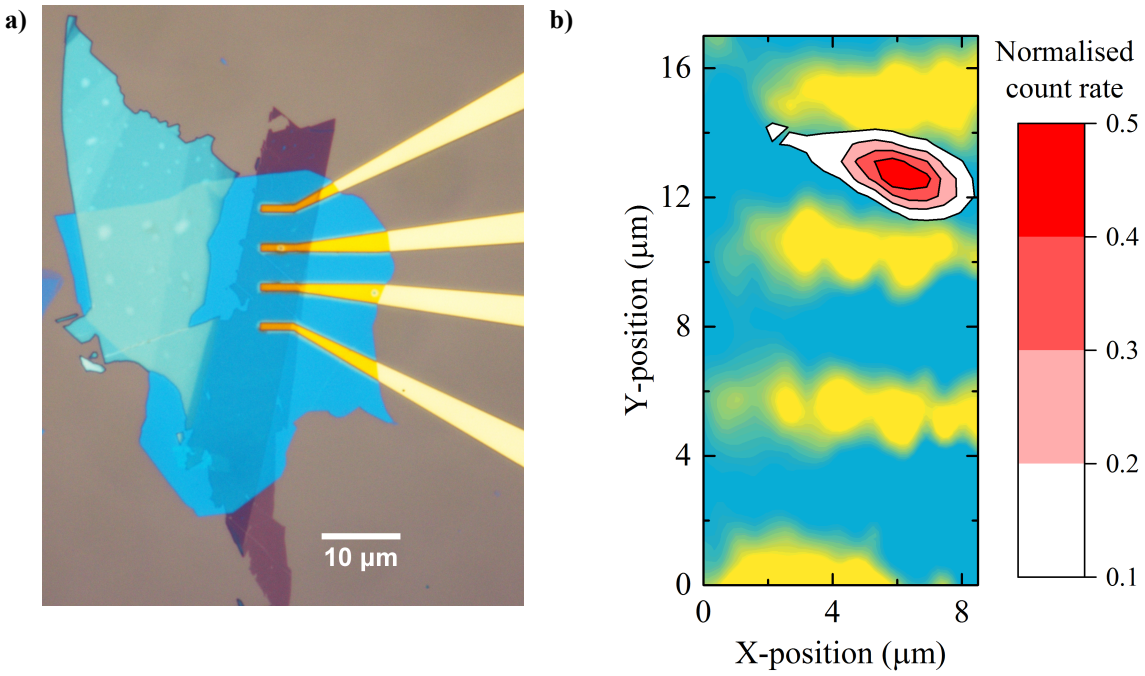

Figure 4.27: a) *A micrograph of sample 19. The few-layered $NbSe_2$ can be seen as a dark purple and the encapsulating hBN is a pale blue.* ***b)*** *A reflection profile of sample 19 at 5 K is shown in blue to yellow, with the four electrical contacts visible. Overlaid in white-red is the count rate measured at a pulse energy of 16 fJ with a bias current of 227 µA applied across the highest two contacts.*

Sample 19 was located optically by mapping the reflected power across the chip at 5 K. The region around the electrical contacts can be seen in figure 4.27b) in blue-yellow. The count rate of the sample to pulsed illumination was measured over the same area and overlaid on the reflection map. The combined figure clearly shows that the optically sensitive area is between the current biased electrical contacts as expected. The confocal microscope was positioned over the area of highest response for further optical testing.

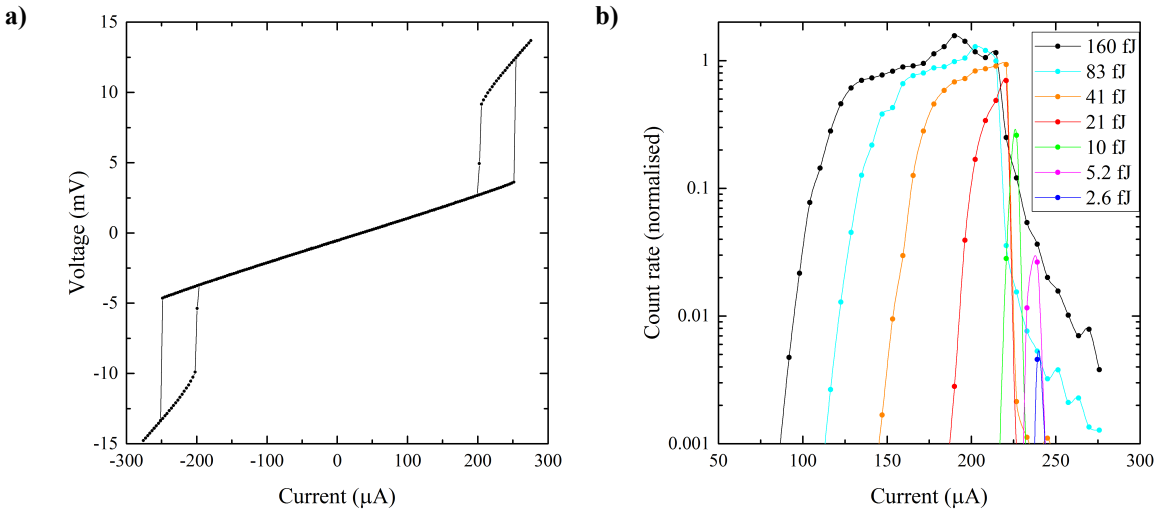

Figure 4.28: a) *The I-V profile of sample 19 at 5 K.* ***b)*** *The count rate measured from sample 19 under pulsed illumination at 5 K with varying optical pulse energy and bias current.*

The two-point I-V profile of sample 19 at 5 K is shown in figure 4.28a). The series resistance of the sample is 16 Ω and it transitions to its normal state value of 53.5 Ω above 251 µA. The transition is hysteretic with a retrapping current of 200 µA.

The count rate of sample 19 to pulsed 1550 nm illumination is plotted in figure 4.28b). As with other samples, the count rate rises with current when far below the switching current and when biased near I_c the highest energy pulses are occasionally counted twice due to reflections in the signal line, as seen before for large pulses. The count rate for the 160 fJ and 83 fJ pulses fall at 215 µA. However, for lower energy pulses the peak count rate occurs at currents closer to I_c with the 2.6 fJ energies peaking at 240 µA, just below I_c. It can actually be seen that when biased near I_c the lower energy pulses result in a higher count rate. This behaviour is an indication that the brighter pulses may be causing the sample to switch to the resistive branch of the I-V curve and therefore become less sensitive to subsequent optical pulses. This behaviour, known as latching occurs when a resistive section of the $NbSe_2$ generates enough Joule heating to overcome the cooling capacity of its environment. The resistive section therefore grows and is sustained by the Joule heating until the current is reduced below the retrapping current.

To investigate this phenomenon further, oscilloscope traces were measured with varying optical pulse energy in the hysteretic region of the I-V curve, at 220 µA.

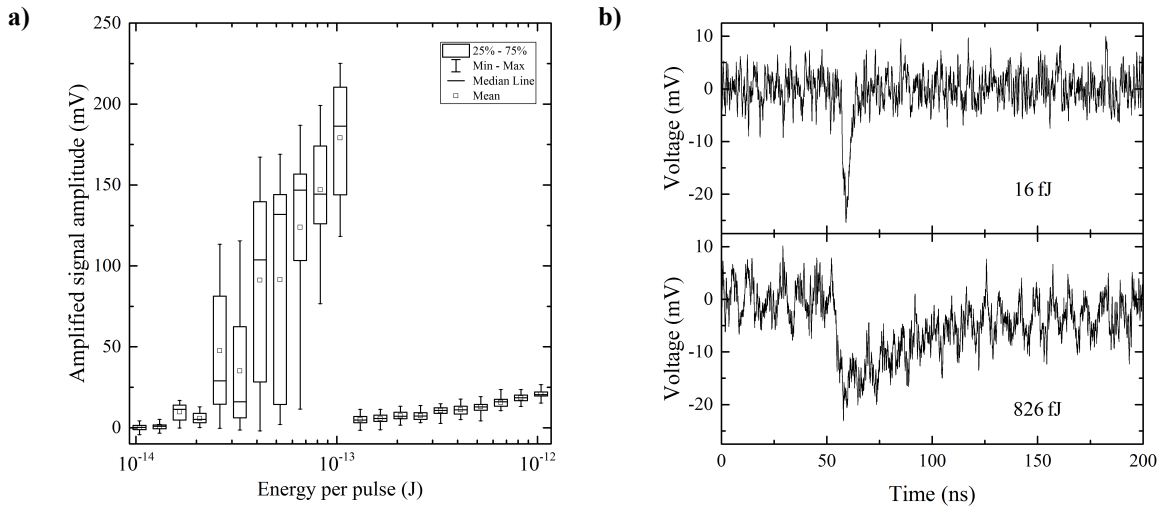

Figure 4.29: *Characteristics of signals recorded with 100 kHz repetition rate, 220 µA bias current at 5 K.* ***a)*** *Box plots showing the distribution of signal amplitudes with varying optical energy.* ***b)*** *Single shot oscilloscope traces of two signals measured at pulse energies of 16 fJ and 826 fJ.*

Figure 4.29a) is a series of box plots showing the distribution of signal amplitudes obtained under 100 kHz repetition rate at 5 K biased in the hysteretic region of the sample's IV curve, at 220 µA. It can be seen that the average signal amplitude increases with energy, reaching a maximum at 104 fJ per pulse. Above this energy the signal amplitude suddenly decreases to around 10 mV and then rises slowly with increasing optical energy. This behaviour is due to the sample switching to the resistive branch of its I-V curve and therefore becoming less sensitive to optical pulses. Figure 4.29b) shows two pulses of approximately equal amplitude,

measured at both extremes of optical energy (16 fJ and 826 fJ). Although the signals are of similar amplitude, their other properties are vastly different. The trace from the lower energy pulse has a 90% to 10% recovery time of 6.4 ns whereas the high energy trace has a recovery time of 60 ns. Additionally there is increased noise at higher optical energy, with the RMS (root mean square) voltage increasing from 2.8 mV to 3.4 mV.

If indeed the observed behaviour is due to the sample latching when a high energy optical pulse is applied, it should be possible to measure a voltage trace that does not recover, indicating a self sustaining switch to a higher resistive state. To achieve this, the PPG driving the laser diode was set to produce single pulses, the bias current was turned off and reset after each laser pulse and an oscilloscope was used to capture the response of the sample.

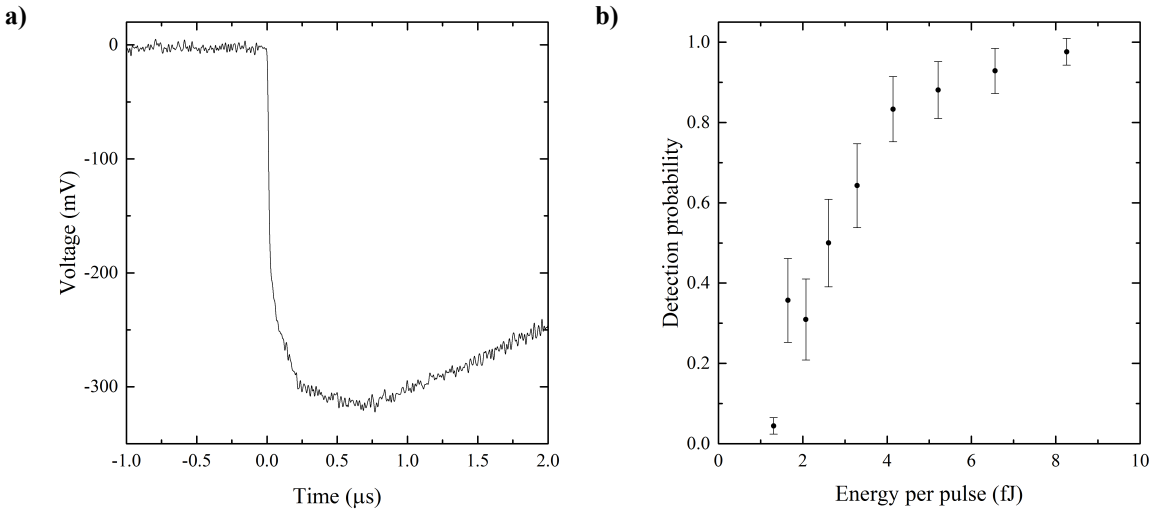

Figure 4.30: a) *An osciloscope trace showing sample 19 latching due to a single laser pulse incident on the detector. 251 µA applied bias current at 5 K.* ***b)*** *The estimated probability of detecting an optical pulse as a function of optical energy at 5 K with an applied bias current of 251 µA. Error bars show the value of the standard error calculated using the Agresti–Coull method [127].*

Biasing sample 19 at the highest stable current (251 µA), single optical pulses were observed to cause the detector to latch. An example of this response is shown in figure 4.30a). The voltage is seen to rise to 300 mV and then slowly decay to zero (~50 µs) due to the limited bandwidth of the amplifier (10 kHz to 500 MHz) and bias tee (80 kHz to 26 GHz) in the readout circuit. See section 3.2.5 for further details.

Figure 4.30b) shows the proportion of optical pulses that resulted in latching as a function of optical energy. Lower energies than previously measured are able to be detected using this technique because the sample is biased much closer to I_c while remaining in the superconducting state. In this high current, low energy regime, optical pulses caused the detector to stochastically latch or have no measurable response.

Reducing the bias current to 230 µA, voltage traces were as shown in figure 4.31. The sample was able to recover superconductivity after optical pulses of 22 fJ or less and it always latched after pulses of 69 fJ or higher energy were used. Between these two energies the sample stochastically latched or recovered with the larger signals being more likely to latch.

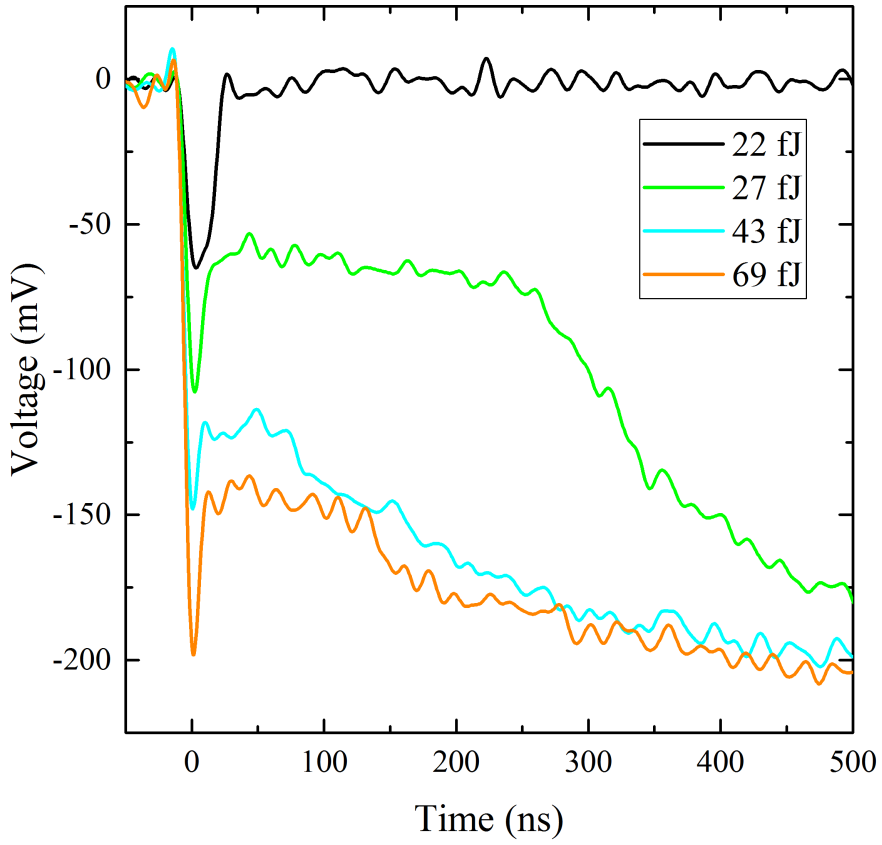

Figure 4.31: *Single shot oscilloscope traces showing the response of sample 19 under 230 µA bias current with varying optical pulse energy at 1550 nm wavelength.*

Unlike as was seen at 251 µA, when biased at 230 µA an optical response which varies according to the input energy is visible for both latched and recovering traces. This can be seen as an initial peak in the traces of figure 4.31. The initial peak decays and the subsequent response is governed by Joule heating which, if large enough, causes a self sustaining region to grow. The magnitude of the latched voltage is independent of optical energy and is determined solely by the bias current.

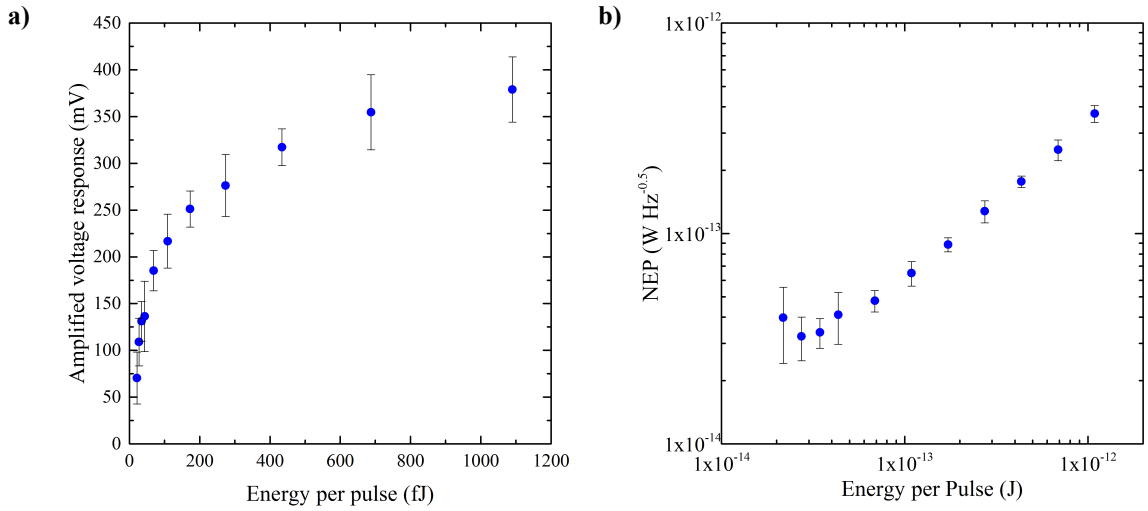

Figure 4.32: a) *Amplitude of voltage signals from single optical pulses at 5 K with a bias current of 230 μA.* ***b)*** *The optical NEP calculated for sample 19 at 5 K and 230 μA bias.*

The amplitude of the optical response with varying pulse energy is plotted in figure 4.32a). At lower energies the amplitude increases with laser energy but at higher energies shows signs of saturation, approaching a steady value of 400 mV. This behaviour can be understood as the laser driving a section of the flake into the resistive state. As the laser energy increases, so does the size of the resistive region. This occurs until the resistive region approaches the total length of the flake, causing saturation of the voltage response.

Figure 4.32b) shows the noise equivalent power (NEP) calculated from the amplitude of optical response according to the method described in section 3.4. The minimum observed NEP was 32 fWHz$^{-0.5}$.

The sample was then cooled to the base temperature of the system (360 mK). The I-V profile shown in figure 4.33a) has a greatly enhanced I_c (693 μA) compared with at 5 K (251 μA) and is highly hysteretic with a retrapping current (I_r) of 342 μA.

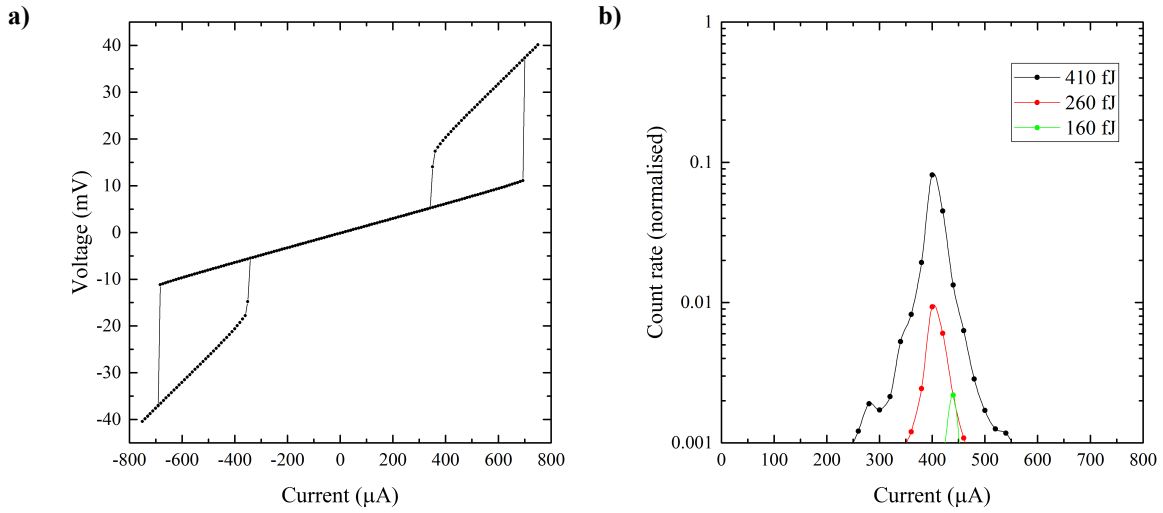

Figure 4.33: a) *The I-V profile of sample 19 at 360 mK.* ***b)*** *The count rate obtained from sample 19 under pulsed illumination at 1 MHz repetition rate with varying bias current and optical pulse energy.*

Figure 4.33b) shows the count rate measured under 1 MHz pulsed illumination. The photoresponse reaches a maximum at 400 µA-450 µA, a current significantly below the measured I_c and marginally higher than I_r. Compared with the same sample at 5 K the minimum detectable optical energy is greatly increased. Its likely that the reduced sensitivity is because the sample is being biased at only ~0.6 I_c when the peak photoresponse occurs. When biased at a higher current, optical pulses cause the sample to latch to the resistive state and therefore it becomes far less sensitive to further illumination. To achieve the expected higher performance at larger bias currents it is therefore necessary to deliver single optical pulses, resetting the bias current between measurements.

Sample 19 was biased as close to I_c as possible and illuminated with single optical pulses. The current was reduced to zero and reset after each pulse. The detector was found to respond stochastically, it either latched or had no observable response. The proportion of pulses which caused latching at varying energy is shown in figure 4.34.

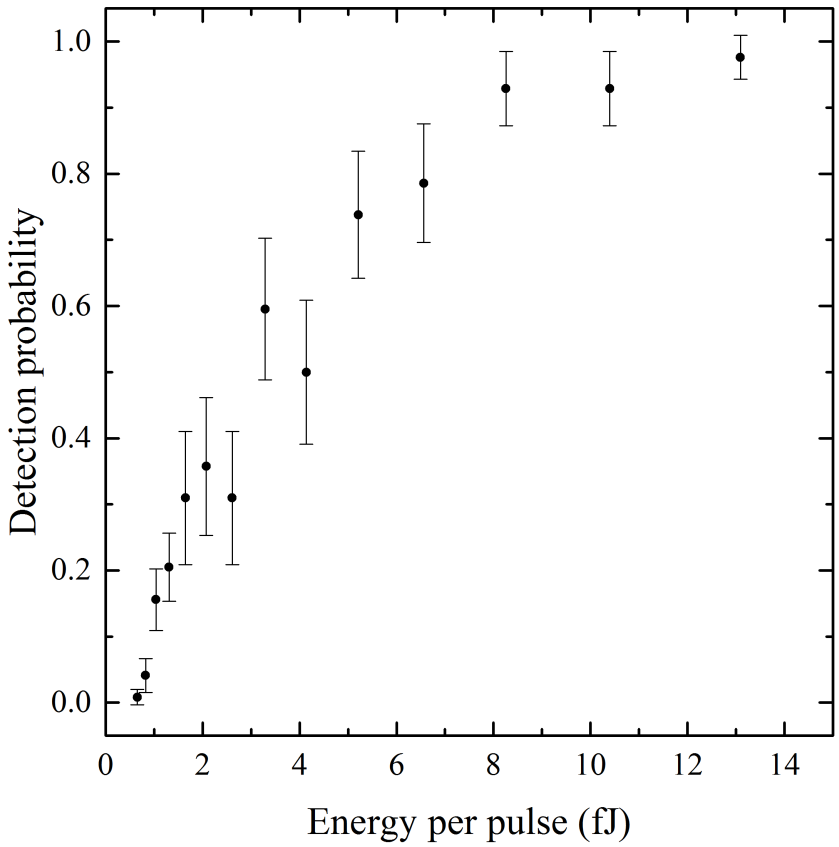

Figure 4.34: *The estimated proportion of pulses that resulted in latching as a function of optical energy, biased at 693 µA at 360 mK. Error bars show the value of the standard error calculated using the Agresti–Coull method [127].*

The use of a higher bias current, enabled by single pulsed illumination, has resulted in a much improved sensitivity for the detector compared with the repetitive pulses measured in figure 4.33b). The sample detected all incident pulses of energy at 13 fJ and dropped to approximately 50% detection rate at 3 fJ. This performance is consistent with that observed

at 5 K when biased near I_c (figure 4.30).

4.4 Shaped $NbSe_2$ detectors

All previous measured devices wave been irregular flakes of $NbSe_2$ which therefore have varying cross sections along the length of the superconductor. It was believed that if the $NbSe_2$ crystals were shaped to have constant widths, electrical constrictions would be eliminated, resulting in higher current densities and improved device performance.

4.4.1 Device layout

The devices, manufactured by Matthew Hamer and Roman Gorbachev from the University of Manchester, consist of few layered $NbSe_2$ crystals, encapsulated on both surfaces by either hBN or single-layer graphene and placed across the ground and signal lines of a tapered coplanar waveguide (CPW). An example image is shown in figure 4.35. The tapered CPW, designed by the author, was implemented to improve high frequency electrical transmission, reducing electrical reflections and distortions of detector outputs.

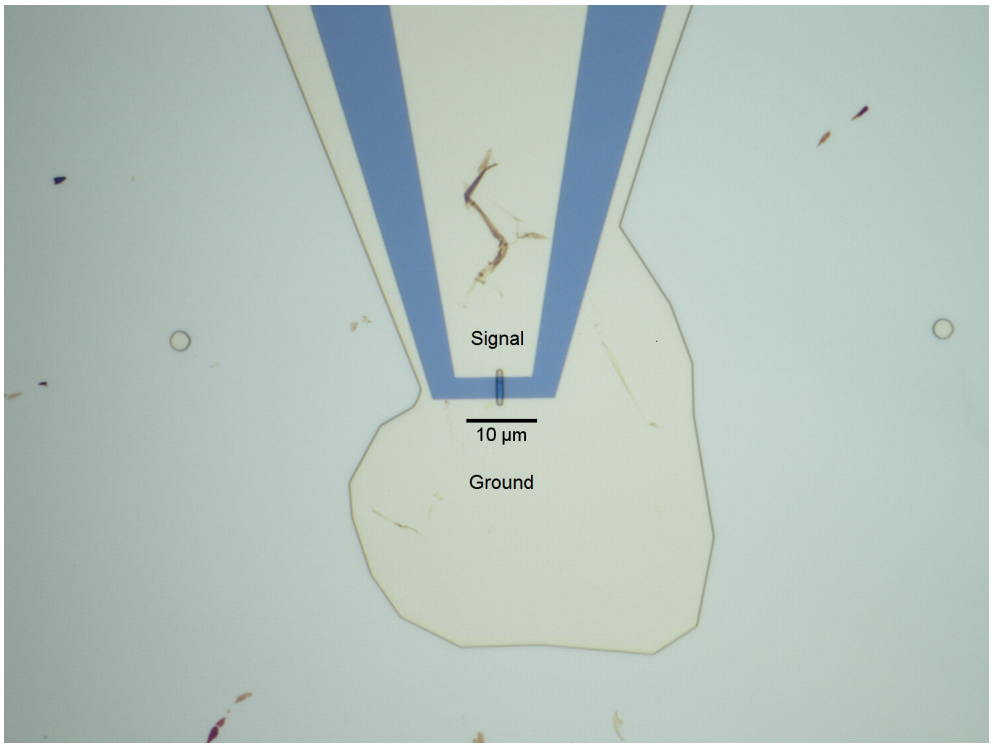

Figure 4.35: *Sample 24, a 1 µm wide strip of $NbSe_2$ which has been encapsulated on both surfaces with graphene and placed in a tapered, gold coplanar waveguide. The border which can be seen surronding the coplanar waveguide is resist which was used in the etching process.*

4.4.2 Characterisation

Seven samples of varying widths were provided, ranging from 150 nm to 5 µm. Four of the samples, including the narrowest two, showed no electrical characteristics of superconductivity at 360 mK, instead showing resistances of several kΩ. This is perhaps due to oxidation

of the $NbSe_2$ from the exposed edges. Of the three remaining samples (20, 21, 23), samples 20 and 23 were found to be superconducting and responsive to optical stimulus.

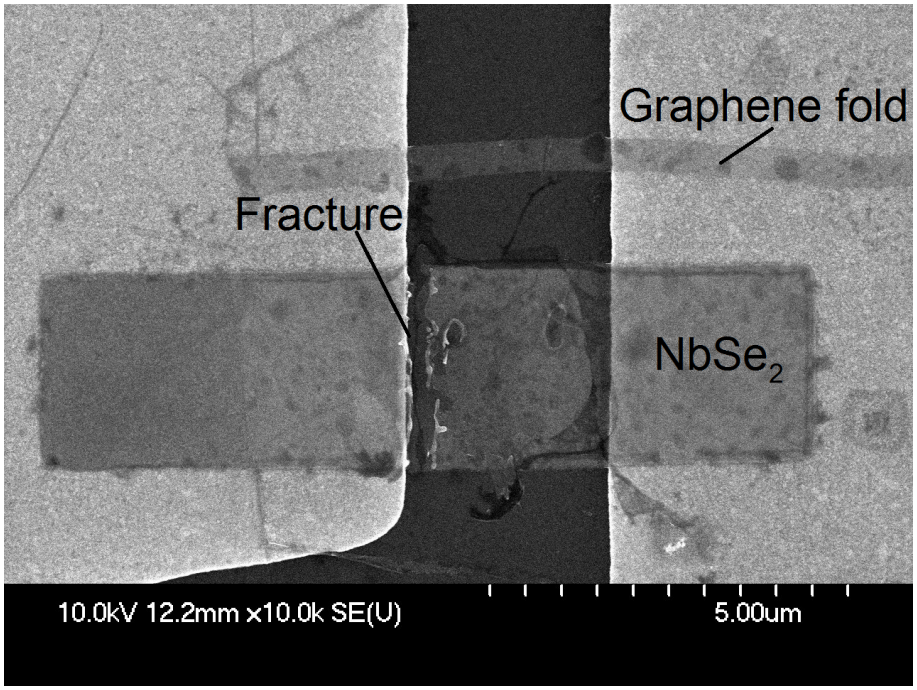

Figure 4.36: *An SEM image of sample 21 showing a fracture in the heterostructure which developed during thermal cycling. The sample has been encapsulated with graphene to prevent oxidation and an unintentional fold in the graphene layer can be seen in this image.*

Unfortunately sample 21 broke during thermal cycling before it could be tested optically. To investigate the behavioural change, a scanning electron microscope (SEM) image was acquired and is shown in figure 4.36. As in evident in the above SEM image, the shaped $NbSe_2$ strip has broken across its entire width at the edge of the gold signal line.

Sample 20

Sample 20 is the narrowest sample that showed superconducting properties. It has been etched into a 500 nm wide strip, encapsulated with graphene and placed across the ground and signal lines of a CPW. From optical contrast it is estimated to be five molecular layers thick.

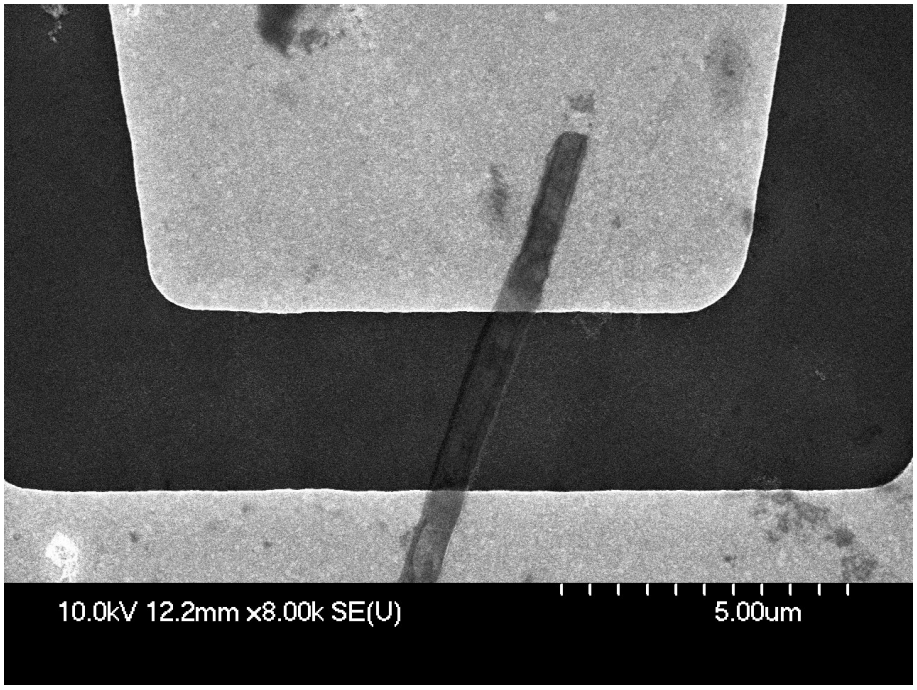

Figure 4.37: *An SEM image of sample 20 showing the narrow width the $NbSe_2$ has been etched into.*

Using a 5 µA applied current, the T_c was measured to be 6.35 K where the sample resistance transitioned from 280 Ω to 143 Ω. The large resistance observed in the superconducting state may be due to the small contact areas at both the gold-graphene and graphene-$NbSe_2$ interfaces. The sample was cooled to around 5 K and located optically as described in section 3.2.4 and optical testing was performed.

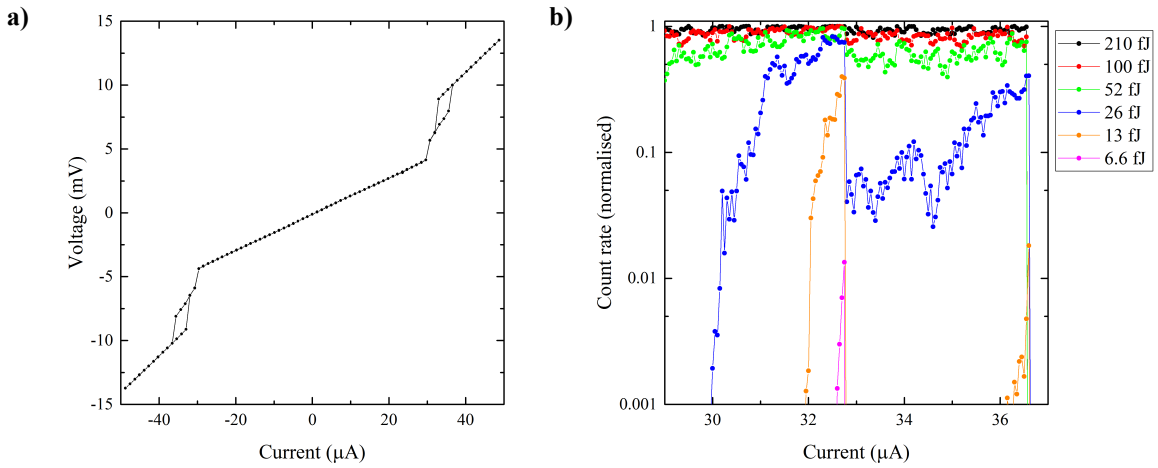

Figure 4.38: ***a)*** *The I-V profile of sample 20 at 5.15 K.* ***b)*** *The count rate measured from sample 20 under 1 MHz pulsed illunation at 5.1 K.*

Figure 4.38a) shows the I-V profile of the sample at 5.15 K. There are two clear switching currents where the resistance increases, 31 µA and 36 µA, the second of which is hysteretic. The count rate shown in figure 4.38b) was measured at 5.1 K. Two peaks in optical sensitivity can be seen at 32.8 µA and 36.6 µA. The peaks in optical sensitivity occur when the sample is biased just below the two switching currents of the sample and correspond well with

the currents measured in the I-V profile taking into account the small temperature change between the two measurements.

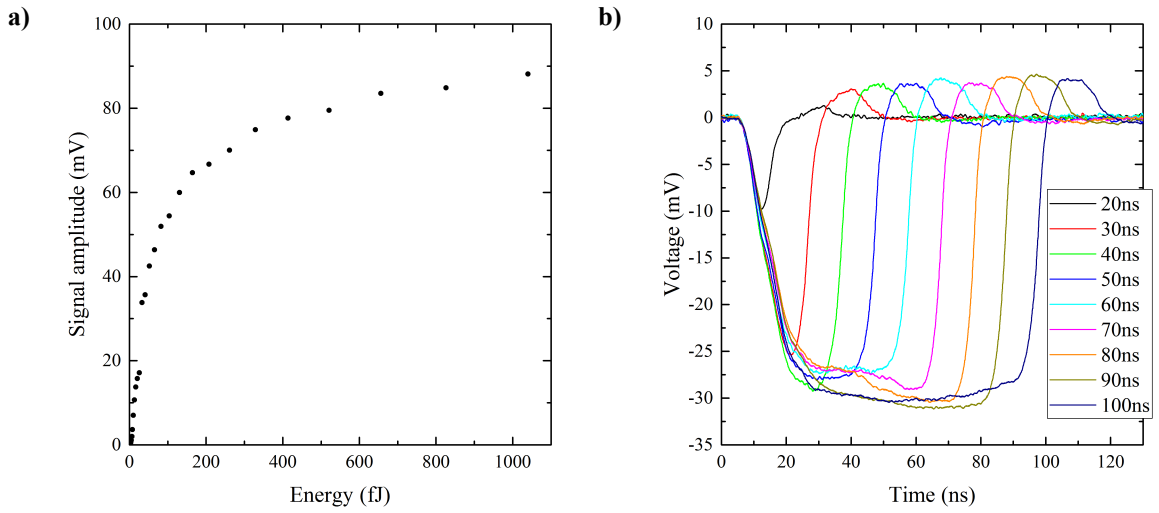

Figure 4.39: a) *Amplitude of voltage signals measured from sample 20 with varying optical energy at 5.1 K with 32 µA bias current.* ***b)*** *Voltage signals measured from sample 20 with varying optical pulse width at 5.1 K with 32 µA bias current.*

The amplitude of voltage signals was measured to be dependent on optical energy as shown in figure 4.39a). The signal amplitude has a strong dependence on optical energy below 100 fJ per pulse but as optical energy is increased further, the signal saturates reaching a maximum response of around 90 mV.

The PPG (Agilent 33220A, 20 MHz bandwidth) used to supply the laser diode was set to supply 1 MHz electrical pulses of duration 20-100 ns and a constant attenuation was applied to the resulting optical pulses (15dB). The resulting signals from sample 20 are plotted in figure 4.39b). The signal duration from the sample clearly follows the laser pulse duration indicating that the detector response is dependent on the incident laser power and can react to changes in incident power on time scales of ~10 ns.

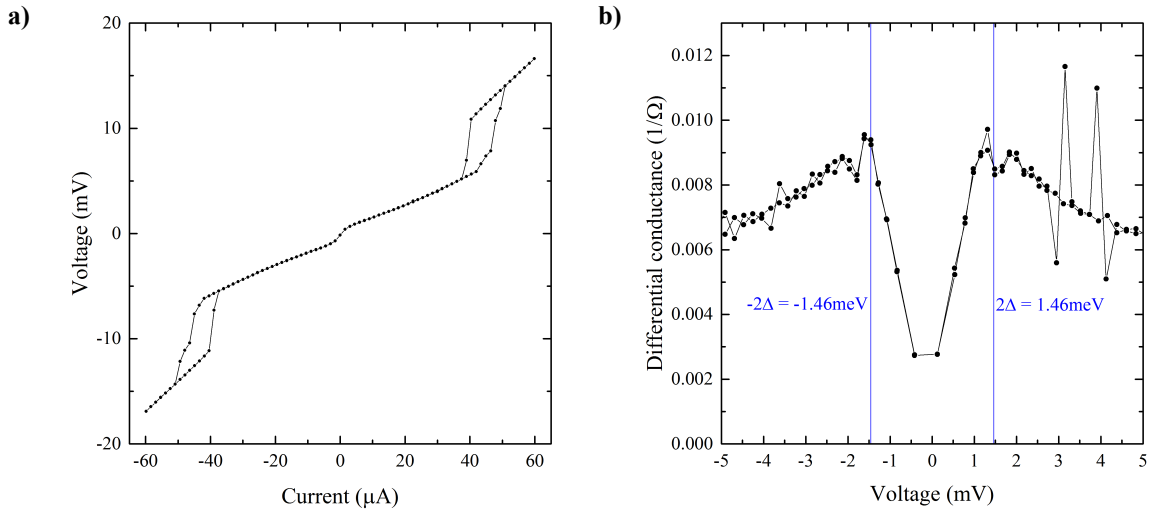

Figure 4.40: a) *The I-V profile of sample 20 at 360 mK.* ***b)*** *The differential conductance of sample 20 in the low current region at 360 mK.*

The I-V profile of the sample when cooled to the base temperature of the system (360 mK) is shown in figure 4.40a). As expected the superconducting switching current is increased and has a larger hysteretic region. Interestingly the conductance of the sample is low around zero bias current, as shown in figure 4.40b). One possible explanation for this behaviour is that the graphene layer between the gold and $NbSe_2$ is acting as a tunnelling barrier. Similar behaviour for $NbSe_2$ heterostructures has been described previously (see references 128 and 129) where similar differential conductance peaks were observed.

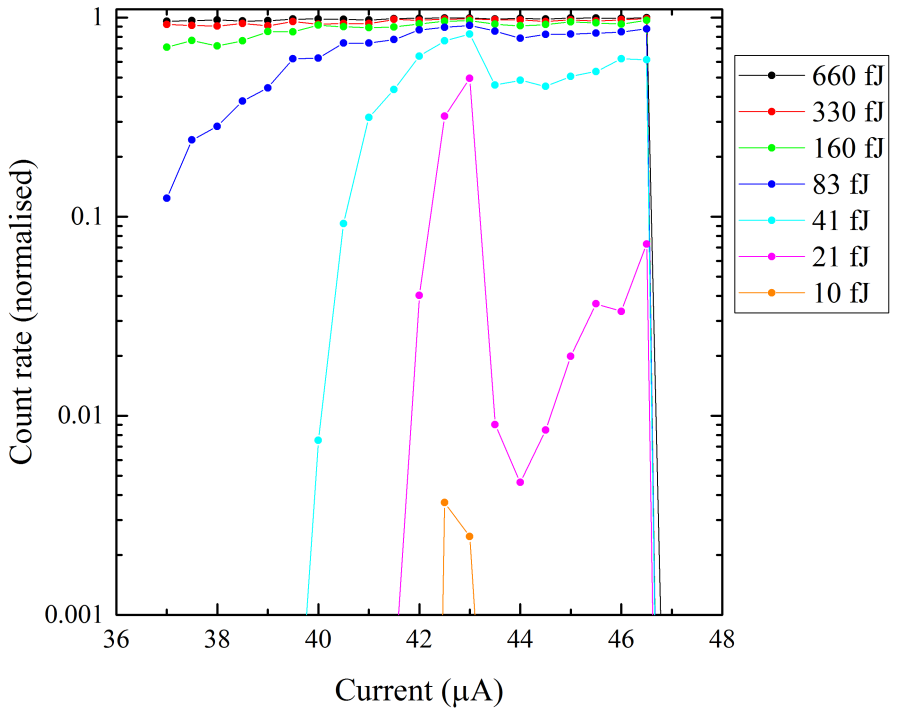

Figure 4.41: *The count rate measured from sample 20 at 360 mK with varying bias current and pulse energy.*

Figure 4.41 shows the count rate measured for sample 20 at 360 mK. Similar to at 5.1 K, there are two bias currents at which the count rate for low energy pulses reaches a local maximum (42.5 µA and 46.5 µA). As before, the lowest energy pulses have higher count rates at the lower of the two currents.

Sample 23

Sample 23, shown in figure 4.42, consists of a 5 µm wide etched flake of $NbSe_2$ that has been encapsulated on both surfaces with graphene and placed across the 3 µm long gap between ground and signal lines of a CPW. From optical contrast the sample is estimated to be 5 molecular layers thick.

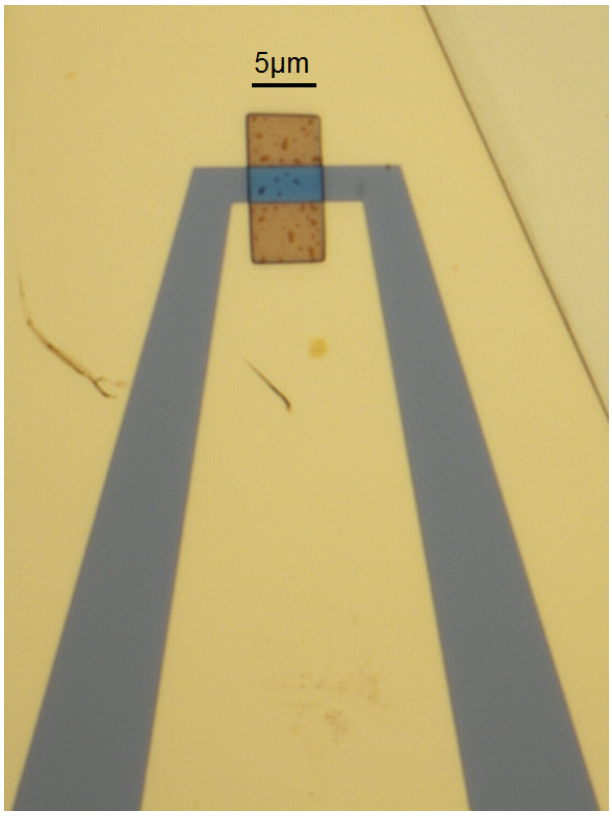

Figure 4.42: *An optical image of sample 23 showing the ground and signal lines of the CPW.*

Using a 10 µA applied current, the T_c was measured to be 6.4 K where the sample resistance transitioned from 45.2 Ω to 30.6 Ω. The sample was cooled to 360 mK and slowly warmed while the applied bias current was swept. The critical and retrapping currents of the sample were found and are plotted in figure 4.43a). Unusually, the retrapping current was found to be proportional to the experimental critical current. This implies that the experimental critical current is strongly influenced by the same physical process that determines the retrapping current. This process is likely to be Joule heating and suggests that the observed switching current may be significantly below the superconducting de-pairing current predicted by Ginzburg-Landau and BCS theories.

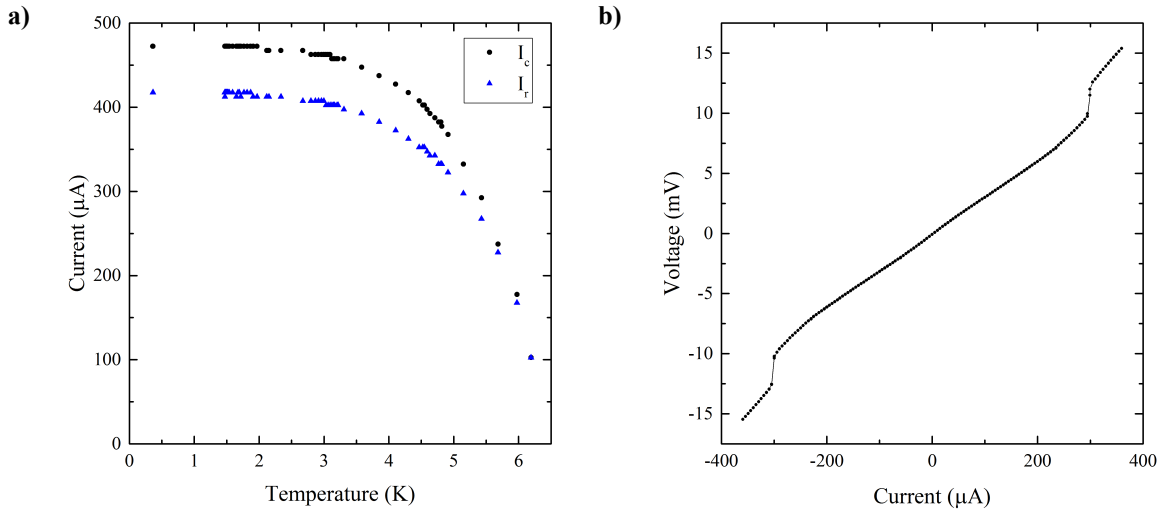

Figure 4.43: a) *The critical current and retrapping currents observed for sample 23 at varying temperature.* ***b)*** *The I-V profile of sample 23 at 5.3 K.*

The I-V profile of sample 23 at 5.3 K is shown in figure 4.43. A single non-hysteretic switching current was observed at 295 μA. The count rate measured with varying current for different pulse energies is shown in figure 4.44a). Similar to previously discussed samples the count rate reaches its maximum at the switching current, above which the count rate drops sharply. However, higher energy pulses can still trigger counts beyond this point, with decreasing probability as the current is increased further.

The count rate measured at 295 μA, where the response of the sample to illumination is highest, is shown in figure 4.44b) with varying optical pulse energy. The count rate dropped below 50% at 9.3 fJ and optical pulses were counted at energies as low as 2.6 fJ.

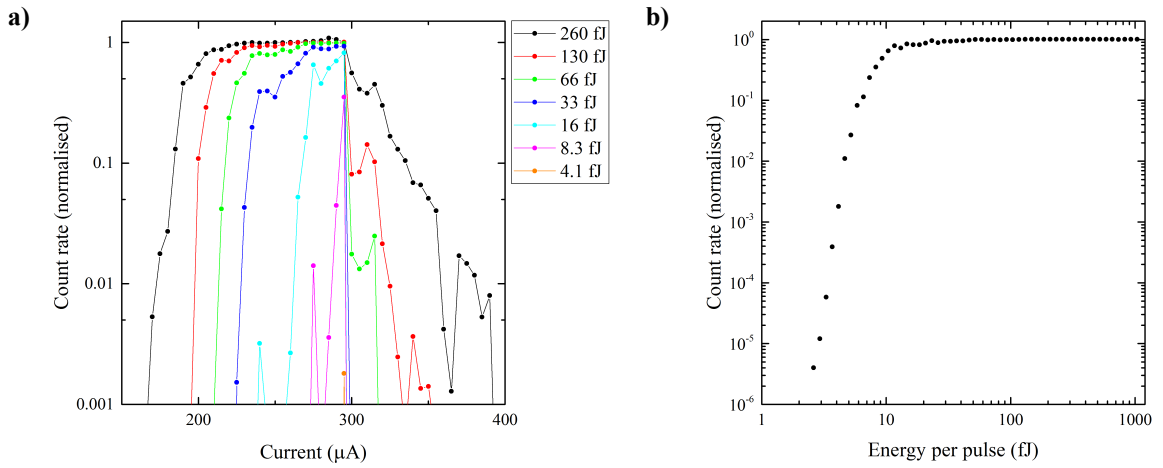

Figure 4.44: *Count rates measured at 5.3 K using 20 ns optical pulses at 1 MHz repetition rate.* ***a)*** *The count rate measured with varying pulse energy and bias current.* ***b)*** *The count rate measured just below I_c at 295 μA with varying pulse energy.*

Figure 4.45a) shows averaged oscilloscope traces obtained under illumination from a 50 MHz repetition rate, narrow pulse width, 1550 nm laser. The laser pulse width is <1 ps and therefore deposition of energy should occur on a time scale much shorter than the device response

time. The device was able to respond to the high repetition rate illumination, showing that it is capable of recovering and has a dead time shorter than 20 ns. The amplitude of device response is shown in figure 4.45b) for bias currents of 250 µA and 300 µA. Under these conditions the signal amplitude was found to have a proportional dependence upon the optical pulse energy.

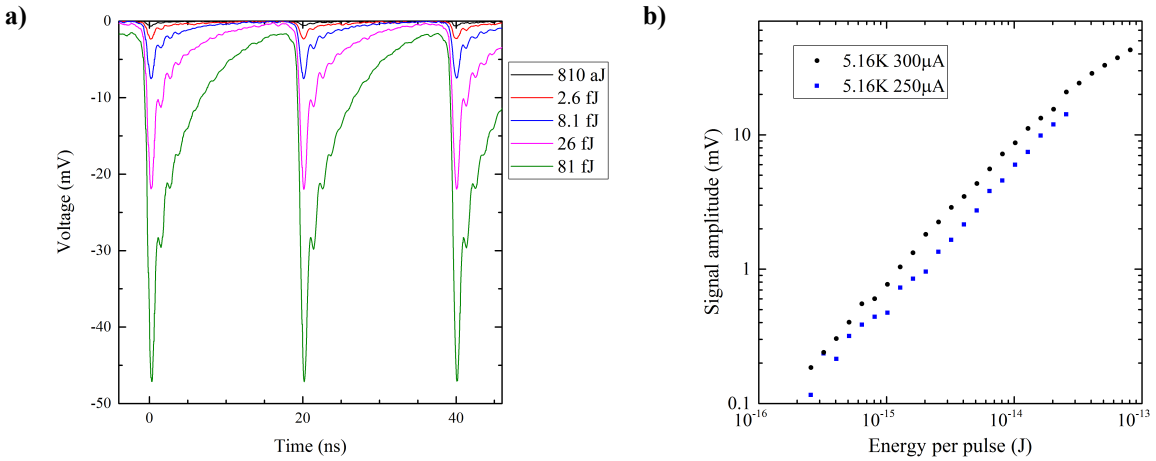

Figure 4.45: *Signal characteristics at 5.16 K using 50 MHz pulsed illumination with short pulse widths (<1 ps).* ***a)*** *Averaged oscilloscope traces at 300 µA bias current.* ***b)*** *The variation of signal amplitude with pulse energy for bias currents of 250 µA and 300 µA.*

4.5 Conclusions

$NbSe_2$ has been used as the basis of several detector designs. Several encapsulation and electrical contact strategies have been used. Electrodes have been designed for and patterned on top of exfoliated crystals and crystals have been dry-transferred onto pre-patterned contacts. Fabrication of such devices has proved challenging, less than half of the devices provided for testing were measured to be superconducting and photosensitive. Of the devices which did prove superconducting, some had visible cracks in the $NbSe_2$ while others showed signs of partial oxidation. A summary of the optical performance of the functional devices is provided in table 4.3.

The design of the detectors was a modification of a SNSPD, a single photon sensitive superconducting detector. It was therefore expected that the detectors would behave as a counter in response to illumination; that the response would be stochastically triggered with no variation in signal amplitude with pulse energy. In reality, the devices manufactured showed markedly different behaviour.

The response of devices to optical illumination was in general found to be dependent on the energy and instantaneous power of the applied illumination. The amplitude of response increased with optical pulse energy and was found to be proportional to the bias current below the experimental critical current (I_c). The majority of devices were able to be biased close to I_c without latching even under strong pulsed illumination. In this regime, since the

amplitude of optical response decreases with decreasing pulse energy, there is a minimum pulse energy that can be practically measured for each bias current. To characterise this property table 4.3 reports the minimum pulse energy resulting in a 50% count rate using a 10 mV threshold ($E_{50\%}$). Several devices displayed multiple experimental switching currents. With the exception of sample 18, the minimum value of $E_{50\%}$ was obtained when the sample was biased below the first switching current.

ID	Encapsulation	Area (μm^2)	I_c (μA)	R_s (Ω)	ΔR (Ω)	$E_{50\%}$ (J)	NEP ($WHz^{-0.5}$)
5	graphene	2.1	265	49	26	1.6×10^{-14}	3.4×10^{-13}
6	graphene	6.7	224	41	15	3.3×10^{-15}	2.2×10^{-13}
9	none	7.2	61	44	113	3.3×10^{-15}	-
10	none	13.0	165	7	40	3.3×10^{-15}	2.5×10^{-13}
15	none	98.1	36	23	48	3.9×10^{-16}	-
18	hBN	17.2	3	20	752	2.9×10^{-14}	-
19	hBN	34.2	693	16	38	2.6×10^{-15}	3.2×10^{-14}
20	graphene $\times 2$	1.7	42	143	133	2.1×10^{-14}	1.1×10^{-12}
23	graphene $\times 2$	21.5	469	31	5	1.0×10^{-14}	1.1×10^{-12}

Table 4.3: *A summary of the performance of the optically sensitive samples that were tested. The area listed is the area of $NbSe_2$ between the two electrical contacts, R_s is the resistiance that was measured in the superconducting state, ΔR is the increase in resistance observed when the sample switches to the resistive state, $E_{50\%}$ is the minimum optical pulse energy detected by the sample with a count rate above 50% of the repetition rate and NEP is the noise equivalent power.*

Graphene was the first encapsulation material tested, it was chosen for its electrical conductivity and high level of transparency. However, contact resistances of approximately 50 Ω were measured for these devices. A large contact resistance such as this may have the effect of heating the $NbSe_2$, resulting in a reduced critical current which will in turn limit the obtainable amplitude of response.

In an effort to reduce the contact resistance and also to clarify the origin of the observed optical behaviour, devices were manufactured without an encapsulation material. The contact resistances of these devices were indeed reduced; however, likely because of partial oxidation of the $NbSe_2$, critical current densities were not significantly increased. The removal of the graphene encapsulation layer also had the effect of removing a parallel conducting path between the gold electrodes. This means that when the $NbSe_2$ is driven to its resistive state there is a greater change in the overall resistance of the device. This value is listed as ΔR in table 4.3. Sample 15 has the lowest measured value of $E_{50\%}$ of any of the measured devices, this is possibly due to a combination of a large area, I_c and ΔR.

The next evolution of the device design was to use hexagonal boron nitride (hBN) as the encapsulation material. As hBN is an insulator, the electrical connections had to be in direct contact with the $NbSe_2$. To reduce atmospheric exposure to the minimum time period possible, gold structures were pre-fabricated and the $NbSe_2$ and hBN layers were dry-transferred on top. This design results in a single conducting path through the superconductor whilst also

preventing oxidation. Unfortunately, placement of the $NbSe_2$ on top of a patterned structure often results in cracks or damage to the crystal. This can be seen in sample 18 where a single large crystal shattered into many pieces.

Sample 19 survived the fabrication process intact and displayed a very large critical current with low sample contact resistance and large ΔR. The encapsulation protected the sample from oxidation well, as is evident in the linear I-V profile and preserved T_c of 6 K. The large signal amplitude generated by sample 19 coupled with its low electrical noise resulted in the lowest NEP of any of the devices measured. The sample is highly hysteretic, this is a result of the large critical current causing significant heating of the sample when I_c is exceeded. The large I_c means that when the sample is biased in its hysteretic region and illuminated, it latches. The Joule heating of the sample exceeds thermal conduction and therefore prevents superconductivity from being recovered until the bias current is reduced. In this latching regime the sample behaves much more like the originally expected manner. There is a minimum energy that must be supplied to trigger the device but the resulting signals are otherwise independent of pulse energy.

The last iteration of the design was to etch the $NbSe_2$ crystals to have an even width across their length (samples varying from 0.5-55 µm width). Variation in width causes a corresponding variation in current density, resulting in sections of a superconducting strip having a varying critical current across its length. Irregular geometry such as this could explain the multiple resistive steps that many samples exhibited in their I-V profiles (samples 5, 10, 15 and 18). The optically sensitive region in an uneven superconductor is likely to be reduced to just the area with smallest cross section, the area being biased at the highest fraction of its critical current. It was hoped that a regular cross section would allow the entire crystal to be biased close to the critical current density of the material and therefore exhibit increased optical sensitivity.

Samples were produced with both hBN and graphene encapsulation layers; however, the only samples which maintained superconductivity were encapsulated by graphene. As with the other graphene encapsulated samples, substantial contact resistances of 143 Ω and 31 Ω were observed for samples 20 and 23. Likely as a result of the high contact resistance, the samples did not display high optical sensitivity as shown in table 4.3.

Twenty six devices were assessed throughout this project, of which nine were found to be superconducting and optically sensitive. Although there are variations in design and device performance, unexpected and largely consistent sample behaviour was observed. These results constitute the first use of a two-dimensional superconducting material as an optical detector. Although the expected sensitivity was not realised, much progress has been made and as fabrication techniques in this novel field develop it is likely that significant performance improvements can be achieved.

4.5.1 Towards single photon sensitivity

None of the tested samples were found to be single photon sensitive, the closest device to this milestone was sample 15 where the lowest input energy which produced a measurable output corresponded to the absorption of approximately 35 photons in the $NbSe_2$ at 1550 nm wavelength. To quantify the efficiency of this detector, figure 4.46 plots the number of counts from the detector per absorbed photon. In the single photon regime (less than 1 photon per laser pulse), this metric will be equal to the single photon detection efficiency of the device (η_{DDE}). The metric reaches a maximum of 0.32% when an estimated 217 photons are absorbed in the detector per laser pulse with a count probability of 70.5%. In figure 4.46, the right side of the curve is of the form $y = 1/x$ as the detector is capable of detecting all laser pulses at high powers. A single photon sensitive detector would be expected to have a flat region in the low power limit however this device shows a peak and a decrease in the low power limit as the count rate vs. input power decreases superlinearly below an energy cutoff.

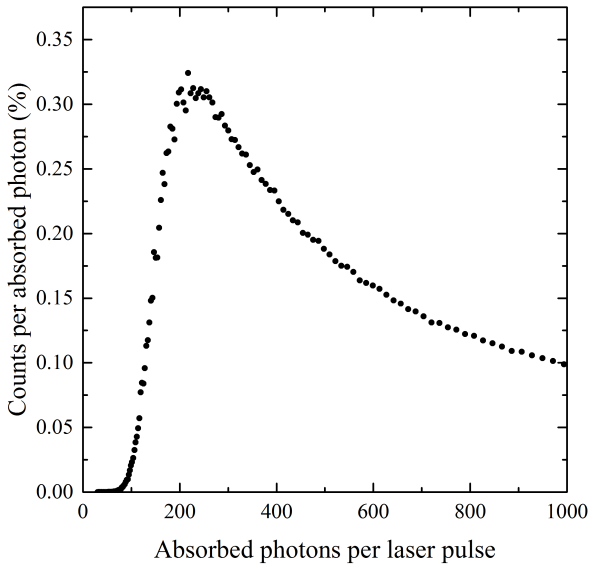

Figure 4.46: *The detection probability per absorbed photon of sample 15 with varying input power. Measurements made at 360 mK with a bias current of 36 μA.*

To achieve single photon detection, the absorption of one photon needs to generate a resistive band across the detector. Following the diffusion based hotspot model [44], photon absorption will generate a resistance in a superconductor only if it reduces the Cooper Pair (CP) density enough that the velocity of carriers, in a slab of thickness equal to the coherence length ξ, exceeds the depairing velocity.

There are several methods which could be used to increase sensitivity to single photons. If the detector is biased closer to its depairing current, then fewer CPs need to be broken. This approach requires a superconducting detector which can support bias currents at higher fractions of its depairing current. It is therefore a fabrication challenge and requires the superconductor to be made to a high degree of homogeneity. Crystal defects, oxidation, variations in width and thickness are all to be avoided.

Alternatively, the relative effect of an absorbed photon can be increased by reducing the cross sectional area of the superconductor, thereby reducing the number of CPs in the thickness ξ. Therefore a lower energy cutoff would be expected if the superconductor thickness or width was reduced, although both of these actions would reduce the coupling efficiency to the detector and so integration with an optical waveguide or cavity may be required.

Chapter 5

Thermal modelling and analysis

Experimentally it has been observed that when an optical pulse is applied to a current biased $NbSe_2$ crystal, a voltage will develop across the device. The amplitude and duration of the voltage will be dependent on the bias current and the intensity of illumination. It has been observed that such devices can recover their original superconducting state or may remain resistive after the laser pulse. In this chapter, the thermal and electrical behaviour of such $NbSe_2$ devices will be modelled to better understand the cause of the observed photoresponse.

5.1 Analytical modelling

In this section, an analytical model is developed which will be used to study the steady state behaviour of a superconducting $NbSe_2$ photodetector. The conditions under which a self-sustaining resistive region will form are investigated and critical phenomena are studied.

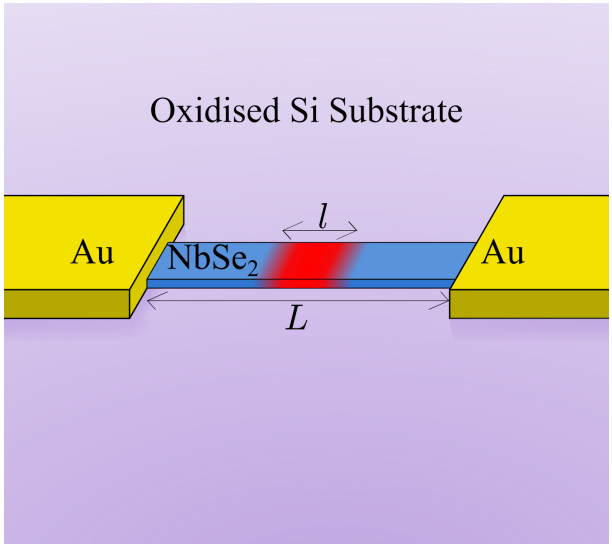

Figure 5.1: *A sketch of a superconducting strip with a self-sustaining resistive region.*

The superconductor is modelled with length L and thickness d. At either end, the superconductor is in thermal contact with gold electrodes which are assumed to be much thicker

and more conductive than the superconductor and therefore maintain each end of the superconductor at the ambient temperature, T_b. The superconductor has a self-sustaining resistive region at its centre of length l, resistivity ρ. The superconductor is biased with current density J and so the normal region generates Joule heating with power per volume $J^2\,\rho$. The superconductor can conduct heat both along its length with thermal conductivity κ and into the substrate with a thermal boundary conductivity per unit area α. The $NbSe_2$ is under vacuum and is modelled without any radiative heat transfer. The temperature distribution will be uniform along the width of the device and so thermal conduction along this axis can be neglected.

The following time dependent heat equation [130] describes the modelled system:

$$\kappa\,\frac{d^2T}{dx^2} + J^2\,\rho - \frac{\alpha}{d}\,(T - T_b) = c\,\frac{dT}{dt} \tag{5.1}$$

where c is the specific heat per unit volume of $NbSe_2$, t is time.

The steady state solution of equation 5.1 is now found by setting the temperature distribution, T, to have no variation with time.

$$\frac{d^2T}{dx^2} = \frac{1}{\eta^2}\,T - \frac{J^2\,\rho\,d}{\alpha\,\eta^2} - \frac{T_b}{\eta^2} \tag{5.2}$$

where the thermal healing length, η, is defined:

$$\eta = \sqrt{\frac{\kappa\,d}{\alpha}} \tag{5.3}$$

Equation 5.2 is an inhomogeneous second order differential equation and it has the particular solution:

$$T = C_1\cosh(A\,x) + C_2\sinh(A\,x) + B \tag{5.4}$$

Therefore,

$$\frac{d^2T}{dx^2} = A^2\,C_1\cosh(A\,x) + A^2\,C_2\sinh(A\,x) \tag{5.5}$$

$$= A^2\,T - A^2\,B \tag{5.6}$$

By comparing the coefficients of equations 5.2 and 5.6:

$$A^2 = \frac{1}{\eta^2} \tag{5.7}$$

$$A^2\,B = \frac{J^2\,\rho\,d}{\alpha\,\eta^2} + \frac{T_b}{\eta^2} \tag{5.8}$$

Therefore,

$$A = \frac{1}{\eta} \tag{5.9}$$

$$B = \frac{J^2\,\rho\,d}{\alpha} + T_b \tag{5.10}$$

$$T = C_1 \cosh\left(\frac{x}{\eta}\right) + C_2 \sinh\left(\frac{x}{\eta}\right) + \frac{J^2\,\rho\,d}{\alpha} + T_b \tag{5.11}$$

5.1.1 The temperature distribution in the resistive region

The constants C_1 and C_2 are found by applying boundary conditions. For the resistive region, where $|x| \leq \frac{1}{2}\,l$, the boundary conditions are:

$$T\left(\pm\,\tfrac{1}{2}\,l\right) = T_c \tag{5.12}$$

Therefore,

$$T_c = C_1 \cosh\left(\frac{l}{2\,\eta}\right) + C_2 \sinh\left(\frac{l}{2\,\eta}\right) + \frac{J^2\,\rho\,d}{\alpha} + T_b \tag{5.13}$$

$$T_c = C_1 \cosh\left(\frac{l}{2\,\eta}\right) - C_2 \sinh\left(\frac{l}{2\,\eta}\right) + \frac{J^2\,\rho\,d}{\alpha} + T_b \tag{5.14}$$

Solving the simultaneous equations 5.13 and 5.14 leads to the following values for C_1 and C_2:

$$C_1 = \left(T_c - T_b - \frac{J^2\,\rho\,d}{\alpha}\right) \operatorname{sech}\left(\frac{l}{2\,\eta}\right) \tag{5.15}$$

$$C_2 = 0 \tag{5.16}$$

The temperature distribution within the resistive region is therefore

$$T = \left(T_c - T_b - \frac{J^2\,\rho\,d}{\alpha}\right) \operatorname{sech}\left(\frac{l}{2\,\eta}\right) \cosh\left(\frac{x}{\eta}\right) + \frac{J^2\,\rho\,d}{\alpha} + T_b \tag{5.17}$$

5.1.2 The temperature distribution in the superconducting region

In the superconducting region ($\frac{1}{2}\,l \leq x \leq \frac{1}{2}\,L$), $\rho = 0$ and the boundary conditions are

$$T\left(\tfrac{1}{2}\,l\right) = T_c \tag{5.18}$$

$$T\left(\tfrac{1}{2}\,L\right) = T_b \tag{5.19}$$

Inserting these values into equation 5.11 generates two equations that can be used to find the values of C_1 and C_2 in the superconducting region.

$$T_c - T_b = C_1 \cosh\left(\frac{l}{2\,\eta}\right) + C_2 \sinh\left(\frac{l}{2\,\eta}\right) \tag{5.20}$$

$$0 = C_1 \cosh\left(\frac{L}{2\,\eta}\right) + C_2 \sinh\left(\frac{L}{2\,\eta}\right) \tag{5.21}$$

Solving for C_1 and C_2:

$$C_1 = -C_2 \tanh\left(\frac{L}{2\,\eta}\right) \tag{5.22}$$

$$T_c - T_b = -C_2 \tanh\left(\frac{L}{2\,\eta}\right) \cosh\left(\frac{l}{2\,\eta}\right) + C_2 \sinh\left(\frac{l}{2\,\eta}\right) \tag{5.23}$$

$$T_c - T_b = C_2 \operatorname{sech}\left(\frac{L}{2\,\eta}\right)\left[\sinh\left(\frac{l}{2\,\eta}\right)\cosh\left(\frac{L}{2\,\eta}\right) - \cosh\left(\frac{l}{2\,\eta}\right)\sinh\left(\frac{L}{2\,\eta}\right)\right] \tag{5.24}$$

$$T_c - T_b = -C_2 \operatorname{sech}\left(\frac{L}{2\,\eta}\right) \sinh\left(\frac{L-l}{2\,\eta}\right) \tag{5.25}$$

$$C_2 = -(T_c - T_b) \operatorname{csch}\left(\frac{L-l}{2\,\eta}\right) \cosh\left(\frac{L}{2\,\eta}\right) \tag{5.26}$$

$$C_1 = (T_c - T_b) \operatorname{csch}\left(\frac{L-l}{2\,\eta}\right) \sinh\left(\frac{L}{2\,\eta}\right) \tag{5.27}$$

Inserting the values of C_1 and C_2, the temperature distribution in the superconducting region is written as:

$$T = (T_c - T_b)\left[\sinh\left(\frac{L}{2\,\eta}\right)\cosh\left(\frac{x}{\eta}\right) - \cosh\left(\frac{L}{2\,\eta}\right)\sinh\left(\frac{x}{\eta}\right)\right] \times \operatorname{csch}\left(\frac{L-l}{2\,\eta}\right) + T_b \tag{5.28}$$

$$T = (T_c - T_b) \sinh\left(\frac{L-2\,x}{2\,\eta}\right) \operatorname{csch}\left(\frac{L-l}{2\,\eta}\right) + T_b \tag{5.29}$$

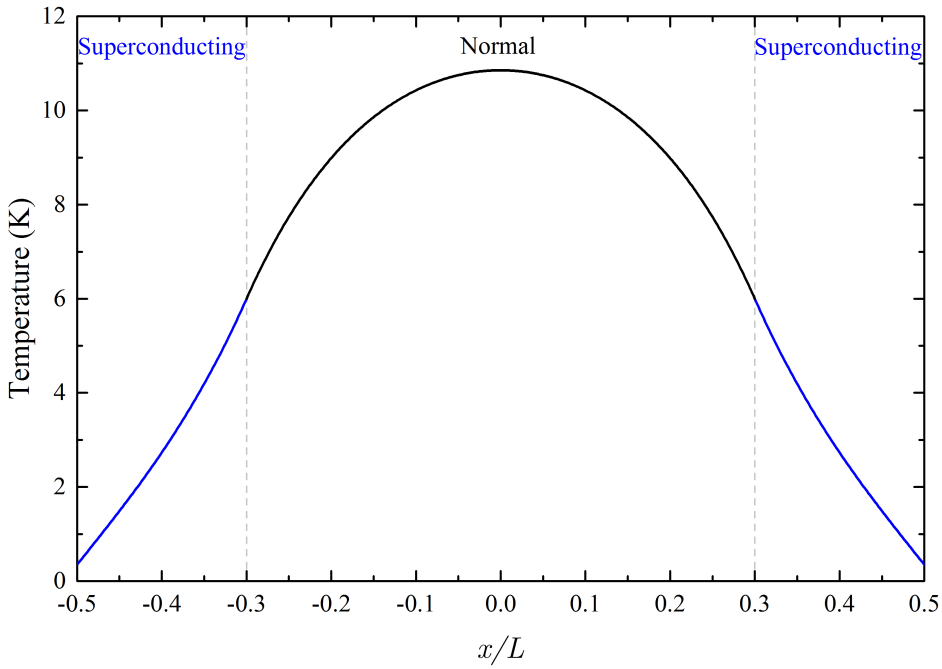

Figure 5.2: *The steady state temperature distribution along the superconductor. Calculated using the values:* $T_b = 0.35\,K$, $T_c = 6\,K$, $l = 0.6L$ *and* $\frac{L}{2\eta} = 3$.

5.1.3 Calculation of the length of the resistive region

Equations 5.17 and 5.29 describe the steady state temperature distributions in the resistive and superconducting regions respectively. However, both of these equations are dependent on the resistive length (l) which will itself change based on the bias conditions and thermal properties of the material. The length of the resistive region is determined by applying the boundary condition that the temperature gradient must be continuous across the superconducting boundary ($x = \frac{1}{2}\,l$).

$$\left.\frac{dT}{dx}\right|_{l/2^-} = \left.\frac{dT}{dx}\right|_{l/2^+} \tag{5.30}$$

$$\frac{1}{\eta}\left(T_c - T_b - \frac{J^2\,\rho\,d}{\alpha}\right)\tanh\left(\frac{l}{2\,\eta}\right) = -\frac{1}{\eta}\left(T_c - T_b\right)\coth\left(\frac{L-l}{2\,\eta}\right) \tag{5.31}$$

$$\left(T_c - T_b\right)\left(\tanh\left(\frac{l}{2\,\eta}\right) + \coth\left(\frac{L-l}{2\,\eta}\right)\right) = \frac{J^2\,\rho\,d}{\alpha}\tanh\left(\frac{l}{2\,\eta}\right) \tag{5.32}$$

$$\frac{\alpha\left(T_c - T_b\right)}{J^2\,\rho\,d} = \frac{\tanh\left(\frac{l}{2\,\eta}\right)}{\tanh\left(\frac{l}{2\,\eta}\right) + \coth\left(\frac{L-l}{2\,\eta}\right)} \tag{5.33}$$

$$\frac{\alpha\left(T_c - T_b\right)}{J^2\,\rho\,d} = \frac{\sinh\left(\frac{l}{2\,\eta}\right)\sinh\left(\frac{L-l}{2\,\eta}\right)}{\sinh\left(\frac{l}{2\,\eta}\right)\sinh\left(\frac{L-l}{2\,\eta}\right) + \cosh\left(\frac{l}{2\,\eta}\right)\cosh\left(\frac{L-l}{2\,\eta}\right)} \tag{5.34}$$

$$\frac{2\,\alpha\left(T_c - T_b\right)}{J^2\,\rho\,d} = \frac{\cosh\left(\frac{L}{2\,\eta}\right) - \cosh\left(\frac{L-2\,l}{2\,\eta}\right)}{\cosh\left(\frac{L}{2\,\eta}\right)} \tag{5.35}$$

$$\frac{2\,\alpha\left(T_c - T_b\right)}{J^2\,\rho\,d} = 1 - \cosh\left(\frac{L-2\,l}{2\,\eta}\right)\operatorname{sech}\left(\frac{L}{2\,\eta}\right) \tag{5.36}$$

$$\cosh\left(\frac{L-2\,l}{2\,\eta}\right) = \cosh\left(\frac{L}{2\,\eta}\right)\left(1 - \frac{2\,\alpha\left(T_c - T_b\right)}{J^2\,\rho\,d}\right) \tag{5.37}$$

$$l = \frac{L}{2} \pm \eta\,\operatorname{arcosh}\left(\cosh\left(\frac{L}{2\,\eta}\right)\left(1 - \frac{2\,\alpha\left(T_c - T_b\right)}{J^2\,\rho\,d}\right)\right) \tag{5.38}$$

Examining equation 5.38, it is clear that for l to have a solution, the argument of the arcosh function must be greater than one. This requirement gives the equation for the minimum current that must be applied for a self-sustaining resistive region to exist, I_{latch}.

$$\cosh\left(\frac{L}{2\,\eta}\right)\left(1 - \frac{2\,\alpha\left(T_c - T_b\right)}{J^2\,\rho\,d}\right) \geq 1 \tag{5.39}$$

$$J^2\,\rho\,d \geq 2\,\alpha\left(T_c - T_b\right)\frac{\cosh\left(\frac{L}{2\,\eta}\right)}{\cosh\left(\frac{L}{2\,\eta}\right) - 1} \tag{5.40}$$

$$I_{latch} = \left(\frac{2\,\alpha\,w^2\,d\left(T_c - T_b\right)}{\rho}\,\frac{\cosh\left(\frac{L}{2\,\eta}\right)}{\cosh\left(\frac{L}{2\,\eta}\right) - 1}\right)^{\frac{1}{2}} \tag{5.41}$$

$$\lim_{L\to\infty} I_{latch} = \left(\frac{2\,\alpha\,w^2\,d\left(T_c - T_b\right)}{\rho}\right)^{\frac{1}{2}} \tag{5.42}$$

The current required for a self sustaining resistive region I_{latch}, varies with the total length

of the superconductor. In the long-device limit, where $L \gg 2\eta$, I_{latch} tends to the value calculated by Skocpol et al. [48]. However, the current required for self-sustaining resistive regions may be far larger than this value for shorter devices, as shown in figure 5.3.

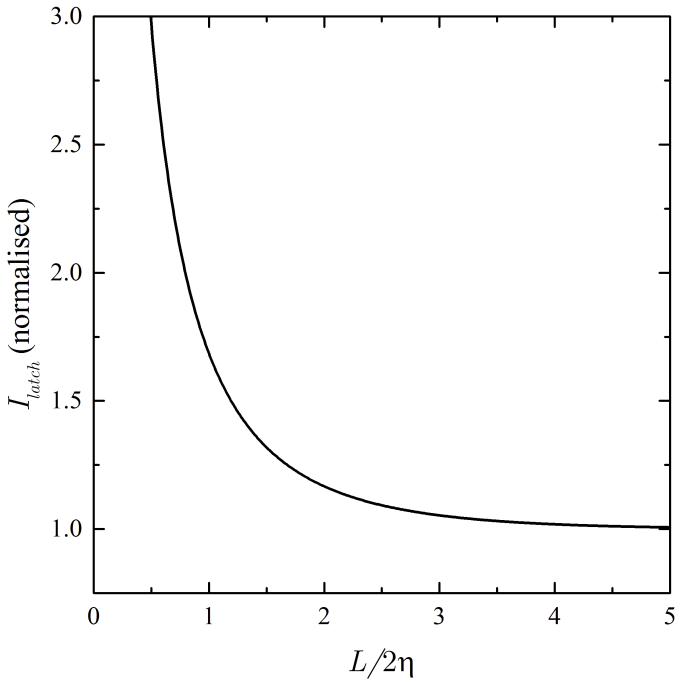

Figure 5.3: *The calculated variation of the latching current with device length.*

If the applied current exceeds I_{latch}, equation 5.38 shows that there are two steady state solutions for the resistive region length, l. The solutions for l are graphed in figure 5.4 for both a long and short device.

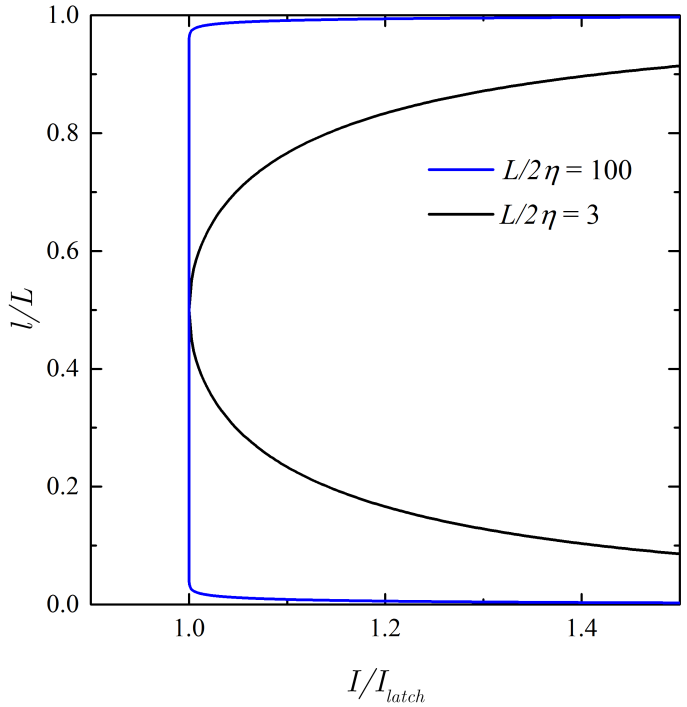

Figure 5.4: *The steady state solutions for the resistive region length which can be self-sustained under current bias. Solutions are plotted in the long and short device regimes ($L/2\eta = 100$ and 3 respectively.)*

As shown in figure 5.4, if the current exceeds I_{latch}, there will be two steady state solutions for the length of the resistive region, l_1 and $l_2 = L - l_1$ with l_1 being the smaller of the two lengths. In the long device limit l_1 and l_2 have very little current dependence above I_{latch} ($l_1/L \approx 0$ and $l_2 \approx L$). However, in the short device regime, l_1 and l_2 have a strong dependence on the bias current which should be experimentally observable.

5.1.4 Stability of the solutions

Rearranging equation 5.35, the electrical power per volume that will sustain a resistive region can be determined as a function of l. This is the electrical power necessary to balance heat flow in the steady state (P_{SS}).

$$P_{SS} = \frac{2\,\alpha\,(T_c - T_b)\,\cosh\left(\frac{L}{2\,\eta}\right)}{d\,\cosh\left(\frac{L}{2\,\eta}\right) - d\,\cosh\left(\frac{L-2\,l}{2\,\eta}\right)} \tag{5.43}$$

If at a certain point in time, the resistive region length l is not equal to a steady state value, the electrical power applied ($J^2\,\rho$) would be different to P_{SS} and therefore the temperature distribution and corresponding resistive region length would evolve with time. For small perturbations away from the steady state solution, the rate of temperature change within the resistive region will be:

$$J^2\,\rho - P_{SS} = c\,\frac{dT}{dt} \tag{5.44}$$

If the temperature in the resistive region increases, it will grow in length and therefore l will increase. Likewise when the temperature gradient is negative, l will decrease. It is clear that a feedback mechanism exists between l and temperature change. A value of l different to a steady state solution will cause temperature changes which will then alter the value of l. The rate of temperature change and the expansion or contraction direction is graphed in figure 5.5 for a superconductor biased such that the steady state solutions are $l_1 = 0.4L$ and $l_2 = 0.6L$.

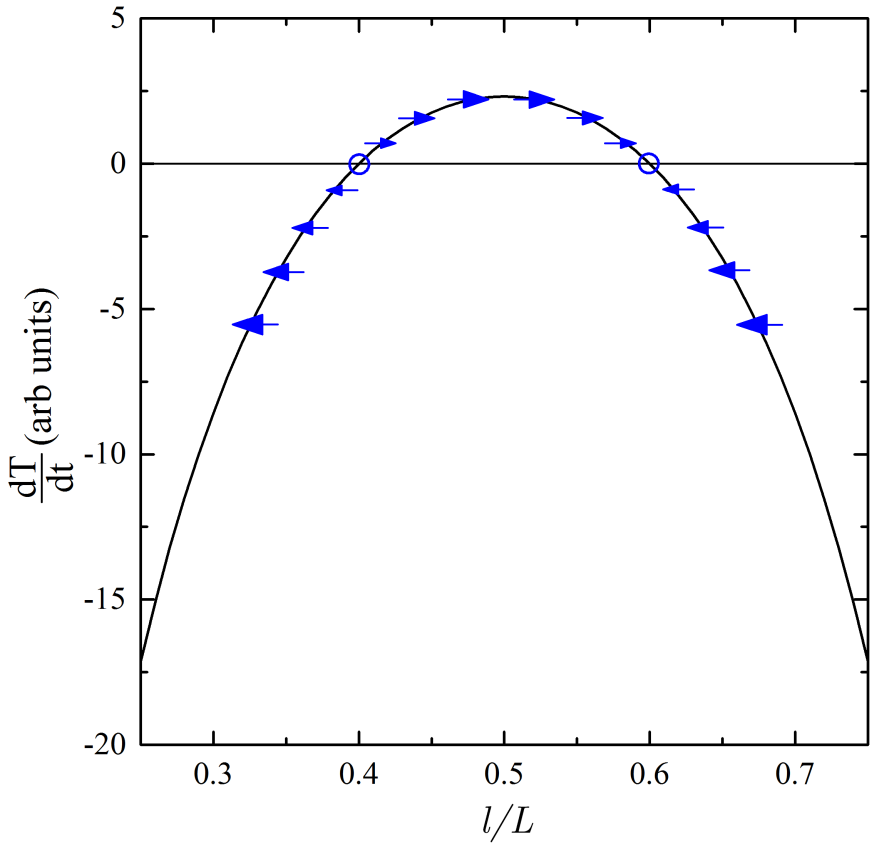

Figure 5.5: *The relationship between resistive length, l, and temperature change. Arrows are used to depict the expansion or contraction of l with time showing that l_1 is an unstable solution and that l_2 is stable. Calculated using the values: $l_1 = 0.4L$, $l_2 = 0.6L$ and $\frac{L}{2\eta} = 3$.*

Starting from a point close to an equilibrium value, a stable solution is one that will be converged to over time. Whereas a system will evolve with time away from an unstable solution. The arrows in figure 5.5 show the direction of time evolution of the hotspot length. It can be seen that the lower equilibrium point (l_1) is unstable as a hotspot length either side of the stationary point will evolve with time away from it. Similarly the higher equilibrium point (l_2) will be stable as a hotspot length either side of it will converge towards the steady state solution.

l_1 is therefore identified as a critical length. A resistive region smaller than l_1 will not be self sustaining and will decay. However, if the interplay of photon absorption and Joule heating under current bias create a resistive region with a length larger than l_1 then it will expand and eventually settle on the steady state value l_2.

5.1.5 Experimental comparisons

In the optical experiments conducted, a pulsed laser was used to heat a section of a current carrying superconductor. This establishes a local resistive region which will have an approximately two-dimensional temperature distribution. When the laser is off, the temperature distribution is assumed to evolve towards becoming one dimensional (this assumption

will be examined in section 5.2). Once heat flow becomes negligible along the width of the device, the analytical model above can be applied.

Several conclusions can be drawn from the model and compared with the experimental data from sample 19:

1. There will be a current (I_{latch}) below which the device will recover superconductivity for any pulsed laser power.

   At 5 K unattenuated 20 ns laser pulses were applied to sample 19. The bias current was increased in 3 µA steps. Latching first occurred at the current 218 µA where every laser pulse resulted in latching. This behaviour is in agreement with the analytical model and the estimated value of I_{latch} at 5 K is therefore 218 µA. Similarly, I_{latch} is estimated to be 390 µA at 360 mK.

2. If a current above I_{latch} is applied, the laser must induce a sufficiently large resistive region ($> l_1$) for latching to occur.

   At 5 K, sample 19 was biased at 224 µA and optical pulses of varying attenuation were applied. The resulting voltage signals were grouped by peak amplitude into 10 mV bins and the percentage of signals which latched is plotted in figure 5.6 a). It was found that the larger pulses latched while the smaller ones recovered superconductivity. The crossover point between the two behaviours occurred when the signals had a peak voltage of approximately 180 mV.

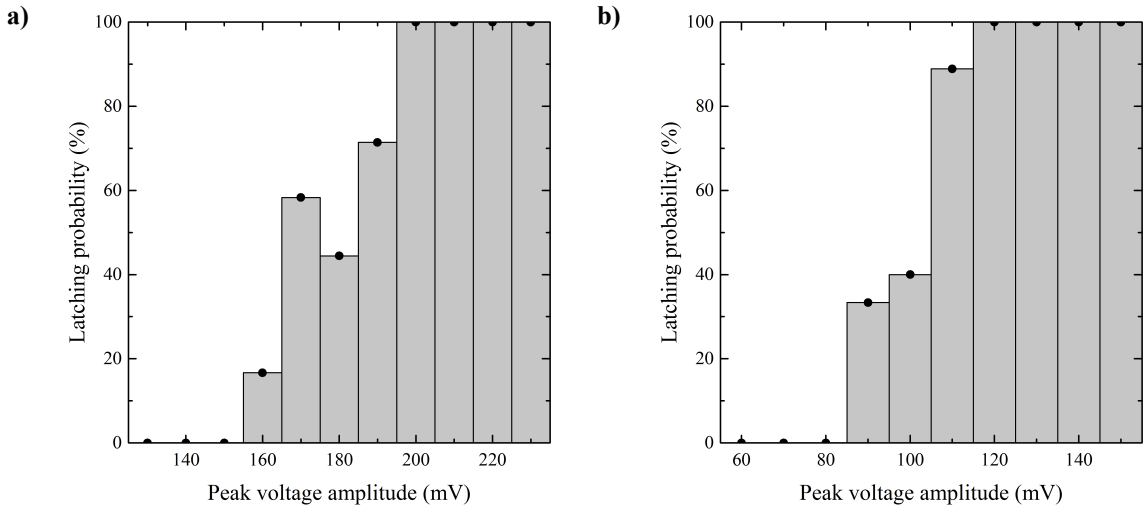

Figure 5.6: *The latching probablilty of voltage signals grouped by peak amplitude into 10mV bins.* ***a)*** *224 µA bias current.* ***b)*** *230 µA bias current.*

3. As the applied current is increased further beyond I_{latch}, the length of the resistive region required for latching, l_1, will decrease.

   Sample 19 was biased at the slightly higher current of 230 µA and the experiment was repeated. Figure 5.6 b) shows that although the bias current has increased, the signals transition to latching at smaller peak voltages than previously, approximately 105 mV.

Therefore, at increased currents, a smaller length of superconductor needs to be driven normal for the region to become self sustaining and latch, agreeing with the model.

4. The steady state resistive length will be independent of the laser pulse energy.

   At 5 K, sample 19 was biased at 224 µA and optical pulses of varying attenuation were applied. The latched voltage was measured 500 ns after the peak amplitude and was found to be independent of the laser pulse energy. The length of the normal region, l, was estimated by assuming that the measured voltage is proportional to the hotspot length and that unattenuated laser pulses drive the full length of the device to the normal state.

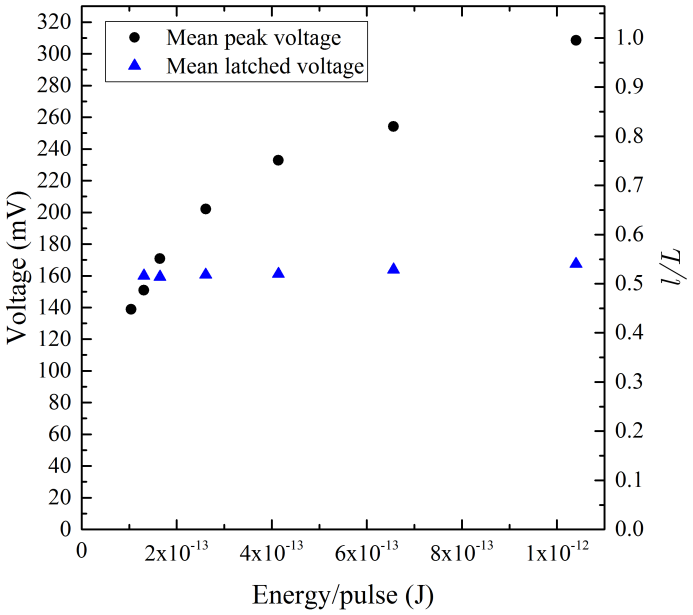

Figure 5.7: *The peak voltage and latched voltage with varying energy per pulse. It can be seen that the latched voltage is independent of the laser energy.*

5. The steady state resistive length will depend on the applied current and be equal to l_2. The current dependence is given by the upper branch of equation 5.38.

   At 5 K unattenuated 20 ns laser pulses were applied to sample 19. The bias current was varied and the latched voltage for each pulse was measured using an oscilloscope. The fraction of length that had latched (l/L) was calculated by dividing the latched voltage by the peak voltage due to the unattenuated laser pulse.

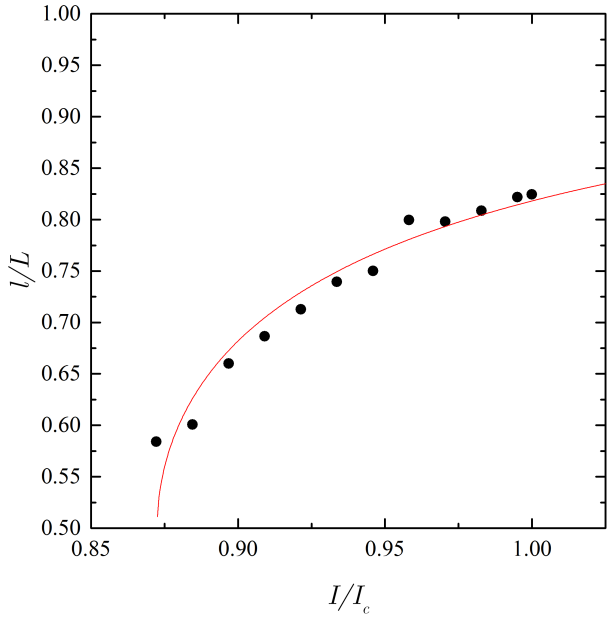

Figure 5.8: *The latched resistive length of sample 19 with varying applied current. The fitted line is the upper branch of equation 5.38 where* $\frac{L}{2\eta}$ *was used as a fitting parameter and determined to be 3.47.*

As shown in figure 5.8, the developed analytical model provides a good fit to the experimental values of hotspot length with varying current. This provides strong evidence that the analytical model captures the essential physics of the steady state behaviour of the system.

6. As the hotspot length evolves with time there will be a critical length, l_1. If the resistive region decreases below this critical length, the hotspot will recover superconductivity. But if the hotspot length remains above l_1, it will eventually settle at the length l_2.

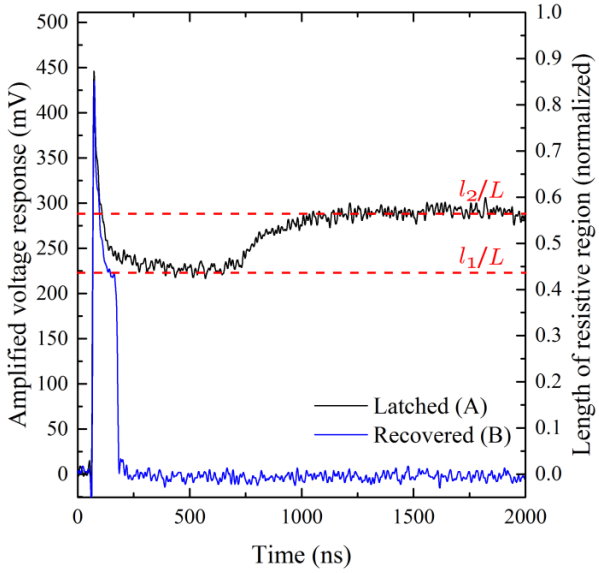

Figure 5.9: *Two voltage traces obained under identical setup conditions at 360 mK. The two traces lie either side of the border between latching and recovering behaviour and demonstrate the dynamics around the critical latching length,* l_1.

In figure 5.9 two voltage traces are shown which have very similar peak amplitudes. However, one trace recovered superconductivity while the other latched. It can be seen that the behaviour of the two traces diverge around the voltage 225 mV (the voltage identified as corresponding with the resistive region length l_1). The decay rate of both traces seems to be decreasing as the traces approach 225 mV. The latching trace stops decreasing, reaches a minimum value just above 225 mV and then, after a slow growth lasting several hundred nano-seconds the trace eventually settles around 290 mV. In contrast, trace (B) decays below 225 mV, at which point its decay rapidly accelerates and it fully recovers superconductivity.

5.1.6 Limitations of the analytical model

The analytical model described above manages to predict a great deal of the steady state dynamics of a short $NbSe_2$ photodetector. However there are several important dynamics that the model cannot take into account. The optical laser pulse which is absorbed by the the $NbSe_2$ is not described. Therefore, the model cannot predict the dynamics of the system with varying optical power or pulse duration. The model is also one dimensional and so it cannot be used to analyse the behaviour of the system until a few tens of nano-seconds after the laser pulse. The material properties used in the model were all assumed to be constant, temperature and state independent variables. These assumptions are unlikely to hold from 360 mK to temperatures exceeding T_c and so the model can only be stated to approximate the characteristics of the system.

To address these limitations, a computational model was developed which is described in the following section. The computational model solves the time dependent heat equation over a two dimensional space. It also includes a source term for the optical laser pulse and uses temperature dependent material properties to more accurately predict the system behaviour.

5.2 Computational modelling

The system will be modelled as two dimensional, therefore assuming that the $NbSe_2$ is sufficiently thin that temperature variations across its height can be neglected. Out of plane conduction to the substrate is also included in the model with the assumption that the substrate temperature remains constant at the ambient temperature, T_b. As in the analytical model, the metal electrodes in contact with the superconductor act as thermal heat sinks, maintaining the temperature at both ends of the strip at the ambient temperature, T_b.

The model will begin with the system at the ambient temperature, current biased and in the superconducting state. A laser pulse, which is modelled as Gaussian in both space and time, is then absorbed in the centre of the $NbSe_2$ strip, causing the temperature to locally rise and the current carrying capacity of that section to decrease. If the current capacity of any cross section of the strip is reduced below the bias current, that cross section will be deemed to have switched to the normal state which will cause a voltage drop and the generation of Joule

heating. Depending on bias conditions and the laser power, the system is capable of returning to the superconducting state or if the Joule heating is large enough, the resistive region can become self sustaining.

The heat equation which models the system is the following:

$$c\,\frac{dT}{dt} = \kappa\,\frac{d^2T}{dx^2} + \kappa\,\frac{d^2T}{dy^2} - \frac{\alpha}{d}\,(T - T_b) + P_J + P_L \tag{5.45}$$

Where: x and y are the distances from centre along the length (direction of current flow) and width (perpendicular to current flow) of the strip respectively, $P_J = J^2\,\rho$ is the power density of Joule heating and P_L is the power density of the Gaussian laser pulse.

To solve the heat equation numerically, the time and spatial derivatives are approximated using finite differences. The time and spatial variables are therefore discretised on a regular grid of points and the temperature distribution is evaluated at those grid points.

5.2.1 The Crank-Nicolson method for a 1D system

The finite difference technique that is used is called the Crank-Nicolson method [131]. This method is unconditionally stable and has second order accuracy for steps in both time and space. This section will describe how the Crank-Nicolson system can be used to solve a 1D problem. The following section will then describe how this method can be extended to a 2D problem.

Using subscript i and superscript n to index the grid steps in space and time respectively, the Crank-Nicolson method evaluates the temperature and its derivatives between time steps as:

$$T \approx \frac{T_i^n + T_i^{n+1}}{2} \tag{5.46}$$

$$\frac{dT}{dt} \approx \frac{T_i^{n+1} - T_i^n}{\Delta t} \tag{5.47}$$

$$\frac{d^2T}{dx^2} \approx \frac{T_{i+1}^n - 2\,T_i^n + T_{i-1}^n + T_{i+1}^{n+1} - 2\,T_i^{n+1} + T_{i-1}^{n+1}}{2\,(\Delta x)^2} \tag{5.48}$$

Therefore the 1D finite difference equation to be solved is:

$$\begin{aligned}\frac{c}{\Delta t}\left(T_i^{n+1} - T_i^n\right) = {} & \frac{\kappa}{2\,(\Delta x)^2}\left(T_{i+1}^n - 2\,T_i^n + T_{i-1}^n + T_{i+1}^{n+1} - 2\,T_i^{n+1} + T_{i-1}^{n+1}\right) \\ & - \frac{\alpha}{2\,d}\left(T_i^n + T_i^{n+1}\right) + \frac{\alpha\,T_b}{d} + P_J + P_L\end{aligned} \tag{5.49}$$

The above equation will be solved starting from time index $n = 0$, progressing forward in time. At $n = 0$, the temperature distribution will be constant throughout the system at temperature T_b. Therefore at all time indexes, the temperatures with index n will be known values and those with index $n + 1$ will need to be solved for.

Separating the unknown $n+1$ terms and labelling factors:

$$\begin{aligned} T_{i-1}^{n+1} \underbrace{\left(\frac{-\kappa\,\Delta t}{2\,c\,(\Delta x)^2}\right)}_{=A_i} + T_i^{n+1} \underbrace{\left(\frac{-\kappa\,\Delta t}{c\,(\Delta x)^2} + \frac{\alpha\,\Delta t}{2\,d\,c} + 1\right)}_{=B_i} + T_{i+1}^{n+1} \underbrace{\left(\frac{-\kappa\,\Delta t}{2\,c\,(\Delta x)^2}\right)}_{=C_i} \\ = \underbrace{T_i^n + \frac{\Delta t}{c}\left(\frac{-\kappa}{2\,(\Delta x)^2}\left(T_{i-1}^n - 2\,T_i^n + T_{i+1}^n\right) - \frac{\alpha}{2\,d}\,T_i^n + \frac{\alpha\,T_b}{d} + P_J + P_L\right)}_{=D_i} \end{aligned} \tag{5.50}$$

Using the above labelled factors (A_i, B_i, C_i and D_i), equation 5.50 can be written as the following matrix equation:

$$\begin{bmatrix} B_0 & C_0 & 0 & 0 & \cdots & 0 \\ A_1 & B_1 & C_1 & 0 & \cdots & 0 \\ 0 & A_2 & B_2 & C_2 & \cdots & 0 \\ 0 & 0 & A_3 & B_3 & \ddots & \vdots \\ \vdots & \vdots & \vdots & \ddots & \ddots & C_{I-1} \\ 0 & 0 & 0 & \cdots & A_I & B_I \end{bmatrix} \begin{bmatrix} T_0^{n+1} \\ T_1^{n+1} \\ T_2^{n+1} \\ \vdots \\ T_{I-1}^{n+1} \\ T_I^{n+1} \end{bmatrix} = \begin{bmatrix} D_0 \\ D_1 \\ D_2 \\ \vdots \\ D_{I-1} \\ D_I \end{bmatrix} \tag{5.51}$$

In equation, 5.51 the only unknown parameters are the temperatures at time step $n+1$. All other parameters can be evaluated using the known temperature distribution at time step n. Therefore, to calculate the T_i^{n+1} terms, we need to pre-multiply the D_i vector with the inverse of the above square matrix. In practice, the above matrix may be thousands of entries square and inverting such a large matrix via a general inversion technique would take prohibitively long to compute. However, the matrix is tri-diagonal i.e. all of the matrix elements are zero except for those along the central three diagonal bands. The matrix equation can therefore be solved far quicker than the general case by utilising Thomas' algorithm [132], see Appendix A.

By implementing appropriate boundary conditions, the above methods can be used to solve the 1D heat equation and calculate the evolution of the system with time.

5.2.2 Two dimensional systems

A two dimensional system will have heat conduction along both the x and y axes. Therefore the temperature change to any element over one time step will be dependent on that element's neighbours along both axes. Implementing the Crank-Nicolson scheme, whereby temperatures are averaged between time steps, means that to fully evaluate the conduction to one point would use a system of simultaneous equations having a total of ten different temperature grid points in each equation, with five of those temperatures being unknown at any time. Solving these implicit equations for both conduction directions simultaneously is a non-trivial exercise.

To make the 2D problem more tractable, the Alternating Direction Implicit (ADI) [133]

method was used. In the ADI method, heat conduction is evaluated in a two step process. In the first step, conduction along one of the axes (e.g. x) is evaluated explicitly using the temperature distribution at time index n while conduction along the second axis is evaluated implicitly at time index $n + 1/2$:

$$\frac{d^2T}{dx^2} + \frac{d^2T}{dy^2} \approx \frac{T^n_{i+1,\,j} - 2\,T^n_{i,\,j} + T^n_{i-1,\,j}}{\Delta x^2} + \frac{T^{n+1/2}_{i,\,j+1} - 2\,T^{n+1/2}_{i,\,j} + T^{n+1/2}_{i,\,j-1}}{\Delta y^2} \tag{5.52}$$

The evaluations given in equation 5.52 are inserted into the heat equation for the system (equation 5.45) along with evaluations for the laser heating, Joule heating and substrate conduction. Using the same method as for the 1D case, a matrix equation similar to equation 5.51 is produced for each grid step in x. Solving all the matrix equations produces the 2D temperature distribution at time step $n + 1/2$.

Then, in the second step of the ADI method, the process is repeated with the implicit and explicit directions swapped. The temperature derivatives are evaluated as the following:

$$\frac{d^2T}{dx^2} + \frac{d^2T}{dy^2} \approx \frac{T^{n+1}_{i+1,\,j} - 2\,T^{n+1}_{i,\,j} + T^{n+1}_{i-1,\,j}}{\Delta x^2} + \frac{T^{n+1/2}_{i,\,j+1} - 2\,T^{n+1/2}_{i,\,j} + T^{n+1/2}_{i,\,j-1}}{\Delta y^2} \tag{5.53}$$

A series of matrix equations are again formed, one equation for each grid point in the y direction. Solving the matrix equations produces the 2D temperature distribution at time step $n + 1$ as desired. Repeatedly applying these methods then allows the time evolution of a 2D system to be calculated.

5.2.3 Simulation parameters

Boundary Conditions

Boundary conditions need to be specified to determine the behaviour at the edges of the modelled grid space. In the x direction, both ends of the $NbSe_2$ are in contact with a relatively thick gold electrode. Therefore, just as in the analytical model, a Dirichlet boundary condition is used: at both x extremities ($i = 0$ and $i = I$) the temperature is held constant at the ambient temperature, T_b.

$$T^n_{0,\,j} = T_b \tag{5.54}$$

$$T^n_{I,\,j} = T_b \tag{5.55}$$

These conditions can be implemented by setting the values of the matrix elements to be the following, at the edges of the grid space:

$$A_{I,\,j} = 0; \tag{5.56}$$
$$B_{0,\,j} = 1; \tag{5.57}$$
$$B_{I,\,j} = 1; \tag{5.58}$$
$$C_{0,\,j} = 0; \tag{5.59}$$
$$D_{0,\,j} = T_b; \tag{5.60}$$
$$D_{I,\,j} = T_b; \tag{5.61}$$

At the y extremities, the situation is more complicated: The temperature at the edge of the $NbSe_2$ crystal should be able to change over time but there should be no thermal flux through the edge of the crystal. This can be accomplished by applying the Neumann boundary condition that the temperature gradient is zero at the edge.

$$\frac{dT(x,\,y,\,t)}{dy} = 0 \;\text{ for: } y = \pm\frac{w}{2} \tag{5.62}$$

To implement the above boundary condition, fictitious grid points were used. Fictitious grid points are points which lie outside of the true simulation domain. In this case, points one Δy step outside of the domain are created where the temperature is specified to be equal to that at one Δy step inside the edge. Therefore, the temperature gradient at the edge will be equal to zero.

$$T^n_{i,\,-1} = T^n_{i,\,1} \tag{5.63}$$
$$T^n_{i,\,J+1} = T^n_{i,\,J-1} \tag{5.64}$$

Material parameters

One of the advantages of using a computational model is that it becomes simple to use temperature and state dependent variables for the material parameters. This should enable the simulation to more accurately agree with measured data.

Volumetric heat capacity, $c(T)$, is temperature and state dependent as discussed in section 2.3.6. The heat capacity of superconducting $NbSe_2$ was studied extensively by C. J. Huang et al. [134]. The reported values of the electronic and phonon heat capacities were used in the simulations.

The cryogenic thermal conductivity, $\kappa(T)$, of bulk $NbSe_2$ was reported by E. Boaknin [135, 136] with a value $\kappa/T = 0.82\ \mathrm{WK^{-2}\ m^{-1}}$ at T_c. However, the samples measured by Boaknin displayed a resistivity approximately four times smaller than the samples measured here. It was found that the trend $\kappa/T = 0.5\ \mathrm{WK^{-2}\ m^{-1}}$ provided much better agreement and was used for the simulations. The discrepancy in resistivity and thermal conductivity values is most

likely due to the difference in bulk and few-layered samples.

Figure 5.10 shows the measured temperature dependence of I_c for sample 19 from 360 mK to T_c. This data was used to determine the current that each volume element in the simulation could support. To determine if a cross section is resistive, the current limits of each volume element in the cross section are summed, giving the critical current of the cross section. If the critical current of the cross section is less than the bias current, that cross section is determined to be resistive.

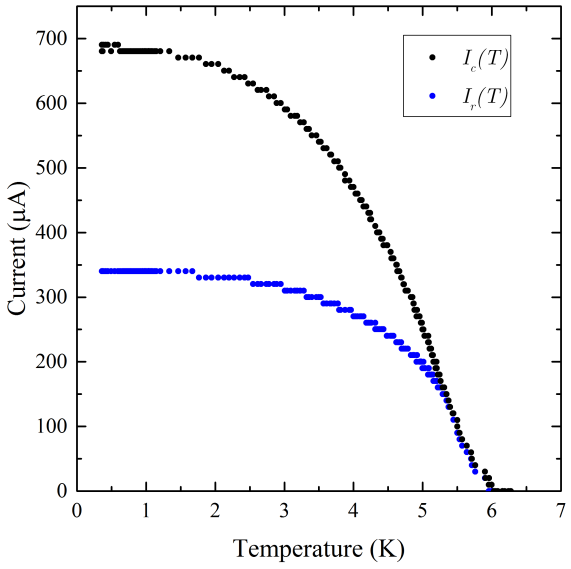

Figure 5.10: *The temperature dependence of I_c used in simulations of sample 19.*

If a cross-section of the superconductor is determined to be resistive, it will have a finite resistivity which is itself temperature dependent. The temperature dependence of $\rho(T)$ was estimated from electrical measurements and the dimensions of the $NbSe_2$ being simulated. For ambient temperatures near T_c the resistive transition is modelled as having finite width, in line with measurements. Below 3 K the transition is modelled as an immediate switch to the normal state resistance.

Optimisations

The simulation was typically ran with approximately 1×10^5 grid points over a 2D space and 1×10^6 time steps. Using the methods described above would require solving approximately 1×10^9 matrix equations of the form shown in equation 5.51. Performing these calculations would take a prohibitively long time, on the order of days, to compute. It was therefore necessary to optimise the calculation as much as possible.

The $NbSe_2$ strip was modelled as rectangular and the laser pulse was modelled with a 2D Gaussian distribution illuminating the centre of the strip. It is therefore possible to predict that the temperature distribution will at all times be symmetric about the x and y axes through the centre of the $NbSe_2$. Therefore, it is not necessary to fully calculate the temperature

distribution across the whole strip, instead only one quarter of the strip needs to be calculated. The temperature distribution in the other three quarters can simply be reflected from the result. This technique reduces the computational requirements by nearly a factor of four while not impacting the simulation accuracy at all.

The boundaries of the $NbSe_2$ strip are modelled as thermally insulating in the y axis and conductive in the x axis. Therefore, in the steady state, there may be heat flux in the x axis but no element in the simulation will have a steady state heat flux along the y axis. Therefore, the temperature distribution will in all cases tend towards becoming one dimensional and so at some point during the simulation, thermal conduction along the y axis will drop to negligible levels. At this point, there will be no need to continue to calculate conduction in the y axis and the simulation can be reduced to being 1D.

After the 2D temperature distribution is calculated for each time step, the temperature at the middle of an edge (0, $\frac{w}{2}$) is compared to the central element (0, 0). If the two temperatures differ by less than 10 mK, the temperature distribution is declared to be effectively one dimensional and so from that point on, a one dimensional Crank-Nicolson scheme is used. This typically occurs approximately 10-20 ns after the intensity peak of the laser pulse.

5.2.4 Simulation results

Initially the simulation was set up to replicate the behaviour of sample 19. Therefore the physical dimensions, resistance, critical temperature and critical current dependence of sample 19 were used. The laser pulse was modelled with a Gaussian intensity profile which peaked 20 ns after the start of the simulation.

Figure 5.10 a) shows the modelled temperature distribution with sample 19 under 370 µA bias current. The temperature distribution is shown at the times: 15 ns, 20 ns, 40 ns and 55 ns. From the same simulation, figure 5.10 b) shows the potential difference across the sample which develops as a result of laser heating and eventually decays as the sample returns to the superconducting state.

At 15 ns, the laser pulse has not yet reached maximum intensity but the centre of the $NbSe_2$ has been heated by the laser to over the critical temperature and is therefore not capable of carrying any resistance-free current. However, there is no voltage drop across the sample yet as the current is able to flow around the central hot region and be carried primarily at the edges of the strip.

At 20 ns, the laser pulse is at maximum intensity. The centre of the $NbSe_2$ has been heated far above T_c and the current can no longer be supported without resistance. Heat is now being generated by the laser and the resistive current and as a result the resistive region is expanding.

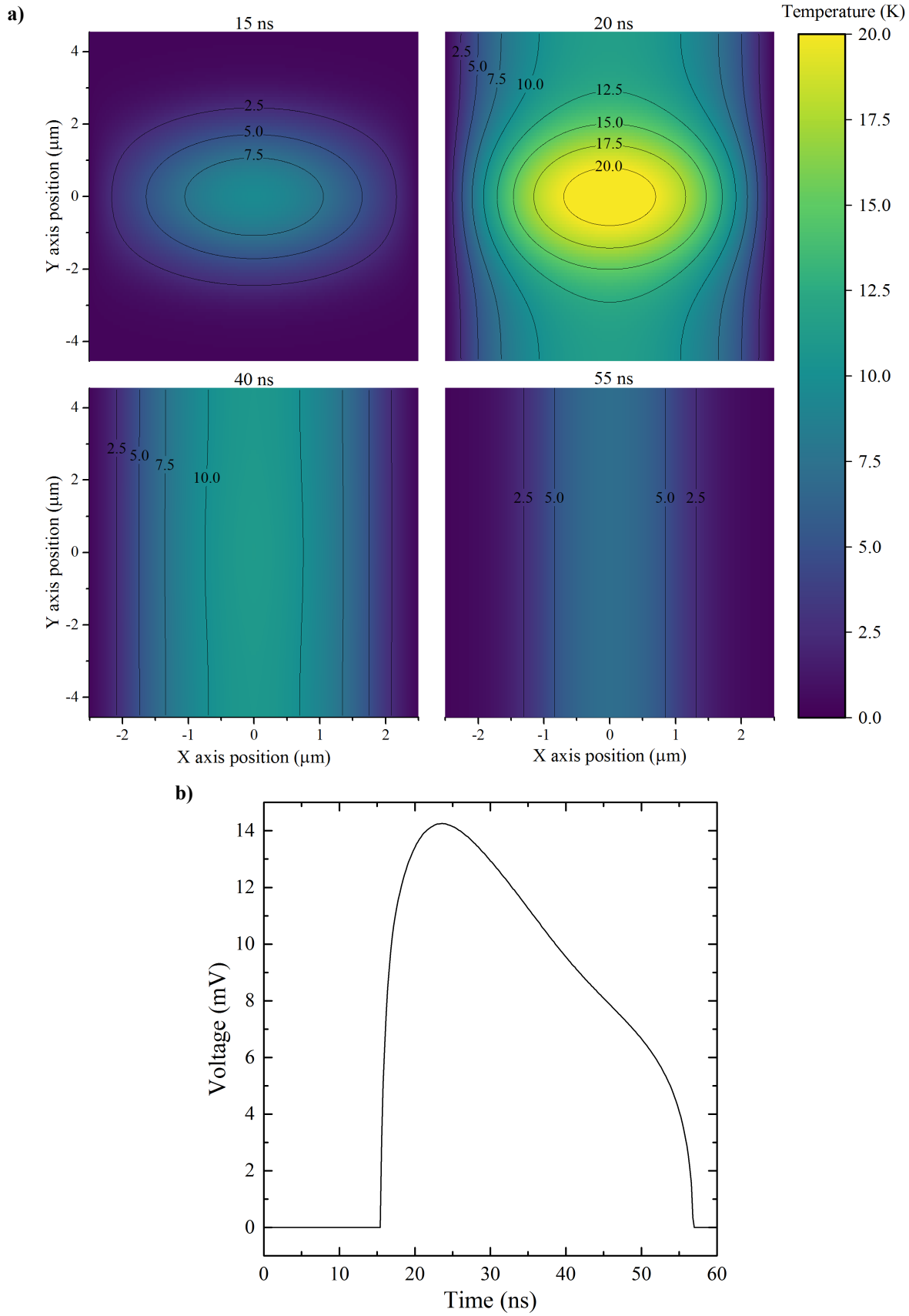

Figure 5.10: a) *Calculated 2D temperature distributions across sample 19, at the ambient temperature 360 mK and current biased at 370 µA. The temperature distribution is shown at 15 ns, 20 ns, 40 ns and 55 ns.* ***b)*** *The resulting voltage drop that is produced across the simulated device as a function of time. The voltage reaches a maximum shortly after the laser intensity peak and decays to zero as the device regains superconductivity.*

At 40 ns, the laser pulse is effectively over and heat conduction has removed most of the temperature variations along the width of the sample. The temperature distribution will continue to move towards becoming 1D and the simulation switches to a 1D calculation at the time 44.2 ns. Joule heating is continuing to heat the centre of the strip but it is not strong enough to overcome heat conduction and so the sample is cooling.

At 55 ns, the resistive region has decreased in length and the voltage across the sample has decreased to approximately 29% of its peak value. The sample is continuing to cool and will become fully superconducting at 56.8 ns.

The simulation was then set to emulate the behaviour of sample 19 with varying bias current. Figure 5.11 shows the measured data and simulated response of sample 19 from 260 µA to 400 µA. In the experiment, unattenuated laser pulses with nominal pulse width of 20 ns were used. In both experiment and simulation, the laser delivered 1.09 pJ per pulse.

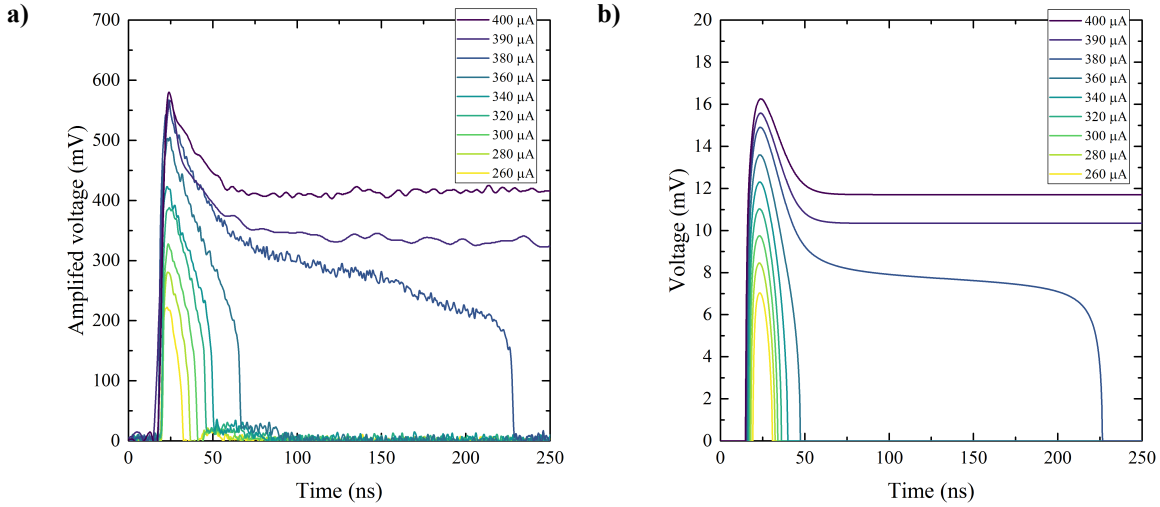

Figure 5.11: *Comparison between measured and simulated device response to illumination with varying bias current.* ***a)*** *Measured response.* ***b)*** *Simulated response.*

The measured and simulated voltage traces, shown in figure 5.11 a) and b) respectively, show very similar characteristics with varying bias current. In both cases the voltage peak and the decay time of the trace increases with bias current. At 380 µA the voltage traces decrease very slowly, falling to zero voltage approximately 200 ns after their peak. Beyond this current, the voltage traces no longer recover superconductivity but instead decay to a self-sustaining resistive state. The steady state voltage is seen to increase as the bias current is increased further.

The similarity between simulated and measured response is strong evidence that the simulation is accurately depicting the underlying behaviour of the system and demonstrating the cause of the detection mechanism in the fabricated $NbSe_2$ devices.

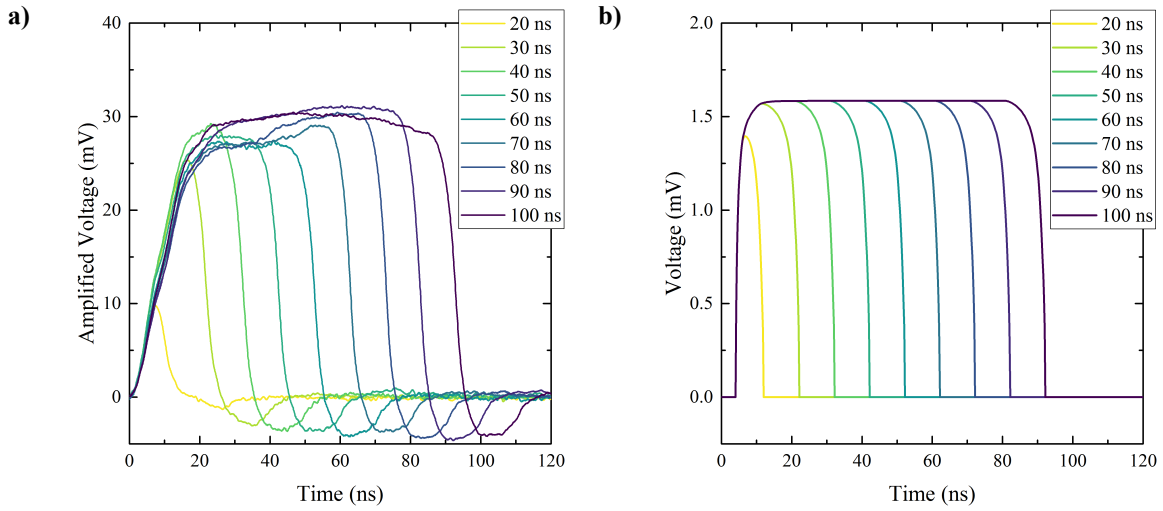

Figure 5.12: *Comparison between* ***a)*** *measured and* ***b)*** *simulated device response to illumination of varying laser pulse width.*

The material parameters within the simulation were then adjusted to match those of sample 20. The sample was modelled as a strip 3.3 µm long with a width of 740 nm. One of the interesting experiments performed on sample 20 was its response to illumination of varying pulse width (see section 4.4.2). Using a fixed bias current of 32 µA with an ambient temperature of 5.1 K the nominal laser pulse width was varied from 20 ns to 100 ns. The resulting voltage traces were observed to have a similar shape to the intensity profile of the applied laser pulses, becoming increasingly long and flat before decaying to zero as the laser pulse width was increased.

In the simulation, the time dependence of the laser intensity was modelled as a trapezium with a gradient and maximum intensity set so that the energy per pulse matched experimental values. This method allowed the laser pulse duration to be easily changed by extending the time of the flat section of the trapezium.

Setting the simulation parameters to match the experimental conditions, the voltage response of the device to varying laser pulse width was modelled. In figure 5.12 both the experimental and simulated device responses are shown. The model was able to reproduce voltage traces with similar characteristics to the experiment, with both measured and simulated data showing increasing voltage duration as the laser pulse width increases.

Some characteristics of the experimental data have not been reproduced by the simulation. The voltage measured experimentally is not as consistent as that shown in the simulations and it drops to negative values before decaying to zero. These characteristics are likely due to poor impedance matching between the electrical transmission line and the sample resulting in reflections, distortions and poor transmissions of the signal. The simulation is not capable of reproducing these effects as the biasing and amplification circuit has not been included in the model.

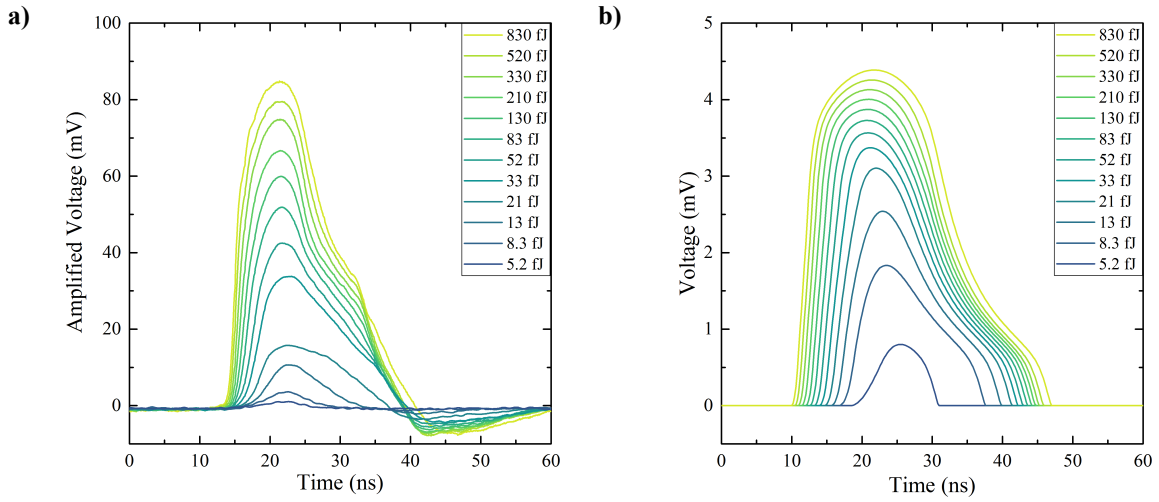

Figure 5.13: *Comparison between* ***a)*** *measured and* ***b)*** *simulated device response to illumination with current variation.*

Finally, it was investigated if the model could replicate the energy dependent response observed in the $NbSe_2$ devices. Figure 5.13 shows the measured and simulated response of sample 20 to pulsed illumination with varying laser attenuation. A bias current of 31 µA was used in both the experiment and simulation at 5.1 K.

The simulation was able to capture the characteristic behaviour observed experimentally with the signal amplitude and duration increasing with the laser pulse energy. In the simulations, the signal amplitude at low pulse energies grows faster than in the experiment, however the overall shape and duration of the voltage signals is extremely similar between experiment and simulation. At high laser energies, the simulation was able to replicate the slowing growth of the signal amplitude with an almost logarithmic dependence on energy in both cases.

5.3 Summary

In this chapter the thermal and electrical behaviour of $NbSe_2$ photodetectors have been studied analytically and with computational methods. The samples were modelled as being under vacuum with thermal conduction paths to both the substrate and gold electrodes. The analytical modelling was limited to viewing the system as being one dimensional; however it was able to explain many of the steady state dynamics that were observed experimentally. It predicts the existence of a minimum current (I_{latch}) which must be exceeded for self sustaining hotspots to be possible. It also can predict the length and therefore the voltage drop across a self-sustaining resistive region. The steady state behaviour is significantly different to that of a detector in the long-device limit, such as an SNSPD. The differences are explained due to the significant lateral heat flow in the system and a device length which is comparable to the thermal healing length (see figure 5.4).

The mathematical model was extended to 2D and the time evolution of the system was simulated computationally. Using computational methods allowed the system to be made much

more complex, introducing temperature and state dependence to the material parameters and modelling the incident laser with both space and time dependence. The temperature distribution evolves over time according to the heat equation with terms added to account for Joule heating and laser absorption. The assumption made in the analytical modelling, that the system will tend towards a 1D temperature distribution, was then shown to be accurate, with the system reducing to 1D approximately 10-20 ns after peak of the laser pulse.

Using the calculated temperature distribution and the measured temperature dependence of the superconducting critical current, the simulation is able to predict a time dependent voltage across the modelled device. The voltage output was compared with the outputs measured from two tested devices. This was done under: varying currents, varying laser power and varying laser pulse duration. The simulated data was overall in strong agreement with the trends that were observed experimentally. Higher energy laser pulses led to larger voltage outputs, longer laser pulses led to longer voltage outputs and the transition from recovering to latching pulses was accurately reproduced with varying current.

The strong agreement between experiment and simulation shows that the heat equation based model can accurately predict the observed phenomena. This provides evidence that the underlying dynamics of the system and the photodetection mechanism at play are well understood in this novel device architecture.

Chapter 6

Conclusions

6.1 Summary of thesis results

In this thesis, exfoliated $NbSe_2$ crystals were used as the superconducting element in novel photodetector designs. Experiments were conducted within a cryogenic optical testing system using a commercial pulse tube and ^{3}He sorption stage to reach a base temperature of 350 mK (see section 3.2). Coupling light to the detectors with a piezoelectric driven confocal microscope, the devices were shown to be sensitive to infrared light from 5 K down to 350 mK, representing the first demonstration of an exfoliated superconductor as an optical detector.

Few-layered $NbSe_2$ must be protected from degradation to maintain superconducting properties and several methods of protection were tested: limited exposure to atmosphere (section 4.2), graphene encapsulation (section 4.1) and hBN encapsulation (section 4.3). Of these methods, hBN encapsulation is the most promising as it is an insulator and therefore does not reduce the normal state resistance of the device however it necessitates the use of prepatterned electrical contacts which makes placement of the exfoliated samples more challenging.

Although there were variations in the device design, unexpected and largely consistent behaviour was observed. Hysteretic I-V profiles were measured, indicating that $NbSe_2$ is capable of carrying superconducting currents large enough to maintain a self-sustaining region [48]. This is a key characteristic which is required for signal amplification in SNSPD devices [137,138]. Unexpectedly however, the samples were found to have power dependent responses to illumination indicating that the whole device was not being driven to its normal state resistance.

A thermal model was developed to explain the origins of the device response. It showed that Joule heating would not drive the sample to be fully resistive, as is the case for long superconducting devices (see figure 5.4). Instead, at high currents, a time-stable resistive region can form with an intermediate resistance which is determined by the bias current (section 5.1.3).

This behaviour is due to the thermal healing length (η) being comparable to the device length so that conduction via the electrodes can maintain a significant proportion of the device in the superconducting state. It was also found that a region of significant size (l_1) needs to be resistive before the region becomes self-sustaining. Therefore, low intensity light will cause transient and power dependent signals like the ones measured in chapter 4.

A two-dimensional, computational model was developed to improve the accuracy of the device modelling and to verify that the observed phenomena can be predicted by a thermal model. The time dependent temperature distribution across a superconducting $NbSe_2$ strip was simulated under pulsed optical illumination and current bias. The resistance across the strip was calculated from the temperature distribution, allowing the potential difference across the device to be generated and compared with experimental measurements. The finite difference model was able to replicate many of the key characteristic behaviours that were observed experimentally: the time scale and shape of voltage signals were replicated accurately, showing a power dependent device response in the non-latching regime and an accurate transition to a latching regime as the current was increased.

Although single photon sensitivity was not achieved in the fabricated $NbSe_2$ devices, they are of a similar performance to graphene based hot electron bolometers and commercial photodiodes [1]. With improving device fabrication methods, it is likely that single photon sensitivity will soon be achieved in exfoliated 2D superconductors.

6.2 Improving device performance

6.2.1 Increasing sensitivity

It is likely that the gold contacts used throughout this project reduced the local superconducting order parameter via the proximity effect. It is therefore probable that the experimentally observed critical current was significantly less than the depairing current. This would have the effect of increasing the number of Cooper pairs that need to be broken before the device is driven resistive, thereby reducing the sensitivity of the device. It has been shown that micron width superconductors can be single-photon sensitive [49, 115, 139] but care must be taken in their design to achieve an experimental critical current which is a large fraction of the depairing current.

One method of achieving a high critical current density is to have the area where the contacts meet the crystal be significantly wider than a photosensitive constriction which is patterned into the superconductor. This ensures that the patterned constriction determines the experimental critical current and therefore light is coupled to the area with the highest critical current density.

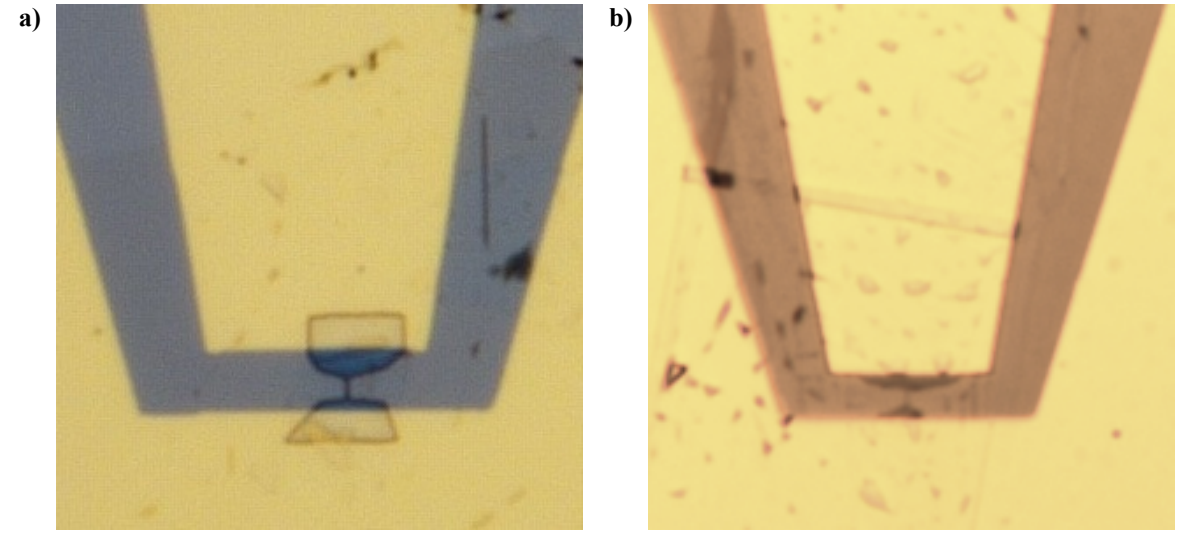

Figure 6.1: *Optical images of samples 25 and 26 which were patterened to have 150 nm width constrictions* ***a)*** *Sample 25.* ***b)*** *Sample 26.*

Samples 25 and 26 were fabricated with an etched constriction in their centre, as shown in figure 6.1. Unfortunately the constriction was made too thin (150 nm) and the devices did not display superconductivity when tested, instead showing low temperature resistances of 7.2 kΩ and 8.9 kΩ. The lack of superconductivity in the samples was probably caused by damage to the material during the etching process or by oxidation at the exposed edges after fabrication. In either case, a slightly wider constriction, e.g. 300 nm, would likely survive the fabrication and be capable of carrying a high current density.

Similarly, a superconducting metal (e.g. niobium or aluminium) could be used instead of gold to make contact with a thin $NbSe_2$ strip. This could cause an enhancement of the order parameter at the ends of the $NbSe_2$ thereby increasing the local critical current density compared to its centre. The use of superconducting contacts would have the secondary benefit of reducing heat conduction through the contacts.

Improvements to the measurement electronics could also increase the signal to noise ratio measured from the $NbSe_2$ devices. A cryogenic amplifier such as the Cosmic Microwave CITLF1 could be installed at the main stage of the pulse tube (approximately 5 K) which would reduce the noise of the system and allow lower amplitude voltage signals to be measured.

6.2.2 Improved optical coupling

As shown in section 3.3, the typical optical coupling efficiency for the tested $NbSe_2$ devices was approximately 5%. The optical losses are primarily due to poor coupling in the direction of propagation because the samples transmit rather than absorb most of the infrared light which is incident on them. However, it has been demonstrated that efficient coupling to 2D materials can be achieved though the use of Fabry-Pérot cavities [97, 140] and waveguide structures [141, 142]. Two dimensional materials are highly suited to integration with pho-

tonic circuits since the optical structures can be fabricated on a pristine substrate and the detector can then be deterministically placed at a later stage [143].

6.3 Recent developments and outlook

The field of 2D materials is rapidly developing and several research groups are pursuing their application as superconducting photodetectors. One such design which uses the small heat capacity of 2D materials is the graphene based Josephson junction [144]. The device functions as an optical detector by measuring a reduction in the switching current which flows across the junction when a photon is absorbed. Efficient optical coupling to such a device is a challenge however recently a graphene Josephson junction has been integrated with a resonator for efficient microwave detection [145].

The realisation of single photon sensitive, high T_c superconducting detectors has been attempted by several groups research groups previously [146–148]. However the superconducting properties of cuprates depend on optimum oxygen doping and it has proved difficult to fabricate high quality, thin films of such materials and then shape them into narrow wires without a reduced transition temperature.

Exfoliation of layered high temperature superconductors from bulk crystals provides a new method of fabricating nanoscale thickness films. $Bi_2Sr_2CaCu_2O_{8+\delta}$ (Bi-2212) has a bulk transition temperature of approximately 90 K and so a detector fabricated from it could be operated at liquid nitrogen temperatures (77 K) which would remove much of the cost and difficulty involved with SNSPD measurements.

It has recently been shown that monolayer Bi-2212 can be exfoliated to monolayer thickness without significant change to the superconducting critical temperature [149]. Prof. Efetov (ICFO, Spain) is leading a project aiming to use superconducting wires from exfoliated Bi-2212 as an optical detector [150]. An inert atmosphere is used to encapsulate the exfoliated superconductor and a focussed helium ion beam is used to pattern the wires which avoids the use of reactive ion etching [151]. If an efficient photon detector can be produced it would be a transformative technology enabling advancements in high temperature sensing applications such as LIDAR and remote gas sensing [152, 153].

2D superconductors are a novel material group which present challenges but offer unique characteristics and fabrication strategies unavailable to conventional materials. Single photon sensitivity in 2D materials will likely occur in the near future, enabling 2D materials to be used in quantum sensing applications such as: Bell inequality tests [154], quantum key distribution [155] and integrated quantum photonics [156].

Appendix A

Simulation details

The computational model described in section 5.2 was written in the coding language C++. C++ is a versatile language which is suited to efficient handling and mathematical manipulation of large quantities of data. The code was written using the C++ standard libraries, no code was copied from any other source. The code is relatively extensive at over 1000 lines long. A graphical user interface hasn't been written as it was not required. Instead, to implement changes, the code was simply modified and compiled into a new Windows compatible executable program.

The program outputs comma separated variable (extension '.csv') files containing the time varying voltage across the modelled device and optionally, the temperature distribution in the modelled space at set periods of time.

Thomas' algorithm

The program solves the time dependent heat equation by using the Crank-Nicolson method [131] as described in section 5.2.1. The tridiagonal matrix equation generated by the Crank-Nicolson method is then solved using Thomas' algorithm [132]. The equation to be solved (also shown in section 5.2.1) is:

$$\begin{bmatrix} B_0 & C_0 & 0 & 0 & \cdots & 0 \\ A_1 & B_1 & C_1 & 0 & \cdots & 0 \\ 0 & A_2 & B_2 & C_2 & \cdots & 0 \\ 0 & 0 & A_3 & B_3 & \ddots & \vdots \\ \vdots & \vdots & \vdots & \ddots & \ddots & C_{I-1} \\ 0 & 0 & 0 & \cdots & A_I & B_I \end{bmatrix} \begin{bmatrix} T_0^{n+1} \\ T_1^{n+1} \\ T_2^{n+1} \\ \vdots \\ T_{I-1}^{n+1} \\ T_I^{n+1} \end{bmatrix} = \begin{bmatrix} D_0 \\ D_1 \\ D_2 \\ \vdots \\ D_{I-1} \\ D_I \end{bmatrix} \tag{A.1}$$

To solve this equation, Thomas' algorithm first eliminates all A_i values from the equations and sets all $B_i = 1$. Starting with the first equation in the matrix (index $i = 0$) and progress-

ing, the process is the following:

From the boundary conditions ($B_0 = 1$ and $C_0 = 0$) the first line is already in the desired form and no further operations are required.

$$1 \cdot T_0^{n+1} = D_0 \tag{A.2}$$

The $i = 1$ line of the matrix equation can be written:

$$A_1\, T_0^{n+1} + B_1\, T_1^{n+1} + C_1\, T_2^{n+1} = D_1 \tag{A.3}$$

Eliminate the A_1 term by using the value T_0^{n+1} from equation A.2. The $i = 1$ line then becomes:

$$B_1\, T_1^{n+1} + C_1\, T_2^{n+1} = D_1 - A_1\, D_0 \tag{A.4}$$

Now divide all terms by B_1, giving the equation:

$$1 \cdot T_1^{n+1} + C_1'\, T_2^{n+1} = D_1' \tag{A.5}$$

where: $C_1' = \frac{C_1}{B_1}$ and $D_1' = \frac{D_1 - A_1\, D_0}{B_1}$

The $i = 1$ line of the matrix is now in the desired form. Using a similar method, the $i = 2$ line can be re-arranged to:

$$1 \cdot T_2^{n+1} + C_2'\, T_3^{n+1} = D_2' \tag{A.6}$$

where: $C_2' = \frac{C_2}{B_2 - A_2\, C_1'}$ and $D_2' = \frac{D_2 - A_2\, D_1'}{B_2 - A_2\, C_1'}$.

This method can be continued for the entire matrix, reducing equation A.1 to the form:

$$\begin{bmatrix} 1 & 0 & 0 & 0 & \cdots & 0 & 0 \\ 0 & 1 & C_1' & 0 & \cdots & 0 & 0 \\ 0 & 0 & 1 & C_2' & \cdots & 0 & 0 \\ 0 & 0 & 0 & 1 & \ddots & \vdots & \vdots \\ \vdots & \vdots & \vdots & \vdots & \ddots & C_{I-2}' & 0 \\ 0 & 0 & 0 & 0 & \cdots & 1 & C_{I-1}' \\ 0 & 0 & 0 & 0 & \cdots & 0 & 1 \end{bmatrix} \begin{bmatrix} T_0^{n+1} \\ T_1^{n+1} \\ T_2^{n+1} \\ \vdots \\ T_{I-2}^{n+1} \\ T_{I-1}^{n+1} \\ T_I^{n+1} \end{bmatrix} = \begin{bmatrix} D_0' \\ D_1' \\ D_2' \\ \vdots \\ D_{I-2}' \\ D_{I-1}' \\ D_I' \end{bmatrix} \tag{A.7}$$

Written in the form shown in equation A.7, it is simple to solve the equation to obtain the temperature values. From the final line of the above matrix, $T_I^{n+1} = D_I'$. This value can be inserted into the penultimate line to obtain the adjacent temperature (T_{I-1}^{n+1}), then this value can be used to solve for T_{I-2}^{n+1} and so on, until all temperatures have been calculated.

Thomas' algorithm can be written in only a dozen or so lines of code. The C++ code used to implement the algorithm, modified slightly for readability, is shown below:

```
// first line of matrix
Cp[0] = 0;
Dp[0] = D[0];
Temp[0] = Tb;

// loop which calculates C’ and D’ values.
for (int i = 1; i != I + 1; i++)
{
        Cp[i] = C[i] / (B[i] - A[i] * Cp[i - 1]);
        Dp[i] = (D[i] - A[i] * Dp[i - 1]) / (B[i] - A[i] * Cp[i - 1]);
}

// back substitution
Temp[I] = Dp[I];
for (int i = I - 1; i != 0; i- -)
{
        Temp[i] = Dp[i] - Cp[i] * Temp[i + 1];
}
```

Appendix B

Presentations and publications

- G. J. Orchin, D. de Fazio, A. C. Ferrari and R. H. Hadfield. Nano-Optical Characterization of Superconducting $NbSe_2$. *Superconductors-based sensors and quantum technologies*, Moscow, April 2016. (Oral presentation)
- J. Paul, G. J. Orchin, R. M. Heath, B. Slater, U. Nasti, K. Erotokritou, S. Miki, H. Terai, M. Sorel, D. Sahin, J. Barreto and R. H. Hadfield. Integrated Superconducting Nanowire Single Photon Detectors for Scalable Silicon Quantum Photonics. *Engineering Quantum Photonic Technologies Event*, London, May 2019. (Poster presentation)
- G. J. Orchin, D. De Fazio, A. Di Bernardo, M. Hamer, D. Yoon, A. R. Cadore, I. Goykhman, K. Watanabe, T. Taniguchi, J. W. A. Robinson, R. V. Gorbachev, A. C. Ferrari, and R. H. Hadfield. Niobium diselenide superconducting photodetectors. *Applied Physics Letters*, 114(25):251103, June 2019. (Journal article)
- G. J. Orchin, J. Paul, U. Nasti, K. Erotokritou, M. Sorel, R. M. Heath, B. Slater, D. Sahin, J. Barreto, M. Thompson and R. H. Hadfield. Integrated Superconducting Nanowire Single Photon Detectors for Scalable Silicon Quantum Photonics. *European Conference on Applied Superconductivity*, Glasgow, September 2019. (Poster presentation)
- G. J. Orchin, D. De Fazio, A. Di Bernardo, M. Hamer, D. Yoon, A. R. Cadore, I. Goykhman, K. Watanabe, T. Taniguchi, J. W. A. Robinson, R. V. Gorbachev, A. C. Ferrari, and R. H. Hadfield. Niobium diselenide superconducting photodetectors. *Superconducting Quantum Devices*, Glasgow, September 2019. (Poster presentation)

Bibliography

[1] G. J. Orchin, D. De Fazio, A. Di Bernardo, M. Hamer, D. Yoon, A. R. Cadore, I. Goykhman, K. Watanabe, T. Taniguchi, J. W. A. Robinson, R. V. Gorbachev, A. C. Ferrari, and R. H. Hadfield. Niobium diselenide superconducting photodetectors. *Applied Physics Letters*, 114(25):251103, June 2019.

[2] K. S. Novoselov, D. Jiang, F. Schedin, T. J. Booth, V. V. Khotkevich, S. V. Morozov, and A. K. Geim. Two-dimensional atomic crystals. *Proceedings of the National Academy of Sciences*, 102(30):10451–10453, July 2005.

[3] C. R. Dean, A. F. Young, I. Meric, C. Lee, L. Wang, S. Sorgenfrei, K. Watanabe, T. Taniguchi, P. Kim, K. L. Shepard, and J. Hone. Boron nitride substrates for high-quality graphene electronics. *Nature Nanotechnology*, 5(10):722–726, 2010.

[4] H. J. Conley, B. Wang, J. I. Ziegler, R. F. Haglund, S. T. Pantelides, and K. I. Bolotin. Bandgap engineering of strained monolayer and bilayer MoS_2. *Nano Letters*, 13(8):3626–3630, 2013.

[5] S. Larentis, B. Fallahazad, and E. Tutuc. Field-effect transistors and intrinsic mobility in ultra-thin $MoSe_2$ layers. *Applied Physics Letters*, 101(22):223104, November 2012.

[6] Y. Saito, T. Nojima, and Y. Iwasa. Highly crystalline 2D superconductors. *Nature Reviews Materials*, 2(1):16094, 2016.

[7] F. H. L. Koppens, T. Mueller, P. Avouris, A. C. Ferrari, M. S. Vitiello, and M. Polini. Photodetectors based on graphene, other two-dimensional materials and hybrid systems. *Nature Nanotechnology*, 9(10):780–793, October 2014.

[8] A. Branny, S. Kumar, R. Proux, and B. D. Gerardot. Deterministic strain-induced arrays of quantum emitters in a two-dimensional semiconductor. *Nature Communications*, 8(May):1–7, 2017.

[9] F. Bonaccorso, Z. Sun, T. Hasan, and A. C. Ferrari. Graphene photonics and optoelectronics. *Nature Photonics*, 4(9):611–622, August 2010.

[10] Y. Zhang, T.-T. Tang, C. Girit, Z. Hao, M. C. Martin, A. Zettl, M. F. Crommie, Y. R. Shen, and F. Wang. Direct observation of a widely tunable bandgap in bilayer graphene. *Nature*, 459(7248):820–3, June 2009.

[11] K. S. Novoselov and A. H. Castro Neto. Two-dimensional crystals-based heterostructures: materials with tailored properties. *Physica Scripta*, T146:014006, 2012.

[12] M. S. El-Bana, D. Wolverson, S. Russo, G. Balakrishnan, D. M. Paul, and S. J. Bending. Superconductivity in two-dimensional $NbSe_2$ field effect transistors. *Superconductor Science and Technology*, 26(12):125020, December 2013.

[13] X. Xi, Z. Wang, W. Zhao, J. H. Park, K. T. Law, H. Berger, L. Forró, J. Shan, and K. F. Mak. Ising pairing in superconducting $NbSe_2$ atomic layers. *Nature Physics*, 12(2):139–143, 2016.

[14] W.-H. Zhang, Y. Sun, J.-S. Zhang, F.-S. Li, M.-H. Guo, Y.-F. Zhao, H.-M. Zhang, J.-P. Peng, Y. Xing, H.-C. Wang, T. Fujita, A. Hirata, Z. Li, H. Ding, C. Tang, M. Wang, Q.-Y. Wang, K. He, S.-H. Ji, X. Chen, J.-F. Wang, Z.-C. Xia, L. Li, Y.-Y. Wang, J. Wang, L.-L. Wang, M.-W. Chen, Q.-K. Xue, and X.-C. Ma. Direct Observation of High-Temperature Superconductivity in One-Unit-Cell FeSe Films. *Chinese Physics Letters*, 31(1):017401, 2014.

[15] G. Li, A. Luican, J. M. Lopes Dos Santos, A. H. Castro Neto, A. Reina, J. Kong, and E. Y. Andrei. Observation of Van Hove singularities in twisted graphene layers. *Nature Physics*, 6(2):109–113, 2010.

[16] X. L. Huang, J. Chai, T. Jiang, Y. J. Wei, G. Chen, W. Q. Liu, D. Han, L. Niu, L. Wang, and X. B. Zhang. Self-assembled large-area $Co(OH)_2$ nanosheets/ionic liquid modified graphene heterostructures toward enhanced energy storage. *Journal of Materials Chemistry*, 22(8):3404–3410, 2012.

[17] S. J. Haigh, A. Gholinia, R. Jalil, S. Romani, L. Britnell, D. C. Elias, K. S. Novoselov, L. A. Ponomarenko, A. K. Geim, and R. Gorbachev. Cross-sectional imaging of individual layers and buried interfaces of graphene-based heterostructures and superlattices. *Nature Materials*, 11(9):764–767, 2012.

[18] E. M. Alexeev, D. A. Ruiz-Tijerina, M. Danovich, M. J. Hamer, D. J. Terry, P. K. Nayak, S. Ahn, S. Pak, J. Lee, J. I. Sohn, M. R. Molas, M. Koperski, K. Watanabe, T. Taniguchi, K. S. Novoselov, R. V. Gorbachev, H. S. Shin, V. I. Fal'ko, and A. I. Tartakovskii. Resonantly hybridized excitons in moiré superlattices in van der Waals heterostructures. *Nature*, 567(7746):81–86, 2019.

[19] M. Tinkham. *Introduction to Superconductivity: Second Edition*. Dover Publications, 2004.

[20] C. P. Poole, H. A. Farach, R. J. Creswick, and R. Prozorov. *Superconductivity*. Elsevier, Amsterdam, 2nd edition, 2007.

[21] V. L. Ginzburg and L. D. Landau. On the Theory of Superconductivity. In *Collected Papers of L.D. Landau*, pages 546–568. Elsevier, 1965.

[22] S. M. Anlage, H. J. Snortland, and M. R. Beasley. A current controlled variable delay superconducting transmission line. *IEEE Transactions on Magnetics*, 25(2):1388–1391, 1989.

[23] J. R. Clem and V. G. Kogan. Kinetic impedance and depairing in thin and narrow superconducting films. *Physical Review B - Condensed Matter and Materials Physics*, 86(17):1–16, 2012.

[24] A. J. Kerman, E. A. Dauler, J. K. W. Yang, K. M. Rosfjord, V. Anant, K. K. Berggren, G. N. Gol'tsman, and B. M. Voronov. Constriction-limited detection efficiency of superconducting nanowire single-photon detectors. *Applied Physics Letters*, 90(10):101110, March 2007.

[25] A. A. Abrikosov. On the Magnetic Properties of Superconductors of the Second Group. *Soviet Physics Jetp*, 5(6):1174–1182, 1957.

[26] L. N. Cooper. Bound electron pairs in a degenerate fermi gas. *Physical Review*, 104(4):1189–1190, 1956.

[27] J. Bardeen, L. N. Cooper, and J. R. Schrieffer. Microscopic Theory of Superconductivity. *Physical Review*, 106(1):162–164, April 1957.

[28] J. Bardeen, L. N. Cooper, and J. R. Schrieffer. Theory of Superconductivity. *Physical Review*, 108(5):1175–1204, December 1957.

[29] L. P. Gor'kov. Microscopic derivation of the Ginzburg-Landau equations in the theory of superconductivity. *Soviet Physics JETP-USSR*, 9(6):1364–1367, 1959.

[30] M. Dressel. Electrodynamics of Metallic Superconductors. *Advances in Condensed Matter Physics*, 2013:1–25, 2013.

[31] C. M. Natarajan, M. G. Tanner, and R. H. Hadfield. Superconducting nanowire single-photon detectors: physics and applications. *Superconductor Science and Technology*, 25(6):063001, June 2012.

[32] J. Wu, L. You, S. Chen, H. Li, Y. He, C. Lv, Z. Wang, and X. Xie. Improving the timing jitter of a superconducting nanowire single-photon detection system. *Appl. Opt.*, 56(8):2195–2200, 2017.

[33] V. Shcheslavskiy, P. Morozov, A. Divochiy, Y. Vakhtomin, K. Smirnov, and W. Becker. Ultrafast time measurements by time-correlated single photon counting coupled with superconducting single photon detector. *Review of Scientific Instruments*, 87(5):053117, May 2016.

[34] W. Pernice, C. Schuck, O. Minaeva, M. Li, G. Goltsman, A. Sergienko, and H. Tang. High-speed and high-efficiency travelling wave single-photon detectors embedded in nanophotonic circuits. *Nature Communications*, 3(1):1325, January 2012.

[35] F. Marsili, V. B. Verma, J. A. Stern, S. Harrington, A. E. Lita, T. Gerrits, I. Vayshenker, B. Baek, M. D. Shaw, R. P. Mirin, and S. W. Nam. Detecting single infrared photons with 93% system efficiency. *Nature Photonics*, 7(3):210–214, February 2013.

[36] V. B. Verma, B. Korzh, F. Bussières, R. D. Horansky, S. D. Dyer, A. E. Lita, I. Vayshenker, F. Marsili, M. D. Shaw, H. Zbinden, R. P. Mirin, and S. W. Nam. High-efficiency superconducting nanowire single-photon detectors fabricated from MoSi thin-films. *Optics Express*, 23(26):33792, 2015.

[37] W. J. Zhang, L. X. You, H. Li, J. Huang, C. L. Lv, L. Zhang, X. Y. Liu, J. J. Wu, Z. Wang, and X. M. Xie. NbN superconducting nanowire single photon detector with efficiency over 90% at 1550 nm wavelength operational at compact cryocooler temperature. *Science China: Physics, Mechanics and Astronomy*, 60(12), 2017.

[38] L. Zhang, L. You, D. Liu, W. Zhang, L. Zhang, X. Liu, J. Wu, Y. He, C. Lv, Z. Wang, and X. Xie. Characterization of superconducting nanowire single-photon detector with artificial constrictions. *AIP Advances*, 4(6):067114, June 2014.

[39] A. N. Zotova and D. Y. Vodolazov. Photon detection by current-carrying superconducting film: A time-dependent Ginzburg-Landau approach. *Physical Review B - Condensed Matter and Materials Physics*, 85(2):1–9, 2012.

[40] A. Engel, J. Lonsky, X. Zhang, and A. Schilling. Detection mechanism in SNSPD: Numerical results of a conceptually simple, yet powerful detection model. *IEEE Transactions on Applied Superconductivity*, 25(3), 2015.

[41] Y. Korneeva, M. Sidorova, A. Semenov, S. Krasnosvobodtsev, K. Mitsen, A. Korneev, G. Chulkova, and G. Goltsman. Comparison of hot spot formation in NbC and NbN single photon detectors. *IEEE Transactions on Applied Superconductivity*, 26(3):1–1, 2016.

[42] G. N. Gol'tsman, O. Okunev, G. Chulkova, A. Lipatov, A. Semenov, K. Smirnov, B. Voronov, A. Dzardanov, C. Williams, and R. Sobolewski. Picosecond superconducting single-photon optical detector. *Applied Physics Letters*, 79(6):705–707, August 2001.

[43] R. Lusche, A. Semenov, K. Ilin, M. Siegel, Y. Korneeva, A. Trifonov, A. Korneev, G. Goltsman, D. Vodolazov, and H. W. Hübers. Effect of the wire width on the intrinsic detection efficiency of superconducting-nanowire single-photon detectors. *Journal of Applied Physics*, 116(4), 2014.

[44] A. Semenov, A. Engel, H.-W. Hübers, K. Il'in, and M. Siegel. Spectral cut-off in the efficiency of the resistive state formation caused by absorption of a single-photon in current-carrying superconducting nano-strips. *The European Physical Journal B*, 47(4):495–501, October 2005.

[45] L. N. Bulaevskii, M. Graf, and V. G. Kogan. Vortex-assisted photon counts and their magnetic field dependence in single-photon superconducting detectors. *Physical Review B - Condensed Matter and Materials Physics*, 85(1):014505–10, 2012.

[46] A. Engel and A. Schilling. Numerical analysis of detection-mechanism models of superconducting nanowire single-photon detector. *Journal of Applied Physics*, 114(21), 2013.

[47] J. J. Renema, R. Gaudio, Q. Wang, Z. Zhou, A. Gaggero, F. Mattioli, R. Leoni, D. Sahin, M. J. A. De Dood, A. Fiore, and M. P. Van Exter. Experimental test of theories of the detection mechanism in a nanowire superconducting single photon detector. *Physical Review Letters*, 112(11):1–5, 2014.

[48] W. J. Skocpol, M. R. Beasley, and M. Tinkham. Self-heating hotspots in superconducting thin-film microbridges. *Journal of Applied Physics*, 45(9):4054–4066, September 1974.

[49] Y. P. Korneeva, D. Y. Vodolazov, A. V. Semenov, I. N. Florya, N. Simonov, E. Baeva, A. A. Korneev, G. N. Goltsman, and T. M. Klapwijk. Optical Single-Photon Detection in Micrometer-Scale NbN Bridges. *Physical Review Applied*, 9(6):64037, 2018.

[50] S. Miki, M. Takeda, M. Fujiwara, M. Sasaki, A. Otomo, and Z. Wang. Superconducting NbTiN Nanowire Single Photon Detectors with Low Kinetic Inductance. *Applied Physics Express*, 2(7):075002, June 2009.

[51] M. Caloz, M. Perrenoud, C. Autebert, B. Korzh, M. Weiss, C. Schönenberger, R. J. Warburton, H. Zbinden, and F. Bussières. High-detection efficiency and low-timing jitter with amorphous superconducting nanowire single-photon detectors. *Applied Physics Letters*, 112(6):061103, February 2018.

[52] J. Li, R. A. Kirkwood, L. J. Baker, D. Bosworth, K. Erotokritou, A. Banerjee, R. M. Heath, C. M. Natarajan, Z. H. Barber, M. Sorel, and R. H. Hadfield. Nano-optical single-photon response mapping of waveguide integrated molybdenum silicide (MoSi) superconducting nanowires. *Optics Express*, 24(13):13931, June 2016.

[53] V. B. Verma, A. E. Lita, M. R. Vissers, F. Marsili, D. P. Pappas, R. P. Mirin, and S. W. Nam. Superconducting nanowire single photon detectors fabricated from an amorphous $Mo_{0.75}Ge_{0.25}$thin film. *Applied Physics Letters*, 105(2):022602, July 2014.

[54] J. Baselmans. Kinetic Inductance Detectors. *Journal of Low Temperature Physics*, 167(3-4):292–304, May 2012.

[55] S. McHugh, B. A. Mazin, B. Serfass, S. Meeker, K. O'Brien, R. Duan, R. Raffanti, and D. Werthimer. A readout for large arrays of microwave kinetic inductance detectors. *Review of Scientific Instruments*, 83(4):044702, April 2012.

[56] S. J. C. Yates, A. M. Baryshev, J. J. A. Baselmans, B. Klein, and R. Güsten. Fast Fourier transform spectrometer readout for large arrays of microwave kinetic inductance detectors. *Applied Physics Letters*, 95(4):042504, July 2009.

[57] J. Van Rantwijk, M. Grim, D. Van Loon, S. Yates, A. Baryshev, and J. Baselmans. Multiplexed Readout for 1000-Pixel Arrays of Microwave Kinetic Inductance Detectors. *IEEE Transactions on Microwave Theory and Techniques*, 64(6):1876–1883, 2016.

[58] P. K. Day, H. G. LeDuc, B. A. Mazin, A. Vayonakis, and J. Zmuidzinas. A broadband superconducting detector suitable for use in large arrays. *Nature*, 425(6960):817–821, October 2003.

[59] P. R. Maloney, N. G. Czakon, P. K. Day, T. P. Downes, R. Duan, J. Gao, J. Glenn, S. R. Golwala, M. I. Hollister, H. G. LeDuc, B. A. Mazin, S. G. McHugh, O. Noroozian, H. T. Nguyen, J. Sayers, J. A. Schlaerth, S. Siegel, J. E. Vaillancourt, A. Vayonakis, P. Wilson, and J. Zmuidzinas. MUSIC for sub/millimeter astrophysics. In W. S. Holland and J. Zmuidzinas, editors, *Proc. of SPIE*, volume 7741, page 77410F, July 2010.

[60] J. Bueno, O. Yurduseven, S. J. C. Yates, N. Llombart, V. Murugesan, D. J. Thoen, A. M. Baryshev, A. Neto, and J. J. A. Baselmans. Photon noise limited performance over an octave of bandwidth of kinetic inductance detectors for sub-millimeter astronomy. In *2016 41st International Conference on Infrared, Millimeter, and Terahertz waves (IRMMW-THz)*, pages 1–2. IEEE, September 2016.

[61] A. E. Hofmann. *Microwave Kinetic Inductance Detectors*. Doctoral thesis, California Institute of Technology, 2004.

[62] S. Doyle, P. Mauskopf, J. Zhang, S. Withington, D. Goldie, D. Glowacka, A. Monfardini, L. Swenson, and M. Roesch. Optimisation of lumped element kinetic inductance detectors for use in ground based mm and sub-mm arrays. *AIP Conference Proceedings*, 1185(2009):156–159, 2009.

[63] P. D. Mauskopf, S. Doyle, P. Barry, S. Rowe, A. Bidead, P. A. Ade, C. Tucker, E. Castillo, A. Monfardini, J. Goupy, and M. Calvo. Photon-noise limited performance in aluminum LEKIDs. *Journal of Low Temperature Physics*, 176(3-4):545–552, 2014.

[64] A. J. Miller, A. E. Lita, B. Calkins, I. Vayshenker, S. M. Gruber, and S. W. Nam. Compact cryogenic self-aligning fiber-to-detector coupling with losses below one percent. *Optics Express*, 19(10):9102, 2011.

[65] J. N. Ullom and D. A. Bennett. Review of superconducting transition-edge sensors for x-ray and gamma-ray spectroscopy. *Superconductor Science and Technology*, 28(8):084003, 2015.

[66] K. D. Irwin, G. C. Hilton, D. A. Wollman, and J. M. Martinis. Xray detection using a superconducting transition edge sensor microcalorimeter with electrothermal feedback. *Applied Physics Letters*, 69(13):1945–1947, September 1996.

[67] A. Peacock, P. Verhoeve, N. Rando, A. van Dordrecht, B. G. Taylor, C. Erd, M. A. C. Perryman, R. Venn, J. Howlett, D. J. Goldie, J. Lumley, and M. Wallis. Single optical photon detection with a superconducting tunnel junction. *Nature*, 381(6578):135–137, May 1996.

[68] T. Peacock, P. Verhoeve, N. Rando, C. Erd, M. Bavdaz, B. G. Taylor, and D. Perez. Recent developments in superconducting tunnel junctions for ultraviolet, optical & near infrared astronomy. *Astronomy and Astrophysics Supplement Series*, 127(3):497–504, February 1998.

[69] P. H. Lv, G. F. Wang, Y. Wan, J. Liu, Q. Liu, and F. C. Ma. Bibliometric trend analysis on global graphene research. *Scientometrics*, 88:399–419, 2011.

[70] A. K. Geim. Graphene: Status and Prospects. *Science*, 324(June):1530–1534, 2009.

[71] F. Xia, T. Mueller, Y.-M. Lin, A. Valdes-Garcia, and P. Avouris. Ultrafast graphene photodetector. *Nature nanotechnology*, 4(12):839–43, December 2009.

[72] A. Pospischil, M. Humer, M. M. Furchi, D. Bachmann, R. Guider, T. Fromherz, and T. Mueller. CMOS-compatible graphene photodetector covering all optical communication bands. *Nature Photonics*, 7(11):892–896, November 2013.

[73] T. J. Echtermeyer, L. Britnell, P. K. Jasnos, A. Lombardo, R. V. Gorbachev, A. N. Grigorenko, A. K. Geim, A. C. Ferrari, and K. S. Novoselov. Strong plasmonic enhancement of photovoltage in graphene. *Nature communications*, 2:458, 2011.

[74] B. S. Karasik, C. B. McKitterick, and D. E. Prober. Prospective performance of graphene HEB for ultrasensitive detection of sub-mm radiation. *Journal of Low Temperature Physics*, 176:249–254, 2014.

[75] X. Cai, A. B. Sushkov, R. J. Suess, M. M. Jadidi, G. S. Jenkins, L. O. Nyakiti, R. L. Myers-Ward, S. Li, J. Yan, D. K. Gaskill, T. E. Murphy, H. D. Drew, and M. S. Fuhrer. Sensitive room-temperature terahertz detection via the photothermoelectric effect in graphene. *Nature Nanotechnology*, 9(10):814–819, 2014.

[76] B. S. Karasik, C. B. McKitterick, T. J. Reck, and D. E. Prober. Normal-Metal Hot-Electron Nanobolometer With Johnson Noise Thermometry Readout. *IEEE Transactions on Terahertz Science and Technology*, 5(1):1–6, 2014.

[77] F. Schwierz. Graphene transistors. *Nature nanotechnology*, 5(7):487–96, July 2010.

[78] K. S. Novoselov, A. K. Geim, S. V. Morozov, D. Jiang, M. I. Katsnelson, I. V. Grigorieva, S. V. Dubonos, and A. A. Firsov. Two-dimensional gas of massless Dirac fermions in graphene. *Nature*, 438(7065):197–200, November 2005.

[79] K. F. Mak, M. Y. Sfeir, Y. Wu, C. H. Lui, J. A. Misewich, and T. F. Heinz. Measurement of the Optical Conductivity of Graphene. *Physical Review Letters*, 101(19):196405, November 2008.

[80] K. S. Novoselov, A. K. Geim, S. V. Morozov, D. Jiang, Y. Zhang, S. V. Dubonos, I. V. Grigorieva, and A. A. Firsov. Electric field effect in atomically thin carbon films. *Science (New York, N.Y.)*, 306(5696):666–669, 2004.

[81] A. Aparecido-Ferreira, H. Miyazaki, S.-L. Li, K. Komatsu, S. Nakaharai, and K. Tsukagoshi. Enhanced current-rectification in bilayer graphene with an electrically tuned sloped bandgap. *Nanoscale*, 4(24):7842–6, December 2012.

[82] M. C. Lemme, F. H. L. Koppens, A. L. Falk, M. S. Rudner, H. Park, L. S. Levitov, and C. M. Marcus. Gate-activated photoresponse in a graphene p-n junction. *Nano Letters*, 11(10):4134–4137, 2011.

[83] N. M. Gabor, J. C. W. Song, Q. Ma, N. L. Nair, T. Taychatanapat, K. Watanabe, T. Taniguchi, L. S. Levitov, and P. Jarillo-Herrero. Hot Carrier-Assisted Intrinsic Photoresponse in Graphene. *Science*, 334(6056):648–652, November 2011.

[84] J. C. W. Song, M. S. Rudner, C. M. Marcus, and L. S. Levitov. Hot carrier transport and photocurrent response in graphene. *Nano Letters*, 11(11):4688–4692, 2011.

[85] M. Freitag, T. Low, and P. Avouris. Increased responsivity of suspended graphene photodetectors. *Nano Letters*, 13(4):1644–1648, 2013.

[86] G. Giovannetti, P. Khomyakov, G. Brocks, V. Karpan, J. van den Brink, and P. Kelly. Doping Graphene with Metal Contacts. *Physical Review Letters*, 101(2):026803, July 2008.

[87] T. Mueller, F. Xia, M. Freitag, J. Tsang, and P. Avouris. Role of contacts in graphene transistors: A scanning photocurrent study. *Physical Review B - Condensed Matter and Materials Physics*, 79(24):1–22, 2009.

[88] E. J. H. Lee, K. Balasubramanian, R. T. Weitz, M. Burghard, and K. Kern. Contact and edge effects in graphene devices. *Nature nanotechnology*, 3(8):486–490, August 2008.

[89] T. Mueller, F. Xia, and P. Avouris. Graphene photodetectors for high-speed optical communications. *Nature Photonics*, 4(5):297–301, March 2010.

[90] J. Yan, M.-H. Kim, J. A. Elle, A. B. Sushkov, G. S. Jenkins, H. M. Milchberg, M. S. Fuhrer, and H. D. Drew. Dual-gated bilayer graphene hot-electron bolometer. *Nature Nanotechnology*, 7(7):472–478, 2012.

[91] C. B. McKitterick, D. E. Prober, and B. S. Karasik. Performance of graphene thermal photon detectors. *Journal of Applied Physics*, 113(4):044512, January 2013.

[92] T. Zhang, P. Cheng, W.-J. Li, Y.-J. Sun, G. Wang, X.-G. Zhu, K. He, L. Wang, X. Ma, X. Chen, Y. Wang, Y. Liu, H.-Q. Lin, J.-F. Jia, and Q.-K. Xue. Superconductivity in one-atomic-layer metal films grown on Si(111). *Nature Physics*, 6(2):104–108, January 2010.

[93] N. Staley, J. Wu, P. Eklund, Y. Liu, L. Li, and Z. Xu. Electric field effect on superconductivity in atomically thin flakes of $NbSe_2$. *Physical Review B*, 80(18):184505, November 2009.

[94] B. Radisavljevic, A. Radenovic, J. Brivio, V. Giacometti, and A. Kis. Single-layer MoS_2 transistors. *Nature nanotechnology*, 6(3):147–150, 2011.

[95] Y. Cao, A. Mishchenko, G. L. Yu, E. Khestanova, A. P. Rooney, E. Prestat, A. V. Kretinin, P. Blake, M. B. Shalom, C. Woods, J. Chapman, G. Balakrishnan, I. V. Grigorieva, K. S. Novoselov, B. A. Piot, M. Potemski, K. Watanabe, T. Taniguchi, S. J. Haigh, A. K. Geim, and R. V. Gorbachev. Quality Heterostructures from Two-Dimensional Crystals Unstable in Air by Their Assembly in Inert Atmosphere. *Nano Letters*, 15(8):4914–4921, 2015.

[96] X. Gan, R.-J. Shiue, Y. Gao, I. Meric, T. F. Heinz, K. Shepard, J. Hone, S. Assefa, and D. Englund. Chip-integrated ultrafast graphene photodetector with high responsivity. *Nature Photonics*, 7(11):883–887, September 2013.

[97] M. Furchi, A. Urich, A. Pospischil, G. Lilley, K. Unterrainer, H. Detz, P. Klang, A. M. Andrews, W. Schrenk, G. Strasser, and T. Mueller. Microcavity-integrated graphene photodetector. *Nano Letters*, 12(6):2773–2777, 2012.

[98] M. Engel, M. Steiner, A. Lombardo, A. C. Ferrari, H. V. Löhneysen, P. Avouris, and R. Krupke. Light–matter interaction in a microcavity-controlled graphene transistor. *Nature Communications*, 3(May):906, 2012.

[99] M. van de Kerkhof, H. Jasper, L. Levasier, R. Peeters, R. van Es, J.-W. Bosker, A. Zdravkov, E. Lenderink, F. Evangelista, P. Broman, B. Bilski, and T. Last. Enabling sub-10nm node lithography: presenting the NXE:3400B EUV scanner. *Proc. of SPIE*, 10143(March 2017):101430D–1.

[100] Z. G. Cambaz, G. Yushin, S. Osswald, V. Mochalin, and Y. Gogotsi. Noncatalytic synthesis of carbon nanotubes, graphene and graphite on SiC. *Carbon*, 46(6):841–849, 2008.

[101] K. S. Kim, Y. Zhao, H. Jang, S. Y. Lee, J. M. Kim, K. S. Kim, J. H. Ahn, P. Kim, J. Y. Choi, and B. H. Hong. Large-scale pattern growth of graphene films for stretchable transparent electrodes. *Nature*, 457(7230):706–710, 2009.

[102] Y. Hernandez, V. Nicolosi, M. Lotya, F. M. Blighe, Z. Sun, S. De, I. T. McGovern, B. Holland, M. Byrne, Y. K. Gun'ko, J. J. Boland, P. Niraj, G. Duesberg, S. Krishnamurthy, R. Goodhue, J. Hutchison, V. Scardaci, A. C. Ferrari, and J. N. Coleman.

High-yield production of graphene by liquid-phase exfoliation of graphite. *Nature Nanotechnology*, 3(9):563–568, 2008.

[103] P. Blake, E. W. Hill, A. H. Castro Neto, K. S. Novoselov, D. Jiang, R. Yang, T. J. Booth, and A. K. Geim. Making graphene visible. *Applied Physics Letters*, 91(6):063124, August 2007.

[104] F. Lemarchand. Online. http://refractiveindex.info/database/data/main/SiO2 /Lemarchand.yml, 2013.

[105] A. C. Ferrari, J. C. Meyer, V. Scardaci, C. Casiraghi, M. Lazzeri, F. Mauri, S. Piscanec, D. Jiang, K. S. Novoselov, S. Roth, and A. K. Geim. Raman Spectrum of Graphene and Graphene Layers. *Physical Review Letters*, 97(18):187401, October 2006.

[106] Y. Y. Wang, Z. H. Ni, T. Yu, Z. X. Shen, H. M. Wang, Y. H. Wu, W. Chen, and A. T. S. Wee. Raman studies of monolayer graphene: The substrate effect. *Journal of Physical Chemistry C*, 112(29):10637–10640, 2008.

[107] A. C. Ferrari and D. M. Basko. Raman spectroscopy as a versatile tool for studying the properties of graphene. *Nature Nanotechnology*, 8(4):235–246, 2013.

[108] F. Bonaccorso, A. Lombardo, T. Hasan, Z. Sun, L. Colombo, and A. C. Ferrari. Production and processing of graphene and 2d crystals. *Materials Today*, 15(12):564–589, 2012.

[109] A. Castellanos-Gomez, M. Buscema, R. Molenaar, V. Singh, L. Janssen, H. S. J. van der Zant, and G. A. Steele. Deterministic transfer of two-dimensional materials by all-dry viscoelastic stamping. *2D Materials*, 1(1):011002, April 2014.

[110] R. Bhatia, S. Chase, S. Edgington, J. Glenn, W. Jones, A. Lange, B. Maffei, A. Mainzer, P. Mauskopf, B. Philhour, and B. Rownd. A three-stage helium sorption refrigerator for cooling of infrared detectors to 280 mK. *Cryogenics*, 40(11):685–691, January 2000.

[111] S. J. Byrnes. Multilayer optical calculations. *arXiv*, (1603.02720), 2016.

[112] M. E. Levinshtein, S. L. Rumyantsev, and M. S. Shur. *Properties of advanced semiconductor materials : GaN, AlN, InN, BN, SiC, SiGe*. John Wiley & Sons, 2001.

[113] A. R. Beal, H. P. Hughes, and W. Y. Liang. The reflectivity spectra of some group V A transition metal oxides. *Journal of Physics C: Solid State Physics*, 8:4236, 1975.

[114] H. H. Li. Refractive index of silicon and germanium and its wavelength and temperature derivatives. *Journal of Physical and Chemical Reference Data*, 9(3):561–658, July 1980.

[115] N. N. Manova, E. O. Smirnov, K. Yu P, A. A. Korneev, and G. N. Goltsman. Superconducting photon counter for nanophotonics applications. *Journal of Physics: Conference Series*, 1410(1):012147, December 2019.

[116] A. Engel, J. J. Renema, K. Il'in, and A. Semenov. Detection mechanism of superconducting nanowire single-photon detectors. *Superconductor Science and Technology*, 28(11):114003, November 2015.

[117] K. Inderbitzin, A. Engel, A. Schilling, K. Il'in, and M. Siegel. An ultra-fast superconducting Nb nanowire single-photon detector for soft x-rays. *Applied Physics Letters*, 101(16):162601, October 2012.

[118] B. Korzh, Q.-Y. Zhao, J. P. Allmaras, S. Frasca, T. M. Autry, E. A. Bersin, A. D. Beyer, R. M. Briggs, B. Bumble, M. Colangelo, G. M. Crouch, A. E. Dane, T. Gerrits, A. E. Lita, F. Marsili, G. Moody, C. Peña, E. Ramirez, J. D. Rezac, N. Sinclair, M. J. Stevens, A. E. Velasco, V. B. Verma, E. E. Wollman, S. Xie, D. Zhu, P. D. Hale, M. Spiropulu, K. L. Silverman, R. P. Mirin, S. W. Nam, A. G. Kozorezov, M. D. Shaw, and K. K. Berggren. Demonstration of sub-3 ps temporal resolution with a superconducting nanowire single-photon detector. *Nature Photonics*, 14(4):250–255, April 2020.

[119] D. Kufer, I. Nikitskiy, T. Lasanta, G. Navickaite, F. H. Koppens, and G. Konstantatos. Hybrid 2D-0D MoS_2-PbS quantum dot photodetectors. *Advanced Materials*, 27(1):176–180, 2015.

[120] J. Yao, Z. Zheng, and G. Yang. All-Layered 2D Optoelectronics: A High-Performance UV–vis–NIR Broadband SnSe Photodetector with Bi_2Te_3 Topological Insulator Electrodes. *Advanced Functional Materials*, 27(33):1–10, 2017.

[121] E. D. Walsh, D. K. Efetov, G.-H. Lee, M. Heuck, J. Crossno, T. A. Ohki, P. Kim, D. Englund, and K. C. Fong. Graphene-Based Josephson-Junction Single-Photon Detector. *Physical Review Applied*, 8(2):024022, August 2017.

[122] E. Revolinsky, G. Spiering, and D. Beerntsen. Superconductivity in the niobium-selenium system. *Journal of Physics and Chemistry of Solids*, 26(6):1029–1034, June 1965.

[123] J. S. Bunch, S. S. Verbridge, J. S. Alden, A. M. van der Zande, J. M. Parpia, H. G. Craighead, and P. L. McEuen. Impermeable Atomic Membranes from Graphene Sheets. *Nano Letters*, 8(8):2458–2462, August 2008.

[124] R. R. Nair, P. Blake, A. N. Grigorenko, K. S. Novoselov, T. J. Booth, T. Stauber, N. M. R. Peres, and A. K. Geim. Fine Structure Constant Defines Visual Transparency of Graphene. *Science*, 320(5881):1308–1308, June 2008.

[125] K. F. Mak, L. Ju, F. Wang, and T. F. Heinz. Optical spectroscopy of graphene: From the far infrared to the ultraviolet. *Solid State Communications*, 152(15):1341–1349, August 2012.

[126] D. Jiang, T. Hu, L. You, Q. Li, A. Li, H. Wang, G. Mu, Z. Chen, H. Zhang, G. Yu, J. Zhu, Q. Sun, C. Lin, H. Xiao, X. Xie, and M. Jiang. High-Tc superconductiv-

ity in ultrathin $Bi_2Sr_2CaCu_2O_{8+x}$ down to half-unit-cell thickness by protection with graphene. *Nature communications*, 5:5708, 2014.

[127] A. Agresti and B. A. Coull. Approximate is Better than "Exact" for Interval Estimation of Binomial Proportions. *The American Statistician*, 52(2):119–126, May 1998.

[128] T. Dvir, F. Massee, L. Attias, M. Khodas, M. Aprili, C. H. Quay, and H. Steinberg. Spectroscopy of bulk and few-layer superconducting $NbSe_2$ with van der Waals tunnel junctions. *Nature communications*, 9(1):598, 2018.

[129] D. K. Efetov, L. Wang, C. Handschin, K. B. Efetov, J. Shuang, R. Cava, T. Taniguchi, K. Watanabe, J. Hone, C. R. Dean, and P. Kim. Specular interband Andreev reflections at van der Waals interfaces between graphene and $NbSe_2$. *Nature Physics*, 12(4):328–332, April 2016.

[130] J. Yang, A. Kerman, E. Dauler, V. Anant, K. Rosfjord, and K. Berggren. Modeling the Electrical and Thermal Response of Superconducting Nanowire Single-Photon Detectors. *IEEE Transactions on Applied Superconductivity*, 17(2):581–585, June 2007.

[131] J. Crank and P. Nicolson. A practical method for numerical evaluation of solutions of partial differential equations of the heat-conduction type. *Mathematical Proceedings of the Cambridge Philosophical Society*, 43(01):50, 1947.

[132] W. Ford. Algorithms. In *Numerical Linear Algebra with Applications*, chapter 9, pages 163–179. Elsevier, Boston, 2015.

[133] D. W. Peaceman and H. H. Rachford, Jr. The Numerical Solution of Parabolic and Elliptic Differential Equations. *Journal of the Society for Industrial and Applied Mathematics*, 3(1):28–41, March 1955.

[134] C. L. Huang, J.-Y. Lin, Y. T. Chang, C. P. Sun, H. Y. Shen, C. C. Chou, H. Berger, T. K. Lee, and H. D. Yang. Experimental evidence for a two-gap structure of superconducting $NbSe_2$: A specific-heat study in external magnetic fields. *Physical Review B*, 76(21):212504, 2007.

[135] E. Boaknin. *Thermal conduction in the vortex state of unconventional superconductors*. Doctoral thesis, University of Toronto, 2003.

[136] E. Boaknin, M. A. Tanatar, J. Paglione, D. Hawthorn, F. Ronning, R. W. Hill, M. Sutherland, L. Taillefer, J. Sonier, S. M. Hayden, and J. W. Brill. Heat Conduction in the Vortex State of $NbSe_2$: Evidence for Multiband Superconductivity. *Physical Review Letters*, 90(11):117003, 2003.

[137] P. Amari, C. Feuillet-Palma, A. Jouan, F. Couëdo, N. Bourlet, E. Géron, M. Malnou, L. Méchin, A. Sharafiev, J. Lesueur, and N. Bergeal. High-temperature superconducting nano-meanders made by ion irradiation. *Superconductor Science and Technology*, 31(1):015019, January 2018.

[138] C. Cirillo, M. Caputo, L. Parlato, M. Ejrnaes, D. Salvoni, R. Cristiano, G. P. Pepe, and C. Attanasio. Ultrathin superconducting NbRe microstrips with hysteretic voltage-current characteristic. *Low Temperature Physics*, 46(4):379–382, 2020.

[139] J. Chiles, S. M. Buckley, A. Lita, V. B. Verma, J. Allmaras, B. Korzh, M. D. Shaw, J. M. Shainline, R. P. Mirin, and S. W. Nam. Superconducting microwire detectors based on WSi with single-photon sensitivity in the near-infrared. *Applied Physics Letters*, 116(24):242602, June 2020.

[140] Q. Wang, J. Guo, Z. Ding, D. Qi, J. Jiang, Z. Wang, W. Chen, Y. Xiang, W. Zhang, and A. T. Wee. Fabry-Perot Cavity-Enhanced Optical Absorption in Ultrasensitive Tunable Photodiodes Based on Hybrid 2D Materials. *Nano Letters*, 17(12):7593–7598, 2017.

[141] X. Wang, Z. Cheng, K. Xu, H. K. Tsang, and J. B. Xu. High-responsivity graphene/silicon-heterostructure waveguide photodetectors. *Nature Photonics*, 7(11):888–891, 2013.

[142] N. Flöry, P. Ma, Y. Salamin, A. Emboras, T. Taniguchi, K. Watanabe, J. Leuthold, and L. Novotny. Waveguide-integrated van der Waals heterostructure photodetector at telecom wavelengths with high speed and high responsivity. *Nature Nanotechnology*, 15(2):118–124, February 2020.

[143] J. F. Gonzalez Marin, D. Unuchek, K. Watanabe, T. Taniguchi, and A. Kis. MoS_2 photodetectors integrated with photonic circuits. *npj 2D Materials and Applications*, 3(1):14, December 2019.

[144] E. D. Walsh, W. Jung, G.-H. Lee, D. K. Efetov, B.-I. Wu, K. F. Huang, T. A. Ohki, T. Taniguchi, K. Watanabe, P. Kim, D. Englund, and K. C. Fong. Josephson-junction infrared single-photon detector. *arXiv*, (2011.02624), November 2020.

[145] G. H. Lee, D. K. Efetov, W. Jung, L. Ranzani, E. D. Walsh, T. A. Ohki, T. Taniguchi, K. Watanabe, P. Kim, D. Englund, and K. C. Fong. Graphene-based Josephson junction microwave bolometer. *Nature*, 586(7827):42–46, 2020.

[146] N. Curtz, E. Koller, H. Zbinden, M. Decroux, L. Antognazza, Ø. Fischer, and N. Gisin. Patterning of ultrathin YBCO nanowires using a new focused-ion-beam process. *Superconductor Science and Technology*, 23(4):045015, April 2010.

[147] O. Shcherbakova, A. Pan, S. Gorman, S. Fedoseev, I. Golovchanskiy, and S. Dou. Inhomogeneities in $YBa_2Cu_3O_7$ thin films with reduced thickness. *Physica C: Superconductivity*, 479:102–105, September 2012.

[148] R. Arpaia, D. Golubev, R. Baghdadi, R. Ciancio, G. Dražić, P. Orgiani, D. Montemurro, T. Bauch, and F. Lombardi. Transport properties of ultrathin YBa_2Cu_3 $O_{7-\delta}$ nanowires: A route to single-photon detection. *Physical Review B*, 96(6):1–11, 2017.

[149] Y. Yu, L. Ma, P. Cai, R. Zhong, C. Ye, J. Shen, G. D. Gu, X. H. Chen, and Y. Zhang. High-temperature superconductivity in monolayer $Bi_2Sr_2CaCu_2O_{8+\delta}$. *Nature*, 575(7781):156–163, 2019.

[150] P. Seifert, J. R. D. Retamal, R. L. Merino, H. H. Sheinfux, J. N. Moore, M. A. Aamir, T. Taniguchi, K. Wantanabe, K. Kadowaki, M. Artiglia, M. Romagnoli, and D. K. Efetov. A liquid nitrogen cooled superconducting transition edge sensor with ultra-high responsivity and GHz operation speeds. *arXiv*, (2006.03130), June 2020.

[151] H. Li, H. Cai, E. Y. Cho, S. J. McCoy, Y.-T. Wang, J. C. LeFebvre, Y. W. Zhou, and S. A. Cybart. High-transition-temperature nanoscale superconducting quantum interference devices directly written with a focused helium ion beam. *Applied Physics Letters*, 116(7):070601, February 2020.

[152] P. Vines, K. Kuzmenko, J. Kirdoda, D. C. Dumas, M. M. Mirza, R. W. Millar, D. J. Paul, and G. S. Buller. High performance planar germanium-on-silicon single-photon avalanche diode detectors. *Nature Communications*, 10(1), 2019.

[153] G. G. Taylor, D. Morozov, N. R. Gemmell, K. Erotokritou, S. Miki, H. Terai, and R. H. Hadfield. Photon counting LIDAR at 2.3µm wavelength with superconducting nanowires. *Optics Express*, 27(26):38147, 2019.

[154] L. K. Shalm, E. Meyer-Scott, B. G. Christensen, P. Bierhorst, M. A. Wayne, M. J. Stevens, T. Gerrits, S. Glancy, D. R. Hamel, M. S. Allman, K. J. Coakley, S. D. Dyer, C. Hodge, A. E. Lita, V. B. Verma, C. Lambrocco, E. Tortorici, A. L. Migdall, Y. Zhang, D. R. Kumor, W. H. Farr, F. Marsili, M. D. Shaw, J. A. Stern, C. Abellán, W. Amaya, V. Pruneri, T. Jennewein, M. W. Mitchell, P. G. Kwiat, J. C. Bienfang, R. P. Mirin, E. Knill, and S. W. Nam. Strong Loophole-Free Test of Local Realism. *Physical Review Letters*, 115(25):250402, December 2015.

[155] H. Semenenko, P. Sibson, A. Hart, M. G. Thompson, J. G. Rarity, and C. Erven. Chip-based measurement-device-independent quantum key distribution. *Optica*, 7(3):238, March 2020.

[156] J. Wang, F. Sciarrino, A. Laing, and M. G. Thompson. Integrated photonic quantum technologies. *Nature Photonics*, 14(5):273–284, May 2020.